UNIVERSITÉ DE GENÈVE
Département de physique nucléaire et corpusculaire

FACULTÉ DES SCIENCES
Prof.M.N.Kienzle-Focacci

Measurement of the $e^+e^- \to W^+W^-$ Cross Section and the W-boson Spin Density Matrix at LEP

THÈSE

présentée à la Faculté des Sciences de l'Université de Genève
pour obtenir le grade de Docteur ès Sciences, mention Physique

par

Evelyne DELMEIRE
de Gent (Belgique)

Thèse N^o 3588

GENÈVE

2004

Contents

Remerciements

Cette thèse de doctorat est le résultat de la collaboration de beaucoup de personnes.

En tout premier, je tiens à remercier sincèrement mon directeur de thèse, Prof.Maria-Novella Kienzle-Focacci, pour son confiance dans mon travail, son enthousiasme et ses encouragements.

Je voudrais aussi exprimer ma gratitude envers mes membres de jurie de thése, Dr.Jean-Jacques Blaising (CERN), Dr.Philippe Busson (Laboratoire Leprince-Ringuet, Ecole Polytechnique, Paris) et Prof.Martin Pohl (Université de Genève), pour le temps qu'ils ont consacré à la lecture attentive de ce manuscript et pour leurs commentaires constructifs.

Ce travail de thèse n'aurait jamais été possible sans les membres du groupe d'analyse de physique de W de l'expérience L3, qui m'ont fait part de leurs connaisances. Des remerciements speciaux vont à Luca Malgeri qui était toujours disponible à libérer du temps pour repondre à mes questions et à présenter des différents points de vue aux problèmes auxquels j'étais confrontée. Je suis aussi reconnaissante envers Arno Straessner, Mark Dierckxsens, John Field, Sonia Natale, Salvatore Mele, Stefano Villa et Natalia Batalova pour les nombreuses discussions. Ma gratitude va aussi aux membres du groupe SDM du LEP, Prof.Cathérine De Clercq (DELPHI) et Dr.Ian Bailey (OPAL) pour les discussions fructueuses lors des réunions au CERN.

Ensuite, je voudrais exprimer mon admiration pour les ingénieurs, informaticiens, physiciens et les techniciens qui se sont investis pour faire fonctionner le colisionneur LEP et l'expérience L3. Je suis particulièrement reconnaissante envers Alexander Eline et Yann-Loic Meunier qui étaient toujours prêts à resoudre mes problèmes d'informatique avec un grand sourire. Un grand merci aussi aux sécretaires du DPNC, Peggy Argentin et Cathérine Blanchard, pour leur dévouement à repondre à toutes mes questions.

Pour tous les moments joyeux et plus difficiles, passés à Genève, je remercie Eduardo Cortina pour m'avoir courageusement soutenu durant les derniers mois fievreux de finalisation de l'analyse et de préparation de soutenance de thèse, Gersende Prior, pour les

moments inoubliables en Suisse et à l'étranger lors des nombreux voyages, Valerie Cardona et Simone Berchtold pour leur précieuse amitié, Pablo Saiz, Sue Nicol, Ans Pardons, Nicole Bangert et Filip Moortgat, pour tous les weekends agréables, Cathelijne Bal, Andrea Valassi, Roberto Chierici et Paolo Azzurri, pour toutes les invitations aux fêtes et aux BBQ, Miran Djordjevic et Rikard Sandstrom, pour les nombreux pauses café et sorties à la *Demi-Lune, Café Sud, La Sixième Heure* et *Fleur de Lys*, Bertrand Echenard pour ses commentaires très utiles pour la soutenance de thèse, Philippe Azarrello et Mercedes Paniccia, pour avoir voulu partager le bureau avec moi et toutes mes états d'esprit, et finalement mon chat Chaussette, pour toutes ses betises et ses calins...

Evelyne Delmeire

Résumé

La physique des hautes énergies étudie les composants élémentaires de la matière et leurs interactions. Les connaissances acquises jusqu'à présent sont incorporées dans un modèle appelé le Modèle Standard de la physique des particules élémentaires.

Selon ce modèle, ils existent quatre interactions fondamentales dans la nature: l'interaction forte, l'interaction faible, l'interaction electromagnétique et l'interaction gravitationelle. Chacune de ces forces est le résultat de l'échange d'un boson vecteur de jauge associé à la symétrie fondamentale $SU(3)_c \otimes SU(2)_L \otimes U(1)_Y$. L'interaction forte est portée par huit gluons. Les gluons sont responsables de la formation d'états liées de trois quarks, les baryons, et de paires de quark-antiquark, les mésons. Dans l'interaction electromagnetique, un photon sans masse est échangée. Les porteurs de l'interaction faible sont les bosons vecteurs massifs W^+, W^- et Z^0, observés pour la première fois en 1983 par les expériences UA1 [1] et UA2 [2] au CERN. Le porteur hypothétique de l'interaction gravitationelle, le graviton, est recherchée dans les ondes gravitationelles.

Selon le Modèle Standard, la matière est composée de deux types de particules: les quarks et les leptons. Ce sont des particules élémentaires de spin 1/2, appelées fermions. Les fermions apparaissent dans trois familles de plus en plus massives

$$\begin{pmatrix} \nu_e \\ e \end{pmatrix} \quad \begin{pmatrix} \nu_\mu \\ \mu \end{pmatrix} \quad \begin{pmatrix} \nu_\tau \\ \tau \end{pmatrix}$$

$$\begin{pmatrix} u \\ d \end{pmatrix} \quad \begin{pmatrix} c \\ s \end{pmatrix} \quad \begin{pmatrix} t \\ b \end{pmatrix}$$

Les quarks ont des charges fractionnaires, +2/3 et -1/3, et participent à toutes les interactions. Les leptons chargés, l'électron, le muon et le tau, ont des charges unitaires mais n'interviennent pas dans l'interaction forte.

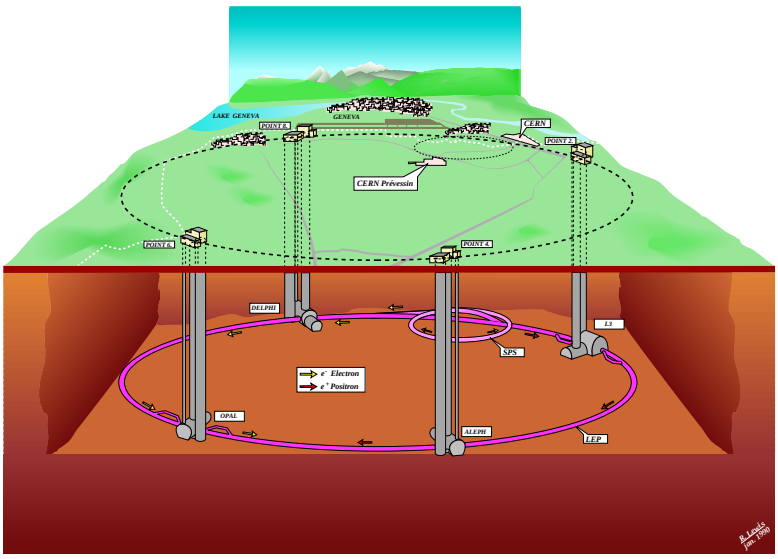

Figure 1: *Le collisionneur électron-positron LEP et les quatres expériences: ALEPH, DELPHI, L3 et OPAL.*

Les neutrinos interagissent seulement par l'interaction faible. La mesure du nombre de neutrinos au LEP exclut une quatrième famille de neutrinos légers:

$$N_\nu = 2.994 \pm 0.012 \text{ [3]}$$

Le boson de Higgs, nécessaire pour expliquer l'origine de la masse des particules et en particulier celle des bosons $W^\pm$ et Z^0, est la pièce manquante du Modèle Standard. A présent, il n'existe aucune preuve expérimentale incontestée de l'existence du boson de Higgs, au plus quelques candidats ont été observés lors des dernières périodes de la prise de données au LEP.

Le collisionneur électron-positron LEP est situé à la frontière franco-suisse, près de Genève (Figure 1). Il est composé d'un accélérateur électron-positron et d'un anneau de stockage d'une circonférence de 26.7 km, à des profondeurs entre 50 mètres et 150 mètres. La construction du LEP a commencée au CERN dans les années 80. Durant la première période de prise de données LEP1 (1989-1995), l'énergie dans le centre-de-masse, $\sqrt{s}$, a été fixée autour de 90 GeV, la masse du boson vecteur Z^0, et environ 16 millions de désintégration de Z^0 ont été observées par les quatre expériences LEP: ALEPH [4], DELPHI [5], L3 [6] and OPAL [7]. Plusieurs mesures de haute précision ont montré un excellent accord avec les predictions du Modèle Standard.

En 1996, le seuil de production de paires de bosons vecteurs W, 161 GeV, a été franchi, ce qui a rendu possible l'étude du boson W jusqu'à des énergies de centre-de masse de 209 GeV. Environ 40 000 désintégrations de paires de W ont été enregistrées par les quatre expériences LEP et les paramètres du boson W sont mesurés avec une bonne précision: la masse du W, les rapports d'embranchement et les couplages triple bosons de gauge.

Les mesures présentées dans cette thèse utilisent les données prises par le détecteur L3 durant la période LEP2 (1996-2000). Avec ces 12 mètres de diamètre et ces 12 mètres de longueur, ce détecteur était le plus grand des quatre détecteurs LEP. Il a été désigné pour des mesures à haute résolution d'électrons, de photons et de muons mais a une structure globale commune à toutes les expériences de physique de particules des hautes énergies. Il est composé de plusieurs couches de sous-détecteurs avec des rôles particulières dans la reconstruction de l'événement de physique.

Le travail de thèse est structuré en 7 Chapitres. Après une introduction, la physique du boson W est approfondie dans le Chapitre 2 qui établit le cadre théorique du Modèle Standard. Le Chapitre 3 résume les programmes de simulation Monte Carlo, et le Chapitre 4 est dédié à la description du détecteur L3. La mesure de la section efficace de production de paires de W est présentée dans le Chapitre 5, la mesure de la matrice de densité de spin du W (SDM) dans le Chapitre 6. L'invariance du processus de désintégration du W sous symétrie CPT et CP est testée et la polarisation du boson W est déterminée. Le chapitre 7 donne les résultats de la mesure des couplages triple bosons de jauge ainsi qu'une étude préliminaire des possibilités offertés par la méthode SDM pour poser des limites sur les couplages qui violent la symétrie CP.

La production de paires de boson W

Au LEP, les bosons W sont produits principalement en paires selon le processus $e^+e^- \to W^+W^-$, est dominante. Les diagrammes de Feynman pour ce processus sont présentés dans Figure 2. Chaque boson W peut se désintégrer en paire de quark-antiquark ($W^- \to \bar{u}d$ or $\bar{c}s$) ou en paire de lepton-antilepton ($W^- \to l^-\bar{\nu}_l$, $l = e, \mu, \tau$), notés qq and $l\nu$ respectivement. Ceci mène à 10 états finaux différents: un état final hadronique, $qqqq(\gamma)$, trois états semi-leptoniques, $qql\nu(\gamma)$, et six états leptoniques $l\nu l\nu(\gamma)$.

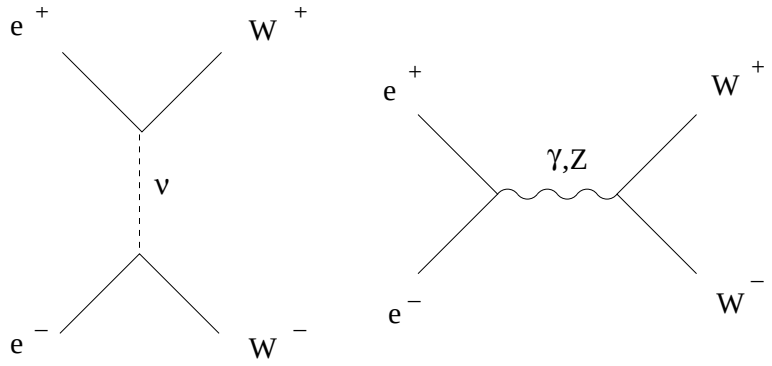

Figure 2: *Le processus de production de bosons W dominant est la production en paires par l'échange d'un neutrino (à gauche) ou par l'échange d'un photon ou boson Z^0 (à droite).*

Sélection des événements $e^+e^- \to qq\tau\nu(\gamma)$

La topologie typique d'un événement $e^+e^- \to qq\tau\nu(\gamma)$ est

- deux gerbes hadroniques, presque dos-à-dos, de grande multiplicité en particules
- un lepton énergétique et isolé, un électron ou un muon,
  issu de $\tau \to e\nu_e\nu_\tau$ (17.8%) ou de $\tau \to \mu\nu_\mu\nu_\tau$ (17.4%)

  ou

  une gerbe de τ de petite multiplicité en particules issue de $\tau \to$ hadrons ν_τ (64.8%)
- de l'énergie et de la quantité de mouvement manquantes, dûes à l'émission de neutrinos

Les coupures de selection font une utilisation optimale des ces caractéristiques afin de mieux distinguer le signal du bruit de fond. La section efficace mesurée de la production de paires de W dans l'état final $qq\tau\nu(\gamma)$ en fonction de $\sqrt{s}$, est présentée dans la Figure 3. Etant donnée la précision expérimentale, les données se trouvent être en bon accord avec la prédiction du Modèle Standard.

Mesure de la section efficace totale de production de paires W

La section efficace totale pour la production de paires de W, σ_{WW}, est obtenue en utilisant un fit de maximum de vraissemblance à partir des nombres d'événements selectionnées dans les 10 états finaux. Une désintégration du boson W selon le Modèle Standard en paires de quark-antiquark et lepton-antileptons connus est supposée. La section efficace WW totale mesurée σ_{WW} est présentée dans la Figure 4. Un excellent accord est trouvé avec le Modèle Standard.

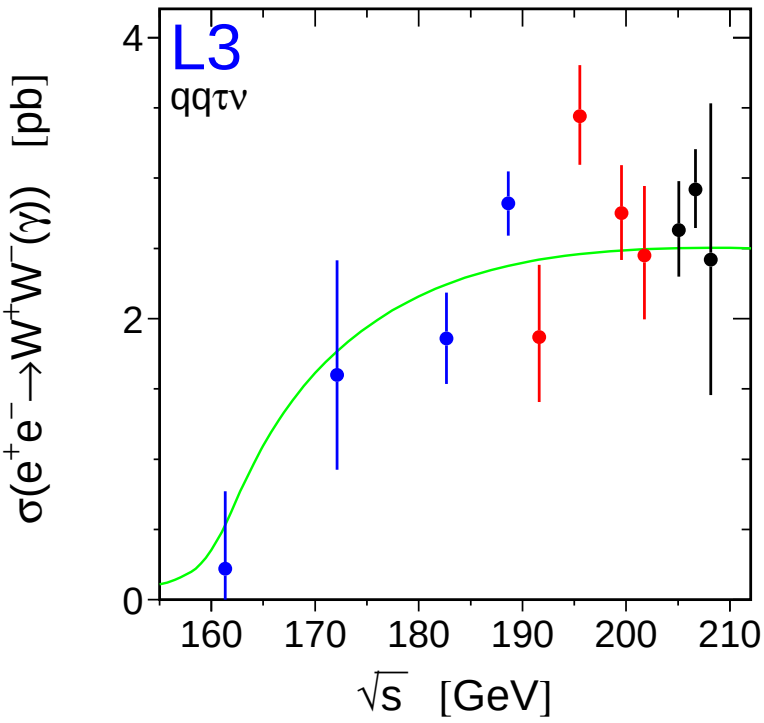

Figure 3: *La section efficace mesurée du process* $e^+e^- \to W^+W^- \to qq\tau\nu(\gamma)$ *en fonction de l'énergie dans le centre-de-masse,* $\sqrt{s}$*. Les points représentent les données prises par l'expérience L3 à des énergies de 161 GeV à 209 GeV, la ligne continue donne la prediction du Modèle Standard. Les barres d'erreur combinent l'incertitude statistique et systématique.*

Rapports d'embranchement de la désintégration du W

Les rapports d'embranchement de la désintégration du W sont obtenus par le même fit de maximum de vraissemblance que la section efficace totale σ_{WW} mais sans utiliser les contraintes predites par le Modèle Standard. L'universalité leptonique pour le courant chargé dans la désintégration du W est aussi testée. Le resultat est présentée dans Table 1. Les rapports d'embranchement leptoniques sont en accord avec le Modèle Standard et sont individuellement compatibles avec le rapport moyen dans 2.4 déviations standard, ce qui confirme l'hypothèse d'universalité leptonique. Les rapports d'embranchement hadroniques sont également en accord avec la prédiction du Modèle Standard.
Les rapports d'embranchement de la désintégration du W dépendent des éléments de la

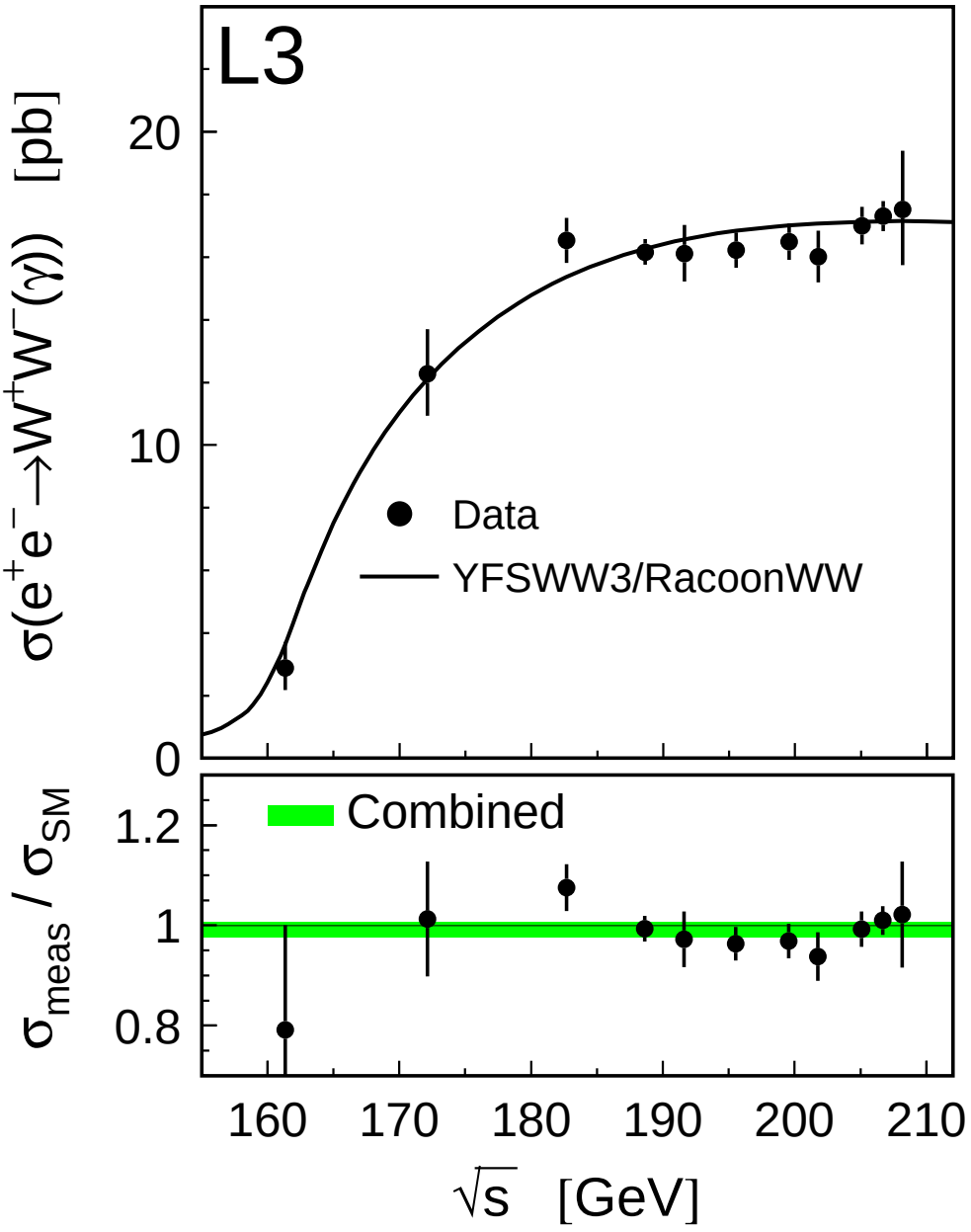

Figure 4: Haut: *La section efficace WW totale mesurée, σ_{WW}, du processus $e^+e^- \to W^+W^- \to ffff(\gamma)$ en fonction de l'énergie de centre-de-masse. Les points représentent les données prises par l'expérience L3 à des énergies de 161 GeV à 209 GeV. La ligne continue donne la prediction du Modèle Standard Les barres d'erreur combinent l'incertitude statistique et systématique.* Bas: *Le rapport de la section efficace mesurée et la prediction du Modèle Standard. La bande grise donne la valeur combiné avec l'incertitude totale* $R = 0.992 \pm 0.015$.

Rapport d'embranchement	Non-Universalité Leptonique	Universalité leptonique	Modèle Standard
Br($W \to e\nu$) (%)	$10.78 \pm 0.29 \pm 0.13$	—	
Br($W \to \mu\nu$) (%)	$10.03 \pm 0.29 \pm 0.12$	—	
Br($W \to \tau\nu$) (%)	$11.89 \pm 0.40 \pm 0.20$	—	
Br($W \to l\nu$) (%)	—	$10.83 \pm 0.14 \pm 0.10$	10.83
Br($W \to qq$) (%)	$67.30 \pm 0.42 \pm 0.30$	$67.50 \pm 0.42 \pm 0.30$	67.51

Table 1: *Les rapports d'embranchement de la désintégration du W avec et sans hypothèse d'universalité leptonique. La prédiction du Modèle Standard est aussi montrée. La première erreur est statistique, la deuxième systématique.*

matrice de mélange des quarks, dite matrice de Cabibbo-Kobayashi-Maskawa [8]

$$V_{CKM} = \begin{pmatrix} V_{ud} & V_{us} & V_{ub} \\ V_{cd} & V_{cs} & V_{cb} \\ V_{td} & V_{ts} & V_{tb} \end{pmatrix}$$

qui relient les états propres d'interaction faible aux états propres de masse/saveur du quark. Utilisant les moyennes mondiales actuelles [3] pour les autres éléments ainsi que leurs incertitudes, la valeur de V_{cs} derivée est

$$V_{cs} = \ 0.977 \ \pm \ 0.020 \ (stat.) \ \pm \ 0.014 \ (syst.)$$

qui est dominée par l'incertitude statistique sur les rapports d'embranchement.

Mesure de la matrice de densité de spin du W

Les éléments de la matrice de densité de spin du W sont obtenus en sommant les hélicités d'un des bosons W, par convention le W^+,

$$\rho^{W^-}_{\tau_1\tau_1'}(s, \cos\theta_{W^-}) \equiv \sum_{\tau_2} \rho_{\tau_1\tau_1'\tau_2\tau_2}(s, \cos\theta_{W^-}) = \sum_{\tau_2} \frac{\sum_\lambda F^\lambda_{\tau_1\tau_2} \ (F^\lambda_{\tau_1'\tau_2'})^\star}{\sum_{\lambda,\tau_1,\tau_2} |F^\lambda_{\tau_1\tau_2}|^2}$$

où $F^\lambda_{\tau_1\tau_2}$ est l'amplitude d'hélicité pour la production d'une paire de bosons W avec hélicités τ_1 et τ_2. Les éléments diagonaux sont réels et donnent la probabilité de produire un W^- avec une polarisation transverse (ρ_{++} et ρ_{--}) ou avec une polarisation longitudinale (ρ_{00}). Les éléments non-diagonaux mesurent l'interférence entre les différentes

amplitudes d'hélicité et diffèrent de zéro si le W est produit comme une superposition linéaire d'états d'hélicité plutôt qu'un état bien défini, comme prédit par le Modèle Standard. La Figure 5 montre la mesure expérimentale des éléments de la matrice de densité de spin du W en fonction du cosinus de l'angle de production du W^-, $\cos\theta_{W^-}$. Un bon accord est trouvé avec la prédiction du Modèle Standard.

Tests d'invariance sous symétrie CPT et CP

L'analyse de la matrice SDM permet de tester, de façon indépendante d'un modèle, l'invariance de la désintégration du W sous des symétries CPT et CP. Toutes les deux sont conservées dans le Modèle Standard. Ces tests sont présentés dans la Figure 6. En considérant l'incertitude totale, la somme aussi bien que la différence sont compatibles avec zéro et confirment l'absence de violation de CPT et CP au niveau d'arbre, comme prédite par le Modèle Standard.

Mesure de la polarisation du W

Contrairement au photon, qui a seulement deux états de polarisation transverse, le boson W a aussi une polarisation longitudinale. Elle est générée lors de la brisure de la symétrie electrofaible par le mécanisme de Higgs qui fait aussi apparaître le fameux boson de Higgs. Ainsi, la mesure de la fraction d'hélicité transverse et longitudinale, fournit un test de la validité du Modèle Standard. La Figure 7 montre la polarisation en fonction du cosinus de l'angle de production du W^-, $\cos\theta_{W^-}$. Les resultats sont compatibles avec la mesure precédente, utilisant une methode de fit [9] et confirment aussi l'existence de la polarisation longitudinale du boson W.

Conclusions

La prise de données à hautes énergies au LEP a produit des larges échantillons d'événements de paires de W. Les données de l'expérience L3 de la réaction $e^+e^- \to W^+W^-$ permettent des mesures précises de la section efficace et des distributions angulaires. L'excellent accord avec le Modèle Standard confirme l'existence des vertex triples boson de jauge $WW\gamma$ et WWZ, et, par conséquent, le comportement non-Abélien des

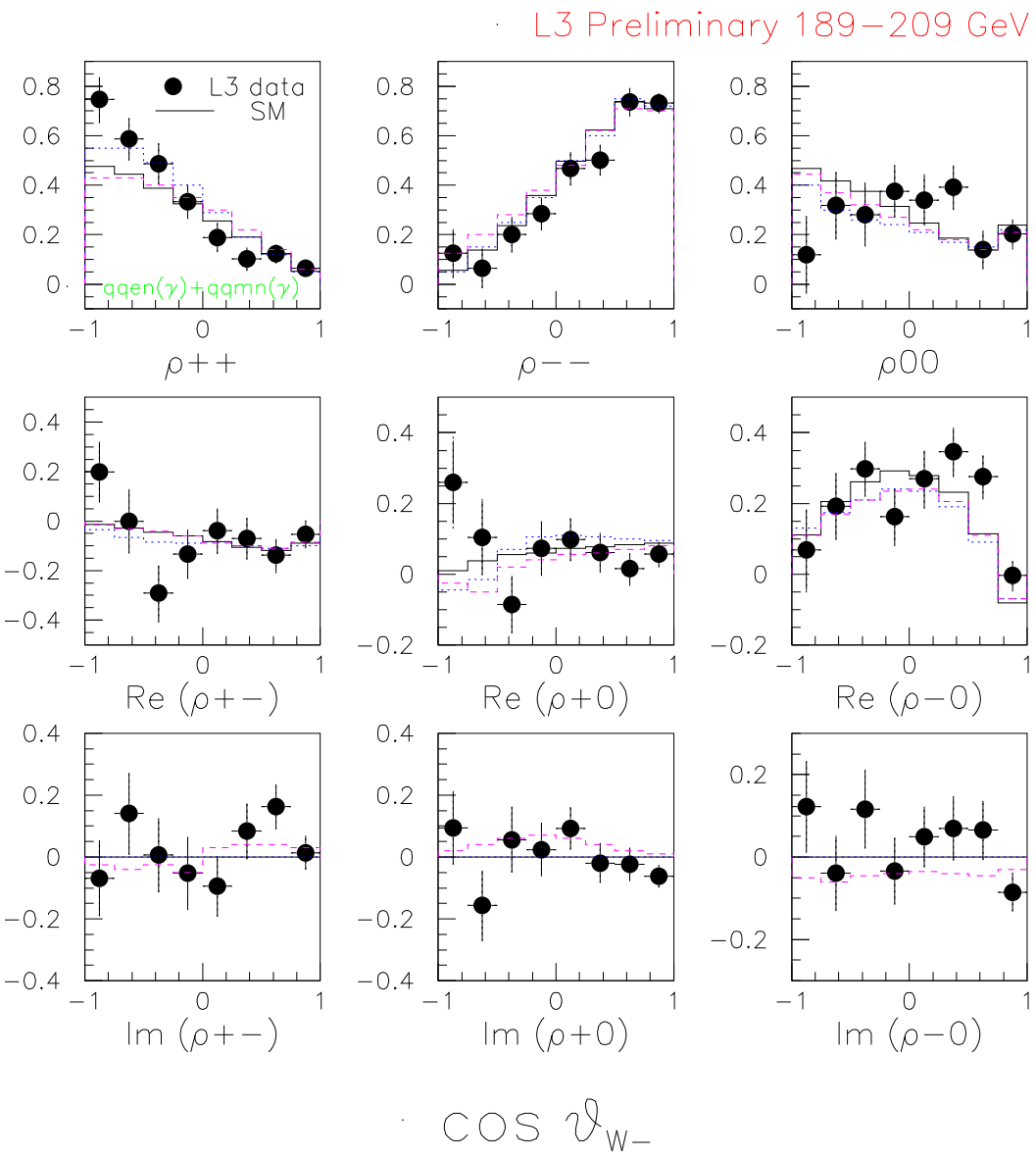

Figure 5: *Les éléments de la matrice de densité de spin du W en fonction du cosinus de l'angle de production du W^-, $\cos\theta_{W^-}$. Les points donnent les résultats obtenus avec les données prises par le détecteur L3 à des énergies de centre-de-masse $\sqrt{s} = 189-209$ GeV. Les barres d'erreur montrent l'incertitude totale qui combine les contributions statistiques et systématiques. La prédiction du Modèle Standard est représentée par la ligne continue. Les distributions en présence d'un couplage anormale sont données par la ligne pointillée pour $\Delta\kappa_\gamma = +0.5$, et par la ligne composée de traits pour $\tilde{\lambda}_Z = -0.5$.*

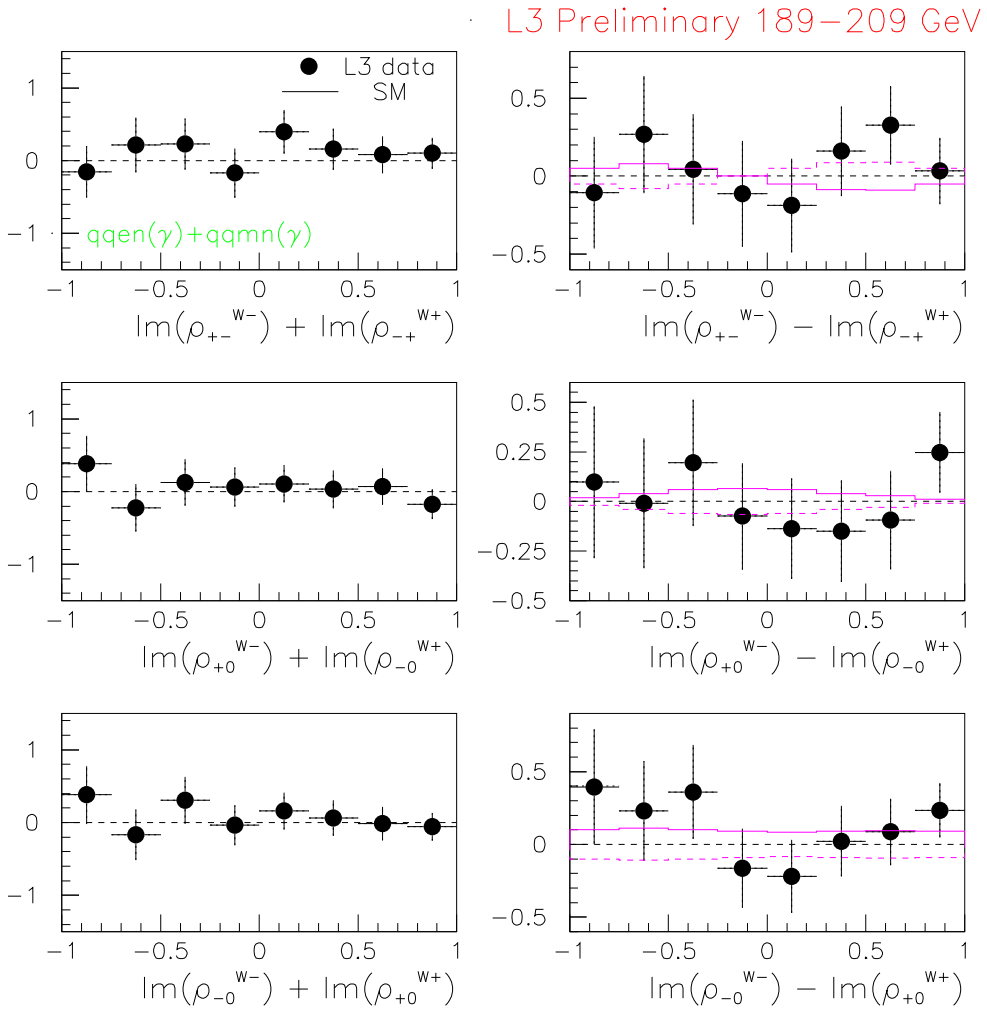

Figure 6: *La somme (à gauche) des parties imaginaires des éléments non-diagonaux de la matrice SDM, sensible à la violation de CPT, et la difference (à droite), sensible à la violation de CP. Les points donnent les résultats obtenus avec les données prises par le détecteur L3 à des énergies de centre-de-masse* $\sqrt{s} = 189 - 209$ *GeV. Les barres d'erreur montrent l'incertitude totale. La prédiction du Modèle Standard est représentée par la ligne horizontale à zero. Les distributions en présence d'un couplage anormale* $\tilde{\lambda}_Z = -0.5$ *sont données par la ligne composée de traits, et* $\tilde{\lambda}_Z = +0.5$ *par la ligne continue.*

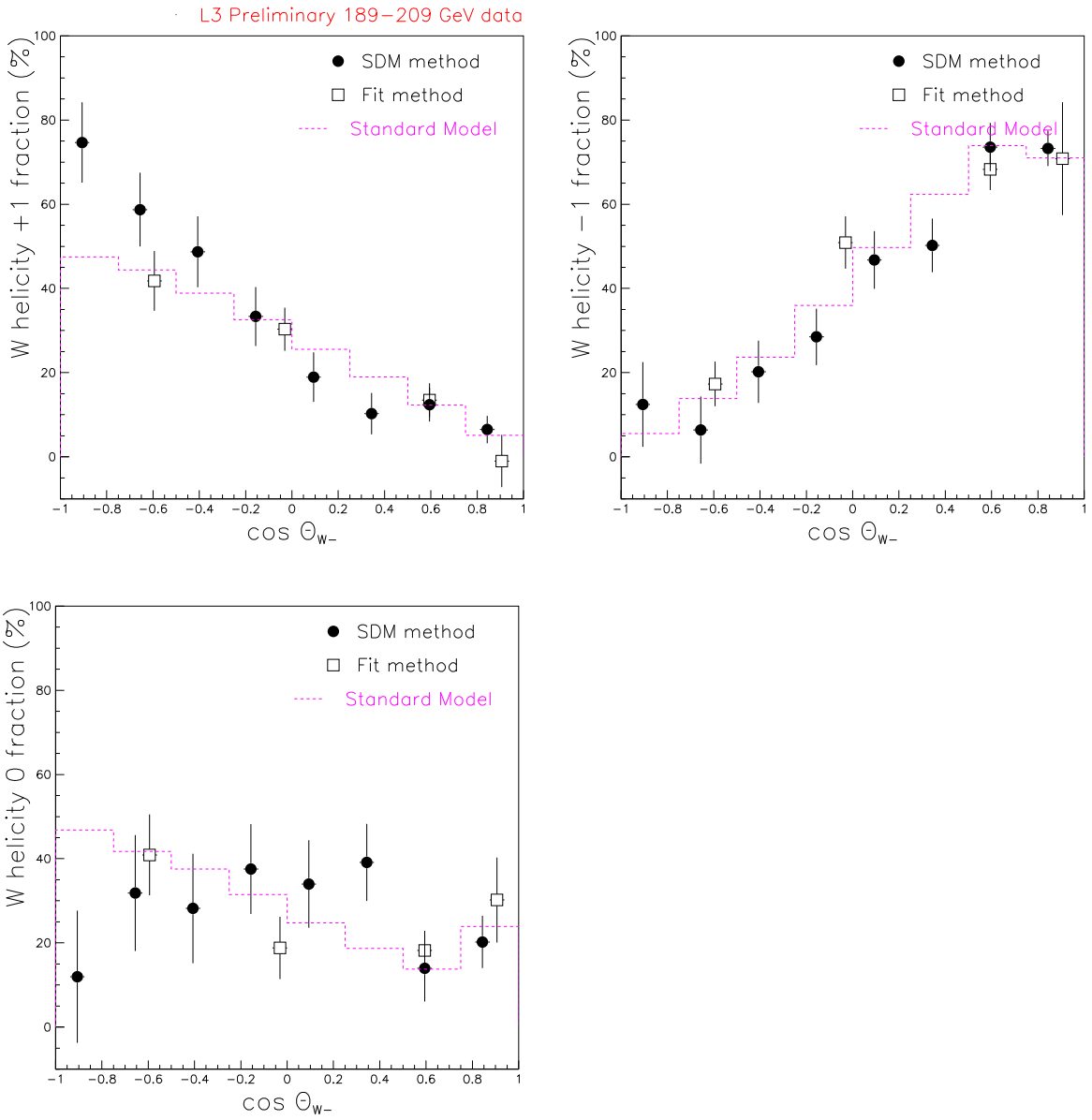

Figure 7: *Les fractions d'hélicité transverse et longitudinale en fonction du cosinus de l'angle de production du* W^-, $\cos\theta_{W^-}$. *Les points donnent les résultats obtenus avec les données prises par le détecteur L3 à des énergies de centre-de-masse* $\sqrt{s} = 189-209$ *GeV. Les barres d'erreur montrent l'incertitude totale. La prédiction du Modèle Standard est représentée par la ligne pointillée. La mesure precédente, utilisant une methode de fit [9], est aussi montrée.*

interactions électrofaibles.

Les mesures faites au LEP ont augmenté la crédibilité du Modèle Standard en étant une théorie qui donne une description correcte de la matière et des interactions. Il est toutefois supposé que sa validité tombera à des énergies plus élevées, inaccessibles au LEP. La prochaine étape dans la compréhension du Modèle Standard sera faite par le Large Hadron Collider, en cours de construction au CERN et dont la prise de données est prévue pour l'été 2007.

Chapter 1

W Physics at LEP

1.1 Historical Introduction

In the beginning of his physics lecture [10], Richard Feynman says *"If, in some cataclysm, all of scientific knowledge were to be destroyed, and only one sentence passed onto the next generation, what statements would contain the most of information in the fewest words? I believe it is the atomic hypothesis, that all things are made of atoms, little particles that move around in perpetual motion, attracting each other when they are a little distance apart, but repelling when squeezed into one another."*.
The idea that the enormous variety of phenomena in nature are the consequence of the motion and the combination of a restricted number of building blocks, is the fundamental idea of today's scientific vision.

A first scientific confirmation of the atomic hypothesis of the Greek philosopher Demokritos came in the 19^{th} century when chemists showed that regularities and numerical proportions in chemical reactions could simply be explained by the exchange of elementary, invariable building blocks. It was Mendeleev who first came up with the periodic table. The systematics in the organisation of the table results from the existence of a substructure within the atom.

In 1897 J.J. Thomson discovered the electron, followed by Rutherfords discovery of the nucleus in the famous α scattering experiment. The neutron was discovered by Chadwick in 1932 and the nucleus was found to be made of protons and neutrons kept together by a much stronger force than the electromagnetic force. Some years before, the mystery of the continuous energy spectrum of the electron in nuclear β decay, incompatible with the kinematics of a two-body decay, was solved by Pauli [11].

He suggested the existence of a very light neutral particle, the neutrino, emitted in the β decay together with the electron with whom it shares the decay energy. The β decay reaction

$$n \rightarrow p + e^- + \overline{\nu}$$

involves the interaction of four particles in one point of space-time. This was the motivation for the quantum field theory of weak interactions developped by Fermi [12] in 1934 and based on the analogie with the vector currents in quantum electrodynamics (QED). Fermi's theory gives a good quantitative description for the electron spectrum in β decay but leads to unitarity violation in the electron-neutrino scattering as the cross section predicted by the theory diverges with increasing energy. The Fermi theory was unrenormalisable.

In 1956 the principle of parity conservation in the weak interactions was given up by Lee and Yang [13]. The experimental confirmation followed a couple of years later in the β decay of cobalt 60 [14]. Because of its parity conservation, the Fermi theory was in disagreement with the experiment. In 1958 Feynman and Gell-Mann [15] proposed a V-A structure for the weak interactions : the weak currents are a combination of vector- and axial-vector currents. This solved the parity breaking problem as left- and right-handed particles could now be considered as fundamentally different particles in weak interactions. The helicity λ is defined as the projection of the spin $\vec{S}$ of the particle onto its direction of motion

$$\hat{\mathcal{H}}\ \psi = \frac{1}{2}\left(\frac{\vec{S}\ .\ \vec{p}}{|p|}\right)\psi = \lambda\ \psi \tag{1.1}$$

where λ= +1/2 for right-handed fermions and λ= -1/2 for left-handed fermions.

Although the V-A structure gives a good description of β decay, it fails at higher energies ($\sqrt{s} \simeq 300$ GeV) due to non-renormalisability. The existence of an Intermediate Vector Boson (IVB) W was postulated by Schwinger [16] and independently by Lee and Yang [17]. They suggested that the weak interaction results from the exchange of this vector boson similarly to the exchange of a photon in the electromagnetic interaction (see Figure 1.1). Due to the short range of the weak interactions the W mass was expected to be large but could not be predicted. The IVB theory resulted in a finite electron-neutrino scattering cross section at higher energies but the problem of unitarity violation and unrenormalisability remained unsolved in the scattering of pairs of W bosons at center-of-mass energies $\sqrt{s} \simeq$1 TeV.

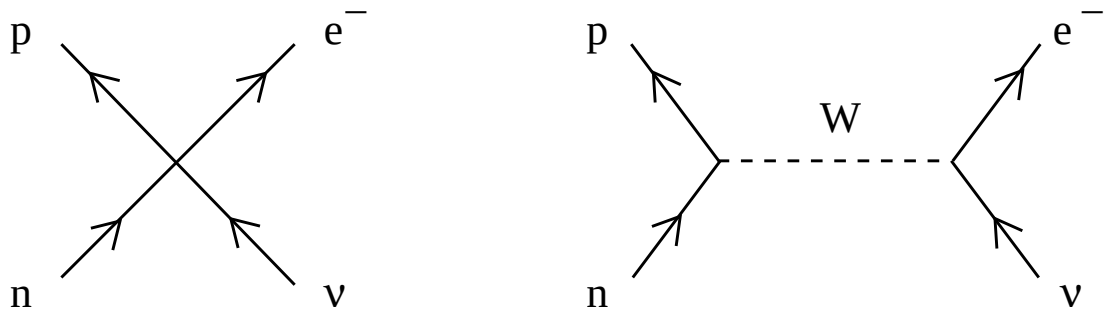

Figure 1.1: *The β decay process $n \rightarrow p + e^- + \overline{\nu}$ in the Fermi theory (Left) and in the Intermediate Vector Boson theory (Right).*

In 1961 Glashow [18] made a first step towards a unification of electromagnetic and weak interactions in an electroweak theory. His work was completed by Weinberg [19] and Salam [20] in 1970. In the Glashow-Weinberg-Salam model (GWS), the introduction of another intermediate vector boson, the Z boson, solved the unitarity problem. In 1971't Hooft [21] proved that the GWS theory is renormalisable.

The GWS theory is based on the local gauge invariance of the electroweak lagrangian under the $SU(2)_L \otimes U(1)_Y$ group and the Higgs mechanism Model [22]. In the spontaneous symmetry breaking of the $SU(2)_L \otimes U(1)_Y$ symmetry a neutral, massive scalar particle, the Higgs boson, and three massless Goldstone bosons appear. They give mass to three vector bosons, $W^{\pm}$ and Z, and the degree of freedom associated to each Goldstone bosons is transformed into the longitudinal polarisation of the massive vector boson.

At the same time, a theory, describing the strong interactions between quarks, the elementary constituents of hadrons, was developped. This gauge theory, called quantum chromodynamics (QCD), is based on a $SU(3)_c$ local gauge symmetry. Each quark has three degrees of freedom, denoted as the colours : red, blue and green. The quarks are confined in hadrons which are color singlets under $SU(3)_c$. The mediators of the strong force are the gluons which form an $SU(3)_c$ color octet.

The GWS and the QCD theory form what is called today the Standard Model [23] (SM) of elementary particle physics. In this model **matter** is composed of two types of particles, the leptons and the quarks, which are **fermions** i.e. spin 1/2 elementary particles (see Table 1.1 [3]).

Generations	**Leptons**							
1^{st}	Electron	e	0.511 MeV	-e	Neutrino e	ν_e	< 3 eV	0
2^{nd}	Muon	μ	105 MeV	-e	Neutrino μ	ν_μ	< 0.19 eV	0
3^{rd}	Tau	τ	1.777 GeV	-e	Neutrino τ	ν_τ	< 18.2 eV	0
Generations	**Quarks**							
1^{st}	Up	u	$\sim 1.5 - 4.5$ MeV	$+2e/3$	Down	d	$\sim 5 - 8.5$ MeV	$-e/3$
2^{nd}	Charm	c	$\sim 1 - 1.4$ GeV	$+2e/3$	Strange	s	$\sim 80 - 155$ MeV	$-e/3$
3^{rd}	Top	t	~ 174.3 GeV	$+2e/3$	Bottom	b	$\sim 4 - 4.5$ GeV	$-e/3$

Table 1.1: *The mass and charge of the three generations of leptons and quarks.*

Fermions appear in three generations of increasing mass

$$\begin{pmatrix} \nu_e \\ e \end{pmatrix} \quad \begin{pmatrix} \nu_\mu \\ \mu \end{pmatrix} \quad \begin{pmatrix} \nu_\tau \\ \tau \end{pmatrix} \tag{1.2}$$

$$\begin{pmatrix} u \\ d \end{pmatrix} \quad \begin{pmatrix} c \\ s \end{pmatrix} \quad \begin{pmatrix} t \\ b \end{pmatrix} \tag{1.3}$$

The **interactions** are mediated by **gauge bosons**

$$W^+, W^-, Z \text{ and } \gamma \rightarrow \text{electroweak interaction}$$
$$\text{gluons} \rightarrow \text{strong interaction}$$

The number of light neutrino's has been determined at LEP from the measurement of the hadronic and leptonic cross section for Z boson production: $N_\nu = 2.994 \pm 0.012$ [3], thus excluding a fourth generation of light neutrinos.

The limit on the **Higgs boson** mass, derived from direct searches, is $M_H > 113$ GeV [24], combining the measurements of the four LEP experiments. There is not yet a clear experimental evidence for the existence of the Higgs boson although a few candidates at ~ 115 GeV were observed at the end of the LEP running.

1.2 W-pair Production

The first experimental evidence for the validity of the electroweak theory came in 1973 with the discovery of neutral currents by the Gargamelle Collaboration [25]. This was followed in 1983 by the direct observation of the $W^{\pm}$ and Z bosons in $p\bar{p}$ collisions by the UA1 [1] and the UA2 [2] Collaborations at CERN.

Until 1996 W bosons were produced inclusively in the reaction $p\bar{p} \rightarrow W^{\pm}X$ in the $p\bar{p}$ colliders at the SPS (CERN) and Tevatron (Fermilab). Due to the high multijet production in hadron colliders, the W mass measurement was restricted to the leptonic W decay channels with a smaller branching ratio but a clearer signature.

In the eighties the construction of the LEP e^+e^- collider started at CERN. During the LEP1 period (1989-1995) the center-of-mass energy was fixed to $\sqrt{s} \cong 90$ GeV, around the value of the Z mass and about sixteen millions of Z decays have been observed by the four LEP experiments: ALEPH [4], DELPHI [5], L3 [6] and OPAL [7]. The main goal of LEP1 was the measurement of the parameters of the Z boson [26]. A high accuracy was achieved and the measurement of cross sections, asymmetry and τ polarisation yielded excellent agreement with the Standard Model predictions. During the LEP2 period (1996-2000) the threshold for W-pair production [27], $\sqrt{s} \cong 161$ GeV$= 2M_W$, was reached and the W boson can be studied with a high statistics sample with energies till $\sqrt{s} = 209$ GeV. In addition to searches for new particles (Higgs, supersymmetric particles, technicolor...), the aim of LEP2 is the precision study of the W-boson parameters, i.e. the W mass, width and branching fractions, as well as the direct study of the gauge boson couplings which are a direct consequence of the non-Abelian structure of the $SU(2)_L \otimes U(1)_Y$ group.

The cross sections of the hadronic final states studied in the e^+e^- collisions at LEP are presented in Figure 1.2 as function of the center-of-mass-energy $\sqrt{s}$.

1.2.1 Signal

At LEP, a single W bosons can be produced, but its main production is in pairs: $e^+e^- \rightarrow W^+W^-$ (Figure 1.3). Each W can decay into a quark-antiquark pair ($W^- \rightarrow \bar{u}d$ or $\bar{c}s$) or a lepton-antilepton pair ($W^- \rightarrow l^-\bar{\nu}_l$, $l = e, \mu, \tau$), in the following denoted as qq and $l\nu$ respectively. The on-shell W decay $W^- \rightarrow \bar{t}b$ is strongly supressed by the high top mass. The W-pair events can be classified in three types of final states or topologies shown in Figure 1.4.

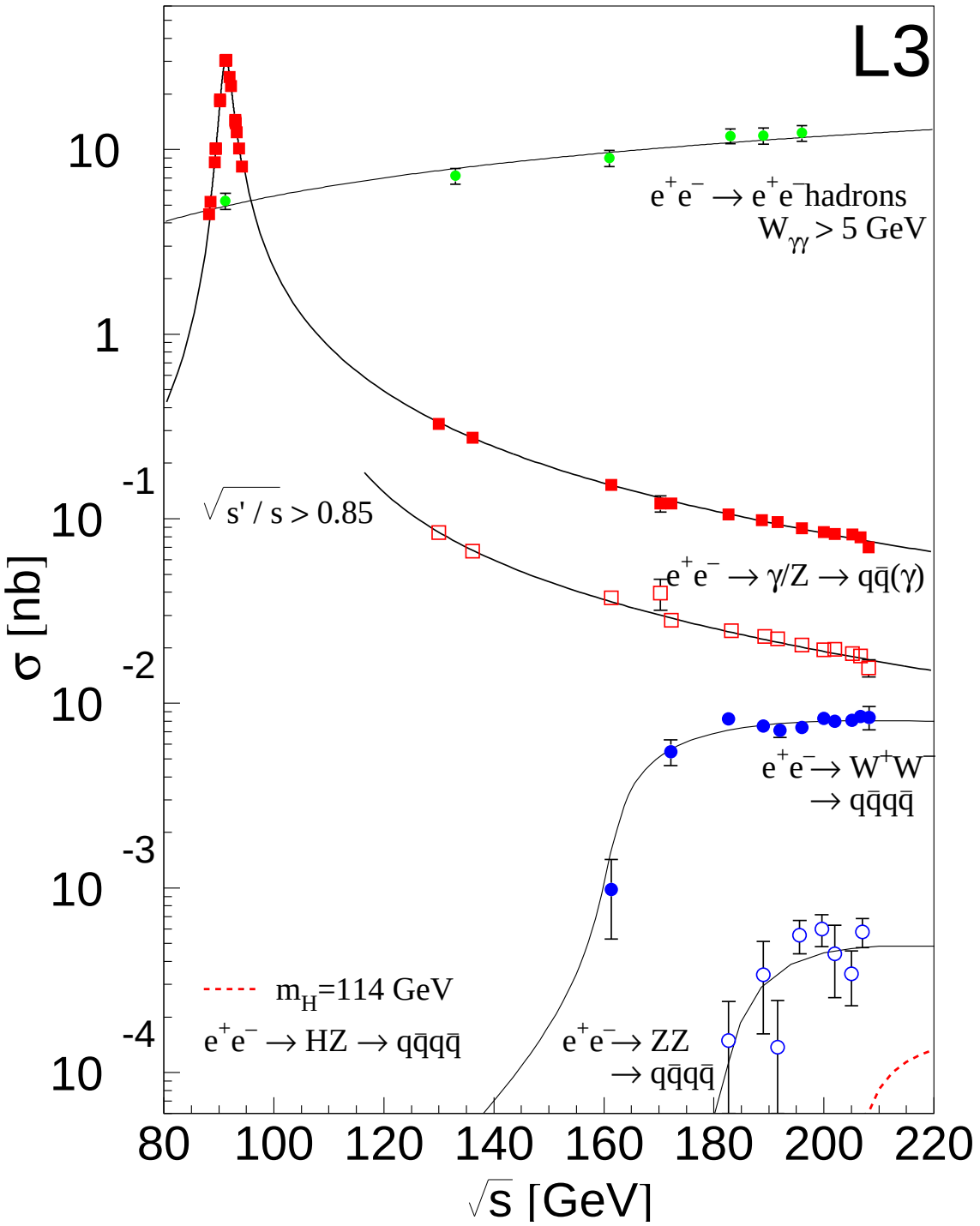

Figure 1.2: *The cross sections of the hadronic final states studied in the e^+e^- collisions at LEP as function of the center-of-mass energy $\sqrt{s}$.*

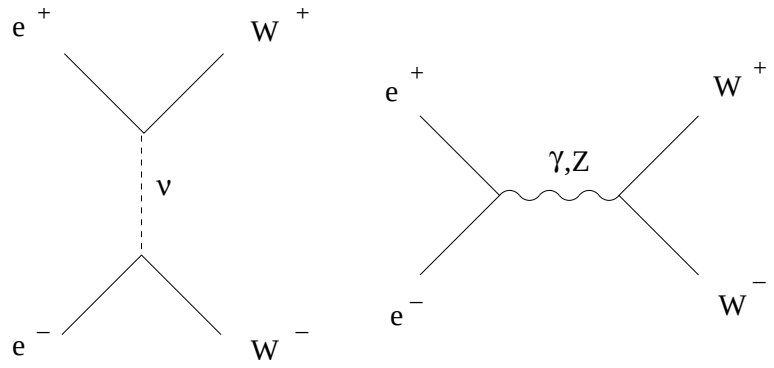

Figure 1.3: *The main W-boson production process at LEP is the production of W bosons in pairs by the exchange of a neutrino (Left) or a photon or Z boson (Right).*

- **Hadronic or four-jet channel**, $W^+W^- \to qqqq(\gamma)$ (BR=45.6%), q= u, d, c, s, b

  Topology: ⋆ 4 energetic jets in the final state

  ⋆ large visible energy, no missing energy

  ⋆ high cluster and track multiplicity

  Main backgrounds: $e^+e^- \to q\bar{q}(\gamma)$, ZZ

- **Semi-leptonic channel**, $W^+W^- \to qql\nu(\gamma)$ (BR=43.8%), $l = e, \mu, \tau$

  Topology: ⋆ 2 energetic jets with high multiplicity and

  ⋆ 1 isolated lepton ($l = e$,μ,τ) or

  1 narrow jet with low multipicity ($l = \tau \to$ hadronic jet)

  ⋆ missing energy and momentum imbalance due to the presence of at least one neutrino

  Main backgrounds: $e^+e^- \to q\bar{q}(\gamma)$, ZZ

- **Leptonic channel**, $W^+W^- \to l\nu l\nu(\gamma)$ (BR=10.6%), $l = e, \mu, \tau$

  Topology: ⋆ 2 isolated charged leptons in the final state

  ⋆ large missing energy and large momentum imbalance

  ⋆ low cluster and track multiplicity

  Main backgrounds: $e^+e^- \to e^+e^-$, $\mu^+\mu^-$, $\tau^+\tau^-$, $e^+e^-f\bar{f}$

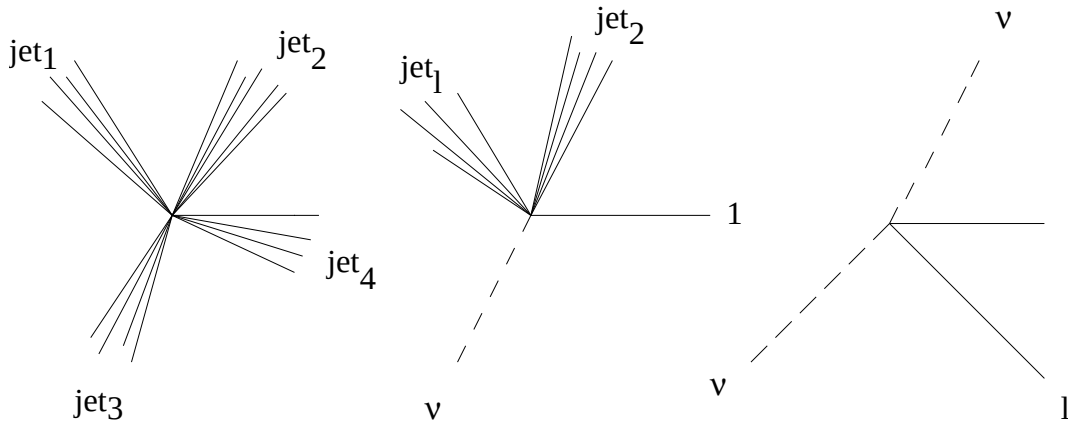

Figure 1.4: *The topology of the W pair production final states.* Left: *the hadronic channel*, Center: *the semi-leptonic channel*, Right: *the leptonic channel.*

where (γ) indicates that the presence of additional radiative photons in the final state is not excluded.

1.2.2 Backgrounds

Two fermion production, presented in Figure 1.5 (a), has a larger cross section than W-pair production and is the dominant background. At LEP1 Initial State Radiation (ISR) i.e. the radiation of one or more photons from the incoming electrons, is strongly suppressed as the center-of-mass energy $\sqrt{s}$ is close to the Z resonance peak. As a consequence the decay fermions are almost back-to-back in space. Above the Z resonance peak there are two possible situations. In the first situation the fermions have an acollinearity close to 180° due to the emission of ISR photons with small energy ("soft" photons) and a virtual photon or Z boson is exchanged in the s-channel. The visible energy of the event is almost equal to $\sqrt{s}$. In the second situation an ISR photon is radiated with such an energy that the effective center-of-mass energy $\sqrt{s'}$ is close to the Z resonance. The invariant mass of the fermion-pair is then close to the Z boson mass. This process is called "radiative return to the Z ".
In case of leptonic W decays, one needs to include the contribution of the Bhabha process with t-channel photon exchange, presented in Figure 1.5 (c).

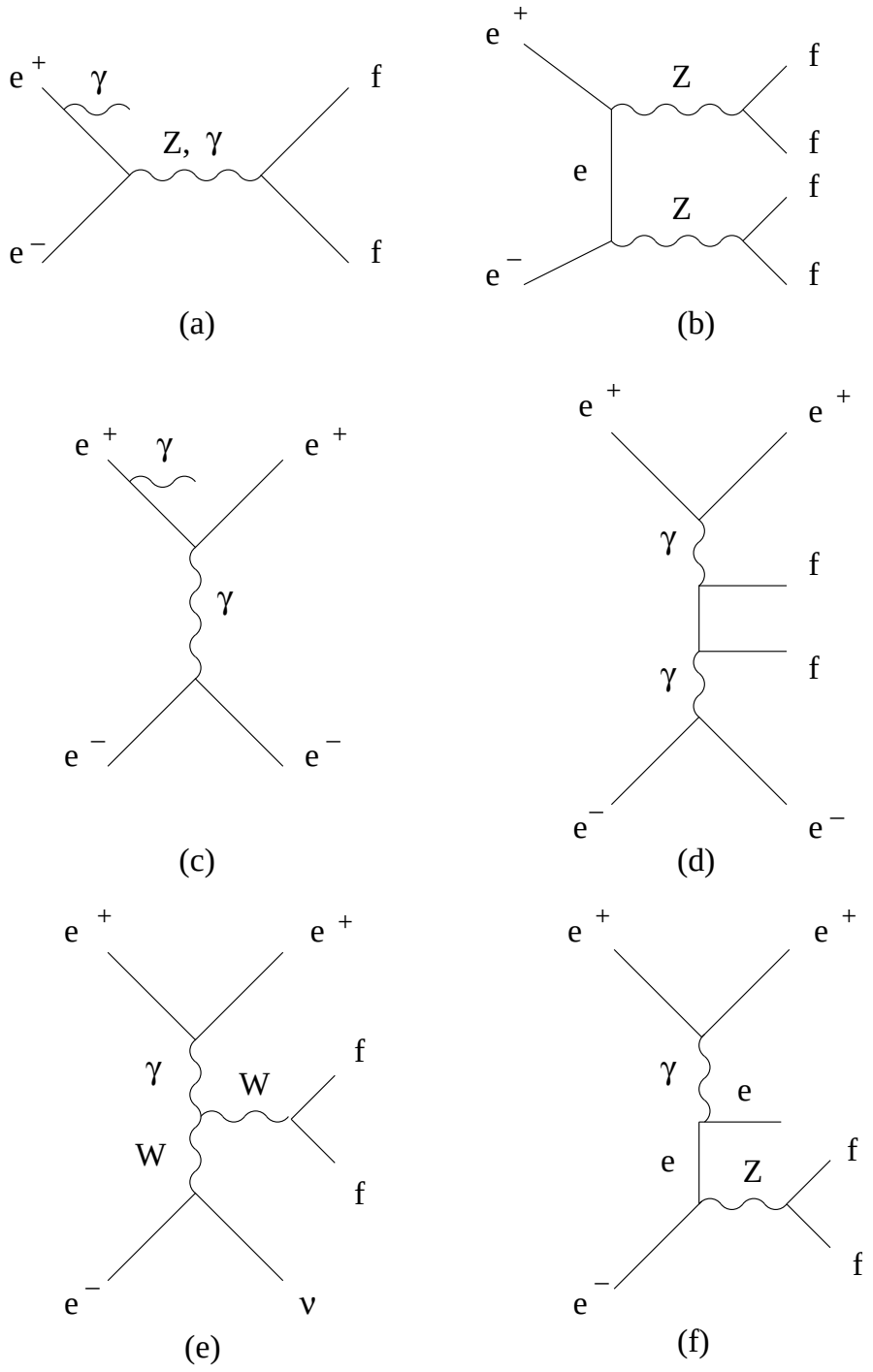

Figure 1.5: *The background processes for W-pair production: (a) two fermion production with emission of an ISR photon, (b) Z-pair production, (c) Bhabha process with t-channel photon exchange and emission of an ISR photon, (d) two photon production (e) single W production and (f) Zee production.*

The Z-pair production process is presented in Figure 1.5 (b). **Four fermion production** becomes important at center-of-mass energies above the threshold for Z-pair production ($\sqrt{s} \cong 180$ GeV). If both Z bosons decay hadronically, this process leads to a topology similar to W-pair production in the hadronic channel (a). Both processes are distinguishable by the measurement of the invariant mass of the fermion pairs. If one or both Z decays leptonically, Z-pair production constitutes a background for W-pair production in the semi-leptonic and leptonic channel.

The **two photon production** is presented in Figure 1.5 (d). In this process a fermion-pair is produced through the interaction of two virtual Bremstrahlung photons emitted by the incoming electrons. The scattered electrons escape into the beam pipe and the event is characterized by a low visible energy and a low fermion-pair invariant mass.

Also the **single W** and **Zee** processes have to be taken into account. The single W process (Figure 1.5 (e)) constitutes a background for W-pair production if the electron escapes undetected into the beam pipe. The Zee process (Figure 1.5 (f)) is a background for W-pair production with an electron-neutrino pair in the final state when the Z decays hadronically and the outgoing electron which escapes into the beam pipe, fakes a neutrino.

1.3 W Mass

The first direct measurements of the W mass were performed by the UA1 and UA2 experiment at the SPS $p\bar{p}$ collider at CERN and by the CDF and the DØ experiment at the Tevatron $p\bar{p}$ collider. They studied the process $p\bar{p} \rightarrow W^{\pm}X \rightarrow l^{\pm}\nu X$ and obtained the combined result [28]

$$M_W^{p\bar{p}+UA2} = 80.41 \pm 0.09 \text{ GeV} \tag{1.4}$$

Indirect measurements of the W mass were done at LEP1 and SLD and used the Fermi constant, G_μ, accurately known from the muon decay, and $\alpha(M_Z^2)$, the electroweak running coupling value at the Z-peak

$$M_W^2 = \frac{\pi\ \alpha(M_Z^2)}{\sqrt{2}G_\mu \sin^2\theta_w} \frac{1}{1-\Delta r} \tag{1.5}$$

with $\sin^2\theta_w = 1 - M_W^2/M_Z^2$. The precision of the electroweak measurements makes them sensitive, through loop corrections, to other fundamental parameters: Δr represents the correction to M_W due to one-loop corrections and depends quadratically on m_t and logarithmically on M_H.

$\delta(M_W)$	M_H=100 GeV	M_H=300 GeV
25 MeV	+86,-54 GeV	+196,-126 GeV
50 MeV	+140,-72 GeV	+323,-168 GeV

Table 1.2: *An estimate of the uncertainty on the Higgs boson mass M_H due to the uncertainty on the W mass $\delta(M_W)$.*

The combination of the LEP1 and SLD results for the indirect measurement of the W mass [29] is

$$M_W^{LEP1+SLD} = 80.332 \pm 0.037 \text{ GeV} \tag{1.6}$$

At LEP2 the direct determination of the W mass is possible using different methods. At threshold, the W pair production cross section, measured at $\sqrt{s} \sim 2M_W \cong 161$ GeV, is compared to the theoretical prediction with M_W as a free parameter. The combination of the threshold measurement of the four LEP experiments led to the following value [30]

$$M_W^{LEP,thres} = 80.40 \pm 0.22 \text{ GeV} \tag{1.7}$$

Above threshold, a direct reconstruction method or a Monte Carlo reweighting method is used to extract the W mass. Both methods use kinematic fits to improve the mass resolution. In the direct reconstruction method, the W mass Breit-Wigner distribution is reconstructed from the W pair final states. The Monte Carlo reweighting method is used by the L3 experiment. In this method the W mass is extracted from a maximum likelihood fit using a baseline Monte Carlo sample reweighted in order to include different values for the W mass.

As the W mass is directly related to the mass of the top quark and the mass of the Higgs boson, the accuracy of the W mass measurement is also used to infer constraints on m_t and M_H. The electroweak radiative corrections are sensitive to m_t and M_H. The solid contour in Figure 1.6 shows the indirect measurement of M_W and m_t at LEP1 and SLD obtained from a global Standard Model fit to all measured quantities (cross sections, asymmetries and τ polarisation). The direct measurement by the $p\bar{p}$ colliders and LEP2 is represented by the dashed contour. Both are in good agreement. The solid line shows the mathematical relation between M_W and m_t for different values of M_H. A low Higgs mass is preferred by both the direct and the indirect measurements [31]. The uncertainty on the W mass has a significant impact on the prediction for the mass of the Higgs boson. Table 1.2 gives an estimate of the uncertainty on the Higgs mass for uncertainties on the W mass of 25 and 50 MeV and assuming a top mass $m_t = 180 \pm 5$ GeV [27].

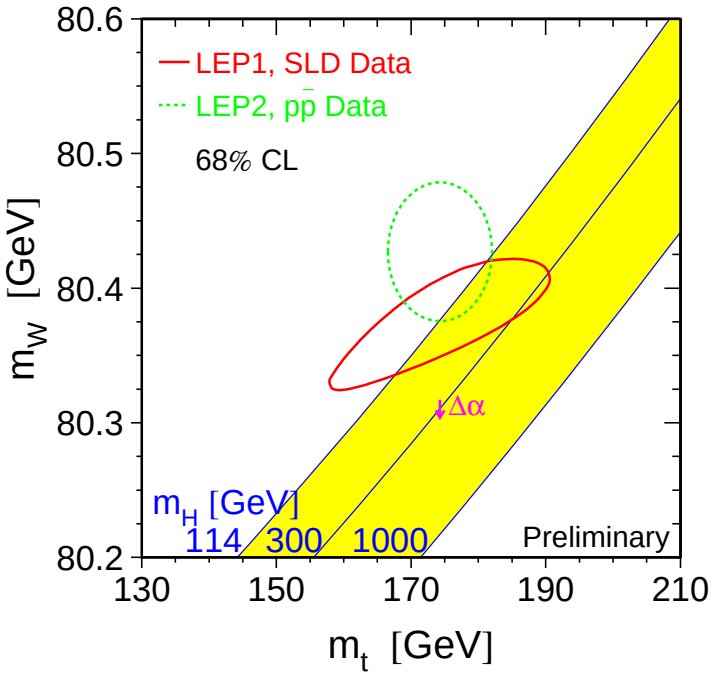

Figure 1.6: *The comparison between the indirect measurement of M_W and m_t at LEP1 and SLD (solid contour) and the direct measurement by the $p\bar{p}$ colliders and LEP2 (dashed contour). The grey band shows the mathematical relation between M_W and m_t for different values of M_H [31].*

The aim of the four LEP collaborations is to achieve a final accuracy of the order of 30-40 GeV on the W mass using the full LEP2 data set.

The thesis work is structured into 7 Chapters. The W boson physics is developped in Chapter 2, which gives the theoretical framework of the Standard Model. Chapter 3 summarises the Monte Carlo programs and Chapter 4 is dedicated to the discription of the L3 detector. The measurement of the cross section for W pair production is presented in Chapter 5, the determination of the W Spin Density Matrix in Chapter 6. Alors the invariance of the W-decay under CPT and CP is tested and the W boson polarisation is measured. Chapter 7 summarises the results of the triple gauge coupling measurements and presents a preliminary study of the possibilities of the SDM method to derive limits on CP violating couplings.

Chapter 2

Theoretical Framework

2.1 The Standard Model

2.1.1 $U(1)_{em}$ gauge invariance

The QED theory [32] describing the electromagnetic interactions is based on a $U(1)_{em}$ local gauge symmetry. Under this symmetry a spinor ψ transforms as

$$\psi(x) \rightarrow \psi'(x) = e^{ie\alpha(x)}\psi(x) \tag{2.1}$$

where e is the electric charge and $\alpha(x)$ an arbitrary function of the space-time position $x \equiv (x_0, \vec{x})$.
The local gauge invariance of the Lagrangian under this symmetry is obtained by replacing the space-time derivative ∂_μ by the covariant derivative D_μ

$$\partial_\mu \rightarrow D_\mu = \partial_\mu + ieA_\mu(x) \tag{2.2}$$

where the gauge field A_μ, the electromagnetic field, satisfies the transformation

$$A_\mu(x) \rightarrow A'_\mu(x) = A_\mu(x) - \partial_\mu\alpha(x) \tag{2.3}$$

The gauge particle corresponding to the electromagnetic field is the photon. As a mass term for the photon would break the local gauge invariance of the Lagrangian, the photon has to remain massless. The QED Lagrangian for a massive fermion interacting with an electromagnetic field is given by

$$\mathcal{L}_{QED} = \ i\bar{\psi}(x)\gamma^\mu(D_\mu - m)\psi(x) - \frac{1}{4}F_{\mu\nu}F^{\mu\nu} \tag{2.4}$$

where the last term represents the kinetic term for the electromagnetic field.

2.1.2 $SU(2)_L$ gauge invariance

Right-handed fermions do not participate in weak interactions and form singlets under $SU(2)_L$, while left-handed fermions are grouped in $SU(2)_L$ doublets.
With $l = e,\ \mu,\ \tau$, $q_u = u, c, t$ and $q_d = d, s, b$, we introduce the following notations

- **left-handed leptons and quarks**

$$L \equiv \begin{pmatrix} \nu_l \\ l \end{pmatrix}_L \qquad Q \equiv \begin{pmatrix} q_u \\ q_d \end{pmatrix}_L$$

- **right-handed leptons and quarks**

$$l_R \text{ and } q_R$$

Under an $SU(2)_L$ transformation, the singlet remains invariant while the doublet is modified as following

$$\chi_L(x) \rightarrow \chi'_L(x) = e^{ig\vec{T}.\vec{\alpha}(x)}\chi_L(x) \tag{2.5}$$

where $\vec{T} = \frac{\vec{\tau}}{2}$ represents the generator of the $SU(2)_L$ group and is related to the Pauli matrices τ_i

$$\tau_1 = \begin{pmatrix} 0 & 1 \\ 1 & 0 \end{pmatrix} \quad \tau_2 = \begin{pmatrix} 0 & -i \\ i & 0 \end{pmatrix} \quad \tau_3 = \begin{pmatrix} 1 & 0 \\ 0 & -1 \end{pmatrix} \tag{2.6}$$

To preserve the local gauge symmetry of the Lagrangian, the space-time deriviative ∂_μ is replaced by the covariant derivative

$$\partial_\mu \rightarrow D_\mu = \partial_\mu + ig\ \vec{T}.\vec{W}_\mu \tag{2.7}$$

and three gauge fields $\vec{W}_\mu$ are introduced

$$\vec{W}_\mu \rightarrow \vec{W'}_\mu = \vec{W}_\mu - \partial_\mu\vec{\alpha}(x) - g\ \vec{\alpha}(x) \times \vec{W}_\mu \tag{2.8}$$

2.1.3 $SU(2)_L \otimes U(1)_Y$ gauge invariance

The unified theory of electroweak interactions is based on the $SU(2)_L \otimes U(1)_Y$ gauge symmetry of the Lagrangian with generators $\vec{T}$, the weak isospin, and Y, the weak hypercharge. Under this symmetry the components of the left- and right-handed components of spinor ψ transforms as following

$$\chi_L(x) \rightarrow \chi'_L(x) = e^{ig\vec{T}.\vec{\alpha}(x)+ig'Y\beta(x)}\chi_L(x) \tag{2.9}$$

$$\psi_R(x) \rightarrow \psi'_R(x) = e^{ig'Y\beta(x)}\psi_R(x) \tag{2.10}$$

where g and g' are the coupling constant of the $SU(2)_L$ and the $U(1)_Y$ group respectively. To preserve this symmetry locally, the space-time deriviative ∂_μ is replaced by a covariant derivative which depends on the helicity of the fermion

- **left-handed fermions**

$$\partial_\mu \rightarrow D_\mu = \partial_\mu - ig\vec{T}.\vec{W}_\mu - i\frac{g'}{2}YB_\mu \tag{2.11}$$

- **right-handed fermions**

$$\partial_\mu \rightarrow D_\mu = \partial_\mu - i\frac{g'}{2}YB_\mu \tag{2.12}$$

while the gauge fields $\vec{W}_\mu$ and B_μ transform as

$$\vec{W}_\mu \rightarrow \vec{W'}_\mu = \vec{W}_\mu - \partial_\mu\vec{\alpha}(x) - g\ \vec{\alpha}(x) \times \vec{W}_\mu \tag{2.13}$$

$$B_\mu \rightarrow B'_\mu = B_\mu - \partial_\mu\beta(x) \tag{2.14}$$

where W^i_μ (i=1,2,3) and B_μ, are the gauge fields of $SU(2)_L$ and $U(1)_Y$. The third component of the weak isospin T_3 and the weak hypercharge Y are related to the electric charge Q by

$$Q = T_3 + Y/2$$

The quantum numbers for leptons and quarks are summarized in Table 2.1.

Leptons	T_3	Q	Y
$\begin{pmatrix} \nu_l \\ l \end{pmatrix}_L$	$+1/2$	0	-1
	$-1/2$	-1	-1
l_R	0	-1	-2
Quarks	T_3	Q	Y
$\begin{pmatrix} q_u \\ q_d \end{pmatrix}_L$	$+1/2$	$+2/3$	$+1/3$
	$-1/2$	$-1/3$	$+1/3$
$q_{u,R}$	0	$+2/3$	$+4/3$
$q_{d,R}$	0	$-1/3$	$-2/3$

Table 2.1: *The third component of the weak isospin, T_3, the electric charge Q and the weak hypercharge Y of the fermions. The indices L and R refer to the left-handed and right-handed fermions.*

The Lagrangian density of the Standard Model can be written as following

$$\mathcal{L}_{SM} = \mathcal{L}_{fermions} + \mathcal{L}_{gauge} + \mathcal{L}_{Higgs} + \mathcal{L}_{Yukawa}$$

where $\mathcal{L}_{fermions}$ describes the interactions for the fermions

$$\mathcal{L}_{fermions} = \overline{l}_R \left(i\gamma^\mu(\partial_\mu + i\frac{g'}{2}YB_\mu)\right) l_R + \overline{q}_R \left(i\gamma^\mu(\partial_\mu + i\frac{g'}{2}YB_\mu)\right) q_R + \tag{2.15}$$
$$\overline{L} \left(i\gamma^\mu(\partial_\mu + i\frac{g'}{2}YB_\mu + ig\vec{T}.\vec{W}_\mu)\right) L + \overline{Q} \left(i\gamma^\mu(\partial_\mu + i\frac{g'}{2}YB_\mu + ig\vec{T}.\vec{W}_\mu)\right) Q$$

and $\mathcal{L}_{gauge}$, the kinetic term of the gauge fields

$$\mathcal{L}_{gauge} = -\frac{1}{4}\vec{F_{\mu\nu}}\vec{F^{\mu\nu}} - \frac{1}{4}G_{\mu\nu}G^{\mu\nu} \tag{2.16}$$

where the field strength tensors are given by

$$\vec{F_{\mu\nu}} = \partial_\mu\vec{W}_\nu - \partial_\nu\vec{W}_\mu - g\vec{W}_\mu \times \vec{W}_\nu \tag{2.17}$$

$$G_{\mu\nu} = \partial_\mu B_\nu - \partial_\nu B_\mu \tag{2.18}$$

The gauge boson fields $\vec{W}_\mu$ and B_μ do not correspond to physical fields.
The last term in Eq.(2.17) is a direct consequence of the non-Abelian structure of the Standard Model symmetry group and introduces couplings between three and four gauge bosons. The term $\mathcal{L}_{Higgs}$ is the Lagrangian density for the Higgs boson, introduced to give mass to the W^+, W^- and Z bosons, while $\mathcal{L}_{Yukawa}$ describes the interaction between the fermions and the Higgs boson and includes the mass term for the fermions, we will describe them in Section 2.1.5..

2.1.4 Higgs mechanism

The introduction of a mass term for the gauge fields destroys the local gauge invariance of the Lagrangian density of the Standard Model and therefore the gauge bosons are must be massless. However, the W and the Z boson are massive. The mass problem is solved by the Higgs mechanism where a $SU(2)$ doublet of complex scalar fields, called the Higgs doublet, is introduced

$$\Phi = \begin{pmatrix} \phi^+ \\ \phi^o \end{pmatrix} \tag{2.19}$$

with

$$\phi^+ = \frac{\phi_1 - i\phi_2}{\sqrt{2}},\ \phi^o = \frac{\phi_3 - i\phi_4}{\sqrt{2}} \tag{2.20}$$

where ϕ_1, ϕ_2, ϕ_3 and ϕ_4 are real scalar fields.

The Lagrangian density for the self-interacting field ϕ can be written as

$$\mathcal{L}_{Higgs} = \partial_\mu \Phi^\dagger\ \partial^\mu \Phi - V(\Phi) \tag{2.21}$$

After applying the $SU(2)_L \otimes U(1)_Y$ symmetry locally i.e. by the substitution $\partial_\mu \rightarrow D_\mu$, the Lagrangian density of the Standard Model $\mathcal{L}_{SM}$ becomes

$$\mathcal{L}_{SM} \rightarrow \mathcal{L}_{EW} = |D_\mu \Phi|^2 - V(\Phi) + \mathcal{L}_{gauge} \tag{2.22}$$

The Higgs potential is given by

$$V(\Phi) = -\mu^2(\Phi^\dagger\Phi) + \frac{\lambda}{4}(\Phi^\dagger\Phi)^2 \tag{2.23}$$

The two-dimensional Higgs potential is presented in Figure 2.1. The arbitrary constants $\lambda > 0$ and $\mu^2 > 0$ are chosen such to ensure that the $SU(2)_L \otimes U(1)_Y$ symmetry is spontaneously broken and the potential has no longer an unique minimum but a continuum of degenerated minima satisfying the condition

$$|\Phi^2_{min}| = \phi_1^2 + \phi_2^2 + \phi_3^2 + \phi_4^2 = \frac{\mu^2}{\lambda} = v^2 \neq 0 \tag{2.24}$$

where v represents the vacuum expectation value. The minima of $V(\Phi)$ correspond to a continuum of ground states which lie on a hypersphere. They are transformed into each other by a phase rotation. Each minimum is acceptable as a vacuum state and we can choose $\phi_1 = \phi_2 = \phi_4 = 0$, $\phi_3 = v$ and

$$\Phi_o = <\Phi> = \frac{1}{\sqrt{2}} \begin{pmatrix} 0 \\ v \end{pmatrix} \tag{2.25}$$

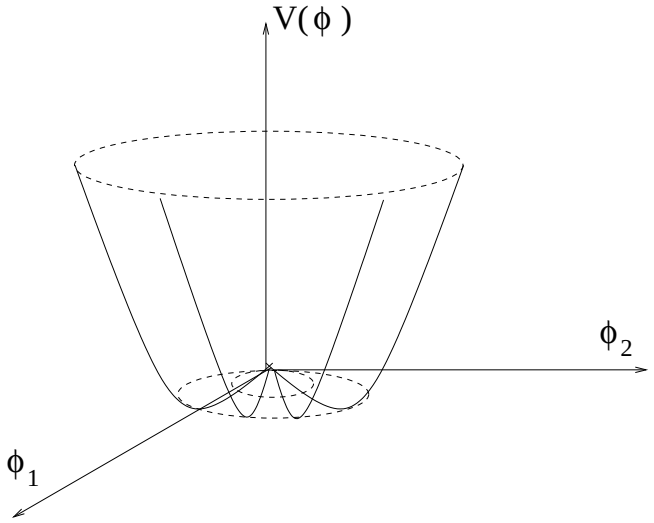

Figure 2.1: *The two-dimensional Higgs potential.*

Expanding around this value, the scalar field is then parametrized as

$$\Phi(x) = \frac{1}{\sqrt{2}} \begin{pmatrix} 0 \\ v + H(x) \end{pmatrix} \tag{2.26}$$

where $H(x)$ is the perturbative Higgs field that describes the physical Higgs boson.

The choice of ϕ_o breaks the local $SU(2)_L \otimes U(1)_Y$ symmetry, but only apparently. The vacuum state is still invariant under this symmetry but no more manifestly. There is a residual symmetry, associated to the subgroup $U(1)_{em}$ which is preserved after the spontaneous symmetry breaking and which keeps the photon massless. The four scalar fields of the Higgs doublet are transformed in a massive scalar field for the Higgs boson and in three massless scalar fields, associated to Goldstone bosons. The latter are a direct consequence of the Goldstone theorem, predicting one scalar massless field for each continuous symmetry of the Lagrangian density, broken by the choice of the vacuum state.

After spontaneous symmetry breaking (SSB),the Lagrangian density of the electroweak theory becomes

$$\mathcal{L}_{EW}^{SSB} = \frac{1}{2}\partial_\mu H \partial^\mu H - \frac{\mu^2}{2} H^2 + \frac{1}{8} g^2 v^2 [(W_\mu^1)^2 + (W_\mu^2)^2] + \frac{1}{8} v^2 (g W_\mu^3 - g' B_\mu)^2 + ... \tag{2.27}$$

The first two terms describe a scalar particle, the Higgs boson, with mass $m_H = \sqrt{2}\mu$.

The third term represents the mass term for two physical, oppositely charged W bosons with mass $M_W = gv/2$. They are given by the linear combination

$$W_\mu^\pm = \frac{1}{\sqrt{2}}(W_\mu^1 \mp W_\mu^2) \tag{2.28}$$

The fourth term expresses the mixing between W^3 and B gauge boson fields and can be written as

$$(W_\mu^3 \quad B_\mu) \begin{pmatrix} g^2 & -gg' \\ -gg' & g'^2 \end{pmatrix} \begin{pmatrix} W^{3\mu} \\ B^\mu \end{pmatrix} \tag{2.29}$$

After diagonalising the coupling constants matrix, the physical neutral gauge bosons A_μ and Z_μ with masses $M_A = 0$ and $M_Z = \sqrt{g^2 + g'^2}v/2$ are obtained. They are connected to W_μ^3 and B_μ by the following matrix relation

$$\begin{pmatrix} A_\mu \\ Z_\mu \end{pmatrix} = \begin{pmatrix} \sin\theta_w & \cos\theta_w \\ \cos\theta_w & -\sin\theta_w \end{pmatrix} \begin{pmatrix} W_\mu^3 \\ B_\mu \end{pmatrix} \tag{2.30}$$

where θ_w is the weak mixing angle referred to as the Weinberg angle and defined as

$$\frac{g'}{g} = \tan\theta_w \tag{2.31}$$

Since no mass term appears for the state A_μ, this masseless state corresponds to the photon

$$M_A = M_\gamma = 0 \tag{2.32}$$

The W and Z bosons obtained masses through the Higgs mechanism, while the photon remains massless as expected from the residual $U(1)_{em}$ symmetry.

2.1.5 Yukawa interactions and fermion masses

The Higgs mechanism generates massive gauge bosons, but the fermions stay fundamentally massless. A mass term $m\overline{\psi}\psi = m(\overline{\psi_L}\psi_R + \overline{\psi_R}\psi_L)$ would violate explicitely the $SU(2)_L \otimes U(1)_Y$ gauge symmetry since fermions with different helicities transform differently under the gauge symmetry. Also in this case, the Higgs field generates a mass for the fermions through its Yukawa interaction with the fermions. The Yukawa terms are introduced as

- **leptons**

$$\mathcal{L}_{Yukawa} = \; y_l \; (\overline{L} \; \Phi \; l_R \; + \; \overline{l}_R \; \Phi^\dagger \; L) = -y_l \; \frac{v}{\sqrt{2}} \; (\overline{L} \; l_R \; + \; \overline{l}_R \; L) \tag{2.33}$$

- **quarks**

$$\mathcal{L}_{Yukawa} = \; -y_q \; (\overline{q}_L \; \Phi_c \; q_R \; + \; \overline{q}_R \; \Phi^\dagger \; q_L) = -y_q \; \frac{v}{\sqrt{2}} \; (\overline{Q} \; q_R \; + \; \overline{q}_R \; Q) \tag{2.34}$$

where Yukawa couplings of the fermion, y_l and y_q ,are completely arbitrary as well as the fermion masses defined by

$$m_f = y_f \frac{v}{\sqrt{2}} \tag{2.35}$$

for the corresponding fermion. Because of its proportionality to v, we expect the fermion mass to be of the same order of the W mass. Only the top quark has a mass of the order of the W mass while all other fermions are much lighter ($m_e/M_W \sim 10^{-6}$). This remains unexplained in the Standard Model.

2.1.6 Discrete symmetries

Beside gauge symmetries, the Standard Model is invariant under certain discrete symmetries. The three discrete symmetries with important consequences on the electroweak theory are the charge conjugation, the parity operator and the time reversal

- **The time reversal operator** T interchanges the initial and final state of the physics process and is violated in the Standard Model. The direction of the particle's momentum vector $\vec{P}$ as well as its spin $\vec{S}$ is reversed by this transformation.

- **The charge conjugation operator** C transforms a particle into the corresponding anti-particle and vice versa. This symmetry is conserved in electromagnetic and strong interactions but violated in weak interactions: under C a left-handed neutrino is transformed into a left-handed anti-neutrino which does not exist in nature.

- **The parity operator** P is responsible for the spatial inversion of coordinates relative to the origin

$$(t, x, y, z) \rightarrow (t, -x, -y, -z) \tag{2.36}$$

  The direction of the particle's momentum vector $\vec{P}$ is reversed by this transformation but its spin $\vec{S}$ remains unchanged. Contrary to electromagnetic and strong

force, parity is maximally violated in weak interactions: a left-handed neutrino is transformed into a right-handed neutrino which does not exist in the Standard Model.

The weak interaction is not invariant under C or P, but CP is conserved: under CP a left-handed neutrino is transformed into a right-handed anti-neutrino. This is only true in a good approximation: CP is violated quark sector as observed in the K^0 decay and other processes involving transitions between the quark flavour states. Without CP violation, the distinction between matter and anti-matter on a cosmic scale is difficult to explain. The discovery of atmospheric and solar neutrino oscillations proofs that the neutrino has a mass and points towards CP-violation in the lepton sector.

The successive operation of C, P and T transformations in any order is called a CPT transformation and is conserved in the standard model. According to the CPT theorem, all physics processes are invariant under CPT transformations. A direct consequence is that particles and anti-particles have the same mass, lifetime etc... Because of the CPT theorem, CP violation implies T violation.

2.2 W-pair Production

There are three levels in the description of W-pair production. At tree level the production of a pair of on-shell W bosons with zero decay width is considered: $e^+e^- \rightarrow W^+W^-$. The next step describes the off-shell production of a W-pair with a finite, non-zero decay width : $e^+e^- \rightarrow W^+W^- \rightarrow 4f$. Finally all diagrams of the reaction $e^+e^- \rightarrow X \rightarrow 4f$ with the same four-fermion final state but different intermediate states X are included. The radiative corrections to the tree level calculation and Final State Interactions (FSI) will be discussed in the Chapter 3. The measurement of the W-pair production cross section is presented in Chapter 5.

2.2.1 Lowest order on-shell W-pair production

In the on-shell approximation, the Standard Model predicts the contribution of three charged current Feynman diagrams, referred to as CC03, presented in Figure 2.2. The t-channel ν-exchange diagram (Left), is dominant at threshold. The s-channel γ or Z-exchange diagrams (Right) contain the triple gauge boson vertex ZWW or γWW.

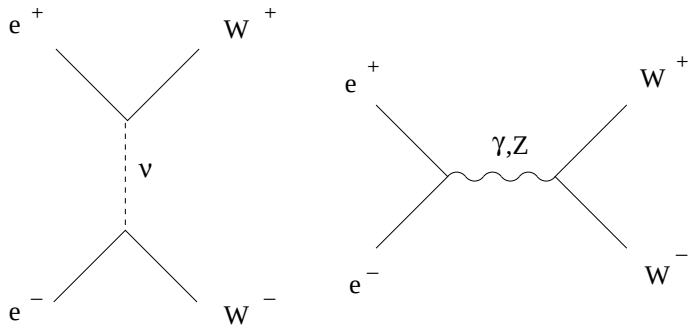

Figure 2.2: *On-shell W-pair production.* Left: *t-channel ν-exchange*, Right: *s-channel γ/Z-exchange*

Here we omit the Higgs-exchange diagram which is suppressed by a factor m_e/M_W and thus completely negligible.

The t-channel process involves left-handed electrons, while in the s-channel process both helicities contribute.

The kinematics of on-shell W-pair production is given by [27]

$$e^+ \ (p_+, \lambda_+) + e^- \ (p_-, \lambda_-) \to W^+ \ (k_+, \tau_+) + W^- \ (k_-, \tau_-)$$

where $\lambda_\pm = \pm 1/2$ is the helicity of the incoming electrons with momenta in the laboratory frame $p^\mu_\pm = E_{beam}(1, 0, 0, \mp 1)$, with the beam energy denoted by E_{beam}.
The W bosons in the final state have helicities $\tau_\pm = -1, 0, 1$ and momenta in the laboratory frame $k^\mu_\pm = E_{beam}(1, \mp\beta \sin\theta, 0, \mp\beta\cos\theta)$ with θ the scattering angle between the e^+ and the W^+ and $\beta = \sqrt{1 - M_W^2/E_{beam}^2}$ the velocity of the W boson.

The Mandelstam variables for this process are

$$s = \ (p_+ + p_-)^2 = (k_+ + k_-)^2 = 4E^2_{beam} \tag{2.37}$$

$$t = \ (p_+ - k_+)^2 = (p_- - k_-)^2 = -E^2_{beam}(1 + \beta^2 - 2\beta\cos\theta) \tag{2.38}$$

$$u = \ (p_+ - k_-)^2 = (p_- - k_+)^2 = -E^2_{beam}(1 + \beta^2 + 2\beta\cos\theta) \tag{2.39}$$

The polarization vectors for the W^+ and W^- bosons are introduced as

$$\epsilon^\mu_\pm(k_\pm, +1) = \frac{1}{\sqrt{2}}(0, \mp\cos\theta, -i, \pm\sin\theta) \tag{2.40}$$

$$\epsilon^{\mu}_{\pm}(k_{\pm},0) = \frac{E_{beam}}{M_W}(\beta, \mp\sin\theta, +i, \mp\cos\theta) \tag{2.41}$$

$$\epsilon^{\mu}_{\pm}(k_{\pm},-1) = \frac{1}{\sqrt{2}}(0, \mp\cos\theta, +i, \pm\sin\theta) \tag{2.42}$$

Neglecting the electron mass, the electron and the positron have opposite helicity

$$\lambda_- = -\lambda_+ = \lambda$$

We represent the helicity amplitude for W-pair production by $\mathcal{M}(\lambda, \tau_+, \tau_-, s, t)$. Requiring CP-invariance, we have

$$\mathcal{M}(\lambda, \tau_+, \tau_-, s, t) = \mathcal{M}(\lambda, -\tau_-, -\tau_+, s, t)$$

From these helicity amplitudes, the differential cross section for unpolarized electrons and W bosons is derived

$$\left(\frac{d\sigma}{d\Omega} \right) = \frac{1}{64\pi^2 s}\frac{\beta}{4}\sum_{\lambda,\tau_+,\tau_-} |\mathcal{M}(\lambda, \tau_+, \tau_-, s, t)|^2 \tag{2.43}$$

At lowest order, the Born amplitude is given by

$$\mathcal{M}_{Born}(\lambda, \tau_+, \tau_-, s, t) = \frac{e^2}{2\sin^2\theta_\omega}\frac{1}{t}\,\mathcal{M}_1^{\lambda}\,\delta_{\lambda_-} - e^2\,[\,\frac{1}{s} - \cot\theta_\omega\; g^{\lambda}_{eeZ}\;\frac{1}{\mathrm{s} - M_Z^2}]\;2\;(\mathcal{M}_2^{\lambda} - \mathcal{M}_3^{\lambda}) \tag{2.44}$$

where θ_ω is the weak mixing angle and $\delta_{\lambda_-} = 1$ for left-handed electrons and $\delta_{\lambda_-} = 0$ for right-handed electrons.
The coupling of the Z boson to the electrons g^{λ}_{eeZ} is given by

$$g^{\lambda}_{eeZ} = \tan\theta_\omega - \delta_{\lambda_-}\frac{1}{2\sin\theta_\omega\cos\theta_\omega} \tag{2.45}$$

and the invariant amplitudes are

$$\mathcal{M}_1^{\lambda} = \overline{v}(p_+)\;[\epsilon_+\;(k_+ - p_+)\;\epsilon_-]\;P_\lambda\;u(p_-) \tag{2.46}$$

$$\mathcal{M}_2^{\lambda} = \overline{v}(p_+)\;[\frac{(k_+ - k_-)}{2}\;(\epsilon_+.\epsilon_-)]\;P_\lambda\;u(p_-) \tag{2.47}$$

$$\mathcal{M}_3^{\lambda} = \overline{v}(p_+)\;[(\epsilon_+\;(\epsilon_-.k_+) - \epsilon_-\;(\epsilon_+.k_-))]\;P_\lambda\;u(p_-) \tag{2.48}$$

where $P_\lambda = P_\pm$ represent the helicity projection operators used to project on right- and left-handed massless fermions

$$P_\pm = \frac{1}{2}(1 \mp \gamma_5) \tag{2.49}$$

The γ_5 matrix is defined as $\gamma_5 = i\gamma^0\gamma^1\gamma^2\gamma^3$.

The Born amplitude can be rewritten in terms of two gauge-invariant subsets

$$\mathcal{M}_{Born} = \frac{e^2}{2\sin^2\theta_w}\mathcal{M}_I\delta_{\lambda_-} + e^2\mathcal{M}_Q \tag{2.50}$$

where

$$\mathcal{M}_I = \frac{1}{t}\mathcal{M}_1^\lambda + \frac{2}{s-M_Z^2}(\mathcal{M}_3^\lambda - \mathcal{M}_2^\lambda) \tag{2.51}$$

$$\mathcal{M}_Q = [\frac{1}{s} - \frac{1}{s-M_Z^2}]2(\mathcal{M}_3^\lambda - \mathcal{M}_2^\lambda) \tag{2.52}$$

The lowest-order cross section describes the global behaviour of W-pair production.
For fixed scattering angles and small β

$$\mathcal{M}_1^\lambda \propto\ 1,\ \mathcal{M}_2^\lambda,\ \mathcal{M}_3^\lambda \propto \beta \tag{2.53}$$

consequently the s-channel matrix elements vanish at threshold, where the t-channel contribution is dominant.
The differential cross section for unpolarized electrons and bosons near threshold is

$$\left(\ \tfrac{d\sigma}{d\Omega}\ \right)_{Born} \approx\ \frac{\alpha^2}{s}\ \frac{1}{4\sin^4\theta_w}\ \beta\ [\ 1 + 4\ \beta\ \cos\theta\ \frac{3\cos^2\theta_w - 1}{4\cos^2\theta_w - 1} + \mathcal{O}(\beta^2)\ ] \tag{2.54}$$

The leading term is proportional to β and originates from the t-channel process only, while the s-channel process contributes to the term proportinal to $\beta^2\cos\theta$. At small values of β the differential cross section is essentially angular independent while for increasing centre-of-mass energy angular dependent terms are introduced. As a consequence, the W bosons are produced isotropically in the threshold region and more and more forward for increasing center-of-mass energies.

The total cross section is given by

$$\sigma_{Born} \approx\ \frac{\pi\alpha^2}{s}\ \frac{1}{\sin^4\theta_w}\ \beta + \mathcal{O}(\beta^3) \tag{2.55}$$

where all terms $\propto \beta^2$ drop out and the s-channel and s-t interference are of $\mathcal{O}(\beta^3)$. The leading term comes entirely from the t-channel ν-exchange. Therefore there is almost no sensitivity to triple gauge couplings at threshold.

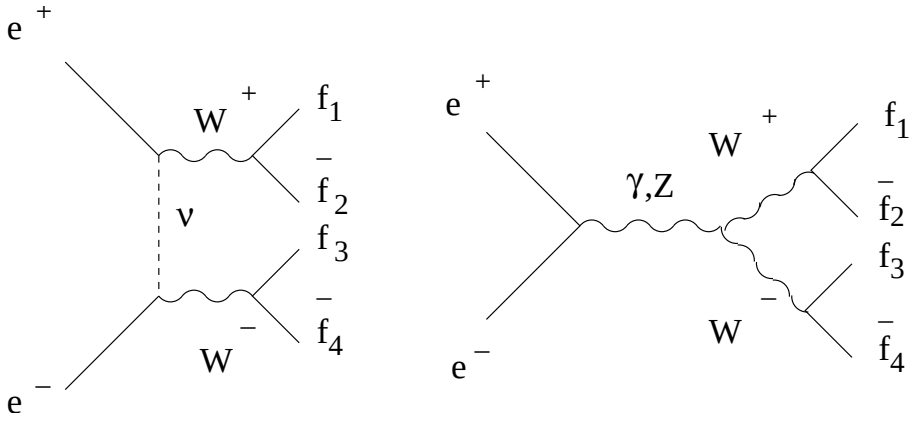

Figure 2.3: *Off-shell W-pair production.* Left: *t-channel ν-exchange*, Right: *s-channel γ/Z-exchange*

2.2.2 Lowest order off-shell W-pair production

Up to now we considered the production of stable W bosons. We will now treat them as a resonances with a finite, non-zero width :

$$e^+e^- \rightarrow W^+W^- \rightarrow f_1\bar{f}_2 f_3\bar{f}_4$$

At lowest order this process is described by the same three Feynman diagrams as in the on-shell approximation but now proceeding through the production of two resonant W bosons, leading to a four-fermion final state. This is presented in Figure 2.3. Comparing to the on-shell case, a non-zero W width has to be implemented. This is done by numerical integration, either by a semi-analytical approach or by a Monte Carlo method.

- *Semi-analytical approach*

  The finite W width is introduced by the convolution of two Breit-Wigner densities $\rho(s)$ with the on-shell CC03 cross section at lowest order (Born level)

  $$\sigma_{WW}^{off-shell,Born}(s) = \int_0^s \rho(s_1)ds_1 \int_0^{(\sqrt{s}-\sqrt{s_1})^2} \rho(s_2)ds_2 \; \sigma_{WW}^{on-shell,Born}(s; s_1, s_2) \quad (2.56)$$

  where $\sqrt{s_1}$ and $\sqrt{s_2}$ are the masses of the W bosons and s the center-of-mass energy.

The relativistic Breit-Wigner density for the W boson is used

$$\rho(s) = \frac{1}{\pi} \frac{\Gamma_W(s)}{M_W} \frac{s}{(s - M_W^2) + s^2 \frac{\Gamma_W^2(s)}{M_W^2}} \tag{2.57}$$

The W width, Λ_W, depends on s as the phase space increases with s

$$\Gamma_W(s) = \frac{s}{M_W^2} \Gamma_W(M_W^2) \tag{2.58}$$

This is called the "running width" definition. In pratice the energy dependence $\rho(s)$ is approximated by the so-called "fixed width" definition

$$\overline{\rho} = \frac{1}{\pi} \frac{\overline{M_W}\ \overline{\Gamma_W}}{(s - \overline{M_W^2})^2 + \overline{\Gamma_W^2}\ \overline{M_W^2}} \tag{2.59}$$

where

$$\overline{M_W} = M_W - \frac{1}{2} \frac{\Gamma_W^2}{M_W} = M_W - \ 26.9 \text{ MeV} \tag{2.60}$$

$$\overline{\Gamma_W} = \Gamma_W - \frac{1}{2} \frac{\Gamma_W^3}{M_W^2} = \Gamma_W - \ 0.7 \text{ MeV} \tag{2.61}$$

This integration technique is used by the GENTLE [33] program.

- *Monte Carlo method*

  In this approach the cross section is directly calculated from the matrix elements by Monte Carlo integration of the differential cross section (Eq. 2.42 and 2.55).

The semi-analytical approach is accurate and is fast. The Monte Carlo approach is slower but has the advantage that the differential distributions are calculated from the kinematic variables of the particles in the final state and the detector simulation can be properly included. The on- and off-shell CC03 cross sections for W-pair production are presented in Figure 2.4 [27].

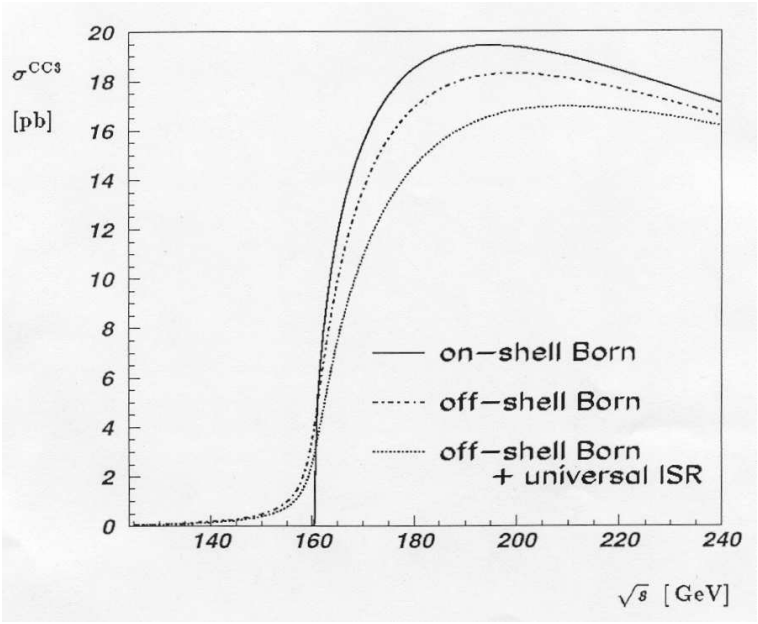

Figure 2.4: *The on- and off-shell CC03 cross sections for W pair production.*

2.2.3 Four-fermion processes beyond tree level

Experimentally there is no possibility to distinguish the four-fermion final states produced by a W-pair and and those proceeding from mechanisms where a single or non-resonant W boson is created. All diagrams with the same initial state and the same final state but a different intermediate state and their interferences have to be considered. The corresponding processes can be devided in charged current final states (CC) and neutral current final states (NC).

Apart from the CC03 diagrams there are at least seven additional diagrams, presented in Figure 2.5(a), to be considered in the description of the semi-leptonic channel. They all contain a Z or γ boson and a singly resonant W in the s-channel. The $qq\mu\nu$ and $qq\tau\nu$ final states are fully represented by these CC10 diagrams.
The $qqqq$ final state has also the contribution from the Z-pair production (Figure 2.5(b)) and is described by the CC11 representation. To describe the $qqe\nu$ final state, one has to introduce the γ/Z scattering diagrams in the t-channel, presented in Figure 2.5 (c),(d),(e) with a singly resonant W in the s-channel and with a non resonant W in the t-channel (f). Together with the CC10 diagrams, they form the CC20 representation. Finally the $l\nu l\nu$ final state is obtained by more than 100 diagrams (CC56+NC56).

So far only diagrams beyond CC03 level with W-boson production were discussed, but also the CC and NC diagrams, without W-boson production but with the same initial state and final state as the W-pair signal process, need to be considered.

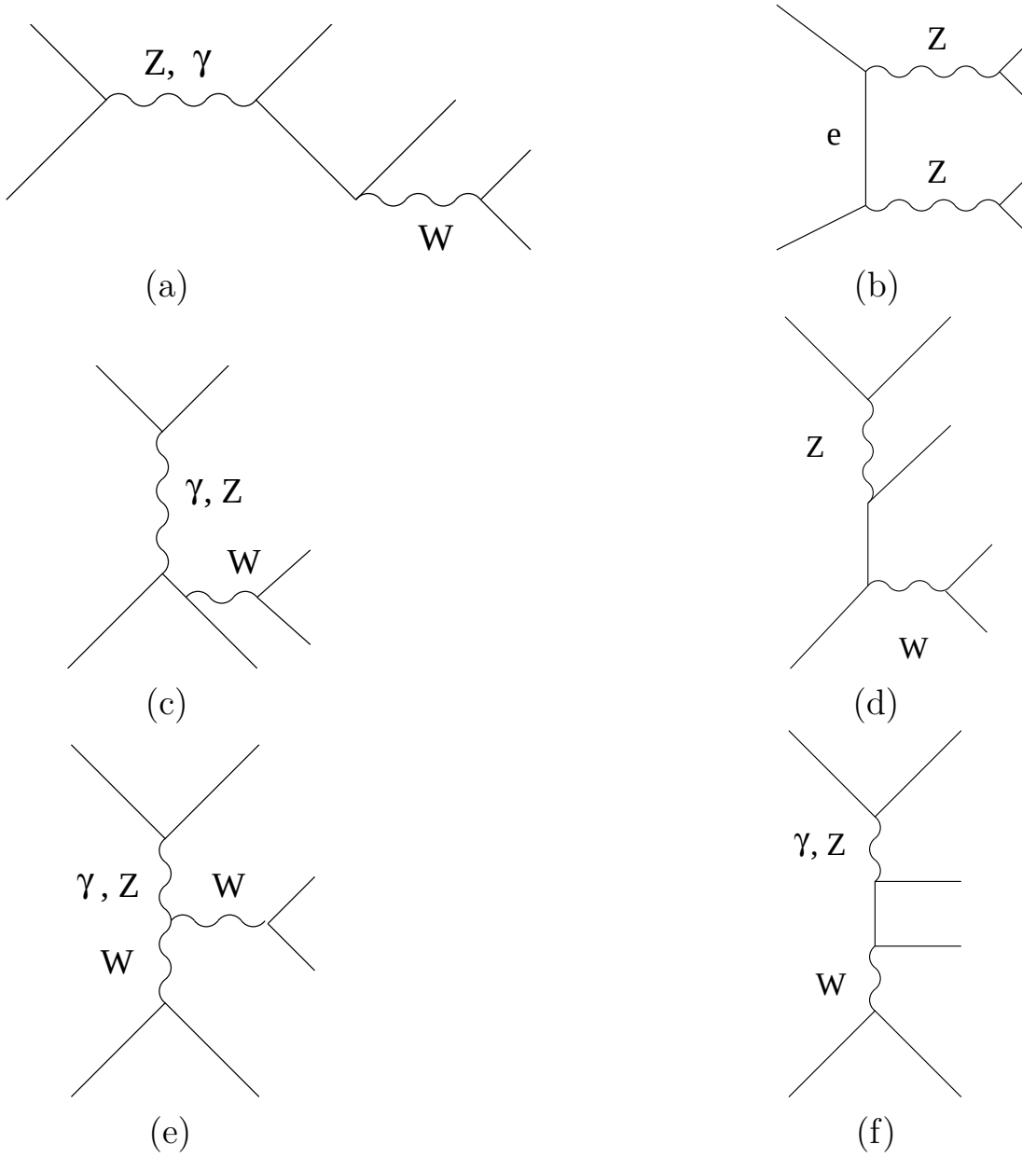

Figure 2.5: *The typical four-fermion diagrams beyond tree level for the semi-leptonic and hadronic final states in W-pair production:* (a), (c), (d), (e) : *singly resonant diagrams*, (f) : *non-resonant diagram*, (b) : $e^+e^- \rightarrow ZZ \rightarrow qqqq$ *background diagram for W-pair production in the hadronic channel.*

Examples of such processes are ZZ- and Zee production, discussed in Section 1.1.4. This increases the number of diagrams for the $l\nu l\nu(\gamma)$ final state to 115 and for the $qqqq(\gamma)$ final state to 214. All remaining processes are reducible backgrounds and have an experimental origin. They are the result of a wrong event reconstruction due to detector effects.

2.3 W Polarisation

Contrary to the massless photon which has only two transverse helicity states, with the photon's spin parallel to its momentum vector, $\tau_\gamma = \pm 1$, the massive W and Z bosons have an additional, longitudinal, helicity state with spin oriented perpendicular to its momentum vector $\tau_{W,Z} = 0, \pm 1$. The longitudinal polarisation is generated through the Higgs mechanism. After spontaneous electroweak symmetry breaking, the massless W boson becomes massive by absorption of a Goldstone boson and the spin degree of freedom associated to this scalar particle is transformed into the longitudinal polarisation of the massive W boson. By the measurement of the fraction of the transverse and longitudinal W helicity fraction, the validity of the Standard Model is tested.

Considering the helicity, the W-pair production process is written as

$$e^+(\lambda')\ e^-(\lambda) \rightarrow W^+(\tau_2)\ W^-(\tau_1)\ , \tag{2.62}$$

where λ, λ' are the helicity of the electron (positron). In the high energy limit, where we can neglect the electron mass, the helicity of the positron is opposite to the electron's helicity: $\lambda' = -\lambda$. The helicities of the W^- and the W^+, denoted by τ_1 and τ_2 respectively, take the value $\tau = \pm 1$ for transversely polarised W bosons and the value $\tau = 0$ for W bosons with a longitudinal polarisation.

Because of the principle of angular momentum conservation in the $e\nu W$, ZWW and γWW vertex, the W-pair final state is characterised by the total angular momentum for

- **the s-channel Z- and γ-exchange processes:**

$$\vec{J}_{tot} = \vec{1},\ |\ J_z\ | = 0, 1 \tag{2.63}$$

- **the t-channel ν-exchange process:**

$$\vec{J}_{tot} = \vec{2},\ |\ J_z\ | = 0, 1, 2 \tag{2.64}$$

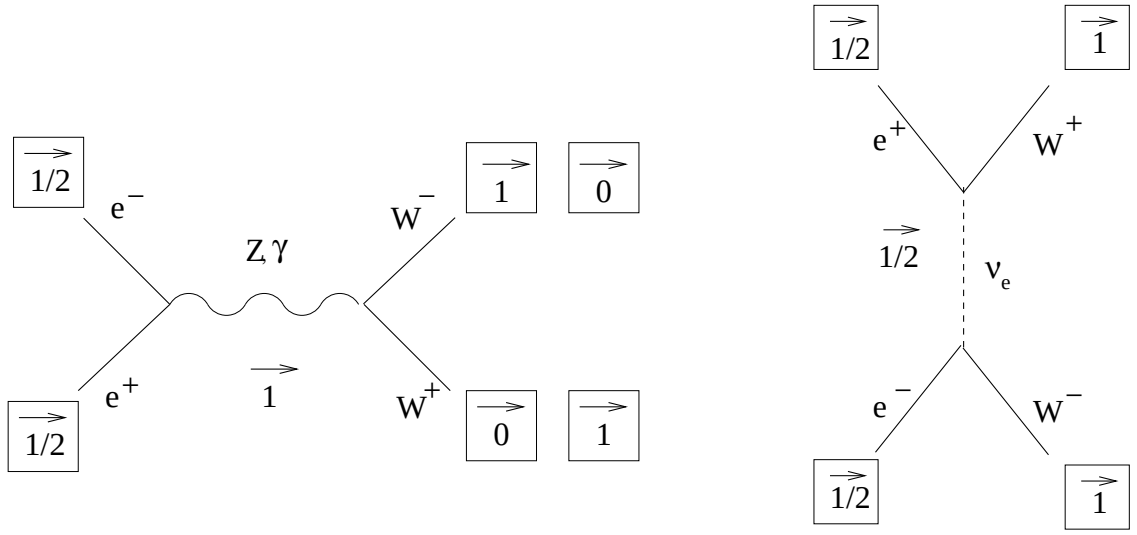

Figure 2.6: *A schematic diagram of the possible spin configurations for the W-pair production process. The s-channel Z- and γ-exchange processes lead to a final state with total angular momentum $\vec{J}_{tot} = \vec{1}$, while for the t-channel ν-exchange , a total angular momentum $\vec{J}_{tot} = \vec{2}$ is reached.*

Figure 2.6 gives a schematic diagram of the possible spin configurations for the W-pair production process. They leads to nine possible helicity configurations for the W-pair final state:

$$TL, LT: \ (+1,\ 0),\ (-1,\ 0),\ (\ 0,+1),\ (\ 0,-1) \tag{2.65}$$

$$TT: \ (+1,+1),\ (-1,-1),\ (+1,-1),\ (-1,+1) \tag{2.66}$$

$$LL: \ (\ 0,\ 0) \tag{2.67}$$

The helicity states (-1,+1) and (+1,-1) are obtained by the ν-exchange only process as they correspond to a total angular momentum projection $J_z = \pm 2$, while all other helicity states are accessible by both processes. The expected Standard Model differential cross section $d\sigma_{WW}/d\cos\theta_{W^-}$ for the $e^+e^- \rightarrow W^+W^-$ process for particular WW helicity configurations at $\sqrt{s}$= 200 GeV is shown in Figure 2.7. The (0, 0) helicity amplitude is smaller than the transverse helicity amplitudes which are dominated by the (-1,+1) helicity.

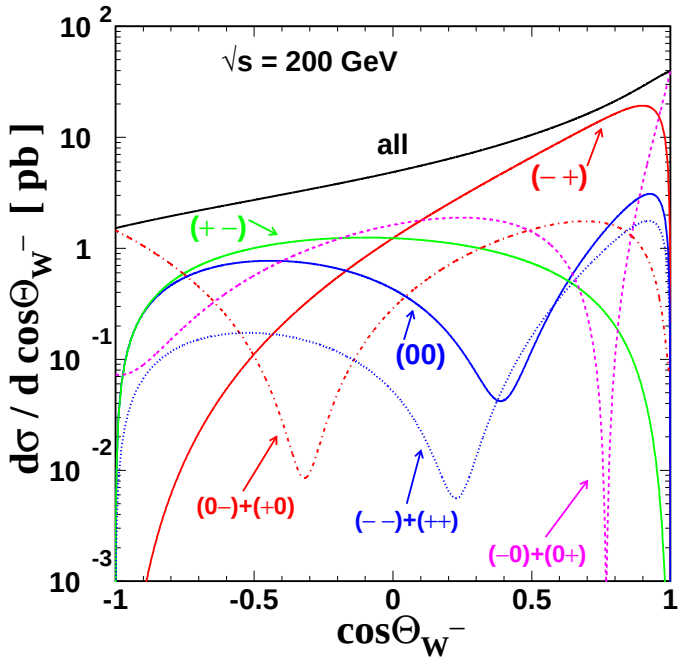

Figure 2.7: *The expected Standard Model differential cross section for the* $e^+e^- \to W^+W^-$ *process for particular* WW *helicity configurations at* $\sqrt{s}$*= 200 GeV.*

2.4 W Triple Gauge Couplings

The most general Lorentz-invariant Lagrangian involving $VWW(V = \gamma, Z)$ vertices is parametrized by seven complex parameters or fourteen real parameters [34]

$$i\mathcal{L}^{WW}_{eff}/g_{WWV} = g^V_1 V^\mu (W^-_{\mu\nu}W^{+\nu} - W^+_{\mu\nu}W^{-\nu}) + \kappa_V W^+_\mu W^-_\nu V^{\mu\nu} +$$

$$\frac{\lambda_V}{M^2_W} V^{\mu\nu} W^{+\rho}_\nu W^-_{\rho\mu} + ig^V_5 \epsilon_{\mu\nu\rho\sigma}((\partial^\rho W^{-\mu})W^{+\nu} - W^{-\mu}(\partial^\rho W^{+\nu}))V^\sigma +$$

$$ig^V_4 W^-_\mu W^+_\nu (\partial^\mu V^\nu - \partial^\nu V^\mu) - \frac{\tilde{\kappa}_V}{2} W^-_\mu W^+_\nu \epsilon^{\mu\nu\rho\sigma} V_{\rho\sigma} - \frac{\tilde{\lambda}_V}{2M^2_V} W^-_{\rho\mu} W^{+\mu}_\nu \epsilon^{\nu\rho\alpha\beta} V_{\alpha\beta} \qquad (2.68)$$

where $g_{WWV} = e$, $g_{WWZ} = e\cot\theta_w$ and ϵ^{ijkl} an anti-symmetric tensor defined by $\epsilon^{0123} = 1$ and where ϵ^{ijkl} takes the value -1 (+1) if $ijkl$ is an odd (even) permutation of 0123 and the value 0 in all other cases. The field strength tensors $W_{\mu\nu}$ and $V_{\mu\nu}$ are defined as

$$W_{\mu\nu} = \partial_\mu W_\nu - \partial_\nu W_\mu$$

$$V_{\mu\nu} = \partial_\mu V_\nu - \partial_\nu V_\mu \qquad (2.69)$$

Coupling	C	P	**Standard Model**
CP-conserving couplings			
λ_γ, λ_Z	$\times$	$\times$	0
κ_γ, κ_Z	$\times$	$\times$	1
g_1^γ,g_1^Z	$\times$	$\times$	1
g_5^γ, g_5^Z			0
CP-violating couplings			
g_4^γ, g_4^Z		$\times$	0
$\tilde{\lambda}_\gamma$, $\tilde{\lambda}_Z$	$\times$		0
$\tilde{\kappa}_\gamma$, $\tilde{\kappa}_Z$	$\times$		0

Table 2.2: *The W triple gauge couplings. The cross indicates if the coupling is invariant under charge conjugation (C), respectively parity transformation (P). The Standard Model value for the couplings is also indicated.*

The 14 parameters in front of each term in the Lagrangian are the W Triple Gauge Couplings (TGC's). Only 4 parameters have a non-zero value at tree level in the Standard Model:

$$g_1^Z = \kappa_Z = g_1^\gamma = \kappa_\gamma$$

Deviations from Standard Model show up as distortions in the angular distributions of the W boson and the decay fermions, especially in the backward direction where the t-channel ν-exchange process is weaker. This could result in a cross section diverging with increasing center-of-mass energies and eventually destroying the gauge cancellation amoung the three CC03 diagrams. Consequently, unitarity is violated unless the effect is compensated by a new physics process.

The W TGC's have a caracteristic behaviour under charge conjugation C and parity transformation P. A summary of the 14 W TGC's, their Standard Model value and their behaviour under C, P and CP transformations is given in in Table 2.2. The eight couplings λ_V, κ_V, g_1^V and g_5^V, are invariant under CP-transformations. and are related to the charge of the W^+, q_W, its magnetic dipole moment, μ_W^{mag}, and its electric quadrupole moment, Q_W^{elec},

$$q_W = e g_1^\gamma \tag{2.70}$$

$$\mu_W^{magn} = \frac{e}{2M_W}(1 + \kappa_\gamma + \lambda_\gamma) \tag{2.71}$$

$$Q_W^{elec} = -\frac{e}{2M_W^2}(\kappa_\gamma - \lambda_\gamma) \tag{2.72}$$

The remaining six couplings, g_4^V, $\tilde{\lambda}_V$ and $\tilde{\kappa}_V$ are CP-violating and are related to the electric dipole moment and magnetic quadrupole moment of the W

$$\mu_W^{elec} = \frac{e}{2M_W}(\tilde{\kappa}_\gamma + \tilde{\lambda}_\gamma) \tag{2.73}$$

$$Q_W^{magn} = -\frac{e}{2M_W^2}(\tilde{\kappa}_\gamma - \tilde{\lambda}_\gamma) \tag{2.74}$$

Requiring electromagnetic gauge invariance, the W charge is fixed. This leads to $g_1^\gamma = 1$ and $g_5^\gamma = 0$. To reduce the number of parameters, extra constraints are applied.
Assumming CP-conservation, five parameters are remain: g_1^Z, κ_Z, κ_γ, λ_Z and λ_γ. The $SU(2)_L \otimes U(1)_Y$ symmetry of the Lagrangian imposes the constraints

$$\kappa_Z = g_1^Z - (\kappa_\gamma - 1)\tan^2\theta_w \qquad\qquad \lambda_\gamma = \lambda_Z \tag{2.75}$$

At the end, only three free parameters are left:

$$g_1^Z,\ \kappa_\gamma \text{ and } \lambda_\gamma$$

The measurement of the W TGC's is presented in Chapter 6.

2.5 Definition of the WW phase space

In absence of polarised beams and for on-shell W-pairs (narrow width approximation), the four-fermion process $e^+e^- \to W^+W^- \to f_1\bar{f}_2 f_3\bar{f}_4$ is completely described by the following five angles

- $\cos\theta_{W^-}$: the cosine of the polar angle of the W^-
- $\phi_f^\star, \cos\theta_f^\star$: the azimuthal angle and cosine of the polar angle of the W^- decay fermion in the W^- restframe
- $\phi_{\bar{f}}^\star, \cos\theta_{\bar{f}}^\star$: the azimuthal angle and cosine of the polar angle of the W^+ decay antifermion in the W^+ restframe

where the e^- direction is taken as the positive z-axis. The angles are shown in Figure 2.8 In the definition of the fermion and antifermion angles, the corresponding W-direction is taken as z-axis and the y-axis is perpendicular to the plane defined by the beam and the W boson: $\vec{y} = \vec{e} \times \vec{W}$.

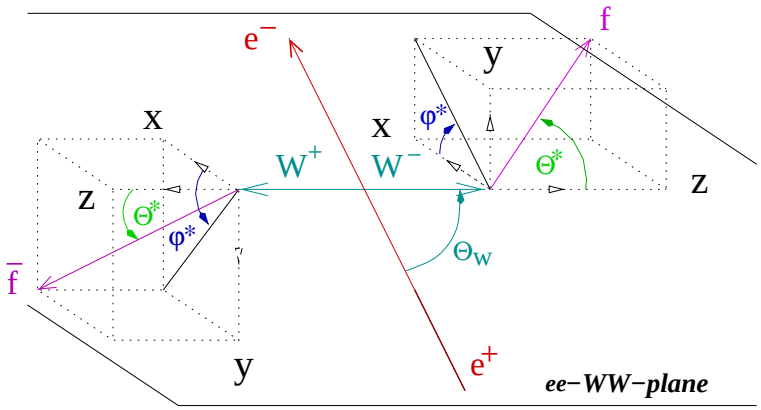

Figure 2.8: *The four-fermion process* $e^+e^- \to W^+W^- \to f_1\bar{f}_2 f_3 \bar{f}_4$ *is completely described by the five angles represented here.*

With this definition of the W restframe, the polar angule distribution of W^+ and W^- decay particles are identical. The azimuthal angle distribution for the antifermion is obtained by the substitution $\theta^\star \to \pi^\star$ - $\theta^\star$ and $\phi^\star \to \pi^\star + \phi^\star$ in the corresponding distribution of the fermion.

All the information available for the TGC measurement is contained in the following five-fold cross section

$$\frac{d^5\sigma(e^+e^- \to f_1\bar{f}_2 f_3\bar{f}_4)}{d\cos\theta_{W^-}\; d\cos\theta^*_f\; d\phi^*_f\; d\cos\theta^*_{\bar{f}}\; d\phi^*_{\bar{f}}} \tag{2.76}$$

The existence of an anomalous coupling modifies the total W-pair production cross section and the angular distributions of the W boson and the decay fermions.

Chapter 3

Monte Carlo Programs

To evaluate the level of agreement between the L3 data and the Standard Model, Monte Carlo events are generated according to the Standard Model theory and subsequently passed to the detector simulation program SIL3 to simulate the response of the L3 detector. The SIL3 software uses the GEANT3 [35] framework to model the L3 detector response and the GHEISHA [36] program to simulate hadronic showers. All simulations include time dependent detector inefficiencies, monitored during the data taking. The tracking of the particles through the detector considers the effects of multiple scattering, energy loss and showering in the detector material. The REL3 program is applied to reconstruct the simulated events and bring them to the same level as real data, ready for analysis and comparison.

3.1 Four-fermion Monte Carlo Generators

The baseline Monte Carlo generator used in the L3 W physics analysis group is the KandY [37] Monte Carlo which runs concurrently the most recent version of the KORALW [38] and the YFSWW3 [39] Monte Carlo's. The KandY Monte Carlo is a full four-fermion (4f) generator including all neutral 4f processes (ZZ and Zee production) and charged 4f processes(WW production) obtained using the full set of Feynman diagrams. The KandY event generation takes place in two steps: first KORALW generates the phase space for the four massive final state fermions including all possible 4f diagrams, second YFSWW3 calculates the $\mathcal{O}(\alpha)$ corrections from the fermion momenta and gives the obtained weight to each KORALW event.

The hadronisation model implemented in the KandY Monte Carlo is the PYTHIA [40] model. The hadronisation models HERWIG [41] and ARIADNE [42] are used as alternatives to the PYTHIA model to estimate the fragmentation and hadronisation systematics. They are discussed in the Section 3.3.

Process	Monte Carlo generator
$e^+e^- \to ffff(\gamma)$	KandY
$e^+e^- \to q\bar{q}(\gamma)$	KK2f
$e^+e^- \to q\bar{q}(\gamma)$	PYTHIA
$e^+e^- \to \mu^+\mu^-(\gamma), \tau^+\tau^-(\gamma)$	KORALZ
$e^+e^- \to e^+e^-(\gamma)$	BHAGENE3
$e^+e^- \to e^+e^-(\gamma)$	BHWIDE
$e^+e^- \to e^+e^-\ \gamma(\gamma)$	TEEGG
$e^+e^- \to e^+e^-\ \gamma\gamma \to e^+e^-\ l^+l^-$	DIAG36
$e^+e^- \to e^+e^-\ \gamma\gamma \to e^+e^-\ l^+l^-$	LEP4F
$e^+e^- \to e^+e^-\ \gamma\gamma \to e^+e^-$ hadrons	PHOJET

Table 3.1: *The four-fermion Monte Carlo generators used to simulate W-pair production process and its backgrounds.*

The KandY Monte Carlo also provides matrix elements on an event-by-event base to calculate the contribution of the CC03 subset or the $\mathcal{O}(\alpha)$ corrections. This is of great importance to derive cross sections and other physical quantities at CC03 level and to evaluate systematic uncertainties. The luminosity of the KandY Monte Carlo is about 45000 pb^{-1} at $\sqrt{s}$ =189, 192, 196, 200, 202, 205 and 206 GeV, and about 23000 pb^{-1} at the highest energy point, $\sqrt{s}$=208 GeV.

The Monte Carlo generators used to simulate the background processes for W-pair production are KK2f [43], PYTHIA, KORALZ [44], BHAGENE3 [45] and BHWIDE [46] for fermion-pair production, denoted as $e^+e^+ \to f\bar{f}(\gamma)$, where $f = e,\ \mu,\ \tau$ or q, TEEGG [47] for radiative $e^+e^+ \to e^+e^+\gamma(\gamma)$ events, DIAG36 [48] and LEP4F [49] for two photon events with lepton-pair final states and PHOJET [50] for two photon events with hadronic final states. They are summarised in Table 3.1.

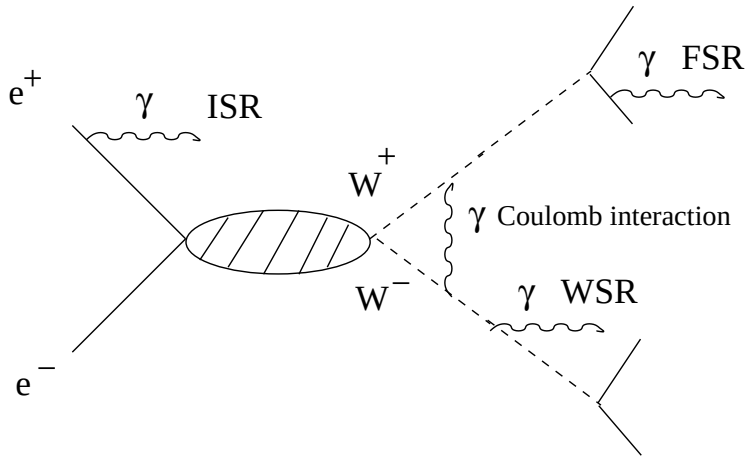

Figure 3.1: *The electroweak radiative corrections : initial and final state radiation and the Coulomb interaction.*

3.2 Electroweak Radiative Corrections

So far, only leading order processes have been discussed in the previous chapter, and no higher order corrections on the calculation of the W-pair cross section were included. The main electroweak radiative corrections of order $\mathcal{O}(\alpha)$ are

- **Initial State Radiation (ISR):**
  the radiation of one or more real photons from the incoming electron or positron
- ***W* intermediate State Radiation (WSR):**
  the radiation of real photons from W bosons in the intermediate state
- **Final State Radiation (FSR):**
  the radiation of real photons from W decay fermions in the final state
- **Coulomb interaction:**
  the exchange of virtual photons between the charged W bosons

They are represented in Figure 3.1.

Experimentally, there is no separation possible between ISR, WSR and FSR photons, unless the FSR or WSR photon is very energetic and emitted at large angle. Only in the Monte Carlo programs, it is possible to separate ISR photons from WSR and FSR photons.

ISR

The presence of ISR photons gives the most important correction. They are emitted at low polar angle and carry away a significant amount of longitudinal momentum when they escape into the beampipe without detection. As a consequence a longitudinal momentum inbalance is given to the reconstructed event. ISR reduces the available effective center-of-mass energy to $\sqrt{s'}$. In case of a ISR photon radiated collinear to the beam-axis, $\sqrt{s}$ is decreased to

$$\sqrt{s'} = \sqrt{s}.\sqrt{(1 - \frac{2E_\gamma}{\sqrt{s}})} \tag{3.1}$$

where E_γ is the energy of the radiated ISR photon. The total cross section as well as the differential cross section are modified: due to the boost of the e^+e^- center-of-mass frame, the angular distribution of the W boson is distorted.

The ISR effect is included in the KandY Monte Carlo up to $\mathcal{O}(\alpha^3)$ in the leading logarithm approximation.

WSR and FSR

The WSR and FSR photons modify the angular distribution of their parent particle and influence therefore the differential cross section. A FSR photon is assigned to the particle with whom it has the smallest angular separation. As the energy loss due to FSR radiation decreases with a power four of the particle's mass, the FSR effect is most important for electrons than the muons or taus.

FSR and WSR are implemented in the KandY Monte Carlo through the PHOTOS package [51], based on a calculation up to $\mathcal{O}(\alpha^2)$ in the leading logarithm approximation.

Coulomb singularity

Before they decay into fermions, the W bosons can echange a virtual photon. As the phenomenon is inversely proportional to the W boson's velocity, the Coulomb interaction diverges at the W-pair production threshold and is therefore called "Coulomb singularity" in the on-shell case, but the divergence is absorbed in the non-zero W width in the off-shell situation. The effect on the reconstructed mass of the W boson is about 5 MeV. It changes the total W-pair production cross section at threshold by few percent and the effect decreases with $\sqrt{s}$.

Virtual $\mathcal{O}(\alpha)$ corrections

There are also significant contributions from the exchange of virtual photons between any pair of charged particles throughout the entire process. If the virtual photon connects particles participating in the same production or decay process, the corrections are conveniently implemented by means of a QCD-like 'structure function' formalism: the Born cross section is multiplied by a so-called radiator function expressing the probability for the electron or positron to emit a photon. This semi-analytical method results in factorisable corrections and is implemented in the GENTLE [33] and EXCALIBUR [52] programs. However, this approach has some additional disadvantages. Both programs simulate ISR but FSR and WSR are not taken into account, neither is their interference with ISR. Only hard photons emitted collinearly to the direction of propagation are generated. This leads to a 2% uncertainty on the total cross section. Monte Carlo generators using this technique can only generate hard photons emitted collinearly to the direction of propagation. Both problems are absent when using a numerical integration method where the evolution equations for the structure function are solved numerically. Furthermore, the semi-analytical approach is not possible when the virtual photon links particles from different processes. In W-pair events, contrary to Z-peak events, charged particles are present in every step of the process and one has to take into account the exchange of virtual photons everywhere in the diagrams, leading to non-factorisable virtual $\mathcal{O}(\alpha)$ corrections. The Yennie-Frautschi-Suura(YFS) exponentiation technique [53] implemented in KandY, provides a numerical integration method treating the virtual $\mathcal{O}(\alpha)$ photon exchange between the initial state and final state and the between the intermediate and the final state.

Ideally one would like to take into account the complete set of $\mathcal{O}(\alpha)$ radiative corrections. At the beginning of LEP2, theoretical predictions were available for ISR, FSR, their interference and the factorisable virtual $\mathcal{O}(\alpha)$ corrections [54]. By neglecting the non-factorisable corrections, the sensitivity of the LEP experiments is reduced: the theoretical uncertainty on the W-pair cross section was estimated to be about 2% while the estimated combined experimental uncertainty at the end of LEP2 is 1%.

More recent calculations apply the Double Pole Approximation(DPA), implemented in Monte Carlo generators like RACOONWW [55] or the Leading Pole Approximation (LPA), applied in YFSWW3. In W-pair production two unstable W resonances are present. The phase space is shared among the W resonances and therefore their masses and widths are correlated. When introducing a finite, non-zero width, the phase space of the off-shell W-pairs needs a carefull mapping on the on-shell phase space. In the DPA, the expansion of the invariant amplitude for W-pair production is restricted to the double-pole residues and the corresponding intrinsic uncertainty is estimated to be ≤ 0.5 % at LEP2 energies. In the LPA, the expansion is restricted to the leading pole.

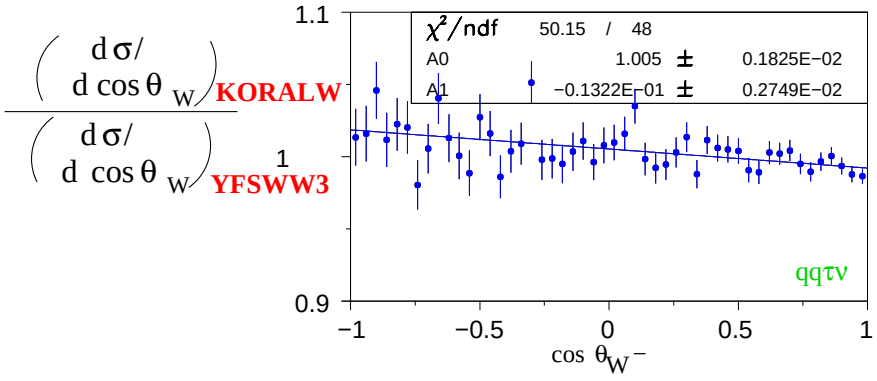

Figure 3.2: *The differential cross section for W-pair production in the $qq\tau\nu(\gamma)$ final state for KORALW compared to YFSWW.*

RACOONWW treats the virtual $\mathcal{O}(\alpha)$ electroweak radiative corrections to the off-shell W-pair production in the DPA, while YFSWW3 approach is to apply the LPA to the on-shell W-pair production. The inclusion of non-factorisable radiative corrections in the LPA reduces the cross section estimation relative to $\mathcal{O}(\alpha)$ corrections of about 2.3%.

The ratio of the differential cross section for W-pair production in the $qq\tau\nu(\gamma)$ final state for the KORALW Monte Carlo, without implementation of non-factorisable radiative corrections, on the corresponding differential cross section for YFSWW, with the LPA approach, is shown in Figure 3.2. A global slope of 1.3% is found. The effect on the W production angle of the $\mathcal{O}(\alpha)$ corrections in the LPA is about 0.7%, the remaining 0.6% is due to the difference in renormalisation scheme used by the two Monte Carlo's, the LEP2-scheme for KORALW and the G_μ-scheme for YFSWW.

3.3 Hadronisation and Fragmentation Models

The simulation of the four-fermion(4f) production process, $e^+e^- \rightarrow W^+W^- \rightarrow q_1\bar{q}_2q_3\bar{q}_4$, consists of four steps, presented in Figure 3.3. for the W bosons decaying into a $q\bar{q}$ pair

- *Step I:*

  The electron and positron annihilate and a W-pair is produced. This is followed by the subsequent decay of each W in a lepton-antilepton pair or a quark-antiquark pair. This level is well discribed by the electroweak theory.

- *Step II:*

  The primary quarks radiate photons and gluons and produce a high energy partonic shower: gluons and quark-antiquark pairs. This fragmentation process is described by perturbative QCD.

- *Step III:*

  The coloured partons are confined into hadrons. This hadronisation process belongs to non-perturbative QCD and is modelled using phenomenological models, tuned by L3 with high precision Z-peak data collected during LEP1.

- *Step IV:*

  The unstable hadrons decay into particles which are experimentally observed by the different detectors.

The available Monte Carlo programs for the simulation of the fragmentation and the hadronisation phase are PYTHIA, ARIADNE and HERWIG. They use matrix elements to simulate the perturbative phase of the fragmentation process. PYTHIA and ARIADNE simulate the non-perturbative phase using the Lünd String Model. In this model the colour flux is represented by strings which connect the partons and form hadrons once broken up. HERWIG implements the non-perturbative phase by a cluster model. In this model the partons are gathered in colourless clusters of different mass which finally decay into hadron pairs. After the fragmentation and hadronisation phase, the hadrons decay according to the branching ratio tables implemented in the Monte Carlo generators.

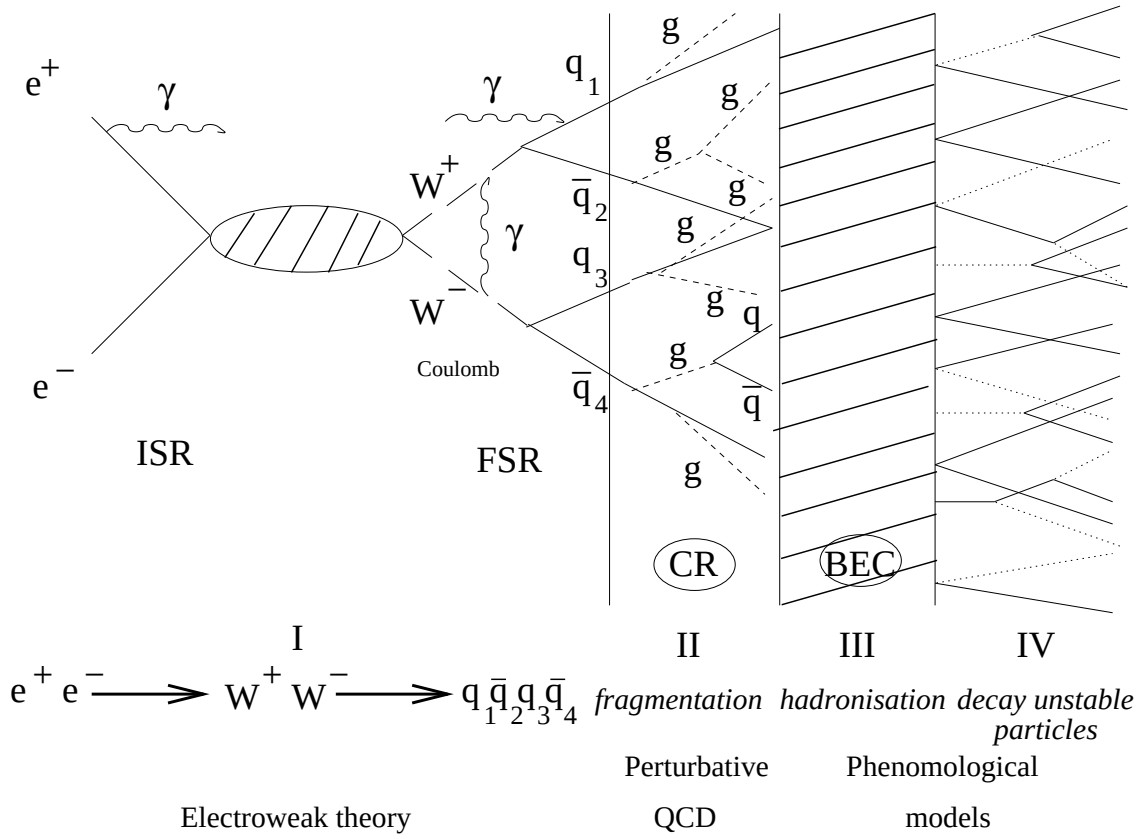

Figure 3.3: *The simulation of the four fermion production process:* $e^+e^- \to W^+W^- \to q_1\bar{q}_2q_3\bar{q}_4$.

3.4 Final State Interactions

During the fragmentation and hadronisation of the W bosons into the final state particles, cross-talk phenomena can occur between the W systems. The distance between the decay vertices is about 0.1 fm, much smaller than the typical hadronisation scale of 1-10 fm; as a consequence, the space-time overlap is significant. There are two main final state interaction phenomena : Bose-Einstein Correlation (BEC) at hadron level and Colour Reconnection (CR) at parton level.

3.4.1 Bose-Einstein Correlations (BEC)

This effect is related to the quantum mechanical interference between identical, low momentum mesons, mainly pions, sharing the same phase space. There are two types of BEC: intra-W BEC between particles resulting from the same W decay and inter-W BEC between particles from different W decays. The results from the L3 experiment show the presence of the intra-W BEC effect, but no evidence for inter-W BEC [56].

The BEC is largest at small values of the four-momentum difference $Q \equiv \sqrt{-(p_1 - p_2)^2}$. The effect is studied by means of the two-particle correlation fonction

$$R_2(p_1, p_2) = \frac{\rho_2(p_1, p_2)}{\rho_0(p_1, p_2)} \tag{3.2}$$

where $\rho_2(p_1, p_2)$ is the two-particle density of particles with four-momenta p_1 and p_2, defined as

$$\rho_2(Q) = \frac{1}{N_{ev}} \frac{dn_{pairs}}{dQ} \tag{3.3}$$

where N_{ev} is the number of selected events and n_{pairs} the number of like-sign track pairs in the N_{ev} events. The density $\rho_0(p_1, p_2)$ is the the same two-particle density in absence of BEC. Figure 3.4 shows the function R_2 for the $\sqrt{s} = 189 - 209$ GeV L3 data for semi-hadronic W pair events (a), where inter-W BEC is absent, and the fully hadronic W pair events (b) where inter-W and intra-W BEC is studied. The solid line is the result of the fit of the R_2 function to the W pair data. The full histogram in Figure 3.4(a) shows the result for the light-quark Z decay data sample, for the dashed histogram all hadronic Z decays are included, so, also b quarks whose production is highly supressed in the W-pair data as the top quark mass is to high for a $W \to tb$ decay. The full histogram in Figure 3.4(b) displays the expectation when inter-W BEC is absent and shows no evidence for BEC between identical pions originating from different W bosons.

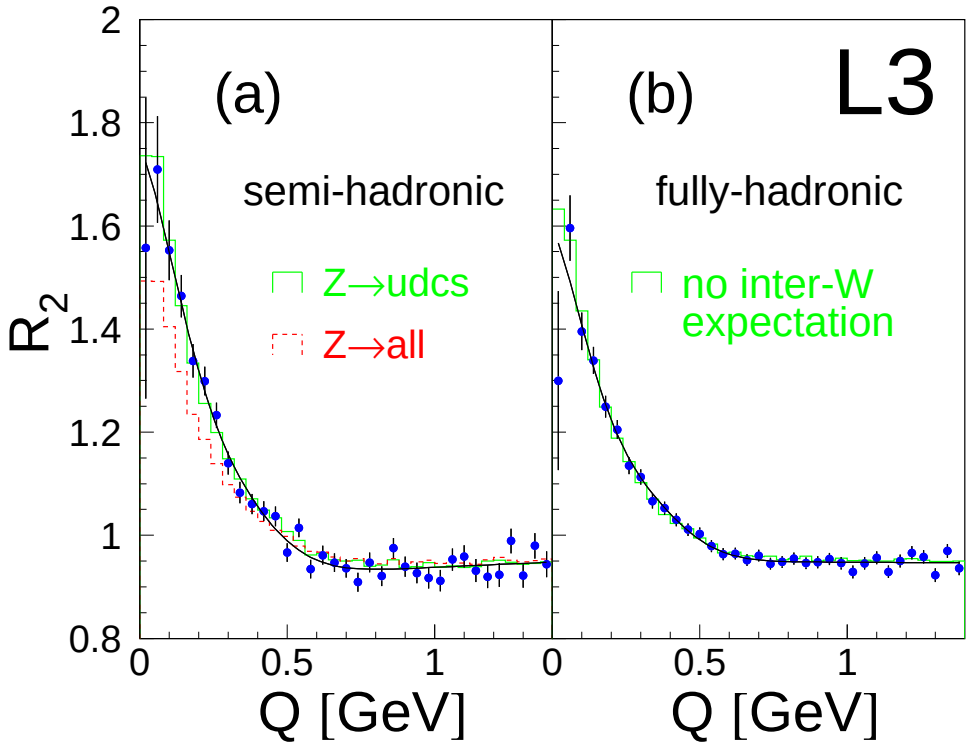

Figure 3.4: *The two-particle correlation function R_2 for the $\sqrt{s} = 189-209$ GeV L3 data for semi-hadronic W pair events (a) and the fully hadronic W pair events (b). The solid line is the result of the fit of the R_2 function to the W pair data. The full histogram in (a) shows the result for the light-quark Z decay data sample, in the dashed histogram all hadronic Z decays are included. The full histogram in (b) displays the expectation when inter-W BEC is absent*

3.4.2 Colour Reconnection effects (CR)

CR is the cross-talk between hadronic W decay products via strong interactions. The partons produced in W decays or in gluon radiation are not free particles due to colour confinement in QCD. They recombine to form mesons and baryons, also colour singlets, but which do no longer correspond to the one of the initial W boson decay.

The CR phenomenon is not well described by QCD and phenomenological models need to be used. Several models have been proposed to discribe the CR effect in $e^+e^- \to W^+W^- \to qqqq(\gamma)$ events and are implemented in the Monte Carlo programs.

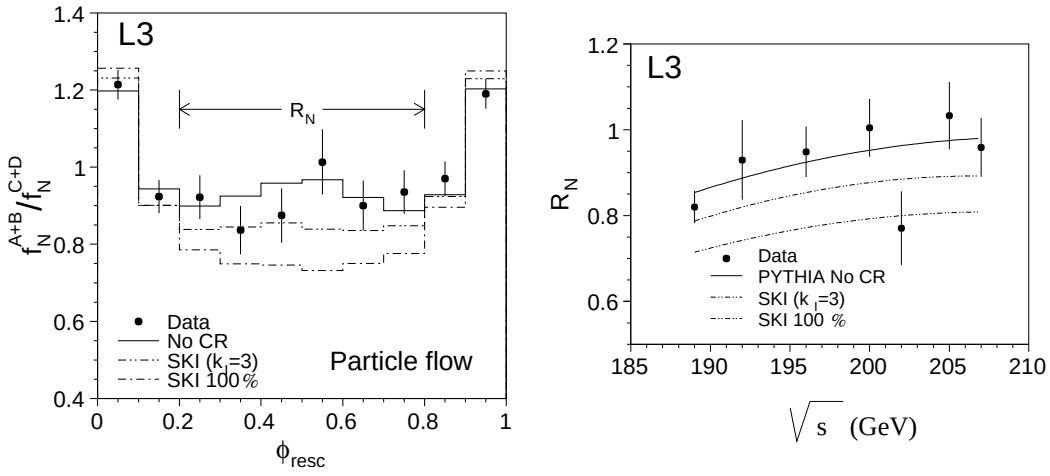

Figure 3.5: Left : *The ratio of the particle-flow distribution in the intra-W regions spanned by the two W bosons (A and B) to that in the inter-W regions (C and D) for the L3 189-209 GeV data, the PYTHIA no-CR, the SKI model with 100% reconnection probability (SKI 100%) and 66% reconnection probability (SKI $k_I = 3$).* Right : *The ratio R_N as function of the center-of-mass energy $\sqrt{s}$ at detector level for the L3 189-209 GeV data, PYTHIA no-CR and the SKI model predictions.*

The ratio of the particle-flow R_N and energy-flow R_E between particles from the same W boson, located in the regions A and B spanned by the corresponding W boson, to that between particles from different W bosons, located in the regions C and D, spanned between the W bosons, are sensitive to cross-talk effects [57] and are defined as

$$R_N = \frac{\int f_N^{A+B} d\phi}{\int f_N^{C+D} d\phi} \qquad R_E = \frac{\int f_E^{A+B} d\phi}{\int f_E^{C+D} d\phi} \tag{3.4}$$

where the particle-flow and energy-flow are defined as

$$f_N = \frac{1}{N_{ev}} \frac{dn}{d\phi} \qquad f_E = \frac{1}{E} \frac{dE}{d\phi} \tag{3.5}$$

with ϕ the angle between the most energetic W jet and the momentum vector of the particle, projected on the plane spanned by the two jets corresponding to the same W decay. Each particle located between the W jets is considered for integration.

Figure 3.5 (Left) displays the ratio of the particle-flow distribution in the intra-W regions spanned by the two W bosons (A and B) to that in the inter-W regions (C and D) for the L3 189-209 GeV data, the PYTHIA Monte Carlo prediction without CR and the SKI models with 66% (SKI $k_I = 3$) and 100% (SKI 100%) reconnection probability.

The SKI model has been developped by Sjöstrand and Khoze [58] and can be varied to generate events samples with different fractions of reconnected events using the free parameter k_I in the reconnection probability

$$P_{reco} = 1 - exp(-fk_I) \tag{3.6}$$

Figure 3.5 (Right) shows the measured R_N as function of the center-of-mass energy $\sqrt{s}$ at detector level for data, PYTHIA no-CR and the SKI model predictions. The R_N value measured in the complete L3 189-209 GeV data set is $R_N^{data} = 0.915 \pm 0.023$ $(stat.) \pm$ 0.021 $(syst.)$. The extreme SKI 100% model, where all events are colour reconnected, predicts $R_N^{data} = 0.762 \pm 0.003$ and is therefore disfavoured by the L3 data by 4.9 σ.

Chapter 4

The L3 Experiment

The Large Electron Positron collider LEP [59], operational from August 1989 to November 2000, was located at the Swiss-French boarder near Geneva. LEP was composed of an electron-positron accelerator and storage ring with a circumference of 26.7 km at a varying depth from roughly 50 m to 150 m. The LEP detectors, ALEPH [4], DELPHI [5], L3 [6] and OPAL [7], were located in four out of the eight interaction points. A schematic view of LEP is presented in Figure 4.1 (Left).

4.1 The Large Electron Positron Collider

The LEP injection system consisted of several accelerators which produced bunches of electrons and positrons with a beam energy of 20 GeV and injected them into the LEP storage ring. The different stages of the LEP injection system are shown in Figure 4.1 (Right).

The LEP Injecteur Linéaire (LIL), a high intensity linear accelerator, brings the electrons first to an energy of 200 MeV before pointing them to a tungsten target where the positrons are produced through bremsstrahlung and e^+e^--pair production. A second linear accelerator boosts the particles to 600 MeV and injects them in an Electron Positron Accumulator (EPA). The EPA stores the electrons and positrons separately and gathers them in bunches of 10^{10} particles which are transfered to the Proton Synchrotron (PS) where they are first accelerated to 3.5 GeV and finally boosted to 20 GeV by the Super Proton Synchrotron (SPS). After injection into the LEP ring, the bunches are accelerated to the required collision energy by radiofrequency accelerating cavities. The energy loss caused by synchrotron radiation, about 3.5 GeV per orbit for a beam energy of 105 GeV, is compensated by these cavities which also provide a longitudinal focalisation of the beam into discrete bunches.

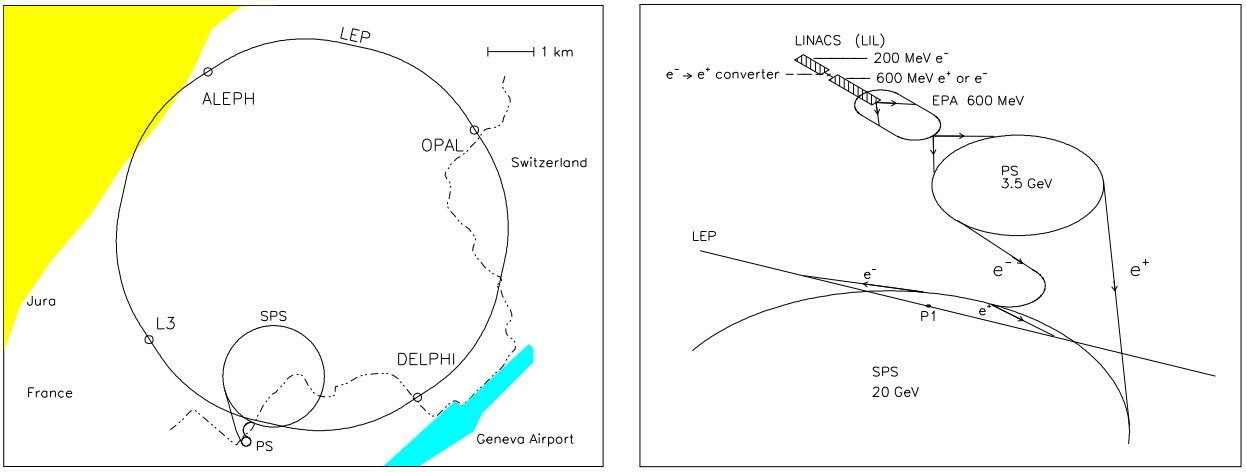

Figure 4.1: Left: *The LEP collider and the four LEP experiments: ALEPH, DELPHI, L3 and OPAL.* Right: *The LEP injection system.*

The electron and positron bunches travelled in opposite directions in the LEP ring and were kept separate by an electrostatic separator located at each interaction point.

The LEP storage ring was composed of 3000 dipole magnets and 2000 quadrupole magnets used to focalise and correct the beam trajectory. At each side of the LEP detectors, superconducting quadrupole magnets focused the bunches to the interaction point and optimised the luminosity by squeezing the bunches in the transverse plane. The LEP ring was kept under a vacuum of $10^{-9} - 10^{-10}$ Torr to minimise collisions with residual gas molecules.

The beam lifetime was of the order of 10 hours and a density of 10^{31} particles per cm^2 and per second was obtained. The beam dimensions were about 10 μm in the vertical direction and 250 μm in the horizontal direction.

During the LEP1 period (1989-1995) the beam energy was fixed near 45.6 GeV, around the Z-peak value and a total luminosity of 208 pb^{-1} was delivered per experiment. The beam energy for the LEP2 period (1996-2000) ranged from 80.5 to 104.5 GeV and the total delivered luminosity per experiment was about 784 pb^{-1}.

4.2 The LEP Beam Energy Measurement

At LEP different methods were used to measure the beam energy. The most precise one is the Resonant Depolarisation (RDP) method [60] based on the relation between the energy of the colliding beams and the strength of the magnetic field measured in the LEP dipole magnets. When the beam is deflected in the dipole magnets, the Sokolov-Ternov effect [61] polarises the spin of the electrons transversely. A horizontally oscillating magnetic field is applied as external dipole field to disturb the polarisation of the beam. The resonant frequency of oscillating field on the moment that the beam depolarises, gives the spin precession frequency and finally the beam energy: the number of spin precessions per revolution ν_{spin} is related to the beam energy E_{beam} by [62]

$$\nu_{spin} = \frac{g_e - 2}{2} \frac{E_{beam}}{m_e} = \frac{E_{beam}}{440.6486} \text{ MeV}^{-1} \tag{4.1}$$

where $(g_e - 2)/2$ is the anomalous magnetic moment of the electron and m_e the electron mass. The achieved precision on the beam energy at LEP1 is less than 1 MeV [63].

However, the use of the RDP method is limited to a maximum beam energy of ~ 55 GeV as the depolarisation increases too fast with energy and the transverse polarisation, necessary for the beam energy measurement, becomes insufficient. Therefore the beam energy at LEP2 is also measured with 16 NMR probes, installed in the LEP main bending dipole magnets. They are used to extrapolate the E_{pol}^{ref} to the energy region 41-61 GeV and finally to the energy of the physics process [62]. The magnetic extrapolation method is presented in Figure 4.2. The NMR probes continually measure the local magnetic field B_{NMR} which is fitted to E_{pol}^{ref} by a linear fit

$$E_{pol}^{ref} = a + b\, B_{NMR} \tag{4.2}$$

where a and b are the parameters of the fit. Once the parameters are determined at low energy, the beam energy at higher values is obtained from the average magnetic field measured by the NMR probes assuming the same linear energy dependence. In reality, this assumption does not hold perfectly and introduces the main systematic uncertainty on the beam energy measurement beside the earth tides, the influence of the temperature and the leakage currents from the passage of TGV trains near CERN.

The uncertainty on the beam energy is about 20 to 25 MeV for the 1998,1999 and 2000 data, depending on the year of running [64]. The beam energy is given as function of time to each LEP experiment.

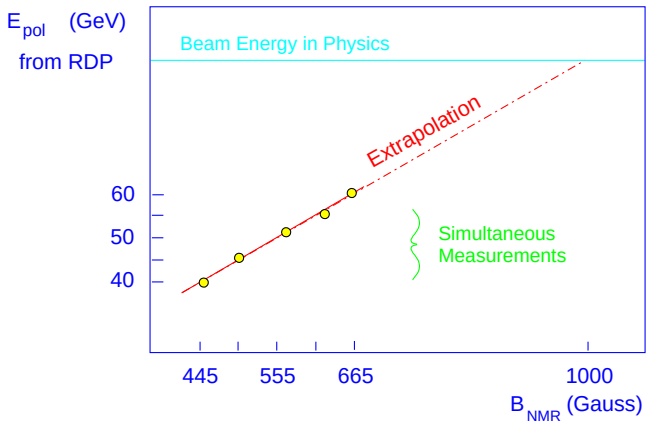

Figure 4.2: *The magnetic extrapolation method: the beam energy measured with the RDP method is extrapolated using NMR probes magnetic field measurements.*

4.3 The LEP and the L3 Luminosity Measurement

The number of physics interaction is proportional to the luminosity $\mathcal{L}$ delivered by the LEP collider which depends on the collider caracteristics: the number of events for a particular physics process with cross section σ is given by $N = \mathcal{L}.\sigma$ [65].

The luminosity is the rate of interaction between electrons and positrons per unit of cross section and is given by

$$\mathcal{L} = \frac{N_{e^+}\ N_{e^-}\ N_{bunch}\ \nu_{rev}}{4\pi\sigma_x\sigma_y} \tag{4.3}$$

with

- N_{e^+}, N_{e^-} the number of electrons, positrons per bunch
- N_{bunch} the number of bunches
- ν_{rev} the revolution frequency of the beam
- σ_x, σ_y the horizontal and vertical dimension of the beam in the transverse plane. They define the effective area of interaction.

At the interaction point, the bunch dimensions are 150 μm and 10 μm in the x and y direction respectively.

The luminosity at the L3 interaction point was measured by the experiment. It is derived from the number of Bhabha events selected with the LUMI detector, N_{sel}^{Bhabha}, the theoretical Bhabha cross section, σ_{th}^{Bhabha}, known to high precision, and the selection efficiency, ϵ_{sel}, estimated from Monte Carlo simulation

$$\mathcal{L} = N_{sel}^{Bhabha}/(\epsilon_{sel}\ \sigma_{th}^{Bhabha}) \tag{4.4}$$

Two highly energetic BGO clusters are required on each side of the LUMI detector.

A relative precision on the measured luminosity is of the order of 0.19-0.23%, dominated by systematics. The theoretical uncertainty is comparable to the total experimental uncertainty,

4.4 The L3 Detector

The measurements described in this thesis use the data taken by the L3 detector during the LEP2 period. The L3 detector was the largest of all four LEP detectors with its 12 m diameter and 12 m length along the beam-axis. The L3 detector was dismounted in the year 2001.

The L3 detector was designed for high resolution measurements of electrons, photons and muons but had a global structure common to most of the high energy physics experiments at present. It was composed of several layers of subdetectors which all play a particular role in the reconstruction of the physics event. From the interaction point to the exterior, we distinguish the central tracking system composed of a Silicon Microvertex Detector (SMD) and a Time Expansion Chamber (TEC), the electromagnetic calorimeter (BGO), the hadronic calorimeter (HCAL), the muon chambers (MUCH) and the Forward Tracking Chambers (FTC). A 7800 ton solenoid magnet surrounded the entire detector and provided a 0.5 Tesla homogeneous magnetic field directed along the beam-axis. The magnetic field curves the trajectory of the charged particles in the transverse plane and makes it possible to determine the charge and the momentum of the particles transversing it. The magnet had an octogonal structure and was composed of 168 spires of aluminium in an iron structure which provided a return of the magnetic flux.

A perspective view of the L3 detector is given in Figure 4.3. The L3 coordinate system is also shown. The right-handed Cartesian coordinate system has its origin in the interaction point. The direction of flight of the electron defines the positive Z-axis.
The positive X-axis points towards the center of the LEP ring, while the positive Y-axis is upwards orientated. The polar angle θ is defined as the angle with respect to the postive Z-axis, the azimuthal angle ϕ as the angle with respect to the positive X-axis in the (X,Y)-plane. Figure 4.4 offers a detailed longitudinal view on the L3 detector. The structure of the small angle calorimeters is also shown.

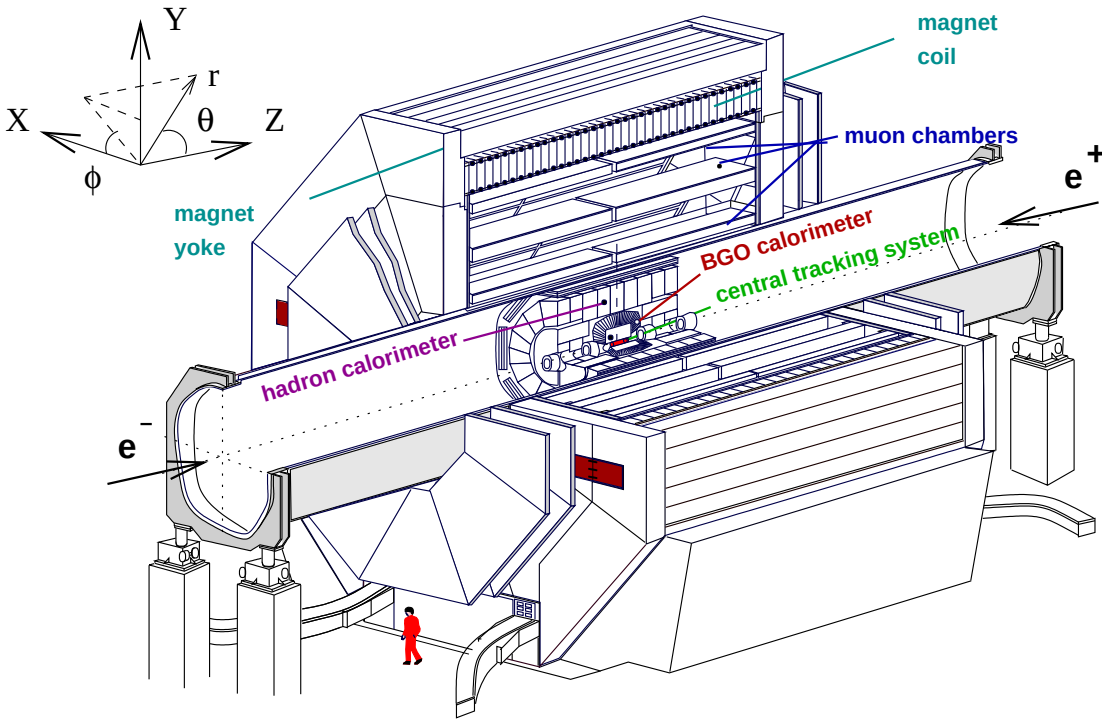

Figure 4.3: *A perspective view on the L3 detector. Also the L3 coordinate system and the definition of the Cartesian coordinates (x,y,z) and the polar coordinates (r, θ, ϕ) are shown.*

4.4.1 The central tracking chamber

The central tracking system consisted of four subdetectors: the Silicon Microvertex Detector, the Time Expansion Chamber, the Z-chambers and the Forward Tracking Chambers. They were used to measure the trajectory of charged particles. Also the ionisation loss, dE/dx, the position of the interaction point of the LEP beams (primary vertex) and secondary vertices were measured. A detail of the a sector ($\Delta\phi = 30°$) of the central tracking system [66] is shown in Figure 4.5.

The Silicon Microvertex Detector

The Silicon Microvertex Detector (SMD) was located closest to the beam pipe and had a length of 35.5 cm. The SMD consisted of two concentrical layers of 12 double sided silicon strip ladders [67] at a distance of 6 cm and 8 cm respectively from the Z-axis.

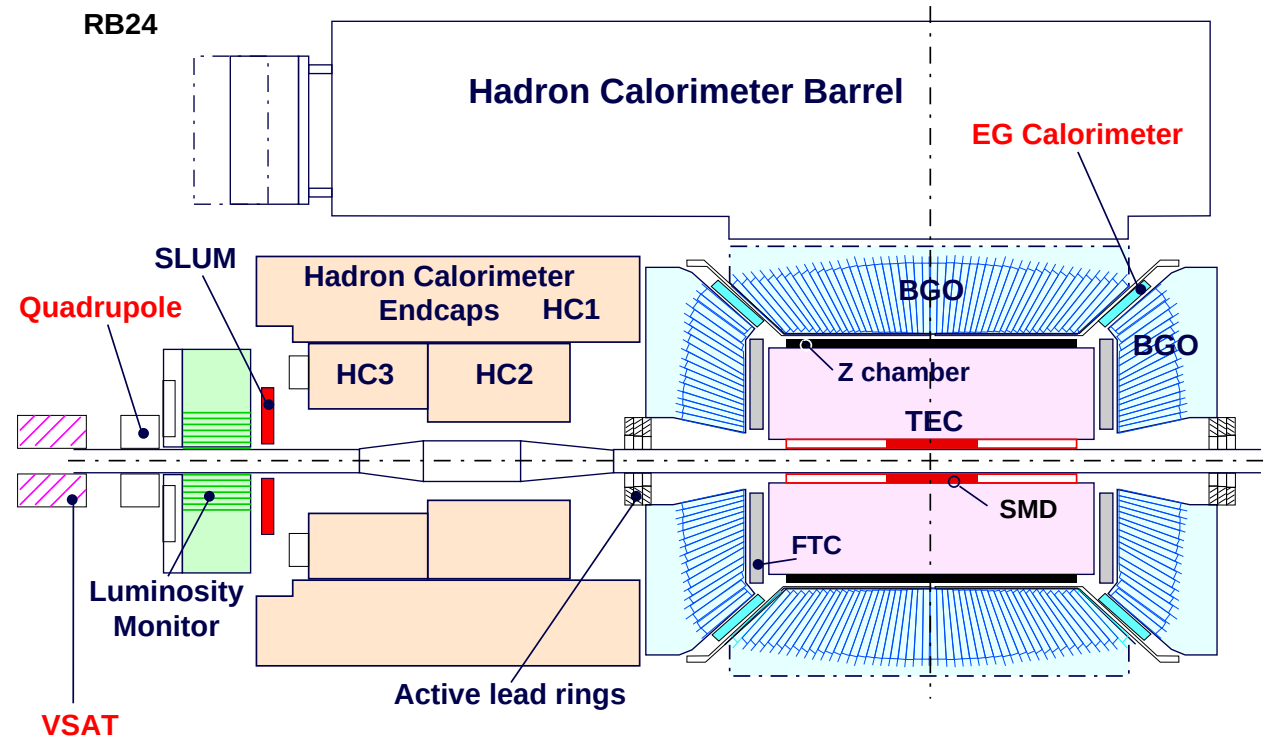

Figure 4.4: *Longitudinal view of the L3 detector.*

The basic detector element of the SMD is an electrically and mechanically joined double-sided silicon strip sensor of dimension 70 mm x 80 mm, made from 300 μm thick n-type silicon of high purity (see Figure 4.6).

The SMD supplied an r-ϕ and the r-z coordinate measurement over a polar angle range $21^\circ < \theta < 159^\circ$. The spatial resolution was 7 μm in the r-ϕ plane and 14 μm in the r-z plane. The Distance of Closest Approch (DCA), defined as the distance between the track and the primary vertex, is also measured by the SMD using the particles trajectory. The resolution on the DCA lied between 25 and 40 μm. The SMD was never used exclusively to reconstruct the particles trajectory, but always in conjunction with an associated TEC-track.

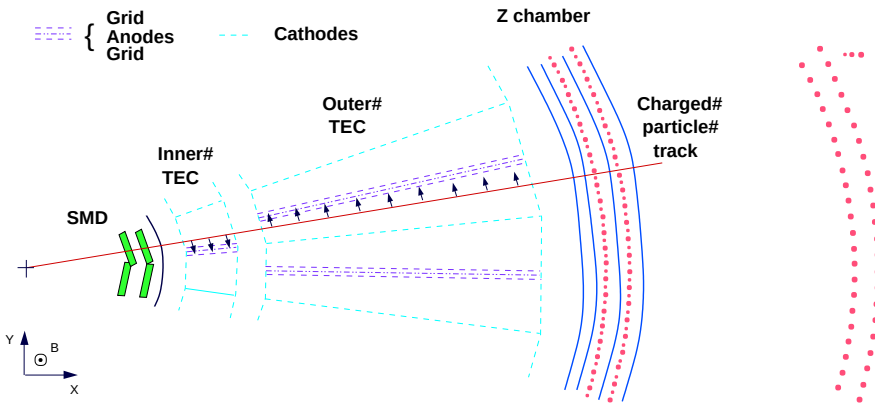

Figure 4.5: *The L3 Central Tracking Chamber: the SMD, the inner and the outer TEC and the Z-chamber.*

The Time Expansion Chamber

The SMD was surrounded by the Time Expansion Chamber (TEC), a multi-wire proportional chamber operating in the Time Expansion Mode [68] and filled with a gas mixture of 80% CO_2 and 20% C_4H_{10} at a pressure of 1.2 bar. The low drift velocity of 6 μm/ns ensured an accurate measurement of the track coordinates.

The TEC had a cylindrical shape of 1 m length with an outer radius of 48 cm and covered 90.6% of the solid angle. There were two parts: the inner TEC, subdivided into 12 ϕ sectors, and the outer TEC, subdivided into 24 ϕ sectors. Two outer sectors were covered by one inner sector. The sectors were separated by a cathode plane, while an anode plane was located in the middle of each sector (see Figure 4.7). The inner TEC sector contained 8 anode wires, while the outer TEC sector had 54 anode wires. There were three types of anode wires

- **standard anode wires** supplied high precision measurements in the r-ϕ plane, perpendicular to the beam-axis. They were read at one side only.
- **charge division anode wires** allowed to determine the z coordinate by comparing the size of the signals read out at the two sides.
- **left-right ambiguity anode wires** resolved the left-right ambiguity. Five grid wires on both sides of the anodes were read out and the signals on either side were compared. This method had a 90% efficiency.

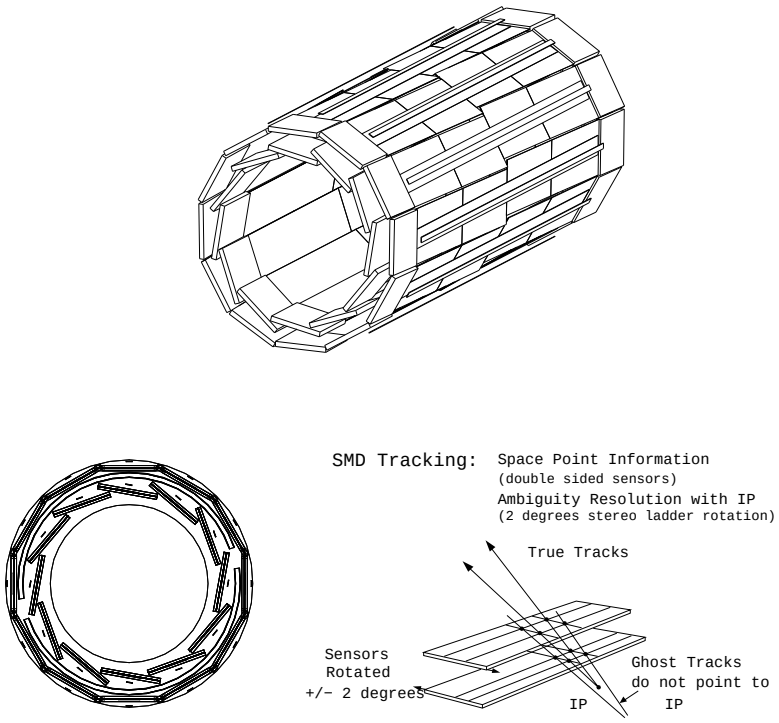

Figure 4.6: *A perspective and a front view on the Silicon Microvertex Detector. The track reconstruction is done with the help of two concentrical layers of double sided silicon strip ladders.*

The spatial resolution in the r-ϕ plane varied from 58 μm for the inner TEC to 49 μm for the outer TEC. At large angle, the resolution on the polar angle θ was 3.4 mrad, while 0.6 mrad for the azimuthal angle. The transverse momentum resolution was $\sigma(P_T) = 0.018 P_T$. The polar angle coverage of the TEC was $25^\circ < \theta < 155^\circ$.

The Z-Chambers

The Z-chambers were two proportional wire chambers mounted on the outside of the TEC and used for a more accurate measurement of the z coordinate. For the operation in drift mode, a gas mixture of 80% Argon, 16% CO_2 and 4% CH_4 was used. The signals were read out from 920 cathode strips. The cathode strips were inclined with respect to the beam direction by 69° and 90° for the inner chamber, and by -69° and -90° for the outer chamber. The z coordinate of an isolated track transversing the Z chamber perpendicularly was measured with a resolution of 320 μm. The coverage in polar angle was $45^\circ < \theta < 135^\circ$.

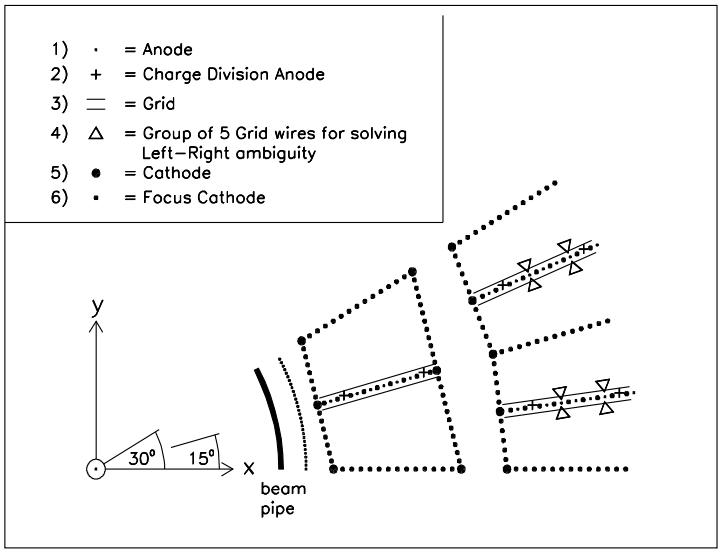

Figure 4.7: *The TEC wire configuration in the transverse plane.*

The Forward Tracking Chambers

The Forward Tracking Chambers (FTC) were proportional wire chambers located perpendicular to the beam-axis between the TEC and the endcaps of the BGO. They were operated in drift mode using a gas mixture of 61.5% argon and 38.5% ethane. The FTC extended the angular coverage of the Z-chambers down towards 10° on either side and provided an additional position measurement in the transverse plane at a fixed value of z. The polar angle regions covered by the FTC are $12° < \theta < 34°$ and $146° < \theta < 168°$. The resolution in the r-ϕ plane was of the order of 200 μm.

4.4.2 The electromagnetic calorimeter

The electromagnetic calorimeter (BGO) consisted in total of 10734 bismuth germanate ($Bi_4Ge_3O_{12}$) crystals [69] which were used both as showering material and as scintillating medium. Because of its high density (7.13g/cm^3) and its short radiation length (λ_{rad}= 1.12 cm), this material is very suitable to identify electrons and photons which produce showers inside the BGO through Bremsstrahlung and e^+e^--pair production and loose hereby nearly all their energy. The approximately 22 λ_{rad} thickness of the BGO cristals absorbs nearly completely most of the electromagnetic showers. Hadronic showers extend beyond the BGO due to the large nuclear interaction length (λ_{nucl}=22 cm): hadrons deposit only a part of their energy in the BGO by nuclear interaction and produce diffuse, largely fluctuating signals.

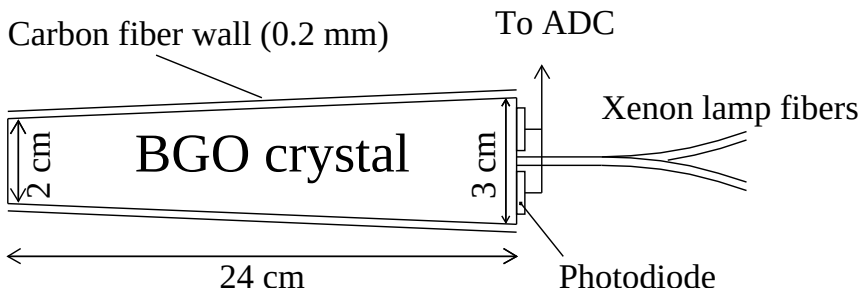

Figure 4.8: *A BGO crystal with at the back face two photodiodes to collect the light signals and optical fibres used for calibration.*

Muons produce a minimum ionizing, energy independent signal.

Each crystal had a truncated pyramid shape with a length of 24 cm, a front face of 2 x 2 cm^2 and a back face of 3 x 3 cm^2 as shown in Figure 4.8. Two silicon photodiods were placed at the back face of each crystal as well as a sensitive charge amplifier producing about 1200 electrons per MeV.The resulting analog signals were digitized by ADC cards mounted inside the L3 detector thus keeping the readout system compact. The response time of the BGO was 300 ns.

Between the LEP fills, a so-called pedestal run was done to read-out the BGO ADC's without the presence of a physics signal. To equalize the crystals response a calibration run was performed with a Xenon light flash system [70]: a network of optical fibres which inject light pulses of known amplitude into the back face of each crystal. Also an RFQ accelerator [71] was used for the calibration. The measured pedestal value for every crystal was substracted from the physics signal of a traversing particle and a correction factor from the calibration was applied.

The BGO was divided in three parts (see Figure 4.9) the barrel calorimeter and the two endcap calorimeters at each side of the beam-axis. The barrel calorimeter was divided into two cylindrical half barrels which contained each 3840 crystals arranged in 24 rings along the beam-axis and covered a polar angle range of $42.3° < \theta < 137.7°$. The endcap calorimeters consisted of two symmetrical parts in the forward and the backward direction and contained 1527 crystals. The polar angle coverage was $10.5° < \theta < 36.7°$ in the forward direction and $143.3° < \theta < 169.5°$ in the backward direction. The BGO covered 92.1% of the solid angle. A space of 5°, called the EGAP, separates the barrel from the endcap calorimeters. In 1995 the EGAP was filled with a calorimeter of scintillating fibers in a lead structure.

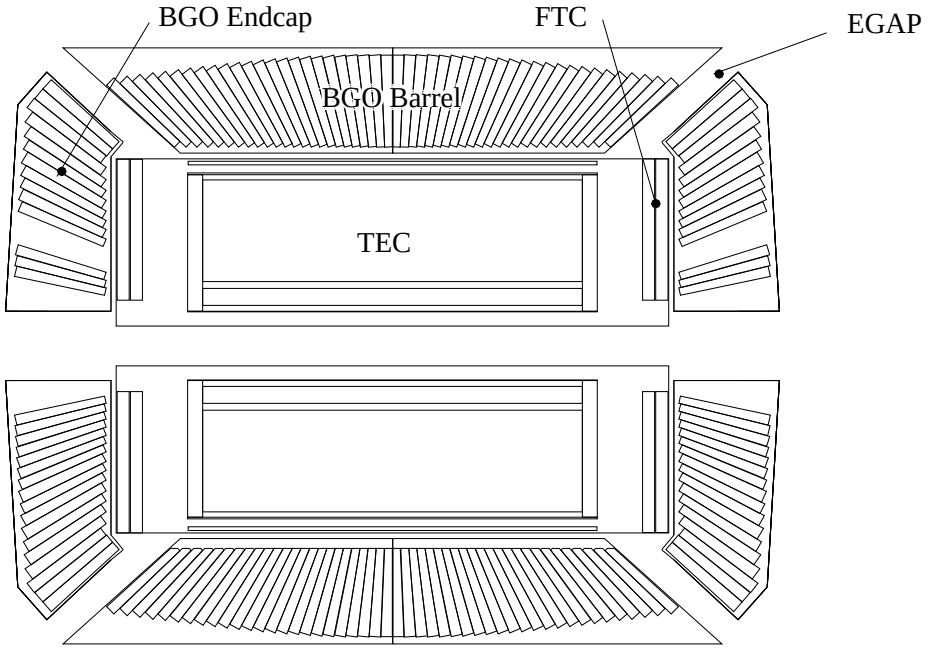

Figure 4.9: *A longitudinal view of the BGO calorimeter.*

The design of the BGO provided an excellent energy resolution for electrons and photons over a large energy range. The BGO energy resolution is expressed by

$$\frac{\delta E}{E} = \sqrt{(\frac{a}{\sqrt{E}} + b)^2 + (\frac{c}{E})^2 + d^2} \tag{4.5}$$

with

$$a = 1.53\ \%\ \sqrt{\text{GeV}} \tag{4.6}$$

$$b = 0.38\ \%$$

$$c = 0.25 \pm 0.15\ \%\ \text{GeV}$$

$$d = 1.18 \pm 0.11\ \%$$

The resolution was about 5% at 100 MeV and less than 2% above 2 GeV as shown in Figure 4.10. The parameters a, b, c, and d were measured in 1991 using a limited number of Bhabha events [72] . Because of the large statistics of Bhabha events, the typical resolution improved to 1% during the last years of data taking. The linearity was better than 1%. The granularity of the BGO allowed also measurements of the particles's direction orginating from the interaction point. The angular resolution was 3.8 mrad for the polar angle θ and 3.6 mrad for the azimuthal angle ϕ.

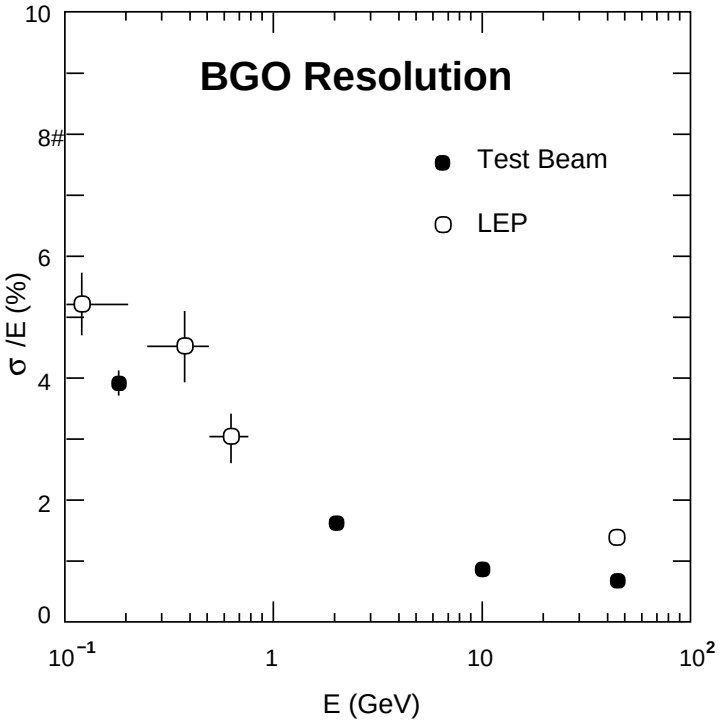

Figure 4.10: *The energy resolution of the BGO calorimeter.*

Between the electromagnetic and the hadronic calorimeter, a system of 30 layers of plastic scintillators [73] covered the polar angle region $34° < \theta < 146°$. The scintillators measured the time of flight of particles with a time resolution of 0.5 ns and provided an efficient way to discriminate events with origin in the interaction point from events produced by cosmic ray muons. The first lead to a zero time difference between the signals recorded by opposite scintillators, while for the second, a time difference of about 5.8 ns is observed.

4.4.3 The hadronic calorimeter

The Hadronic Calorimeter (HCAL) surrounded the electromagnetic calorimeter and consisted of Uranium 238 absorber plates intersparsed with rectangular proportional chambers [74] filled with a gas mixture of 80% Argon and 20% CO_2.

Due to the short nuclear absorption length of Uranium 238 ($\lambda_{nucl} = 0.5cm$), the low-energy particle showers, generated by the passage of hadrons, are stopped rapidly, while non-showering particles like muons, pass the HCAL and reach the muon chambers.

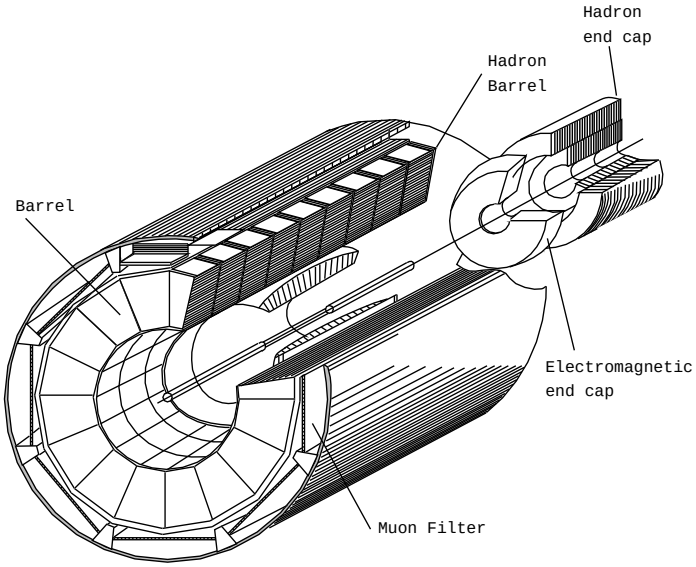

Figure 4.11: *A perspective view on the hadronic calorimeter.*

The HCAL was divided in three parts (see Figure 4.11): the barrel HCAL and two endcap HCAL's at each side of the beam-axis. The barrel HCAL consisted of 9 rings along the beam-axis while the endcap HCAL's consisted of 3 rings: an outer ring (HC1) and two inner rings (HC2 and HC3). The polar angle coverage of the HCAL was $5.5^\circ < \theta < 174.5^\circ$ which was 99.5% of the solid angle.

The energy resolution of the HCAL is parameterised as

$$\frac{\delta E}{E} = (\frac{55\ \%}{\sqrt{E}}) + 5\ \% \tag{4.7}$$

where the energy E is measured in GeV. The jet-axis was measured with an angular resolution of about 44 mrad.

4.4.4 The muon chambers

The muon spectrometer (MUCH) was installed between the support tube and the magnet coil and covered the polar angle region $36^\circ < \theta < 144^\circ$ and full azimuth. It was made up of 16 independent octants [75] where each octant contained 3 detector layers: the outer layer MO, the layer MI located just outside the support tube and the layer MM which resided in between. Each octant was made up of 5 precision P- drift chambers and 6 Z-chambers. The Z-chambers are located on either surface of the inner and the outer P-chambers. A typical octant is presented in Figure 4.12.

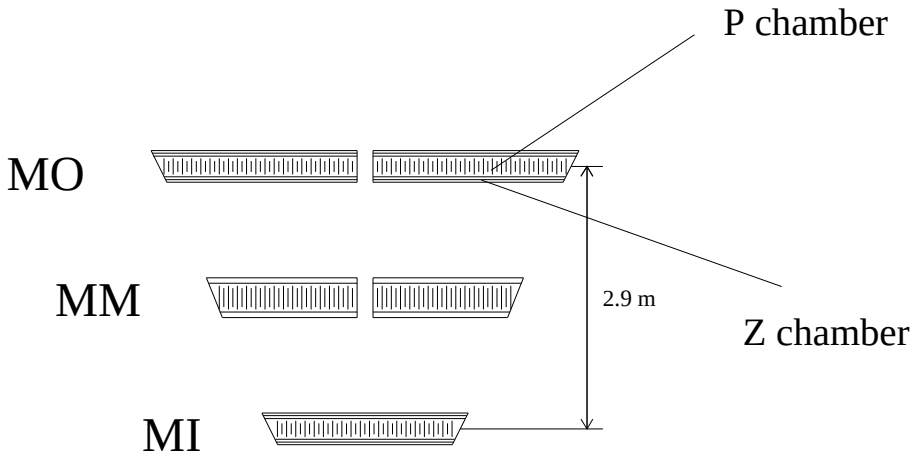

Figure 4.12: *The front view of a muon spectrometer octant.*

The P- drift chambers (2 each per MO and MM, 1 per MI) provided a high accuracy measument of coordinates in the bending plane, while the Z-chambers (each 4 per MO and 2 per MI) measured the z coordinate. The resolution in the r-ϕ plane was 110-250 μm, while the achieved resolution on the z coordinate is about 500 μm. The resolution on the transverse momentum was 2.5 % for a 45 GeV muon. The angular resolution was 4 mrad.

The forward and backward muon chambers were located on the magnet door on either side of the interaction point and extended the polar angle coverage of the MUCH to $22^\circ < \theta < 158^\circ$. The average spatial resolution of forward and backward muon chambers was 200 μm. The achieved momentum resolution of the track was about 20% and limited by the multiple scattering of the muons on the one-meter thick iron magnet door.

A muon filter was placed on the exterior of the HCAL to protect the muon detector from hadrons coming from the HCAL. It consisted of proportional chambers and was also used to identify hadrons that were not observed by the HCAL.

4.4.5 The low angle forward-backward detectors

The L3 detector was equipped with a system of low polar angle calorimeters to complete the hermiticity of the detector and for a precise measurement of the luminosity: the Luminosity Monitor (LUMI), the Very Small Angle Tagger (VSAT) and the Active Lead Rings (ALR).

The Luminosity Monitor

The Luminosity Monitor (LUMI) [76] was especially designed to record the rate of the small angle Bhabha events $e^+e^- \rightarrow e^+e^-(\gamma)$. The LUMI consisted of two cylinders wrapped around the beam-axis and located in the forward and the backward direction, 2.65 m from the interaction point. The LUMI contained 608 BGO crystals arranged in 8 rings and covered the polar angle region 32 mrad $< \theta <$ 62 mrad. A silicon strip detector (SLUM) was placed in front of each luminosity counter to improve the spatial resolution (see Figure 4.4).

The Very Small Angle Tagger

The Very Small Angle Tagger (VSAT) had as main purpose the detection at very small angle of the scattered beam electron or positron from two-photon interactions.
The VSAT [77] was made up of four aluminium boxes containing 24 BGO crystals and positioned in the horizontal plane on each side of the beam pipe and at each side of the interaction point, at 8.05 m from the interaction point behind the beam quadrupole. The crystals were cut to a size of 9 x 18 x 220 mm^3. The VSAT acceptance region was from 5 to 10 mrad in the polar angle θ. The resolution was about 0.25 mrad in the polar angle, while 40 mrad in the azimuthal angle ϕ.

The Active Lead Rings

The Active Lead Rings (ALR) [78] were located between the endcap BGO calorimeter and the endcap hadronic calorimeter as can be seen on Figure 4.4. The rings were first installed to protect the TEC from the damage caused by off-momentum beam electrons, later they were intersparsed by 5 layers of plastic scintillator to measure also the polar and azimuthal angle of isolated particles. Each layer of scintillator was divided into 16 azimuthal segments, read out individually by photodiods.

The angular coverage of one ALR was $3.9^\circ < \theta < 8.67^\circ$ and its spatial resolution was 4.5° in θ and 2.7° in ϕ.

4.5 The L3 Trigger System

A trigger system is a system of electronics and software which decides, in between two bunch crossings, if an event is of physics interest or a background event. Events of physics interest are recorded, while background events, mainly due to scattering between beam particles and residual gas molecules in the beampipe, are rejected. Occasionally also cosmic ray particles and electronic noise occur as background events.

The LEP beam crossing rate was about 45 kHz in the 4 X 4 bunch mode and 90 kHz for the 8 X 8 bunch mode adopted from 1995 on. Only a rate of 1-2 Hz of all the beam crossings corresponds to an e^+e^- interaction. The read-out time of all the signals from the L3 detector was ranging from 500 μs to few milliseconds and represented dead time for the data acquisition system as the time between two beam crossings was about 11 μs. Therefore a set of triggers was designed to reject rapidly the background events without significant loss of interesting data.

The L3 trigger system has three levels. The level-1 trigger decided if a event is of physics interest within the time between two beam crossings and reduced the rate to approximately 10 Hz. The level-2 and level-3 triggers had a decision time of less than 1 ms and 100 ms respectively and reduced the rate down to 2 Hz.

4.5.1 The level-1 trigger

The level-1 trigger based its decision on the analog signals coming from several subdetectors which are processed by FASTBUS, VME and CAMAC crates. It is the logical OR of 5 subtriggers: the calorimetric trigger, the TEC trigger, the luminosity trigger, the scintillator trigger and the muon trigger.

The calorimetric trigger

The calorimetric trigger selected events with a significant energy deposit in the electromagnetic and the hadronic calorimeter [79]. It is composed of 4 subtriggers whose decision algorithms used the following 4 quantities and compared them to preset thresholds

- the total calorimeter energy
- the total BGO energy
- the calorimeter energy
- the BGO energy in the barrel region

- *the cluster subtrigger* searched for energy deposits of at least 7 GeV, localised in θ and ϕ. The energy threshold was lowered to 3 GeV in case of an associated TEC track.
- *the total energy trigger* asked for at least 10 GeV in the barrel of the BGO calorimeter or 15 GeV in the barrel of the BGO and the HCAL calorimeters or 20 GeV including also the endcaps.
- *the single photon subtrigger* tried to identify events containing one single isolated electromagnetic cluster with an energy larger than 2 GeV. An anticoincidence with TEC trigger was required.
- *the hit counting trigger* asked for at least two BGO crystal groups or HCAL modules with more than 5 GeV.

The calorimeter triggers had a trigger rate of about 5 Hz.

The TEC trigger

The TEC trigger was composed of two subtriggers which selected events with charged tracks in the external TEC for the TTEC tigger [80] and in the internal TEC for the ITEC trigger [81]. At least two tracks with a minimum transverse momentum of 150 MeV and an accolinearity of less than 60° were required to pass the TTEC trigger. The ITEC trigger is based on a neural network. The TEC trigger had an efficiency around 95% and a trigger rate between 1 and 10 Hz.

The luminosity trigger

The luminosity trigger selected small angle Bhabha events and two-photon events. For the back-to-back trigger, an energy deposition of at least 15 GeV in two opposite sectors of the LUMI was required. The trigger rate was about 1.5 Hz.

The scintillator trigger

The scintillator trigger [82] was used to select high multiplicity events by requiring a coincidence of 5 out of 16 scintillator pairs. The trigger rate was about 0.1 Hz.

The muon trigger

The muon trigger required at least one particle penetrating the muon chambers with a momentum larger than 1 GeV. In order to reduce the trigger rate due to cosmic muons,

a coincidence with the scintillator trigger was required. The trigger rate was about 1 Hz. The typical level-1 trigger rate was about 10 Hz.

4.5.2 The level-2 trigger

The level-2 trigger [83] was based on a system of transputers and aimed to reject background events which passed the level-1 trigger selection. The rejection factor was about 30 %. An event triggered by more than one level-1 subtrigger is always accepted. If an event was triggered by only one level-1 subtrigger, it was further checked using the following three criteria

- there is a correlation in θ and ϕ coordinates between the clustered energies in the electromagnetic calorimeter on one hand and the two lateral layers of the hadronic calorimeter on the other hand.

- a vertex is recognised when a rough vertex reconstruction is performed using the TEC information.

- a balance between the clustered energies in both longitudinal and transverse direction is required.

The typical level-2 trigger rate was about 6 Hz. The level-2 trigger decision was made in less than 1 ms and so, did not contribute to the dead time. On twenty events rejected by the level-2 trigger, one event was flagged and recorded as such to monitor the level-2 trigger efficiency off-line.

4.5.3 The level-3 trigger

Only the level-3 trigger [84] had access to the complete digitized data reconstructed during the decision time of the level-1 and level-2 triggers which made a more precise analysis and event selection possible. It was based on a system of two VAX stations running in parallel. Several complex algorithms were used in the level-3 trigger event selection. If the event passed the level-3 trigger, the corresponding information was transferred to the main acquisition system and subsequently written to disk and to tape. The level-3 trigger rate was about 2 Hz and the decision time less than 100 ms. Also here one event out of twenty was flagged and recorded as such to monitor the level-3 trigger efficiency. All events that passed the level-3 trigger were written to disk and used as input for the off-line event reconstruction program and analysis. A copy of the raw data was saved on tape to make a rerun of the reconstruction possible.

4.6 The L3 Data Acquisition System

The data from the subdetectors was organised in two streams: the full data stream and the trigger data stream. The full data stream was monitored by an on-line computer system which wrote the information from the different subdetectors into databases. The trigger data stream contained less information and is processed between two beam crossings.

4.7 The L3 Data Reconstruction System

Figure 4.13 offers a schematic view of the L3 data reconstruction system. All data that passed the three levels of the L3 trigger system were transferred to the off-line farm for event reconstruction.

4.7.1 The event reconstruction

The event reconstruction was done by the REL3 off-line reconstruction program [85]. Two formats are created to store the events for physics analysis

- **Data Summary tapes (DSU)** offered a compressed version of the detectors information available for each event together with the reconstructed variables.

- **Data Avanti tapes (DVN)** contained only reconstructed variables.

First, the digitized raw data from the different subdetectors was interpreted as tracks and clusters and converted into physical quantities such as energy, momentum and position. Each event was reconstructed across the whole L3 detector and the corresponding detector calibration constants were applied by the REL3 program. Also the information on the alignment of the subdetectors was used. The temperature dependence of the BGO crystals response, the aging of the detector material as well as energy losses due to radiation damage were taken care of. Time dependent detector inefficiencies, monitored during the data taking and stored in data bases, were consulted during the reconstruction.

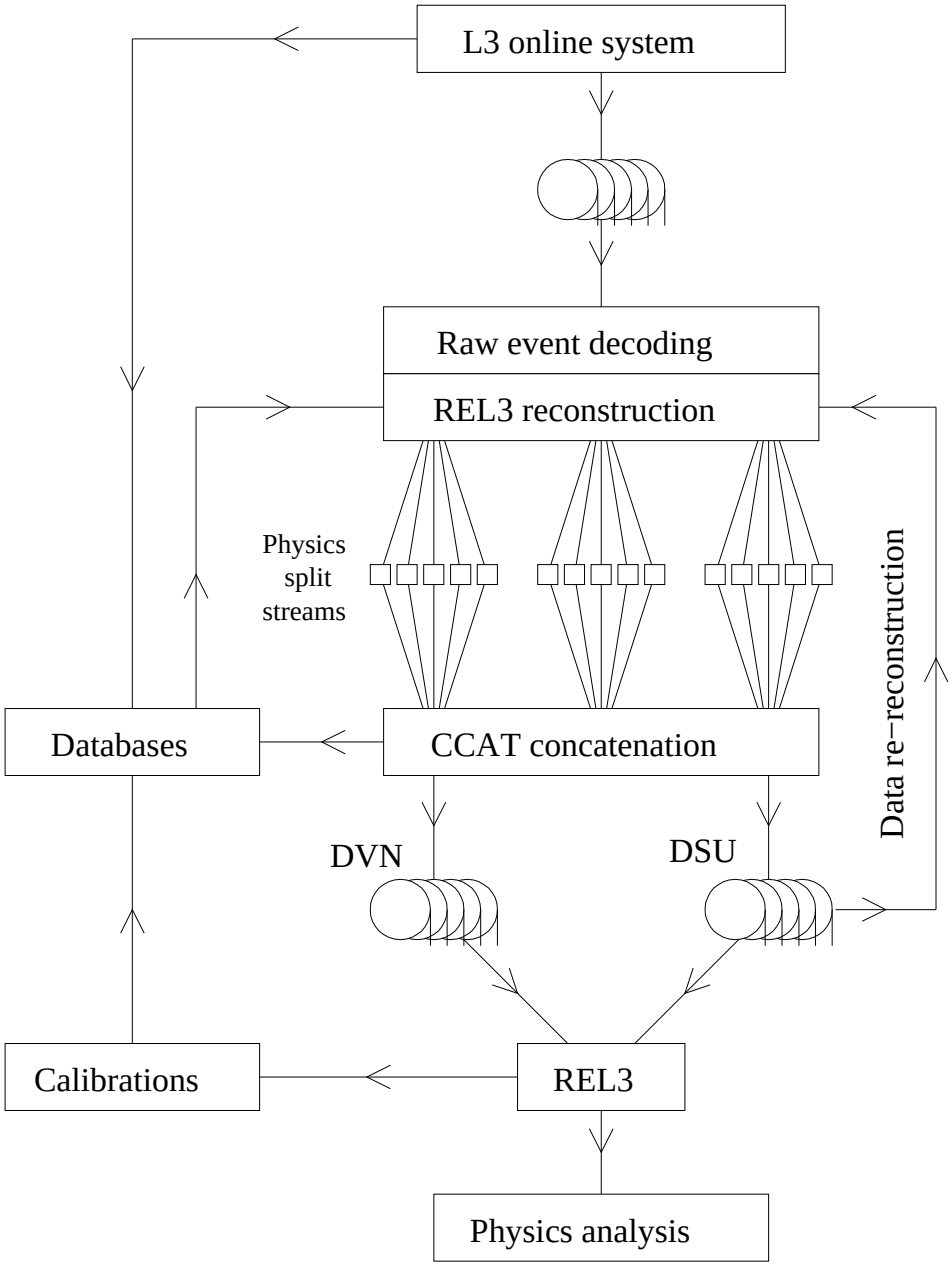

Figure 4.13: *A schematic view of the L3 data reconstruction system.*

Second, the physical quantities were interpreted as objects like tracks and energy clusters.

- The TEC tracks were reconstructed using a pattern recognition algorithm and extrapolated to the Z-chamber and SMD to identify associated tracks. This will be explained in the next section.
- The muon tracks were obtained by a similar algorithm on the muon chamber segments.
- A BGO cluster was defined as a group of adjacent crystals with an individual energy deposit above 10 MeV and a total cluster energy exceeding 40 MeV.
- A HCAL cluster was reconstructed from the corresponding HCAL hits if it energy deposit surpassed 9 MeV. The HCAL hits were grouped together into geometrical clusters by a clustering algorithm and the position of the HCAL cluster was determined by energy weighting.

The DVN tapes, used for the analysis discussed in this thesis, contains several data banks with objects which correspond almost to real particles

- **ATRK (A TRacK)** contains information on TEC tracks that are associated to calorimeter clusters.
- **AMUI (A MUon Identified)** includes the muon tracks with or without associated TEC track or energy deposit in the BGO or HCAL.
- **ASRC (A Smallest Resolvable Cluster)** gathers the clusters with an energy deposit in the BGO and the HCAL.

4.7.2 The track reconstruction

The track reconstruction was done by a pattern recognition program [86] which consisted of two steps.

In the first step, signals produced in the SMD and in the TEC by a single charge particle were searched for. For a single track, a maximum of 62 coordinate measurements (hits) was achieved if it was produced at a polar angle between 44° and 136°. Outside this interval, the number of TEC-wires is decreasing and tends to zero for angles lower than 10° or larger than 170°. The resolution on the coordinate measurement of a track was 50 μm per TEC-wire. The hit efficiency was 80%. The trajectory of a charged particle in a homogeneous magnetic field forms a helix, curling around the direction of the field which coincides with the Z-axis in case of the L3 coordinate system.

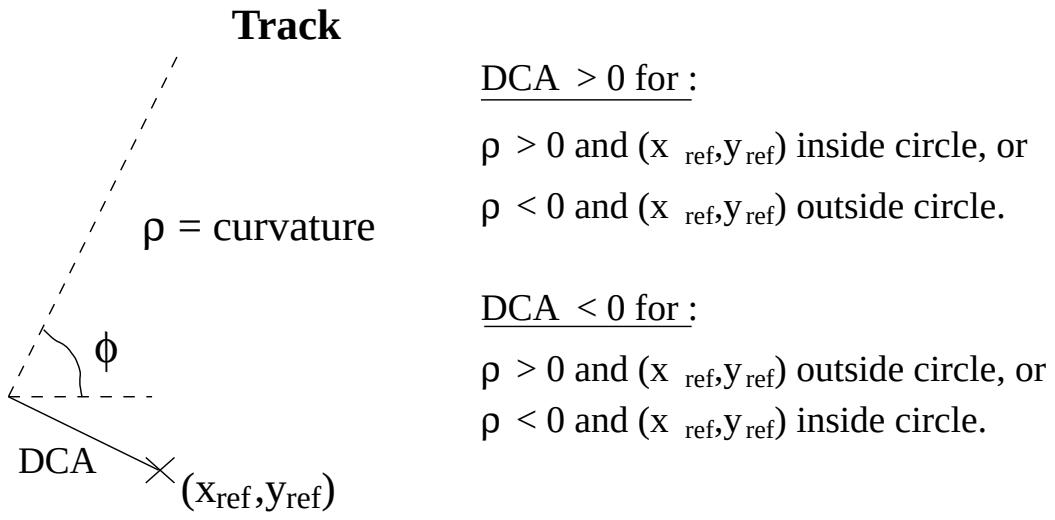

Figure 4.14: *The definition of the track fit parameters: the DCA, the curvature ρ of the tracks and the angle ϕ between the X-axis and the tangent of the track.*

Therefore it can be represented by a superposition of circles in the transverse plane with a constant drift in the z direction.

In the second step, the hit coordinates are fitted with a circle in the r-ϕ-plane as a function of three parameters: the DCA, the curvature ρ of the trajectory and the angle ϕ between the X-axis and the tangent of the track. They are picturally presented in Figure 4.14. From the curvature ρ of the trajectory, the sign of the charge is deduced and also the transverse momentum is measured

$$p_T = 0.3 \, \frac{B}{\rho} \tag{4.8}$$

where B represents the 0.5 Tesla magnetic field surrounding the detector. Once the tracks are reconstructed in the transverse plane, the information on the z coordinate from the SMD and the Z-chambers are considered and associated to the track to determine the polar angle θ.

4.7.3 The particle identification

Each of the particles produced in a physics event gives a typical signature in the detector, which is used in to identify the particle.

Electrons and photons

Electrons and photons leave all their energy in the BGO in the form of a narrow, symmetric shower, while hadrons produce much broader, asymmetric showers. The shape is experimentally quantified by E_9/E_{25}, the ratio between the energy deposit in a group of 3 x 3 crystals and the energy deposit in a group of 5 x 5 crystals around the most energetic signal. The only difference between the signature of the electron and the photon is the presence of a track in the central tracking system, left by the charged electron but absent for the neutral photon.

Muons

After the central tracking system, the muon traverses the BGO and the HCAL with almost no energy loss and is finally detected in the muon chambers.

Two types of muons are reconstructed. The first are muons associated to hits registered in more than one layer of the P-chambers of the muon spectrometer and classified as AMUI. Each layer of the muon chambers is used in a pattern recognition program to form track segments and a helix is fitted to the associated segments if at least two P-chamber segments can be connected. The AMUI muons can be "doublet"s or "triplet"'s depending on whether two or three P chamber segments were used in the reconstruction of the muons trajectory. The momentum of the AMUI is computed using the information from the TEC and the muon chambers taking in account the average energy loss of muons in the calorimeters.

The second type of muons are Minimum Ionising Particle (MIP) muons which are not reconstructed by the P-chambers but by a track in the central tracking system and a minimum ionizing signal in the BGO and HCAL calorimeters.

Taus

The tau lepton has a very short liftime (0.3 ps) and decays almost immediately into a electron, muon or an odd number of charged hadrons and at least one neutrino. Hence, the experimental signature of a tau lepton is that of the corresponding decay particle. The decays into 1 charged particle are called 1-prong, the decay into 3 charged particles, the most common multi-prong decay mode, are referred to as 3-prong.

Jets

Due to confinement, a quark produces a jet of hadrons. The hadrons are absorbed by the calorimeters before they can reach the muon chambers. The energy of the hadronic showers generated by the hadrons is measured by the BGO and HCAL calorimeters. If the hadrons are charged, they leave a track in the central tracking system.

The typical signature of a jet structure is defined by a number of tracks and a cluster multiplicity in the direction of the original hadron. There are several algorithms to reconstruct jets. The most communly used algorithm at LEP2 is the Durham algorithm [87]. For each pair of objects i and j in the event with energies E_i, respectively E_j, a variable y_{ij} is defined as

$$y_{ij} = \frac{2min(E_i^2, E_j^2)}{E_{vis}^2}(1 - \cos\theta_{ij})$$

where θ_{ij} is the angle between the objects and E_{vis} the total visible energy in the event. The minimum of y_{ij} is searched for and the corresponding objects are combined into one object. The procedure is repeated until y_{ij} reaches a preset cut value y_{cut}.
An alternative algorithm used at LEP and called the cone algorithm, defines the jet geometrically as a combination of particles contained in a cone of a given half-opening angle [88].

Neutrinos

As the neutrino is not charged and only weakly interacting with the detector material, it is not detected. However, the missing momentum due to the emission of the neutrino is reconstructed from energy-momentum conservation. For semi-leptonic events $e^+e^- \rightarrow j_1 j_2 l\nu$,

$$\vec{P}_{miss} = -(\vec{P}_l + \vec{P}_{j1} + \vec{P}_{j2}) \tag{4.9}$$

where $\vec{P}_l$ is the momentum vector of the lepton associated to the neutrino, $\vec{P}_{j1}$ and $\vec{P}_{j2}$ are the momentum vectors of the jets in the semi-leptonic W-pair event.

4.8 Detector Resolution and Calibration

The resolution on the measured quantities as well as the polar angle coverage of the principal L3 subdetectors are summarised in Table 4.1. A good knowledge of the detector response to hadrons and leptons is crucial for all measurements. At the Z-peak, jet and lepton pairs are produced with well known energy and momentum ($\sqrt{s}/2 \sim 45$ GeV) and a high statistics data sample is available. Therefore, L3 data collected at the Z-peak are used as calibration runs and to study the level of agreement between data and Monte Carlo on the reconstructed energy and angles.

The calibration and the resolution on the jet energy and angles is studied using jets from $e^+e^- \rightarrow q\bar{q}$ events without ISR photons, selected at the Z-peak ($\sqrt{s} \approx$ 91 GeV) and in higher energy LEP2 Z-data.The results are presented in Figure 4.15. The squares represents the data taken at the year 2000 Z-peak calibration runs, while the dots show the resolution implemented in the Monte Carlo at 207 GeV. A good agreement is found between data and Monte Carlo. The resolution is 16% for the jet energy and about 2° for the jet angles. These numbers are consistent with results obtained for the 1998 and 1999 Z-peak calibration data. The calibration of the jet energy and polar angle is presented in Figure 4.15 for the 2000 Z-peak data. The jet energy is compared to the beam energy. The central value of the distribution of the rescaled jet energy gives the precision of the energy calibration scale. The energy resolution follows from the width of the Gaussian fit. Similary, the angular calibration scale and resolution is derived by comparing the sum of the jet angles to 180°.

A simular study of the energy and angles of leptons is performed on $e^+e^- \rightarrow l^+l^-$ events without ISR photons, selected at the Z-peak and in higher energy LEP2 data. The observed difference between the calibration and resolution implemented in the Monte Carlo and these present in the Z-peak data are subject to small variations during the years of data acquisition. The maximal observed additional calibration and resolution are taken into account in the study of the detector systematics and summarised in Table 4.2. All quoted numbers are obtained with the full statistics Z-peak data taken at the 1998, 1999 and 2000 calibration runs and corresponding to a total integrated luminosity of 11 pb^{-1}.

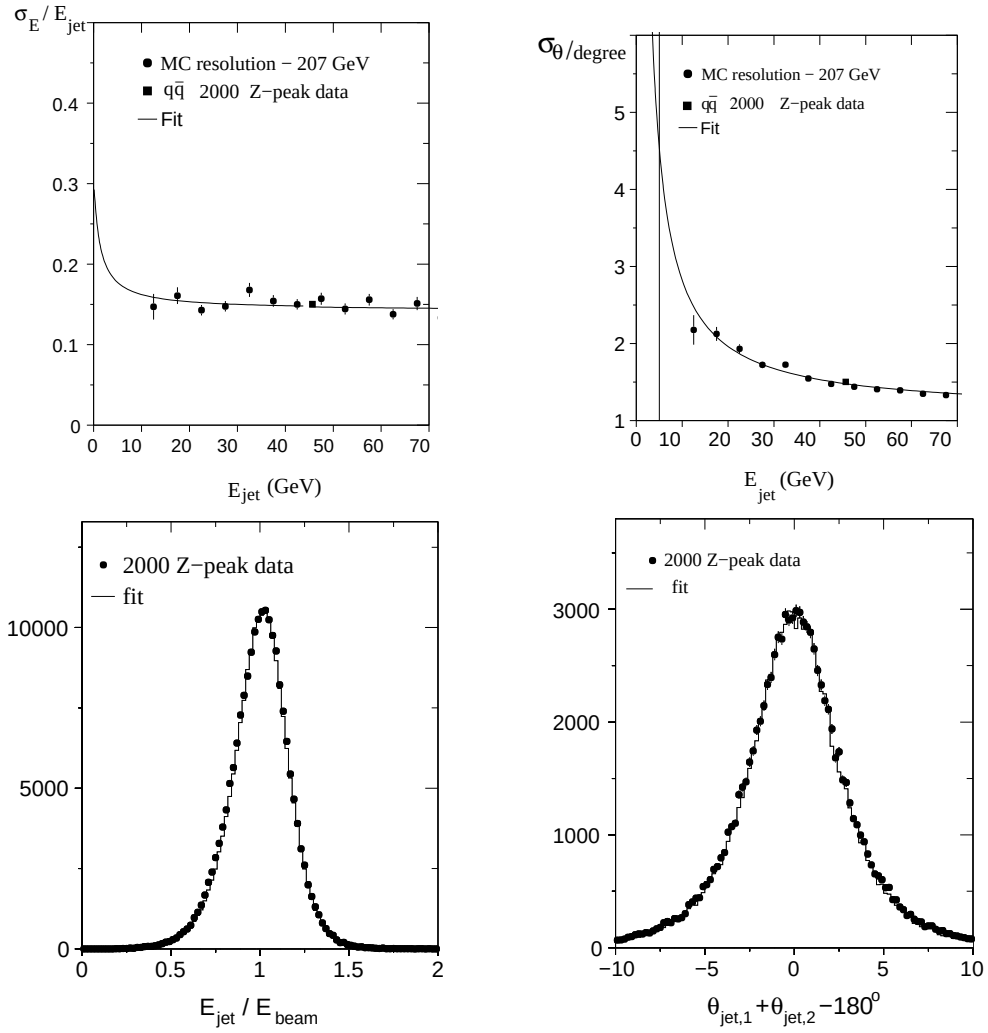

Figure 4.15: *Above: The jet energy and angular resolution as function of the jet energy for the year 2000 Z-peak data (squares) and the resolution of the Monte Carlo at 207 GeV (dots). A good agreement is found. Below: The corresponding maximal observed additional calibration and resolution is obtained by a Gaussian fit in the peak region.*

4.9 Kinematic Fit

The energy and angles of leptons and jets, reconstructed in the $e^+e^- \to W^+W^- \to f_1\bar{f}_2 f_3\bar{f}_4(\gamma)$ event are measured up to their detector resolution. As the energy and momentum of the initial state are well known, the principle of energy-momentum conservation is used to fit the measured quantities improving their resolution and that of the physical quantities like W invariant mass, W polar angle etc...

The principle of energy-momentum conservation is expressed mathematically as

$$E_{f_1} + E_{\bar{f}_2} + E_{f_3} + E_{\bar{f}_4} = \sqrt{s} \tag{4.10}$$

$$\vec{P}_{f_1} + \vec{P}_{\bar{f}_2} + \vec{P}_{f_3} + \vec{P}_{\bar{f}_4} = 0 \tag{4.11}$$

The kinematic fit is performed by a χ^2-minimization with as input the measured energy, angles of the reconstructed jets and leptons and the corresponding resolutions. In the case of a 4C kinematic fit, the χ^2 is given by

$$\chi^2 = \sum_{i=1}^{4} \frac{(x_i - \mu_i)^2}{\sigma_i^2} = \sum_{i=1}^{4} \frac{(E_i - E_i^{meas})^2}{\sigma_E^2} + \sum_{i=1}^{4} \frac{(\theta_i - \theta_i^{meas})^2}{\sigma_\theta^2} + \sum_{i=1}^{4} \frac{(\phi_i - \phi_i^{meas})^2}{\sigma_\phi^2} + \; constraints \tag{4.12}$$

where E_i^{meas}, ϕ_i^{meas} and θ_i^{meas} represent the measured energy, azimutal angle and polar angle of the four fermions in the final state. The corresponding uncertainties on these quantities are σ_E, σ_ϕ and σ_θ. All resolutions are assummed Gaussian. The fit parameters are E_i, $\vec{P}_i$, ϕ_i and θ_i. The output are new values for these quantities which satisfy the constraints and minimise the difference with the measured values. The constraint of energy-momentum conservation represents a four constraints (4C) kinematic fit for the four-jet channel and a one constraint (1C) fit for the semi-leptonic channels as the momentum conservation constraint is used to reconstruct the four-momentum of the neutrino. As an extra constraint, the two reconstructed W bosons can be forced to have an equal mass. For the four-jet channel this represents a five constraints kinematic fit (5C), while for semi-leptonic channel a two constraints kinematic fit (2C).

In the four-jet final state an ambiguity occurs in the jet pairing and the kinematic fit is applied to all three possible combinations. The χ^2 corresponding to each pairing is used as discriminator for the best pairing i.e. the pairing with the lowest χ^2. This criterium is correct in 60% of the cases, in 25% of the cases the correct pairing is the one with the second best χ^2.

A considerable fraction of the hadronic W-pair events contains hard gluon radiation or ISR photons and are rejected by the 5% probability cut of the kinematic fit. They are recovered by fitting the event as a five jet event instead of a 4 jet event.

Detector	Polar angle coverage	Resolution on the measured quantity						
		E, p_T	θ	ϕ	z	r-ϕ	r-z	DCA
SMD	[21° : 159°]					7 μm	14 μm	
SMD+TEC	[25° ; 155°]	$\delta p_T/p_T \sim 1.8$ %	3.4 mrad	0.6 mrad		49-58 μm		25-40 μm
Z-chamber	[45° ; 135°]				320 μm			
FTC	[12° ; 34°] [146° ; 168°]					200 μm		
BGO	[10.5° ; 36.7°] [42.3° ; 137.7°] [143.3° ; 169.5°]	$\delta E/E \sim 1\%$	3.8 mrad	3.6 mrad				
HCAL	[5.5° ; 174.5°]	$\delta E/E \sim 16\%$	44 mrad					
MUCH	[36° ; 144°]	$\delta p_T/p_T \sim 2.5\%$	4 mrad		500 μm	110-250 μm		

Table 4.1: *The resolution on the measured quantities as well as the polar angle coverage of the principal L3 subdetectors.*

Jets	E_{jet}	θ_{jet}	ϕ_{jet}
Resolution HCAL	16%	2°	
Maximal additional resolution	4%	0.5°	
Maximal additional calibration	0.1%	~ 0	
Electrons	E_e	θ_e	ϕ_e
Resolution	1%	0.2°	
Maximal additional resolution	0.5%	0.1°	0.01°
Maximal additional calibration	0.02%	~ 0	~ 0
Muons	P_μ	θ_μ	ϕ_μ
Resolution	2%	0.2°	
Maximal additional resolution	1.0%	0.1°	0.01°
Maximal additional calibration	0.1%	$\sim 0^\circ$	

Table 4.2: *The energy and angular resolution for jets and leptons and the maximal observed additional resolution and calibration. The results are based on a study of di-jet and di-lepton events without ISR photons, selected at the Z-peak ($\sqrt{s} = 91$ GeV) and in higher energy LEP2 data.*

Chapter 5

Measurement of the W-pair Production Cross Section

This chapter presents the measurement of the cross section for the $e^+e^- \to W^+W^-(\gamma)$ reaction with the L3 detector [89] at LEP. The analysis includes the L3 data collected during the years 1998, 1999 and 2000, at center-of-mass energies ranging from $\sqrt{s} = 189$ to 209 GeV and corresponding to a total integrated luminosity $\mathcal{L}_{data} = 629.4$ pb^{-1}.
A total of 9834 four-fermion W-pair events has been selected by the WW selections. The data sample is devided into eight $\sqrt{s}$ bins: in the years 1998 and 1999, the center-of-mass energy was fixed to distinct energy values, while in the year 2000, a wider range of energies was delivered. The center-of-mass energy range, the average energy and the integrated luminosity are summarised in Table 5.1.

First, the selection of $e^+e^- \to W^+W^- \to qq\tau\nu(\gamma)$ events, under my responsability since the year 1999, is described in detail. Up to then, the selection was optimised for center-of-mass energies up to 189 GeV, and a re-evalutation of the selection performance was necessary for the energy range from $\sqrt{s} = 189$ to 209 GeV. A clean sample caracterised by a low background contamination and a signal acceptance as high as possible, is aimed for. The other WW selections and their performances are also described for completeness.

In the second part, the W-pair production cross section in $qq\tau\nu(\gamma)$ final state is measured, followed by the determination of the total W-pair production cross section for which all the W-pair production final states are considered. Also the branching ratios of W decays into fermion-antifermion pairs and the CKM matrix element V_{cs} are derived.

The chapter is closed by the discussion of the different sources of systematic uncertainty on the measured cross section.

Year	Reference name	$\sqrt{s}$ range	$\langle\sqrt{s}\rangle$ GeV	$\mathcal{L}_{data}$ (pb^{-1})
1998	189 GeV	fixed	188.6	176.8
1999	192 GeV	fixed	191.6	29.8
	196 GeV		195.5	84.1
	200 GeV		199.6	83.3
	202 GeV		201.8	37.1
2000	205 GeV	$201.6 \leq \sqrt{s} \leq 205.8$ GeV	204.8	79.0
	206 GeV	$205.8 \leq \sqrt{s} \leq 207.2$ GeV	206.5	130.5
	208 GeV	$207.2 \leq \sqrt{s} \leq 209.0$ GeV	208.0	8.6

Table 5.1: *The center-of-mass energy range, the average energy and the integrated luminosity for each $\sqrt{s}$ bins of the L3 1998, 1999 and 2000 data. Also the reference name is given.*

5.1 Selection of $e^+e^- \to qq\tau\nu(\gamma)$ Events

The typical topology of a $e^+e^- \to qq\tau\nu(\gamma)$ event is

- two almost back-to-back hadronic jets with high multiplicity from the hadronic W decay
- one isolated, energetic lepton, electron or muon,
  from $\tau \to e\nu_e\nu_\tau$ (17.8%) or $\tau \to \mu\nu_\mu\nu_\tau$ (17.4%)

  or

  1 narrow τ-jet with low multiplicity
  from $\tau \to$ hadrons ν_τ (64.8%)
- missing energy and momentum due to the emission of neutrinos.

The missing energy in the $e^+e^- \to qq\tau\nu(\gamma)$ final state is more important than in the the semi-leptonic final states $qqe\nu(\gamma)$ and $qq\mu\nu(\gamma)$ due to the emission of at least two neutrinos since the τ decay introduces at least one additional neutrino in the final state

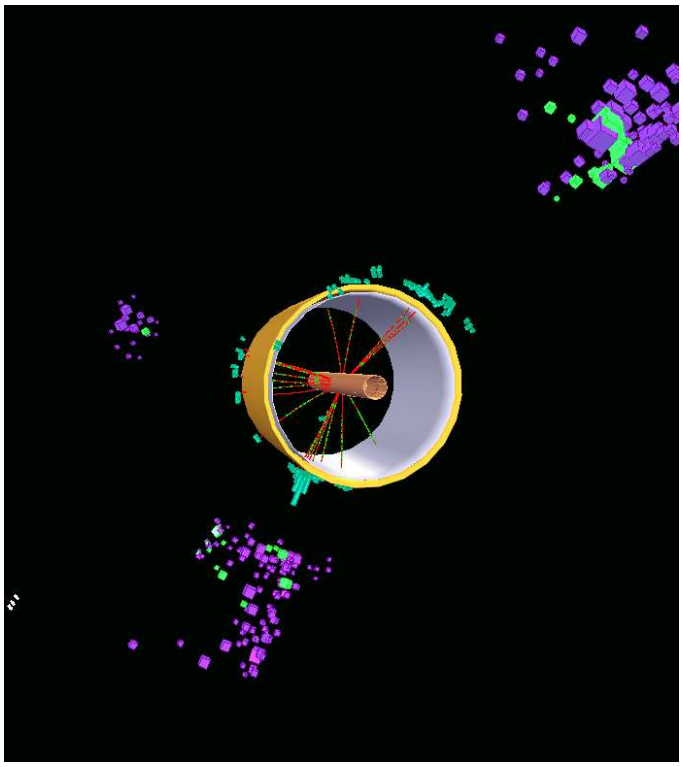

Figure 5.1: *Event display of an $e^+e^- \to qq\tau\nu(\gamma)$ event candidate with hadronic τ decay. The SMD detector and the TEC-chamber support tube are visible.*

$$\tau \to e\nu_e\nu_\tau$$

$$\tau \to \mu\nu_\mu\nu_\tau$$

$$\tau \to \text{hadron } \nu_\tau$$

Figure 5.1 shows a $e^+e^- \to qq\tau\nu(\gamma)$ event candidate with hadronic τ decay.

The selection procedure tries to make an optimal use of the described event characteristics to distinguish the $qq\tau\nu(\gamma)$ signal from the background. The background is composed of other WW decays wrongly classified as a $qq\tau\nu(\gamma)$ final state: the semi-leptonic final states $qqe\nu(\gamma)$ and $qq\mu\nu(\gamma)$ and the fully hadronic channel, $qqqq(\gamma)$, and non-WW background, mainly radiative hadronic Z events, $e^+e^- \to Z \to q\bar{q}\gamma$, where the photon is lost in the beampipe, and in decreasing importance $e^+e^- \to ZZ$, Zee events and two photon events.

The distributions of the physical variables, shown in the following sections, are of the type $N-1$ i.e. they contain these events passing all selection criteria except the one on the plotted variable. In this way the discriminating power of the cut becomes visible.

5.1.1 Preselection

The following cuts are applied at preselection level

- the TEC tracks and the calorimeter clusters satisfy

  $$N_{ATRK} > 5$$
  $$N_{ASRC} > 15 \text{ with } E_{ASRC} \geq 0.1 \text{ GeV}$$

  to ensure a high multiplicity. The cuts reject background events from low multiplicity purely leptonic final states.

- the background from the fully hadronic final states like $qq(\gamma)$ and $qqqq(\gamma)$, characterised by a total visible energy E_{vis} close to $\sqrt{s}$ and a small missing momentum P_{mis}, is reduced by requiring

  $$E_{vis} - P_{mis} < 200 \text{ GeV}$$

- the background from $qq(\gamma)$ events, the main non-WW background, is furthermore reduced by the requirement

  $$E_{\parallel} < 80 \text{ GeV}$$

  where $E_{\parallel}$ is the energy of the event, longitudinal to the beam direction.

5.1.2 Identification of the τ-jet

First events with leptonic τ decays are searched for, if no isolated electron or muon is found, a hadronic τ-jet is reconstructed.

Leptonic τ decays

The τ decay electrons are identified by the same isolation criterium as for the electron in the $e^+e^- \rightarrow qqe\nu(\gamma)$ channel

$$E_e/E^{15^\circ}_{ECAL} > 0.95$$

where $E^{15^\circ}_{ECAL}$ is the electron energy deposited in the BGO and included in a 15° cone around the electron's direction of flight.

The τ decay muons are identified by a track in the muon chamber corresponding to a reconstructed track in the TEC. Muons with a MIP signature are discarded.

Hadronic τ-decays

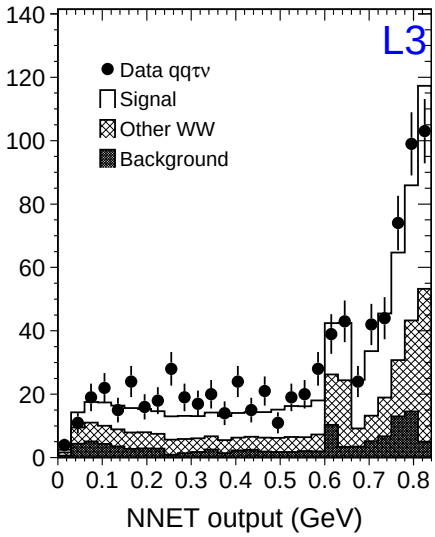

Figure 5.2: *The neural network output. The τ-jet is identified among the three highest energy jets using a neural network. The jet with the highest output value of the neural network is considered as τ-jet candidate.*

If no isolated electron or muon is found, jets are reconstructed by clustering all particles inside a cone of 15° half-opening angle [90] around the main energy deposits. At least three reconstructed jets are required. The τ-jet is identified among the three highest energy jets using a neural network with input variables

- the number of TEC tracks and calorimetric clusters associated to the jet
- the half-opening angle of the jet
- the electromagnetic energy
- the jet invariant mass

These input variables improve the distinction between hadronic jets from quarks and hadronic τ-jets which are characterised by a lower multiplicity, a narrower jet opening angle, a higher fraction of energy deposit in the electromagnetic calorimeter and a lower jet invariant mass. The neural network output is presented in Figure 5.2. The enhancement around 0.6 is due to hadronic τ-jets without any reconstructed track. A cut on the neutral network output is performed at 0.7 for events with a transverse momentum less than 20 GeV. The neural network is applied to all the jets reconstructed in the events. The jet with the highest output value of the neural network is considered as τ-jet candidate with less than 20% probability of misidentification [91]. Once the τ-jet identified, the two hadronic jets from the $W \to q\bar{q}$ decay are reconstructed.

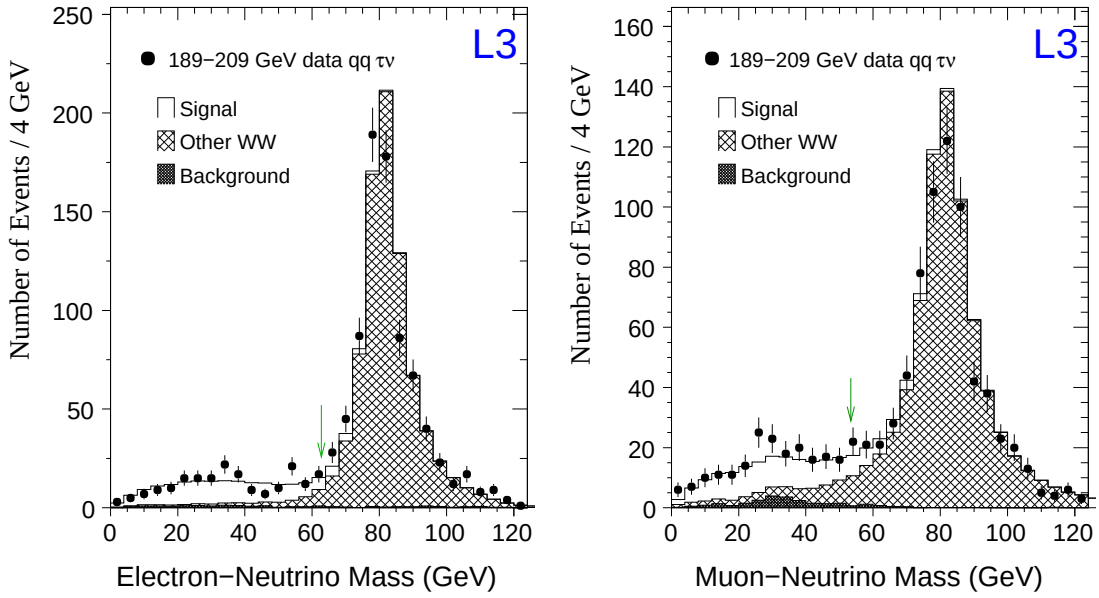

Figure 5.3: *The invariant mass of the lepton-neutrino system for a τ decay into an electron-neutrino (Left) and for a τ decay into a muon-neutrino (Right). A cut is performed at 63 GeV and 53 GeV respectively.*

5.1.3 Separation cuts with the $qqe\nu(\gamma)$ and $qq\mu\nu(\gamma)$ final states

The difference in kinematics between the $qq\tau\nu(\gamma)$ final state with leptonic τ decay, $\tau \rightarrow e\nu_e\nu_\tau$ or $\tau \rightarrow \mu\nu_\mu\nu_\tau$, and the $qqe\nu(\gamma)$ and $qq\mu\nu(\gamma)$ final states, is clearly visible in the invariant mass of the lepton-neutrino system

$$M_{inv}^{l\nu} = \sqrt{(E_l + E_{mis})^2 - (\vec{P}_l + \vec{P}_{mis})^2} \tag{5.1}$$

where E_l and $\vec{P}_l$ are the energy and the momentum vector of the lepton, while E_{mis} and $\vec{P}_{mis}$ are the missing energy and the missing momentum vector obtained from energy-momentum conservation. As for the $qqe\nu(\gamma)$ and $qq\mu\nu(\gamma)$ final states the missing momentum and energy is that of only one neutrino, the invariant mass distribution peaks around $M_W = 81$ GeV without asymetric tails towards lower mass values. On the contrary, for the $qq\tau\nu(\gamma)$ final state, at least two additional neutrino's are emitted in the τ-decay, in general not back-to-back. As a consequence, the invariant mass of the lepton-neutrino system shows a continuous spectrum towards lower mass values. This is clearly seen in the lepton-neutrino mass distribution for a τ-decay into an electron and into a muon, shown in Figure 5.3.

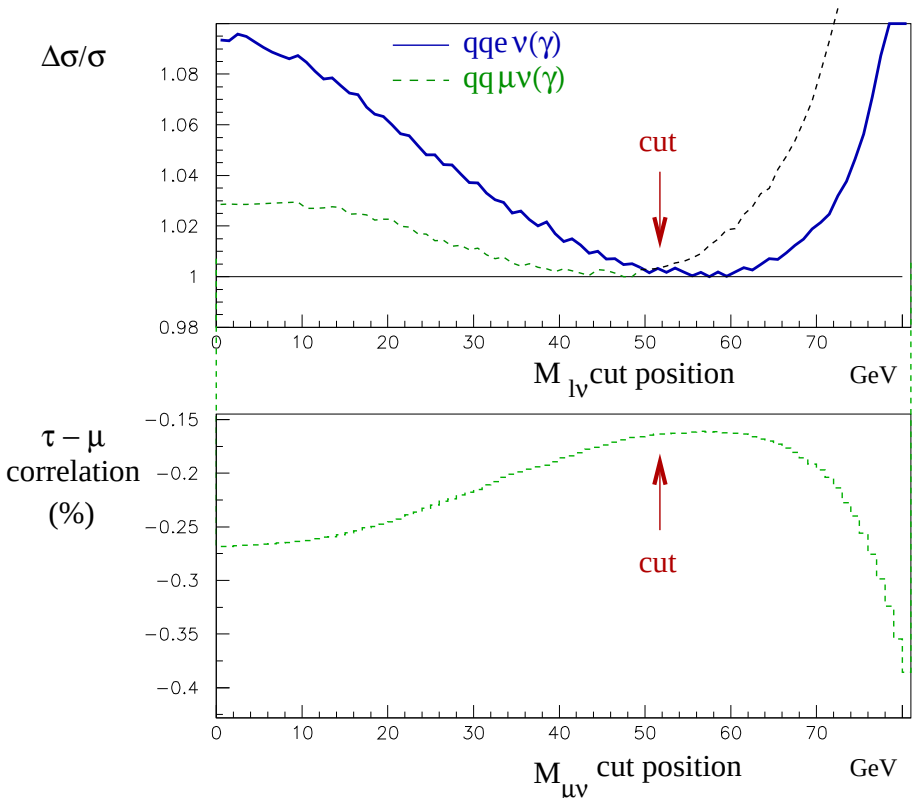

Figure 5.4: *The separation cut between the $e^+e^- \to qq\tau\nu(\gamma)$ channel and the $e^+e^- \to qqe\nu(\gamma)$ channel (full line) is set at 63 GeV, while the separation with the the $e^+e^- \to qq\mu\nu(\gamma)$ channel (dashed line) is set at 53 GeV. Top: The relative cross section change as a function of the cut position on the lepton-neutrino invariant mass $M_{l\nu}$, Bottom: the τ-μ correlation as a function of the cut position on $M_{\mu\nu}$.*

To avoid double counting between the $qq\tau\nu(\gamma)$ final state with leptonic τ-decay and the $qqe\nu(\gamma)$, respectively $qq\mu\nu(\gamma)$ final state, a separation cut is applied on the lepton-neutrino mass and chosen such to minimise the correlations among the semi-leptonic W decays and consequently, among the W-decay branching ratios. The optimisation study is shown in Figure 5.4. The optimal separation cuts are found to be 63 GeV and 53 GeV for the $e^+e^- \to qqe\nu(\gamma)$ and $e^+e^- \to qq\mu\nu$ channel respectively. The relative cross section change and the τ-μ correlation as function of the cut position on the invariant mass of the muon-neutrino system shows a minimum at 53 GeV.

To reduce furthermore the background from $e^+e^- \to qqe\nu(\gamma)$ events where the electron is not identified, τ-jets with an energy deposit larger than 35 GeV in the electromagnetic calorimeter and smaller than 2 GeV in the hadronic calorimeter are rejected.

In the EGAP region ($0.73 < |\cos\theta| < 0.81$) where the electron identification is less efficient, either the energy deposit by the τ jet in the hadronic calorimeter must be larger than 5 GeV or the momentum of the associated track must be smaller than 20 GeV.
The background from $e^+e^- \rightarrow qq\mu\nu(\gamma)$ events with no identified muon in the muon chambers, is reduced by rejecting events where the τ-jet is compatible with a minimum ionizing particle (MIP) in the hadron calorimeter.

5.1.4 Background reduction

To reduce the contamination from $e^+e^- \rightarrow q\bar{q}(\gamma)$ and $e^+e^- \rightarrow qqqq(\gamma)$ events, the event is forced in a dijet topology using the Durham clustering algorithm and the following cuts are applied on

- the difference between the total visible energy and the momentum

$$E_{vis} - P_{tot} < 135 \text{ GeV}$$

- the sum of the total momentum and the visible mass in the dijet event

$$P_{tot} + M_{tot} < 110 \text{ GeV}$$

- the total transverse momentum, presented in Figure 5.5 (Left)

$$P_{\perp} > 10 \text{ GeV}$$

For hadronic τ decay, additional cuts are performed on

- the polar angle of the missing momentum direction, shown in Figure 5.5 (Right),

$$|\cos\ \theta_{miss}| < 0.91$$

  to exclude $q\bar{q}\gamma$ events with a photon escaping along the beam pipe.

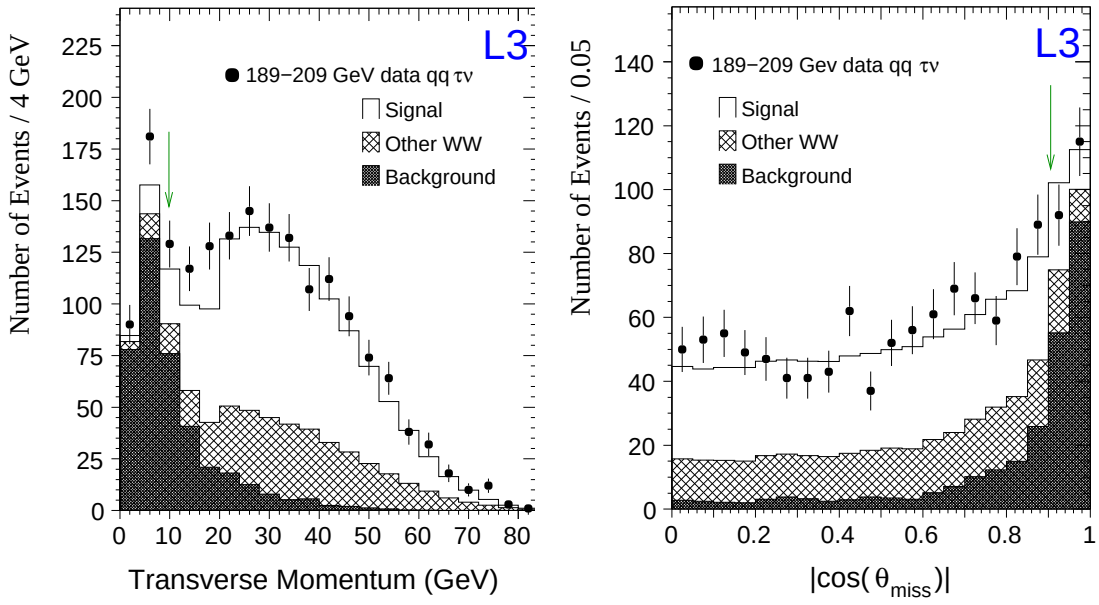

Figure 5.5: Left: *The transverse momentum when forcing the $e^+e^- \to qq\tau\nu(\gamma)$ event in a di-jet topology. A cut is applied at 10 GeV which reduces the background from $q\bar{q}(\gamma)$ events.* Right: *The cosine of the missing momentum direction. The cut position is chosen at 0.91 to exclude $q\bar{q}(\gamma)$ events with a photon escaping along the beam pipe.*

- the number of TEC tracks contained in the hadronic τ-jet

$$N_{ATRK}^{\tau\to h} < 4$$

  because of the very small branching ratio for a τ decay in more than three charged particles (0.1%).

- the solid angle spanned by the the jets from the two quarks and the hadronic τ-jet,

$$\omega < 6 \text{ srad}$$

- the difference in polar angle of the thrust-axis of the hadronic jets

$$\Delta\ \theta_{jets} < 2.5 \text{ rad}$$

  which rejects predominantly the $e^+e^- \to Zee$ background.

The last two cut variables are presented in Figure 5.6.

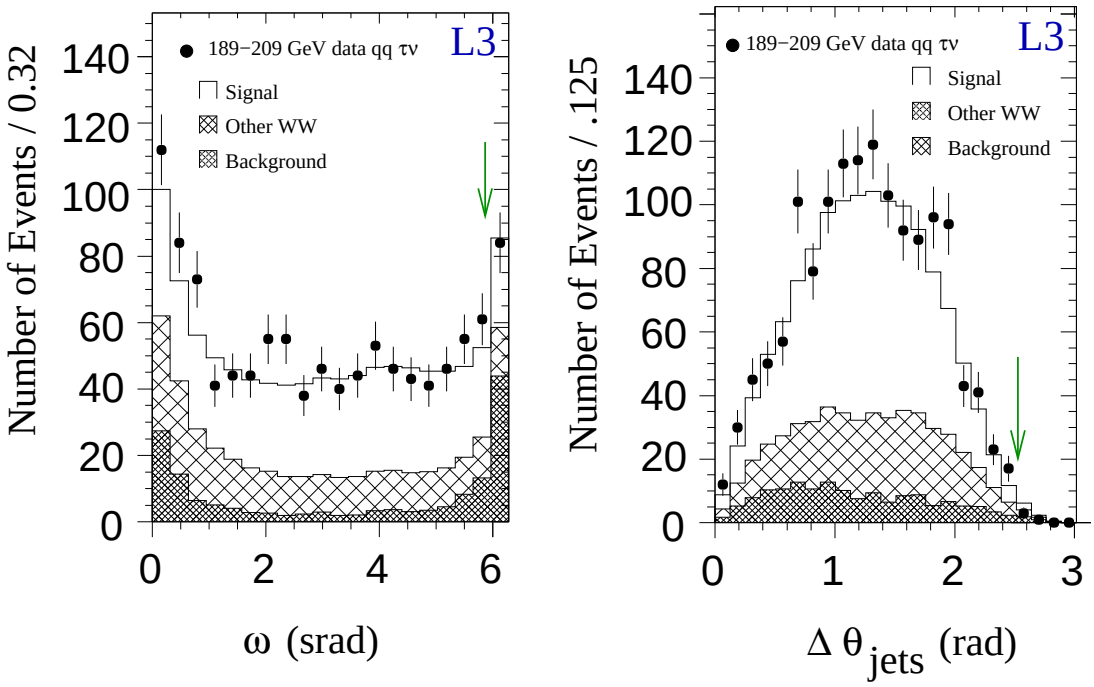

Figure 5.6: Left: *The 3-dimensional space angle between the jets from q, $\bar{q}$ and the hadronic τ jet for events with no reconstructed tracks in the τ-jet. A cut is performed at 6 srad to reduce the $q\bar{q}(\gamma)$ background.* Right: *The difference in polar angle of the thrust-axis of the hadronic jets for events with no reconstructed tracks in the τ-jet. A cut is applied at 2.5 rad.*

Finally, the following requirements on the invariant mass need to be satisfied

- for the jet-jet system

$$50 \text{ GeV} < M_{inv}^{jj} < 110 \text{ GeV}$$

  which garantees that the event is compatible with the production of a W boson.

- for the tau-neutrino system

$$M_{inv}^{\tau\nu} > 35 \text{ GeV}$$

Both are presented in Figure 5.7. The cuts are most efficient against the two photon background.

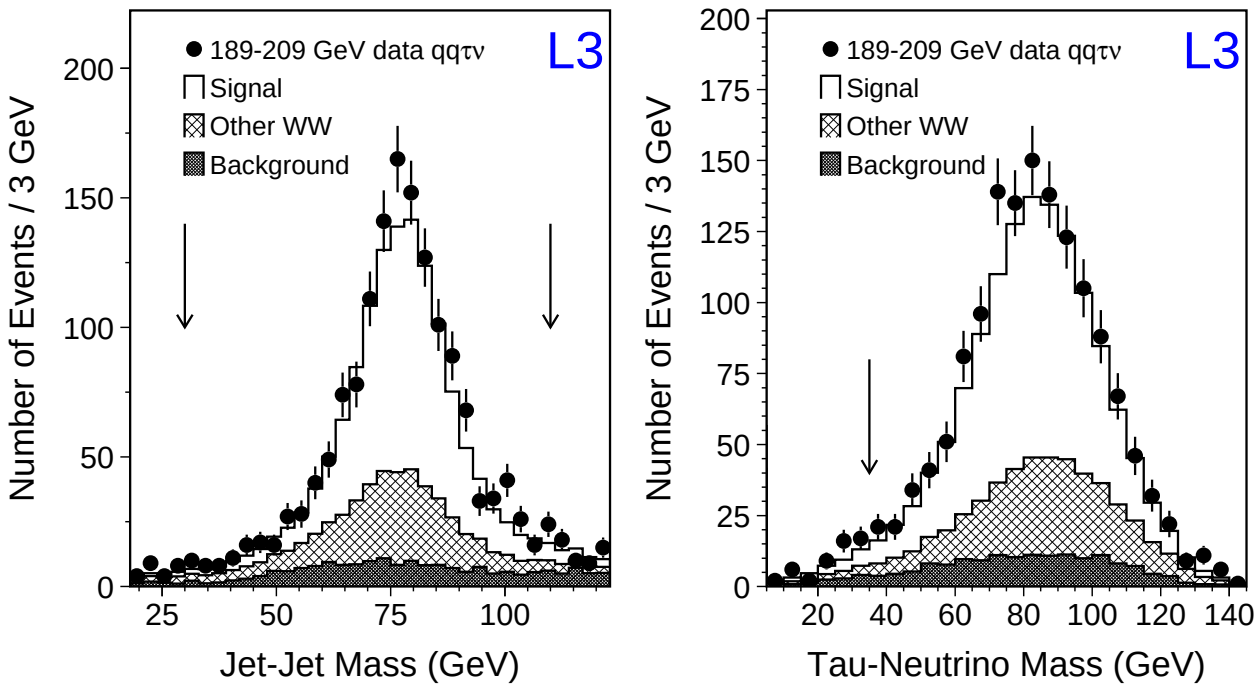

Figure 5.7: *Left: The invariant mass of the jet-jet system. Only events in the interval 50 GeV* $< M^{jj}_{inv} <$ *110 GeV are retained.* Right: *The invariant mass of the tau-neutrino system. The events with an tau-neutrino mass below 35 GeV are rejected.*

5.1.5 Study of trackless τ-jets

The number of tracks in the hadronic τ jet is presented in Figure 5.8 (Left) for the 189 GeV $qq\tau\nu(\gamma)$ data. The events with 4 or more tracks in the τ-jet are rejected, however τ-jets without reconstructed tracks are accepted. The latter are due to an insufficient number of TEC-hits available for the track reconstruction in case of τ leptons emitted at low polar angle. Figure 5.8 (Right) shows such an event. The energy deposits in the electromagnetic calorimeter are clearly visible, but the τ-jet, emitted at low polar angle, has no corresponding track in the TEC.

A study of the angular resolution of the τ-jets using the 189 GeV KoralW Monte Carlo showed no significant difference in jet reconstruction quality between τ-jets with at least one reconstructed track and the trackless τ-jets, where the angular information is deduced from the energy deposits in the electromagnetic calorimeter only. The results of the study are presented in Table 5.2 which gives the fraction of events with a difference between reconstructed and generated angle for the τ-jet smaller than 0.1 rad

$$R_{\tau-jets}(\Delta\alpha < 0.1 \text{ rad}) = \frac{\mathrm{N}_{\tau-\mathrm{jets}}(\Delta\alpha < 0.1 \text{ rad})}{\mathrm{N}^{\mathrm{tot}}_{\tau-\mathrm{jets}}} \tag{5.2}$$

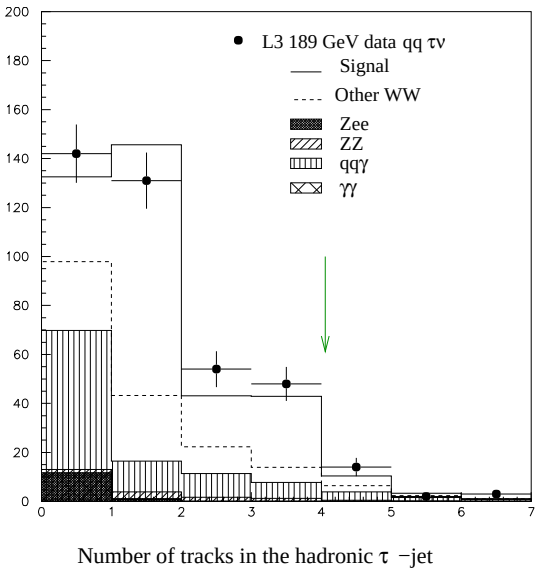

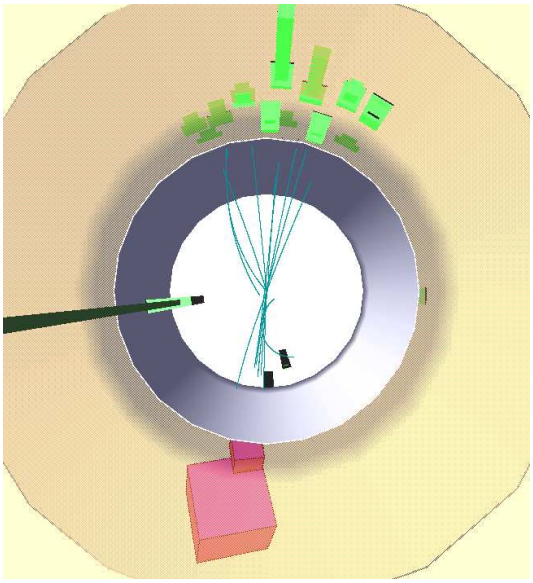

Figure 5.8: Left: *The number of TEC tracks in the hadronic τ jet. The events with more than three tracks in the τ-jet are rejected, while τ-jets without reconstructed track are accepted.* Right: *An event display of a τ-jet emitted at low polar angle, with no corresponding reconstructed track in the TEC while the energy deposit in the electromagnetic calorimeter is clearly visible.*

No significant difference is found between trackless τ-jets and the full sample. The trackless τ-jets have a good jet reconstruction from the calorimeter clusters and are therefore accepted.

The background introduced by the events without reconstructed tracks, consist mainly of $q\bar{q}(\gamma)$ events but is reduced by the cut on the solid angle ω spanned by the three jets in the event and by an appropriate cut on the minimum accolinearity for trackless τ-jets, i.e. the cosine of the minimum angle in the 3-dimensional space between the hadronic τ-jet and the jets associated to the quarks: $\cos\alpha_{min} < 0.95$.

$\Delta\alpha < 0.1$ rad	$R(\tau$-jets)	R(trackless τ-jets)
$\Delta\theta = \mid \theta_{rec} - \theta_{gen} \mid$	87.4 ± 0.4 %	86.5 ± 1.4%
$\Delta\phi = \mid \phi_{rec} - \phi_{gen} \mid$	87.2 ± 0.4 %	86.5 ± 1.4%

Table 5.2: *The fraction of events with a difference between reconstructed and generated angle smaller than 0.1 rad for all τ-jets and for trackless τ-jets only, where the angular information is deduced from the energy deposits in the electromagnetic calorimeter only. The 189 GeV KoralW Monte Carlo was used for the study.*

5.2 W-pair Selections

5.2.1 Selection $e^+e^- \to qqqq(\gamma)$

After a series of preselection cuts retaining hadronic events with a small missing energy and a high multiplicity, a neural network is trained to discriminate the signal from the dominant $e^+e^- \to q\bar{q}(\gamma)$ background events with four reconstructed jets. The preselected events are clustered into a four-jet topology by the DURHAM algorithm and a kinematic fit, assuming four-momentum conservation, is performed to improve the energy and angular resolution. The discriminating neural network variables are

- the spherocity
$$S = min\ \frac{(\sum_i |\vec{n} \times \vec{p}_i|)^2}{(\sum_i |\vec{p}_i|)^2} \tag{5.3}$$
where the sum runs over all particles in the event and where $\vec{p}_i$ is the momentum vector of the particle i. The spherocity varies between zero and one: events with back-to-back jets like $q\bar{q}(\gamma)$ events have a spherocity close to zero, while for the more isotropic W-pair events the spherocity tends towards one. The spherocity after the preselection is presented in Figure 5.9 (Left) for all 189-209 GeV data.

- the lowest jet multiplicity
Occasionally $q\bar{q}\gamma$ events with an energetic ISR photon are misidentified as four-jet events but with a much lower multiplicity than W-pair four-jet events.

- y_{34}, the smallest value of y_{ij} when a four-jet topology is imposed on the event using the DURHAM algorithm. When forcing events with two or three jets in a four-jet topology, a small value of y_{34} is obtained.

- the sum of the cosine of the six inter-jet angles in the four-jet event

- the energy of the most and the least energetic jet after 4C kinematic fit

- the energy difference between the second and the third most energetic jet after 4C kinematic fit

- the jet broadening of the most and the least energetic jet after 4C kinematic fit, expressed as
$$\sqrt{\frac{\sum_i |\vec{p}_{T,i}|}{\sum_i |\vec{p}_{tot,i}|}} \tag{5.4}$$
where $\vec{p}_{tot}$ and $\vec{p}_T$ are the total momentum and the transverse momentum of the particle relative to the jet thrust-axis.

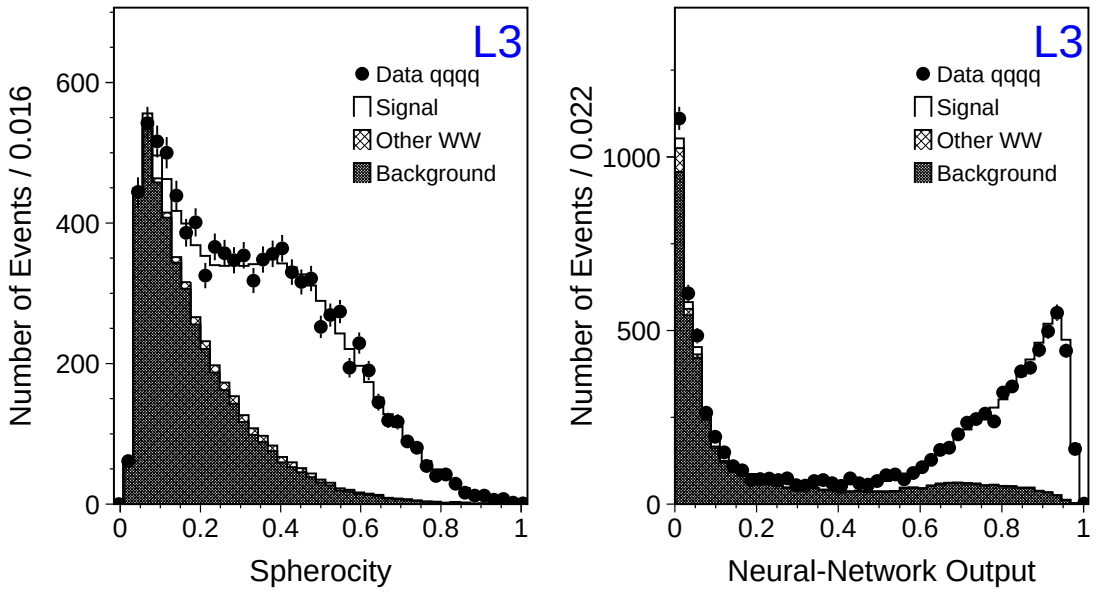

Figure 5.9: *The spherocity, used as input variable for the neural network, and the neural network output for the $qqqq(\gamma)$ final state after preselection. All 189-209 GeV L3 data are included. A cut is performed on the neural network output at 0.6.*

- the 4C kinematic fit probability

The neural network output after preselection for all 189-209 GeV data is presented in Figure 5.9 (Right). The signal peaks at one, while the background is concentrated at zero. A cut is performed on the neural network output at 0.6 to maximise the quality factor defined as the square root of the product of the selection efficiency, ϵ_{sel}, and the purity, π,

$$Q = \sqrt{\epsilon_{sel} \times \pi} \tag{5.5}$$

At $\langle\sqrt{s}\rangle = 206.5$ GeV, the selection efficiency is 84 % and the purity is 80 %. A summary of the performance of the selection is given in Table 5.4. The accepted background is dominated by the $q\bar{q}(\gamma)$ final state with a gluon radiation (59%) leading two additional jets, and Z-pair final states (41%) with four reconstructed jets.

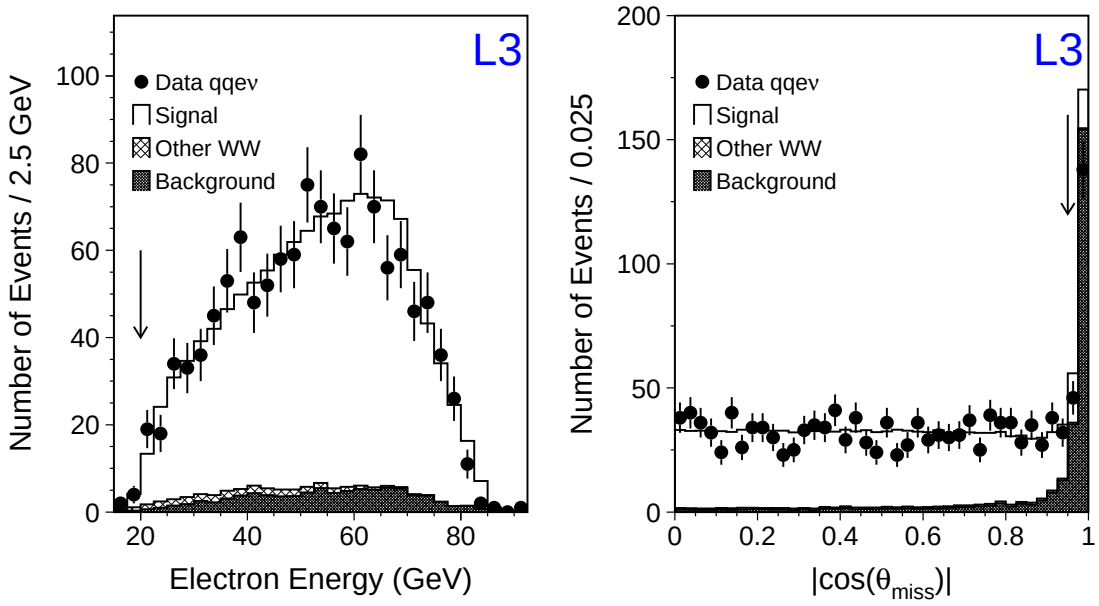

Figure 5.10: *The energy of the electron and the absolute value of the cosine of the polar angle of the missing momentum for the $qqe\nu(\gamma)$ final state. All 189-209 GeV L3 data are included. The arrow indicates the cut position. All cuts are applied except the one on the plotted variable.*

5.2.2 Selection $e^+e^- \to qqe\nu(\gamma)$

The selection of the $qqe\nu(\gamma)$ final state is based on a series of cut values on discriminating variables which exhibit a good separation between the signal and the background contributions. The cuts are listed below:

- a high cluster multiplicity

$$N_{ASRC} \geq 14 \tag{5.6}$$

  where a cluster has an energy of at least 100 MeV. This reduces the contribution of leptonic two-photon and fermion-pair production events.

- at least one energetic, isolated electron

$$N_e \geq 1,\ E_e > 20 \text{ GeV} \tag{5.7}$$

  The energy of the electron, E_e, is presented in Figure 5.10 (Left) for all 189-209 GeV L3 data.

- $$E_e/E^{15^\circ}_{ECAL} \geq 0.8 \tag{5.8}$$

  where $E^{15^\circ}_{ECAL}$ represents the electron energy deposited in the BGO and included in a cone with half-opening angle 15° around the electrons direction. The cut avoids the selection of electrons produced by a leptonic decay inside a hadronic jet.

- the missing momentum associated to the neutrino, must point inside the detector

  $$|\cos\theta_{miss}| < 0.95 \tag{5.9}$$

  with θ_{miss} the polar angle of the missing momentum vector. This variable is presented in Figure 5.10 (Right) for all 189-209 GeV data.

- the reconstructed jet-jet invariant mass needs to satisfy

  $$M^{inv}_{jj} > 45 \text{ GeV} \tag{5.10}$$

  to reduce the contribution of hadronic two-photon events. The electron-neutrino invariant mass must be

  $$M^{inv}_{e\nu} > 63 \text{ GeV} \tag{5.11}$$

  to separate the $qqe\nu(\gamma)$ final state from the $qq\tau\nu(\gamma)$ final state with $\tau \to e\nu_e\nu_\tau$.

- the solid angle spanned by the directions of the electron and the two hadronic jets

  $$\Omega < 5.3 \text{ srad} \tag{5.12}$$

  to reduce the $qq(\gamma)$ background characterised by a large solid angle.

- if a muon is identified in the event, it needs to be close to the nearest hadronic jet

  $$P^{\mu}_{T} \leq 12 \text{ GeV} \tag{5.13}$$

  where the transverse direction is defined relative to the nearest jet. Only muons from a leptonic decay of hadrons inside a jet are accepted. This excludes the selection of electrons from an isolated muon decay, thus the $qq\mu\nu(\gamma)$.

At $\langle\sqrt{s}\rangle = 206.5$ GeV, the selection efficiency is 73% and the purity is 91%. A summary of the performance of the selection is given in Table 5.5. The accepted non-WW background is dominated by the processes leading to $qqe\nu(\gamma)$ final states (71%), mainly single W boson production, followed by Z-pair and Zee production, and $e^+e^- \to q\bar{q}(\gamma)$ events (29%).

5.2.3 Selection $e^+e^- \to qq\mu\nu(\gamma)$

The selection of the $qq\mu\nu(\gamma)$ final state is also based on a series of cut values on discriminating variables which exhibit a good separation between the signal and the background contributions. The cuts are listed below:

- a high cluster multiplicity
$$N_{ASRC} \geq 10 \tag{5.14}$$
where a cluster has an energy of at least 100 MeV, to reduce the contribution from leptonic two-photon and fermion-pair production events.

- at least one energetic, isolated muon
$$N_{AMUI} \geq 1 \; or \; N_{MIP} \geq 1 \tag{5.15}$$
The most energetic AMUI is taken as the muon candidate. If no AMUI is present, the MIP with the largest momentum is chosen. where $\psi_{\mu j}$ represents the angle between the muon and the closest jet and θ_{miss} the polar angle of the missing momentum vector. This selection variable is presented in Figure 5.11 (Left) for all 189-209 GeV data.

- the reconstructed jet-jet invariant mass must be close to the W mass
$$25 < M_{jj}^{inv} < 125 \text{ GeV} \tag{5.16}$$
when the reconstructed muon is a MIP, the required window is tighten to
$$50 < M_{jj}^{inv} < 98 \text{ GeV} \tag{5.17}$$
The cuts remove hadronic two-photon events characterised by a much lower invariant mass. This jet-jet invariant mass is presented in Figure 5.11 (Right) for all 189-209 GeV data.

- the missing momentum associated to the neutrino, points inside the detector
$$\psi_{\mu j} \times |\sin\theta_{miss}| \geq 5.5^\circ \text{ (AMUI)} \tag{5.18}$$
$$\psi_{\mu j} \times |\sin\theta_{miss}| \geq 20^\circ \text{ (MIP)} \tag{5.19}$$

- the reconstructed muon-neutrino invariant mass needs to satisfy
$$M_{\mu\nu}^{inv} > 53 \text{ GeV} \tag{5.20}$$
to separate the $qq\mu\nu(\gamma)$ final state from the $qq\tau\nu(\gamma)$ final state with $\tau \to \mu\nu_\mu\nu_\tau$ and so, to avoid overlap between the two channels. In case of a muon identified as a MIP,

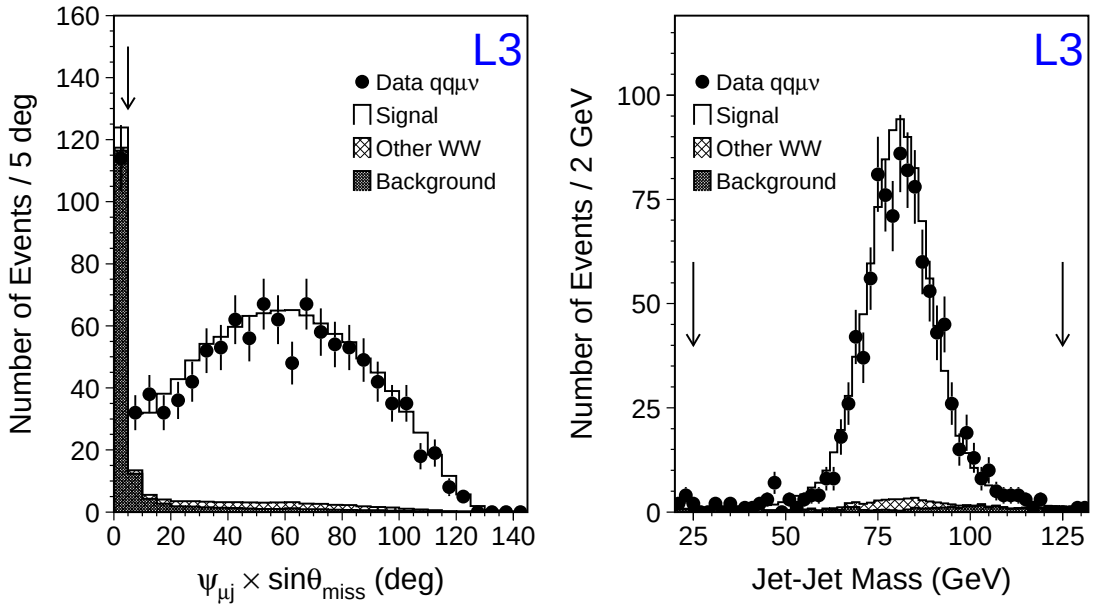

Figure 5.11: *The variable $\psi_{\mu j}.|\sin\theta_{miss}|$ where $\psi_{\mu j}$ represents the angle between the muon and the closest jet and θ_{miss} the polar angle of the missing momentum vector,and the jet-jet invariant mass for the $qq\mu\nu(\gamma)$ final state. All 189-209 GeV L3 data are included. The arrow indicates the cut position. All cuts are applied except the one on the plotted variable.*

the cut is omitted. To furthermore reduce the contamination of $e^+e^- \rightarrow qq\tau\nu(\gamma)$ events, the following cut is performed on the variable

$$P^\star = |p_\mu| - 10 \text{ GeV} \times (\cos\theta^\star + 1) > 18.5 \text{ GeV} \tag{5.21}$$

where p_μ is the muon momentum and $\cos\theta^\star$ the angle of the muon in the reconstructed W boson restframe. For MIP muons, the cut value is lowered to 15 GeV. The cut variable exploits the fact that muons from a $\tau \rightarrow \mu\nu_\mu\nu_\tau$ decay have a lower momentum and so, less boosted into the direction of the W boson. Therefore the muon decay angle in the W restframe is larger.

- if an ISR photon is present in the case of an AMUI, it needs to satisfy

$$E_\gamma \leq 0.9\ E_\gamma^{exp} \tag{5.22}$$

where $E_\gamma^{exp} = (\sqrt{s}/2)(1 - M_Z^2/s)$. The requirement reduces the contamination of $e^+e^- \rightarrow q\bar{q}(\gamma)$ background events with an ISR photon that reduces the effective center-of-mass energy $\sqrt{s}$ to the mass of the Z boson (return to Z).

- the events containing MIP muons compatible with the ZZ background are rejected

$$\beta_W > 0.34 - 0.49 \tag{5.23}$$

where the relativistic velocity of the W boson, β_W, has to be greater than a $\sqrt{s}$-dependent value ranging from 0.34 to 0.49.

At $\langle\sqrt{s}\rangle = 206.5$ GeV, the selection efficiency is 74% and the purity is 90%. A summary of the performance of the selection is given in Table 5.5. The accepted non-WW background is dominated by $e^+e^- \to q\bar{q}(\gamma)$ (52%) and Z-pair production $e^+e^- \to ZZ \to q\bar{q}\mu^+\mu^-$ events (31%).

5.2.4 Selection $e^+e^- \to l\nu l\nu(\gamma)$

There are three classes of events depending on the number of identified electrons and muons. They are referred to as jet-jet ($\tau\nu\tau\nu$), lepton-jet and lepton-lepton classes. The selection of the $l\nu l\nu(\gamma)$ final state is again based on a series of cut values on discriminating variables. The cuts are listed below:

- two charged leptons
- for events with at least one electron, the event is selected if the polar angle of at least one electron satisfies

$$|\cos\theta_e| < 0.92 \tag{5.24}$$

to reduce the background from Bhabha scattering i.e. $e^+e^- \to e^+e^-$ events. The same requirement is applied to the two most energetic jets for events containing τ-jets only.

- the acoplanarity, defined as the complement of the angle between of the two reconstructed particles in the plane transverse to the beam axis, needs to be larger than 8° (14° for the jet-jet classes). This is needed to suppress the background from lepton-pair production and cosmic rays. The acoplanarity is presented in Figure 5.12 (Left) for all 189-209 GeV data. The excess in the first bin is due to cosmic ray events which are poorly reproduced by the Monte Carlo.
- the signals in the scintillator time-of-flight counters, associated to the leptons, are requested to be compatible with a beam crossing.
- for the missing momentum in the plane transverse to the beam axis

$$P_{T,miss} > 8 \text{ GeV} \tag{5.25}$$

This variable is presented in Figure 5.12 (Right) for all 189-209 GeV data.

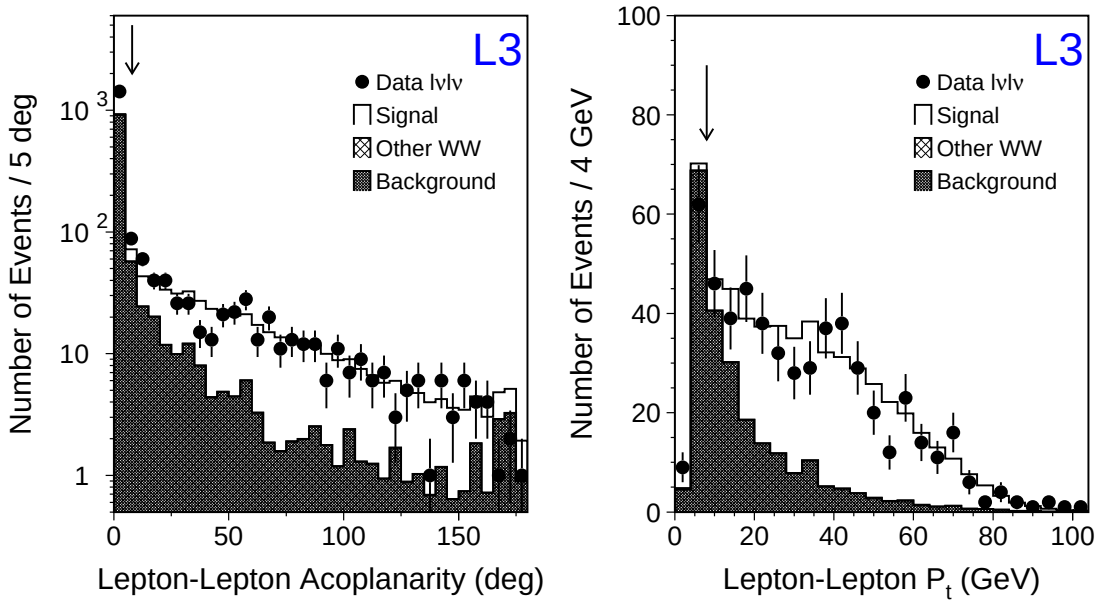

Figure 5.12: *The lepton-lepton accoplanarity and the momentum imbalance in the plane transverse to the beam direction for the $l\nu l\nu(\gamma)$ final state. All 189-209 GeV L3 data are included. The arrow indicates the cut position. All cuts are applied except the one on the plotted variable.*

- the energy of the most energetic lepton has to fullfil the following requirements

$$E_l{}^{most} > 20 \text{ GeV } (\text{jet} - \text{jet}, \text{lepton} - \text{jet}) \tag{5.26}$$

$$E_l{}^{most} > 25 \text{ GeV } (\text{lepton} - \text{lepton}) \tag{5.27}$$

  while for the least energetic lepton

$$E_l{}^{least} > 6 \text{ GeV } (\text{jet} - \text{jet}) \tag{5.28}$$

$$E_l{}^{least} > 8 \text{ GeV } (\text{lepton} - \text{jet}) \tag{5.29}$$

$$E_l{}^{least} > 5 \text{ GeV } (\text{lepton} - \text{lepton}) \tag{5.30}$$

The selection efficiency at $\langle\sqrt{s}\rangle = 206.5$ GeV varies from 55 % for the $e\nu e\nu(\gamma)$ final state to 17 % for the $\tau\nu\tau\nu(\gamma)$ final state, and the purity is 72%. A summary of the performance of the selection is given in Table 5.4. The accepted background is dominated by leptonic two-photon events (50%) and fermion-pair production events (24%). As the data statistics in the purely leptonic final state is limited, the quoted numbers combine the different flavours of the two-lepton final states, referenced as $l\nu l\nu(\gamma)$.

5.3 Definition of the Single-channel Cross Section

The cross section for a particular signal process is measured as

$$\sigma_{meas} = \frac{N_{data}^{sel} - N_{bkg}^{exp}}{\epsilon_{sig}\ \mathcal{L}_{data}} \tag{5.31}$$

where

- $\mathcal{L}_{data}$ represents the total integrated data luminosity
- N_{data}^{sel} is the number of data events selected by the signal selection procedure
- ϵ_{sig} is the signal selection efficiency defined as

  $$\epsilon_{sig} = \frac{N_{sign}^{gen+sel}}{N_{sign}^{gen}} \tag{5.32}$$

  where $N_{sig}^{gen+sel}$ is the number of selected signal Monte Carlo events on a total number of generated signal events N_{sig}^{gen}.
  The selection efficiency is obtained from Monte Carlo simulation by passing the generated signal events through the full detector simulation. Due to the limited detector acceptance and resolution, and due to the selection cuts, chosen to separate the signal from the background, a fraction of the signal events is not selected.

- N_{bkg}^{exp} is the number of expected background events, calculated as

  $$N_{bkg}^{exp} = \sum_{bkg\ k} \epsilon_{bkg}^{k}.\sigma_{bkg}^{k}.\mathcal{L}_{data} \tag{5.33}$$

  with σ_{bkg}^{k} the theoretical prediction for the cross section of the background process k. The background selection efficiency ϵ_{bkg}^{k} is evaluated by applying the signal selection procedure on Monte Carlo samples of background events

  $$\epsilon_{bkg}^{k} = \frac{N_{bkg\ k}^{gen+sel}}{N_{bkg\ k}^{gen}} \tag{5.34}$$

The statistical uncertainty on the measured cross section is

$$\delta_{stat}(\sigma_{meas}) = \frac{\sqrt{N^{sel}_{data}}}{\epsilon_{sig}.\mathcal{L}_{data}} \tag{5.35}$$

where the number of expected background events N^{exp}_{bkg} is fixed. The uncertainty on the background estimation enters as a source of systematics on the cross section measurement

As the experimental data contain all possible four-fermion (4f) final states, the measured cross section is the one of the four-fermion process $e^+e^- \rightarrow ffff(\gamma)$

For the $qq\tau\nu(\gamma)$ and $qq\mu\nu(\gamma)$ channels, the three CC03 diagrams are dominant and the effect of the additional 4f diagrams is negligible within the available statistics. This is not the case for the $qqe\nu(\gamma)$ channel, described by the 20 diagrams of CC20, and the $l\nu l\nu(\gamma)$ channels, with 115 contributing diagrams. Also for the $qqqq(\gamma)$ channel, the contribution of the 214 diagrams leading to the same $qqqq(\gamma)$ final, is sizeable [92].

It is conventional in the LEP community to quote results for the CC03 subset with inclusion of initial state radiation. The other four-fermion processes contribute as irreducible background. There are two different approaches to calculate the CC03 cross section taking into account all 4f diagrams and their interference:

- additive approach: the 4f processes beyond CC03 are treated as background
- multiplicative approach: all 4f processes are considered as signal and the measured cross section is corrected to the CC03 level of description by a multiplicative factor $f_{4f \rightarrow cco3}$.

The additive approach is chosen for the cross section measurement.
The CC03 efficiencies are calculated with an event-by-event reweighting of the KandY Monte Carlo events with a factor

$$\omega^{ev}_{cco3} = \frac{\mid \mathcal{M}_{\mathrm{CCO3}}\ (p_1, p_2, p_3, p_4) \mid^2}{\mid \mathcal{M}_{\mathrm{4f}}\ (p_1, p_2, p_3, p_4) \mid^2} \tag{5.36}$$

where (p_1, p_2, p_3, p_4) are the momenta of the four fermions in the final state, and $\mathcal{M}_{\mathrm{CC03}}$ and $\mathcal{M}_{\mathrm{4f}}$ are the matrix element corresponding to the CC03 subset and the full set, respectively.

The relative difference between the CC03 and the four-fermion cross section is of the order of some percent for the $qqe\nu(\gamma)$ channel and rised to 10 % for the $l\nu l\nu(\gamma)$ channels, while the effect is at the permille level for the other channels.

$e^+e^- \to qq\tau\nu(\gamma)$						
$\langle\sqrt{s}\rangle$ (GeV)	$\mathcal{L}_{data}$ (pb^{-1})	N^{sel}_{data}	N^{exp}_{tot}	N^{exp}_{sign}	N^{exp}_{bkg}	ϵ_{sel} (%)
188.6	176.8	413	373.2	227.8	145.4	54.2
191.6	29.8	57	63.9	38.8	25.1	53.8
195.5	84.1	222	181.3	110.2	71.1	53.2
199.6	83.3	181	173.7	106.0	67.6	51.3
201.8	37.1	77	77.6	47.6	30.0	51.4
204.8	79.0	164	157.6	99.5	58.1	50.4
206.5	130.5	287	260.6	162.7	98.0	49.8
208.0	8.6	17	16.6	10.3	6.3	49.3

Table 5.3: *The number of selected data events, N^{sel}_{data}, compared to the total number of expected events, N^{exp}_{tot}, from the signal, N^{exp}_{sign}, and from the background, N^{exp}_{bkg}, for the $e^+e^- \to qq\tau\nu(\gamma)$ reaction including all 1998, 1999 and 2000 data with total integrated luminosities $\mathcal{L}_{data}$ and average center-of-mass energies $<\sqrt{s}>$. Also the efficiency of the selection, ϵ_{sel} is given. The number of expected events are obtained using the YFSWW3 Monte Carlo.*

5.4 Performance of the WW Selections

- $qq\tau\nu(\gamma)$ **selection**

After applying all $e^+e^- \to qq\tau\nu(\gamma)$ selection cuts, the signal efficiency of the obtained sample varies from 49.3 % to 54.2%, while the purity ranges from 60.7 % to 63.1%, depending on the center-of-mass energy. The purity of the sample is defined as

$$\pi = \frac{N^{exp}_{sig}}{(N^{exp}_{sig} + N^{exp}_{bkg})} \tag{5.37}$$

where N^{exp}_{sig} represents the number of expected signal events, calculated as

$$N^{exp}_{sign} = \epsilon_{sign}.\sigma_{sign}.\mathcal{L}_{data} \tag{5.38}$$

with σ_{sign} the theoretical prediction for the cross section of the signal process.

The accepted WW background is dominated by the other semi-leptonic W-pair production channels, while the accepted non-WW background consists mainly of $qq(\gamma)$ events (54%) and $qqe\nu(\gamma)$ final states not originating from W-pair production, mainly single W production (46%).

Details on the number of selected data events for the $qq\tau\nu(\gamma)$ final state, are presented in Table 5.3, together with the number of expected events for the signal and the background, including all 1998, 1999 and 2000 data grouped into eight $\sqrt{s}$ bins with integrated luminosity $\mathcal{L}_{data}$ and at average center-of-mass energy $< \sqrt{s} >$. Also the selection efficiency, ϵ_{sel} is displayed. The quoted numbers are obtained using the YFSWW3 Monte Carlo. For the expected signal and the WW background contribution, the CC03 cross section and luminosity at the corresponding center-of-mass energy were used.

- **Other WW selections**

Table 5.4 and Table 5.5 give the results for the other W-pair final states.

The number of expected events is in agreement with the number of observed data events except for a 3σ-excess in the $qq\tau\nu(\gamma)$ channel and a 2σ-deficit in the $qq\mu\nu(\gamma)$. Several studies were performed to understand the origin of these deviations. No evidence was found for a transfer of events between the $qq\tau\nu(\gamma)$ and the $qq\mu\nu(\gamma)$ channels. A similar but less significant deviation is observed by the other LEP experiments.

$e^+e^- \to qqqq(\gamma)$						
$\langle\sqrt{s}\rangle$ (GeV)	$\mathcal{L}_{data}$ (pb^{-1})	N^{sel}_{data}	N^{exp}_{tot}	N^{exp}_{sign}	N^{exp}_{bkg}	ϵ_{sel} (%)
188.6	176.8	1477	1486.2	1154.0	332.2	88.0
191.6	29.8	236	255.1	197.0	58.1	87.3
195.5	84.1	665	715.8	561.0	154.9	86.8
199.6	83.3	726	706.3	554.0	152.4	85.6
201.8	37.1	301	312.8	247.7	65.1	85.5
204.8	79.0	656	660.4	522.2	138.2	84.6
206.5	130.5	1108	1080.6	859.0	221.7	84.0
208.0	8.6	65	68.7	54.5	14.2	83.5

$e^+e^- \to l\nu l\nu(\gamma)$						
$\langle\sqrt{s}\rangle$ (GeV)	$\mathcal{L}_{data}$ (pb^{-1})	N^{sel}_{data}	N^{exp}_{tot}	N^{exp}_{sign}	N^{exp}_{bkg}	ϵ_{sel} (%)
188.6	176.8	235	202.3	145.1	57.2	60.2
191.6	29.8	35	33.8	23.4	16.4	57.8
195.5	84.1	105	97.4	67.2	30.2	57.8
199.6	83.3	87	83.7	57.7	26.0	55.6
201.8	37.1	40	41.2	28.9	12.3	55.7
204.8	79.0	85	84.1	59.1	25.0	55.0
206.5	130.5	128	139.9	97.3	42.6	54.7
208.0	8.6	11	8.5	6.1	2.4	52.9

Table 5.4: *The number of selected data events, N^{sel}_{data}, compared to the total number of expected events, N^{exp}_{tot}, from the signal, N^{exp}_{sign}, and from the background, N^{exp}_{bkg}, for the $qqqq(\gamma)$ and the $l\nu l\nu(\gamma)$ reaction including all 1998, 1999 and 2000 data with total integrated luminosities $\mathcal{L}_{data}$ and average center-of-mass energies $<\sqrt{s}>$. Also the efficiency of the selection, ϵ_{sel} is given. The number of expected events are obtained using the YFSWW3 Monte Carlo.*

$e^+e^- \to qqe\nu(\gamma)$						
$\langle\sqrt{s}\rangle$ (GeV)	$\mathcal{L}_{data}$ (pb^{-1})	N_{data}^{sel}	N_{tot}^{exp}	N_{sign}^{exp}	N_{bkg}^{exp}	ϵ_{sel} (%)
188.6	176.8	347	359.1	328.8	30.4	78.1
191.6	29.8	73	61.0	55.6	5.4	77.1
195.5	84.1	168	173.9	159.0	14.9	76.8
199.6	83.3	152	169.0	153.5	15.5	74.3
201.8	37.1	70	76.5	69.5	7.0	75.1
204.8	79.0	176	160.3	145.2	15.1	73.5
206.5	130.5	269	264.1	239.8	24.3	73.3
208.0	8.6	14	16.9	15.5	1.5	74.2

$e^+e^- \to qq\mu\nu(\gamma)$						
$\langle\sqrt{s}\rangle$ (GeV)	$\mathcal{L}_{data}$ (pb^{-1})	N_{data}^{sel}	N_{tot}^{exp}	N_{sign}^{exp}	N_{bkg}^{exp}	ϵ_{sel} (%)
188.6	176.8	341	343.7	309.1	34.6	77.8
191.6	29.8	63	59.5	54.0	5.6	76.9
195.5	84.1	157	174.7	156.7	18.0	76.8
199.6	83.3	142	168.3	151.2	17.1	75.9
201.8	37.1	79	75.7	68.2	7.5	75.4
204.8	79.0	142	153.7	138.2	15.4	74.8
206.5	130.5	240	260.2	232.7	27.4	74.2
208.0	8.6	23	16.6	15.0	1.6	74.8

Table 5.5: *The number of selected data events, N_{data}^{sel}, compared to the total number of expected events, N_{tot}^{exp}, from the signal, N_{sign}^{exp}, and from the background, N_{bkg}^{exp}, for the $qqe\nu(\gamma)$ and the $qq\mu\nu(\gamma)$ reaction including all 1998, 1999 and 2000 data with total integrated luminosities $\mathcal{L}_{data}$ and average center-of-mass energies $< \sqrt{s} >$. Also the efficiency of the selection, ϵ_{sel} is given. The number of expected events are obtained using the YFSWW3 Monte Carlo.*

5.5 Measurement of the WW Cross Section

5.5.1 Fit method

To take into account the cross-feed between the different W-pair final states and the signal process in the measurement of the total WW cross section and the single-channel cross sections, a single, global maximum likelihood fit is performed which allows the cross sections of all signal processes to vary simultaneously.

The total likelihood is constructed as the product of the Poissonian probabilities for the different W-pair channels

$$L = \prod_{channel\ i} P(N_i, \mu_i) \tag{5.39}$$

where Poissonian probability for each W-pair channel i

$$P(N_i, \mu_i) = \frac{\mu_i^{N_i} e^{-\mu_i}}{N_i!} \tag{5.40}$$

gives the probability to select the number of events N_i for the signal process i if the corresponding number of expected events is μ_i. The latter is calculated as following

$$\mu_i = (\sum_{j=1}^{10} \epsilon_{ij}\sigma^j + \sigma^i_{bkg}) \ . \ \mathcal{L}_{data} \tag{5.41}$$

The first term is the sum over the the 10 W-pair final states j which cross feed with the studied signal final state i. Beside the hadronic final state, $qqqq(\gamma)$, and the 3 semi-leptonic final states, $qqe\nu(\gamma)$, $qq\mu\nu(\gamma)$ and $qq\tau\nu(\gamma)$, there are 6 purely leptonic final states: $e\nu e\nu(\gamma)$, $e\nu\mu\nu(\gamma)$, $e\nu\tau\nu(\gamma)$, $\mu\nu\mu\nu(\gamma)$, $\mu\nu\tau\nu(\gamma)$, $\tau\nu\tau\nu(\gamma)$. The cross efficiency matrix ϵ_{ij} is a 10 X 10 matrix which relates the generated four-fermion events at CC03 level to the selected ones on reconstruction level and is determined at each center-of-mass energy. The result for $< \sqrt{s} >= 206.5$ GeV is presented in Table 5.6, but is only marginally different for the other center-of-mass energies.

The second term σ^i_{bkg} is the accepted background cross section

$$\sigma^i_{bkg} = \sum_{bkg\ k} \epsilon^{ik}_{bkg}\ \sigma^k_{bkg} \tag{5.42}$$

where there is summed over all backgrounds processes k for the signal process i. The sum includes the non-CC03 WW four-fermion final states as well as the four-fermion final states without W boson production.

Efficiency (%) for $e^+e^- \to$										
Selection	$qqqq$	$qqe\nu$	$qq\mu\nu$	$qq\tau\nu$	$e\nu e\nu$	$e\nu\mu\nu$	$e\nu\tau\nu$	$\mu\nu\mu\nu$	$\mu\nu\tau\nu$	$\tau\nu\tau\nu$
$qqqq$	84.0	0.1		0.4						
$qqe\nu$		73.3	0.2	1.6						
$qq\mu\nu$		0.1	74.2	4.2						
$qq\tau\nu$	0.1	6.2	10.1	49.8						
$e\nu e\nu$					54.7	0.8	11.4		0.1	1.5
$e\nu\mu\nu$						47.6	8.4	1.4	10.1	2.2
$e\nu\tau\nu$					6.0	1.7	27.8		0.4	7.5
$\mu\nu\mu\nu$								41.0	6.9	0.9
$\mu\nu\tau\nu$						2.6	0.3	3.0	23.1	4.8
$\tau\nu\tau\nu$					0.2	0.1	2.1		1.3	16.7

Table 5.6: *The CC03 selection efficiencies for signal processes in the fully hadronic $qqqq(\gamma)$ final state, the 3 semi-leptonic final states $qql\nu(\gamma)$ and the 6 purely leptonic final states $l\nu l\nu(\gamma)$ at $<\sqrt{s}>= 206.5$ GeV. For the $qqqq(\gamma)$ selection the quoted numbers are for a neural network output larger than 0.6.*

Similarly as for the CCO3 WW background, ϵ^{ik}_{bkg} represents the efficiency of selection procedure for the signal process i to accept events from the background process k with cross section σ^k_{bkg}.

The 10 CC03 single-channel cross sections, σ^j, one for each W-pair final state, are the parameters of the fit and the total likelihood is maximized.

For the $qqqq(\gamma)$ final state, the likelihood as function of the single-channel cross section, obtained from a fit to the neural network output, is used instead of the Poissonian probability.

As the data statistics in the purely leptonic final state is limited, the six cross sections corresponding to the different flavours of the two-lepton final states, obtained from the global fit, are combined and quoted in the following as the cross section for the $l\nu l\nu(\gamma)$ final state.

5.5.2 Single-channel cross sections

The measured CC03 cross section for the $qq\tau\nu(\gamma)$ final state as function of the average center-of-mass energy $\sqrt{s}$ is visually presented in Figure 5.13. The study of the sources of systematic uncertainty on the cross section measurement is presented in the Section 5.7.

Table 5.7 summarizes the results for the measured CC03 cross section for all W-pair production final states together with their statistical and systematic uncertainties.

	$e^+e^- \to qqqq(\gamma)$		$e^+e^- \to l\nu l\nu(\gamma)$	
$\langle\sqrt{s}\rangle$ (GeV)	σ^{cco3}_{meas} (pb)	σ^{cco3}_{SM} (pb)	σ^{cco3}_{meas} (pb)	σ^{cco3}_{SM} (pb)
188.6	$7.17 \pm 0.24 \pm 0.12$	7.42	$1.87 \pm 0.17 \pm 0.06$	1.72
191.6	$6.79 \pm 0.56 \pm 0.15$	7.56	$1.67 \pm 0.41 \pm 0.07$	1.76
195.5	$6.92 \pm 0.34 \pm 0.11$	7.68	$1.76 \pm 0.25 \pm 0.06$	1.79
199.6	$7.91 \pm 0.36 \pm 0.13$	7.76	$1.68 \pm 0.27 \pm 0.06$	1.80
201.8	$7.10 \pm 0.52 \pm 0.12$	7.79	$1.47 \pm 0.35 \pm 0.07$	1.81
204.8	$7.66 \pm 0.37 \pm 0.13$	7.81	$1.58 \pm 0.26 \pm 0.05$	1.82
206.5	$8.07 \pm 0.29 \pm 0.13$	7.82	$1.42 \pm 0.19 \pm 0.06$	1.82
208.0	$7.28 \pm 1.16 \pm 0.11$	7.82	$2.23 \pm 0.86 \pm 0.06$	1.82

	$e^+e^- \to qqe\nu(\gamma)$		$e^+e^- \to qq\mu\nu(\gamma)$		$e^+e^- \to qq\tau\nu(\gamma)$	
$\langle\sqrt{s}\rangle$ (GeV)	σ^{cco3}_{meas} (pb)	σ^{cco3}_{SM} (pb)	σ^{cco3}_{meas} (pb)	σ^{cco3}_{SM} (pb)	σ^{cco3}_{meas} (pb)	σ^{cco3}_{SM} (pb)
188.6	$2.29 \pm 0.14 \pm 0.03$	2.38	$2.25 \pm 0.14 \pm 0.04$	2.38	$2.82 \pm 0.22 \pm 0.07$	2.38
191.6	$2.95 \pm 0.37 \pm 0.04$	2.42	$2.61 \pm 0.36 \pm 0.05$	2.42	$1.87 \pm 0.48 \pm 0.05$	2.42
195.5	$2.36 \pm 0.20 \pm 0.03$	2.46	$2.14 \pm 0.20 \pm 0.08$	2.46	$3.44 \pm 0.34 \pm 0.08$	2.46
199.6	$2.21 \pm 0.20 \pm 0.03$	2.48	$2.05 \pm 0.20 \pm 0.07$	2.48	$2.75 \pm 0.32 \pm 0.07$	2.48
201.8	$2.26 \pm 0.30 \pm 0.03$	2.49	$2.62 \pm 0.33 \pm 0.05$	2.49	$2.45 \pm 0.47 \pm 0.06$	2.49
204.8	$2.78 \pm 0.23 \pm 0.04$	2.50	$2.30 \pm 0.22 \pm 0.04$	2.50	$2.63 \pm 0.33 \pm 0.07$	2.50
206.5	$2.56 \pm 0.17 \pm 0.03$	2.50	$2.28 \pm 0.17 \pm 0.04$	2.50	$2.92 \pm 0.27 \pm 0.07$	2.50
208.0	$2.02 \pm 0.61 \pm 0.03$	2.50	$3.59 \pm 0.81 \pm 0.05$	2.50	$2.43 \pm 1.03 \pm 0.06$	2.50

Table 5.7: *The measured CC03 cross section, σ^{cco3}_{meas}, for all W-pair final states, including all analysed 1998, 1999 and 2000 L3 data at average center-of-mass energies $< \sqrt{s} >$. The first uncertainty is statistical, the second systematic. The single-channel cross sections are derived from a global fit assuming a Standard Model W-decay but without constraining the W-decay branching ratios individually to their Standard Model prediction. The theoretical expectation for the Standard Model CC03 cross section, σ^{cco3}_{SM}, as calculated with the YFSWW3 Monte Carlo, is also displayed.*

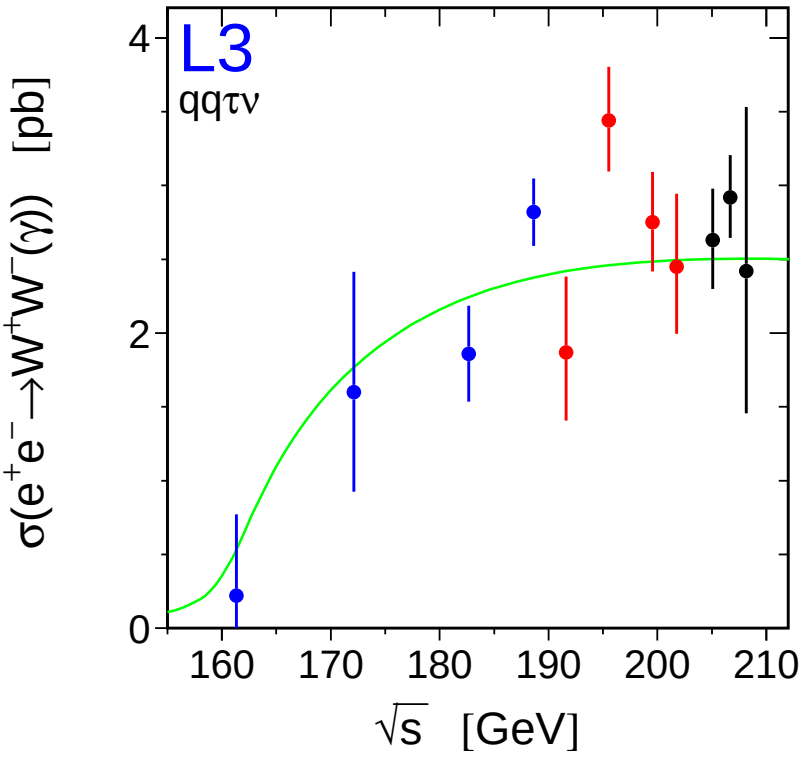

Figure 5.13: *The measured CC03 cross section for the process* $e^+e^- \to W^+W^- \to qq\tau\nu(\gamma)$ *as function of the average center-of-mass energy* $\sqrt{s}$*. The dots represent the L3 161-209 GeV data, the solid line represents the Standard Model expectation as calculated with YFSWW3 Monte Carlo. The error bars combine the statistical and systematic uncertainty, added in quadrature.*

The theoretical expectation for the Standard Model CC03 cross section, as calculated with the YFSWW3 Monte Carlo, is also given. The theoretical uncertainty on the YFSWW3 cross section is of the order of 0.5%.

The cross efficiency matrix is not diagonal and therefore, the five single-channel cross sections are correlated. The largest correlations appear between the $qqe\nu(\gamma)$ final state and the $qq\tau\nu(\gamma)$ final state (-10.3%) and between the $qq\mu\nu(\gamma)$ final state and the $qq\tau\nu(\gamma)$ final state (-17.6%). All other correlations are smaller than 1%.

5.5.3 Total WW cross section

The total WW cross section, σ_{WW}, is derived from the global maximum likelihood fit by replacing in Eq. 5.41 the single-channel cross section σ^j by the product $r^j\sigma_{WW}$ where r^j is related to the W-decay branching ratios

$$r^{qqqq} = \mid Br(W \to qq) \mid^2 \tag{5.43}$$

$$r^{qql\nu} = \; 2\; Br(W \to qq) \times Br(W \to l\nu) \tag{5.44}$$

for leptons with an identical flavour

$$r^{l\nu l\nu} = \mid Br(W \to l\nu) \mid^2 \tag{5.45}$$

for leptons with a different flavour

$$r^{l\nu l'\nu'} = \; 2\; Br(W \to l\nu) \times Br(W \to l'\nu') \tag{5.46}$$

The parameters of the fit are the total WW cross section and the W-decay branching ratios. A Standard Model W-decay into a quark-antiquark or a lepton-neutrino pair is assumed and so, W-decays into invisible non-Standard Model particles are excluded. The W-decay branching ratios are constrained individually to their Standard Model prediction.

Table 5.8 gives the measured CC03 cross section for the $qqqq(\gamma)$, $qql\nu(\gamma)$ and $l\nu l\nu(\gamma)$ W-pair final states, summed over all lepton species, and the total WW CC03 cross section for all analysed 1998, 1999 and 2000 L3 data. Charged-lepton universality is assumed. The measured WW cross sections are in good agreement with the Standard Model expectation.

The total W pair production cross section, σ_{WW}, of the $e^+e^- \to W^+W^- \to ffff(\gamma)$ process as function of the center-of-mass energy $\sqrt{s}$ is presented in Figure 5.14. Also the published measurements [93]-[94] at 161 GeV, 172 GeV and 183 GeV are displayed. The Standard Model expectation is calculated with YFSWW3 in the whole energy range and with RACOONWW for $\sqrt{s} \geq 170$ GeV. Both theoretical predictions are consistent and have a theoretical uncertainty varying from 2% in the threshold region down to 0.5% [95] for $\sqrt{s} \geq 170$ GeV where the LPA or DPA approach is used. The L3 data agree with both predictions.

The ratio of the measured WW cross section with respect to the Standard Model expectation, calculated with YFSWW3, is derived and the combined value for all energy points is

$$\mathcal{R}_{WW} = \frac{\sigma_{WW}^{meas}}{\sigma_{th}^{SM}} = 0.992 \pm 0.011 \pm 0.009 \pm 0.005 \tag{5.47}$$

where the first uncertainty is statistical, the second systematic and the third theoretical.

$\langle\sqrt{s}\rangle$(GeV)	σ^{qqqq}_{meas}	$\sigma^{qql\nu}_{meas}$	$\sigma^{l\nu l\nu}_{meas}$	σ^{WW}_{meas}	σ^{WW}_{SM}
188.6	7.17 ± 0.24 ± 0.12	7.19± 0.24 ± 0.	1.88 ± 0.16 ± 0.07	16.17 ± 0.37 ± 0.17	16.27
191.6	6.78 ± 0.56 ± 0.12	7.69± 0.61 ± 0.	1.66 ± 0.39 ± 0.07	16.11 ± 0.89 ± 0.17	16.57
195.5	6.92 ± 0.34 ± 0.11	7.58± 0.36 ± 0.	1.78 ± 0.24 ± 0.07	16.22 ± 0.54 ± 0.16	16.84
199.6	7.91 ± 0.36 ± 0.13	6.81± 0.35 ± 0.	1.75 ± 0.25 ± 0.06	16.49 ± 0.55 ± 0.17	17.02
201.8	7.09 ± 0.52 ± 0.12	7.34± 0.54 ± 0.	1.51 ± 0.34 ± 0.07	16.01 ± 0.81 ± 0.17	17.08
204.8	7.66 ± 0.37 ± 0.13	7.68± 0.39 ± 0.	1.58 ± 0.24 ± 0.05	17.00 ± 0.58 ± 0.17	17.12
206.5	8.07 ± 0.29 ± 0.13	7.6± 0.30 ± 0.	1.44 ± 0.18 ± 0.06	17.31 ± 0.45 ± 0.18	17.14
208.0	7.29 ± 1.16 ± 0.11	8.18± 1.21 ± 0.	2.23 ± 0.86 ± 0.06	17.52 ± 1.81 ± 0.17	17.15

Table 5.8: *The measured CC03 cross section for the $qqqq(\gamma)$, $qql\nu(\gamma)$ and $l\nu l\nu(\gamma)$ W-pair final states, summed over all lepton species, and the total WW cross section, including all analysed 1998, 1999 and 2000 L3 data for the center-of-mass energies $\langle\sqrt{s}\rangle$. Charged-lepton universality is assumed. The first uncertainty is statistical, the second systematic. The measured total WW cross section σ^{WW}_{meas} is derived from a global fit, assuming Standard Model W-decay branching ratios. The Standard Model CC03 cross section for W-pair production σ^{WW}_{SM} is calculated with the YFSWW3 Monte Carlo. The theoretical uncertainty on the YFSWW3 cross section is of the order of 0.5%.*

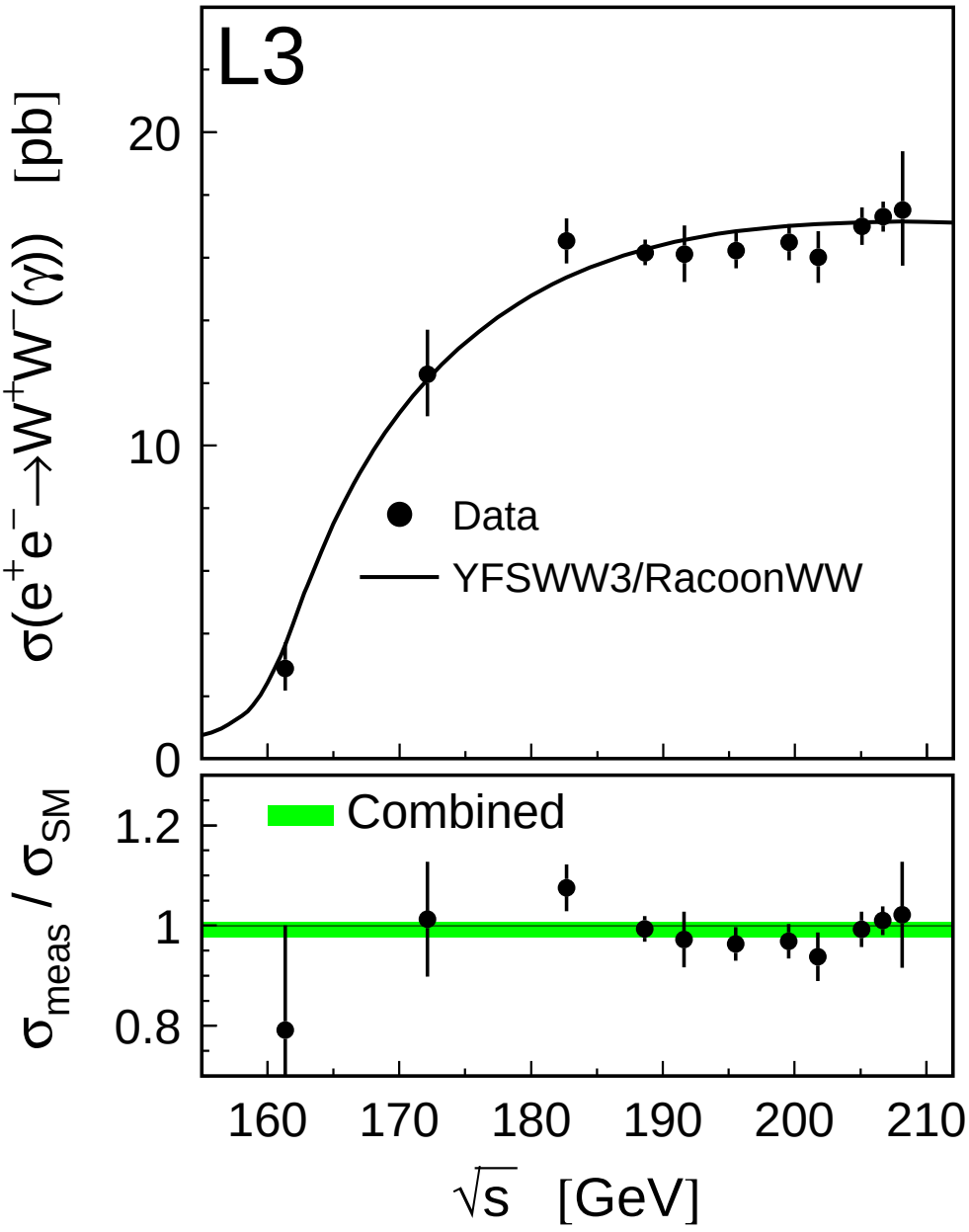

Figure 5.14: *The total WW cross section, σ_{WW}, of the $e^+e^- \to W^+W^- \to ffff(\gamma)$ process as function of the center-of-mass energy $\sqrt{s}$. The dots represent the L3 data, the solid line represents the Standard Model expectation as calculated with YFSWW3 in whole energy range and the RACOONWW for $\sqrt{s} \geq 170$ GeV. The error bars combine the statistical and systematic uncertainty added in quadrature. The lower plot shows the ratio R of the measured cross section with respect to the Standard Model expectation calculated with YFSWW3. The grey band gives the combined value with its total uncertainty $R = 0.992 \pm 0.015$*

Branching Ratio	Lepton Non-Universality	Lepton Universality	Standard Model
Br($W \to e\nu$) (%)	$10.78 \pm 0.29 \pm 0.13$	—	
Br($W \to \mu\nu$) (%)	$10.03 \pm 0.29 \pm 0.12$	—	
Br($W \to \tau\nu$) (%)	$11.89 \pm 0.40 \pm 0.20$	—	
Br($W \to l\nu$) (%)	—	$10.83 \pm 0.14 \pm 0.10$	10.83
Br($W \to qq$) (%)	$67.30 \pm 0.42 \pm 0.30$	$67.50 \pm 0.42 \pm 0.30$	67.51

Table 5.9: *The W-decay branching ratio with and without assumption of charged-lepton universality. Also the Standard Model prediction is shown. The first error is statistical, the second systematic.*

5.6 Measurement of the W-decay Branching Ratios

The W-decay branching ratios are derived from the global maximum likelihood fit simultaneously with the total WW cross section, and are determined both with and without the assumption of lepton universality for the charged current in W decay. First, the leptonic branching ratios are determined without assumption of charged-lepton universality, second, the hadronic branching ratio are obtained by constraining the sum of the hadronic and the three leptonic branching ratios to unity. Finally the hadronic and leptonic branching ratios are also derived assuming charged-lepton universality.

The leptons are assumed massless in the calculation which is a good approximation for the electron and muon, but doesn't hold anymore for the tau. The branching ratio for the $W \to \tau\nu$ is therefore corrected for the phase space corresponding to a massive tau. The correction is less than 0.1%.

The results presented in Table 5.9, include also the data taken at lower center-of-mass energies: $\sqrt{s} = 161 - 209$ GeV. Also the Standard Model prediction is shown. The first uncertainty is statistical, the second systematic. Also the correlations among the channels are taken into account. The probability to get a χ^2 larger than the observed one is 0.8%, which corresponds to 2.6 standard deviations. The latter value includes statistical and systematic correlations. The correlation coefficients between leptonic branching ratios are -0.016, -0.279 and -0.295 for $((e\nu)(\mu\nu))$, $((e\nu)(\tau\nu))$ and $((\mu\nu)(\tau\nu))$ respectively.

The W-decay hadronic branching ratios depend on the six elements V_{ij} of the Cabibbo-Kobayashi-Maskawa quark mixing matrix V_{CKM} [8] which relates the quark's weak interaction eigenstates to the quark's flavor or mass eigenstates

$$V_{CKM} = \begin{pmatrix} V_{ud} & V_{us} & V_{ub} \\ V_{cd} & V_{cs} & V_{cb} \\ V_{td} & V_{ts} & V_{tb} \end{pmatrix} \tag{5.48}$$

which do not involve the top quark [27]: V_{ud}, V_{us}, V_{ub}, V_{cd}, V_{cs} and V_{cb}.

From the relation

$$1/Br(W \to l\nu) = 3 + 3\ [1 + \alpha_S(M_W^2)/\pi]\ V^2, \tag{5.49}$$

using $\alpha_S = 0.119 \pm 0.002$ [96], the derived value of V^2 is

$$V^2 = \sum_{i=u,\ c;\ j=d,\ s,\ b} |V_{ij}|^2 = \ 2.002\ \pm\ 0.038\ (stat.)\ \pm\ 0.027\ (syst.) \tag{5.50}$$

The sensitivity is largest for the dominant diagonal elements of V_{ud} and V_{cs}. The diagonal element V_{ud}, studied in nuclear β-decay processes, is known much preciser than V_{cs} and therefore it's most interesting to derive a value for the element V_{cs}.
Using the current world-average values and the uncertainties on the other CKM elements [3] without constraining to unitarity, V_{cs} is

$$|\ V_{cs}\ | = \ 0.977\ \pm\ 0.020\ (stat.)\ \pm\ 0.014\ (syst.) \tag{5.51}$$

The statistical uncertainty contains the uncertainty on α_S and the other contributing CKM elements but is dominated by the statistical uncertainty on the W-decay branching ratios.

5.7 Systematic Uncertainties

The systematic uncertainties are summarised in Table 5.11. The uncertainty on the luminosity measurement and the systematics due to the limited Monte Carlo statistics affect all final states in common and are discussed first. The remaining sources of systematic uncertainty are of two categories: uncertainties in the detector response and modelling, and uncertainties in theoretical predictions. Both categories depend on the considered W-pair final state and influence the signal selection efficiency as well as the accepted background and consequently, the measured cross section.

5.7.1 Luminosity

The uncertainty on the luminosity measurement (Section 4.3) affects directly the measured W-pair cross section. A total uncertainty of 0.22 % is taken as systematic uncertainty [65].

5.7.2 Limited Monte Carlo statistics

The effect of the limited Monte Carlo statistics is estimated by varying the selection efficiency by its statistical uncertainty

$$\delta_{stat}(\epsilon) = \sqrt{\frac{\epsilon\ (1-\epsilon)}{N^{gen}}} \tag{5.52}$$

both for the signal and the background. The effect varies between 0.1% and 0.8% for the signal and between 0.2% and 1.6% for the background.

5.7.3 Detector modelling

Cut variation technique

The most important source of systematic uncertainty results from detector acceptance and resolution effects on the reconstructed variables used in the selection procedure. To assign the detector systematics, the cut variation technique is used. In this technique the relative change in the measured cross section as function of the selection cut position is monitored. The range of the cut variation is chosen such that it covers several times the resolution on the selection variable. Any change larger than the statistical accuracy is retained as a systematic uncertainty. Some examples of the cut variation are presented in Figure 5.15 for the $qq\tau\nu(\gamma)$ selection. The main contribution comes from variables related to the missing momentum. The systematic uncertainties due to the different selection cuts are added in quadrature to obtain the final systematic uncertainty. For the $qq\tau\nu(\gamma)$ final state, this gives is 2%. For the remaining W-pair final states, the effect varies between 1% and 2%, depending on the final state.

Jet and lepton reconstruction

The cuts on energy and angular variables of jets and leptons are influenced by the detector resolution and calibration which are propagated to the Monte Carlo samples in the detector simulation and reconstruction phase. As a cross-check to the results obtained with the cut variation technique, the dependence of the selection efficiency on an additional detector calibration and resolution is studied. The jet energy and angles are modified according to the maximal observed additional resolution and calibration obtained from the study of Z-peak events summarised in Table 4.2. The shift in efficiency $\Delta\epsilon$ is monitored as function of the center-of-mass energy $\sqrt{s}$. The result is presented in Figure 5.16 for the jet energy (Left) and the jet polar angle (Right).

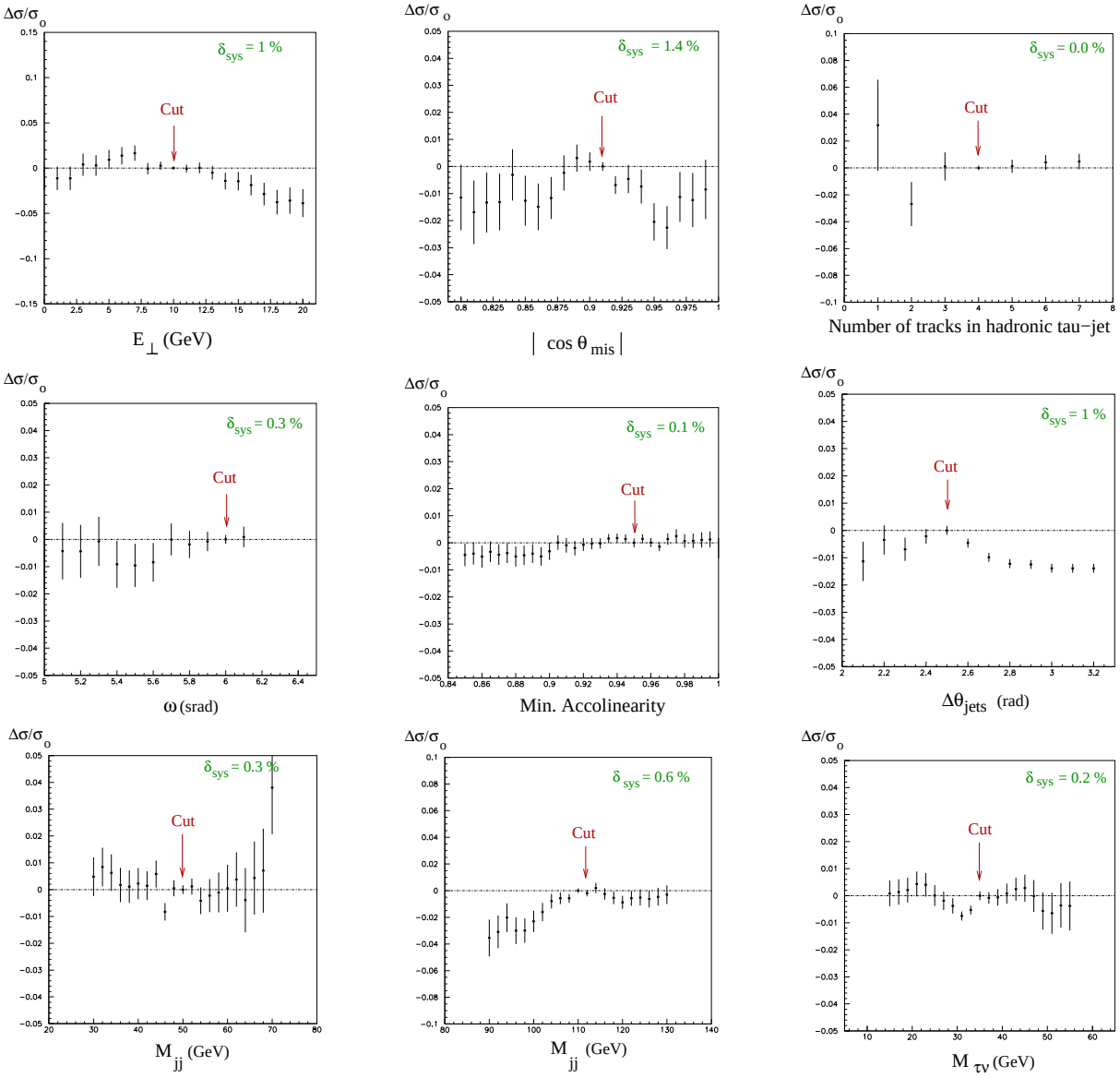

Figure 5.15: *The systematic uncertainty related to the detector modelling is studied by a cut variation technique. The relative change in the measured cross section as function of the selection cut position is monitored. The maximum deviation larger than the statistical accuracy is retained as a systematic uncertainty. The systematic uncertainties due to the different selection cuts are added in quadrature.*

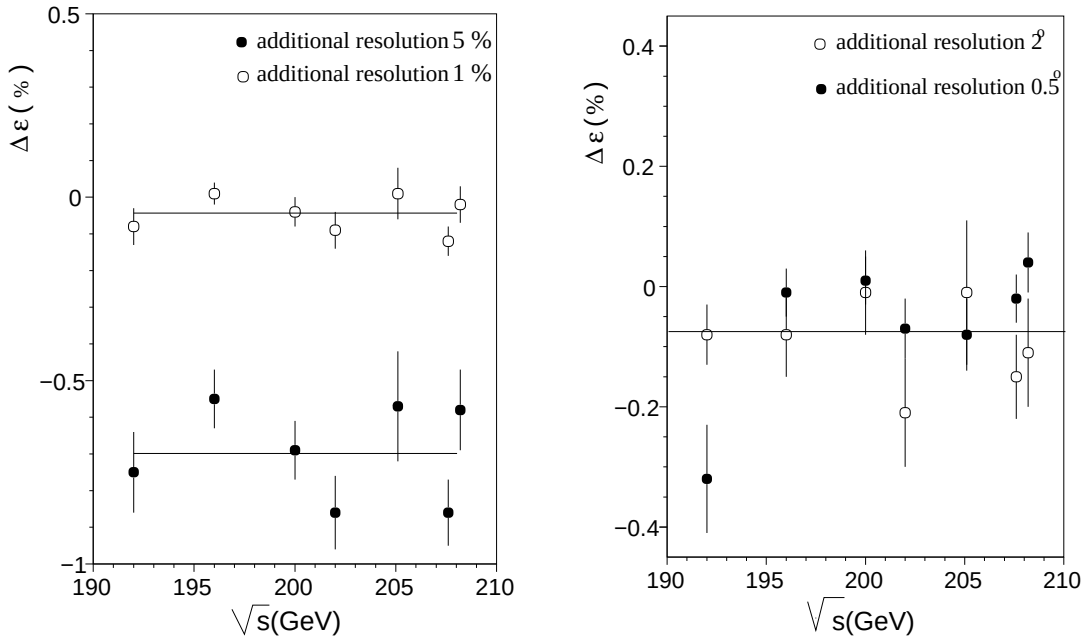

Figure 5.16: *Efficiency variation fo an additional resolution of 5% or 1%, for the jet energy (Left),* 2° *or* 0.5° *for the jet polar angle (Right), for the center-of-mass energy* $\sqrt{s}$ *corresponding to the 1999 and 2000 L3 data.*

For both variables the shift is $\sqrt{s}$-independent within the statistical accuracy. A fit with a constant for a 5% additional jet energy resolution is extrapolated to 4%, the corresponding maximal observed additional resolution. An upper limit of 0.1% on the associated systematic uncertainty is obtained. For the jet angles, the fit result for a 2° additional jet angle resolution is extrapolated to 0.5° and also leads to an upper limit of 0.1% on the associated systematic uncertainty.

The efficiency dependence on an additional calibration of the energy scale is presented in Figure 5.17 for the center-of-mass energies $\sqrt{s}$ corresponding to the 1999 and 2000 data separately. The extrapolation to the maximal observed additional shift of 50 MeV gives an upper limit of 0.1% for the systematic uncertainty associated to the energy calibration scale.

For the semi-leptonic and leptonic WW final states, similar checks are performed for the energy and angles of the leptons. For all WW final states, the studies show much smaller effects than that obtained from the cut variation technique.

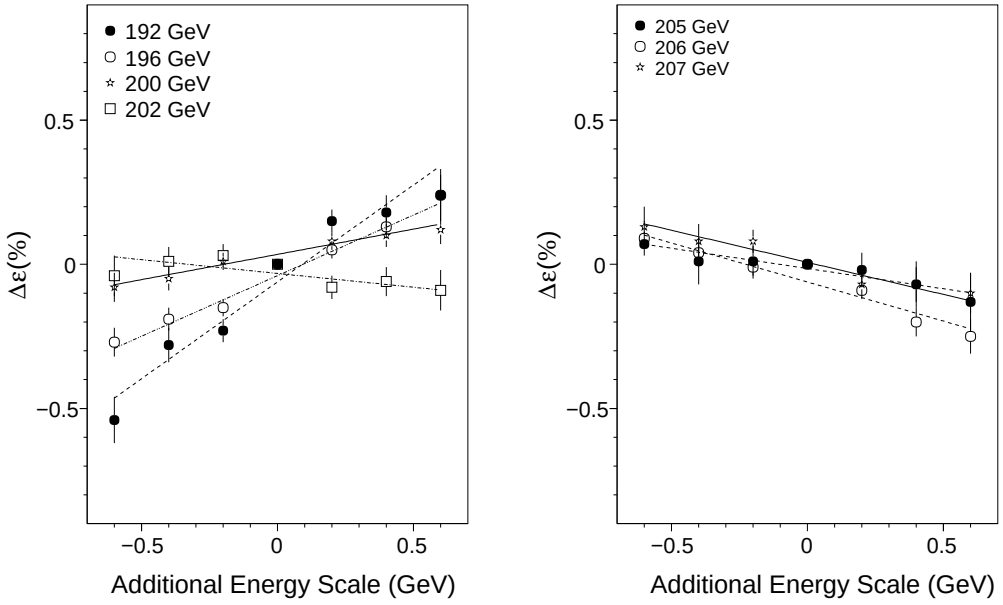

Figure 5.17: *The efficiency dependence on an additional jet energy calibration for the center-of-mass energies $\sqrt{s}$ corresponding to the 1999 L3 data (Left) and the 2000 L3 data (Right).*

5.7.4 Theoretical uncertainties

Hadronisation

The uncertainty in the hadronisation and fragmentation model, might influence the signal selection efficiency as well as the simulation of the $q\bar{q}(\gamma)$ background. The signal and background hadronisation systematics are estimated by comparing the selection efficiency obtained with different hadronisation model: PYTHIA [40], implemented in the KandY Monte Carlo, ARIADNE [42] and HERWIG [41]. As no model can be favorised a priori, the average difference relative to PYTHIA is retained as systematic uncertainty. For the signal hadronisation modelling, the effect varies between 0.5% and 1.2%, depending on the final state. The effect of the background hadronisation modelling is found negligble for the semi-leptonic channels. This is not the case for the $qqqq(\gamma)$ channel. As the rate of $q\bar{q}(\gamma)$ events with a four-jet topology is poorly reproduced by the available Monte Carlo programs, the $q\bar{q}(\gamma)$ Monte Carlo events are corrected by an event-by-event reweighting. The ratio data-Monte Carlo of the y_{34} variable in hadronic Z decays at $\sqrt{s}$=91 GeV is used as weight. This increases the expected $q\bar{q}(\gamma)$ background for a neural network output larger than 0.6 by 12.7 %. Half the effect of the y_{34} reweighting on the measured $qqqq(\gamma)$ cross section is assigned as systematic uncertainty related to the background hadronisation modelling and amounts to 0.9%.

Background cross sections

The theoretical uncertainty on the background cross section of the two photon events, the neutral-current four-fermion and two-fermion events of respectively 50%, 2% and 1% is propagated to the cross section measurement and the change in measured cross section is retained as systematic uncertainty. The observed change varies from 0.2% to 0.6%, depending on the final state.

ISR simulation

The effect of Initial State Radiation (ISR) is included in the KandY Monte Carlo up to $\mathcal{O}(\alpha^3)$ in the leading logarithm approximation. The systematic uncertainty due to the ISR modelling in KandY, and so, the missing higher order contributions, are evaluated by comparing the results when only ISR up to $\mathcal{O}(\alpha^2)$ is considered. The selection efficiency is re-evaluated on Monte Carlo signal events reweighted according to the ratio of the matrix elements

$$\mid \mathcal{M}[\mathcal{O}(\alpha^2)] \mid^2 / \mid \mathcal{M}[\mathcal{O}(\alpha^3)] \mid^2 \tag{5.53}$$

as provided by the KandY Monte Carlo generator. The effect on the measured cross section is found negligible. As a cross-check, the Monte Carlo events have also been reweighted to simulate a 10% increase of ISR photons of more than 100 MeV in energy or transverse momentum. Also here the effect is negligible. An upper limit of 0.01% is put on the systematic uncertainty related to the ISR simulation.

FSR simulation

Final State Radiation (FSR) is implemented in the KandY Monte Carlo through the PHOTOS package, based on a leading logarithm approximation. Hard non-collinear photon radiation is incurrately simulated by the package and a possible source of systematics. To estimate the effect, the Monte Carlo signal events have been reweighted to simulate a 50% increase of FSR photons with an energy exceeding 30 GeV. An effect on the measured cross section between 0.1% and 0.2% is observed, depending on the final state, and assigned as systematic uncertainty related to FSR simulation.

Virtual $\mathcal{O}(\alpha)$ corrections

The effect of the virtual $\mathcal{O}(\alpha)$ corrections is estimated by comparing the selection efficiencies obtained with the KandY program (LPA approach) with those obtained with the RacoonWW program (DPA approach). No significant effect is observed.

Final State Interactions

The effect of Final State Interactions (FSI), like Bose-Einstein correlations (BEC) and Color Reconnection (CR), explained in detail in Chapter 3, is analysed by comparing the selection efficiency obtained from the KandY Monte Carlo generator with and without the implementation of the FSI.

For the semi-leptonic channels, only intra W BEC between particles originating from the same W decay is relevant. The strength of intra W BEC is significant and in agreement with the one for the Z decays restricted to light-quarks and with the LUBOEI BE32 model [97] used as default in the L3 Monte Carlo simulations [57]. The inter W BEC between particles originating from different W decays are strongly disfavoured by the L3 data [56]. The effect of intra W BEC on the selection efficiency is found negligible within statistical accuracy and an upper limit of 0.01% is assigned as systematic.

To estimate a possible effect of inter W BEC on the measured $qqqq(\gamma)$ cross section, a quarter of the strenght expected in the BE32 model with full correlations, is simulated. Only a negligible change (0.03%) in measured cross section is observed.

The $qqqq(\gamma)$ final state has an additional source of systematics, related to the possiblility of Colour Reconnection (CR) between the hadronic systems. The influence of CR is evaluated by comparing different CR models: HERWIG [98], ARIADNE (model 1 and 2) [99] and PYTHIA [58] (model SKI with reconnection parameter $k = 0.6$). The observed average shift with respect to PYTHIA amounts to 0.1% and is taken a systematic uncertainty on the measured $qqqq(\gamma)$ cross section.

W mass and width

The values of the W mass and width, implemented in Monte Carlo simulations of the W-pair production, are obtained from theoretical predictions. They are represent also a potential source of systematics on the cross section measurement. The effect of these two parameters is studied by comparing Monte Carlo samples with different inputs for the mass and width of the generated W boson. As a first study, the KORALW Monte Carlo generated at $\sqrt{s} = 200$ GeV was used and the W mass was varied between 79.5 GeV and 81.2 GeV for a fixed W width ($\Gamma_W = 2.1$ GeV). The result is shown in Figure 5.18 (Left). Considering a mass shift of 40 MeV, the world average uncertainty on the W mass, gives an upper limit of 0.1%. Figure 5.18 (Right) shows the W width variation between 1.5 and 2.7 GeV for a fixed W mass ($M_W = 80.35$ GeV).

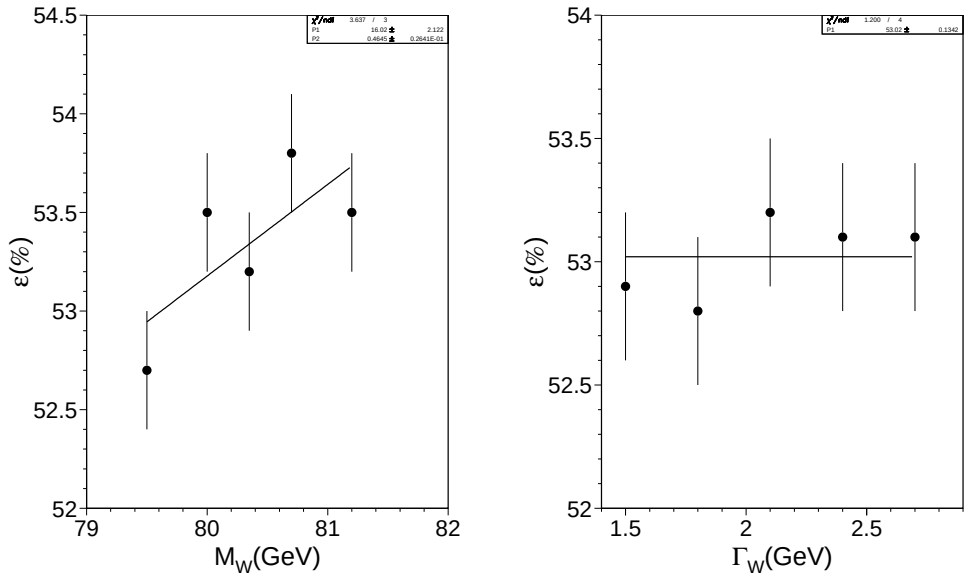

Figure 5.18: *The efficiency as function of the W mass (Left) and the W width (Right). The KORALW Monte Carlo at* $\sqrt{s} = 200$ *GeV was used to generate sample with different W mass and width values. The corresponding systematic uncertainty is smaller than 0.1%.*

Within the limited statistics, the efficiency is independent of the implemented width value. Extrapolation to a 60 MeV world average uncertainty on the W width, gives an upper limit of 0.1%.

The effect on the measured cross section is smaller than 0.3%, depending on the final state, and assigned as systematic uncertainty.

5.7.5 Combination

The systematic uncertainties on the cross section measurement from all identified sources, are summarised in Tabel 5.10 for $\langle\sqrt{s}\rangle$=206.5 GeV. The values at different center-of-mass energies are only marginally different. The correlations among sources of systematic uncertainty are taken into account. Depending on the source, the systematics are taken 100% correlated or uncorrelated among channels, except for the detector systematics which are taken 50 % correlated. All systematic uncertainties are added in quadrature to obtain a final systematic uncertainty on the cross section measurement.

Systematic Uncertainties on σ (%)					
Source	Final state				
	$qqqq(\gamma)$	$qqe\nu(\gamma)$	$qq\mu\nu(\gamma)$	$qq\tau\nu(\gamma)$	$l\nu l\nu(\gamma)$
Luminosity	0.22				
MC statistics (signal)	0.11	0.25	0.25	0.44	0.80
MC statistics (background)	0.22	0.23	0.28	0.75	1.57
Detector Modelling	1.00	1.00	1.20	2.00	2.00
Hadronisation (signal)	0.45	0.77	0.58	1.17	—
Hadronisation (background)	0.90	—	—	—	—
Background cross sections	0.40	0.21	0.22	0.40	0.59
W mass ($\pm$ 0.04 GeV)	0.06	0.03	0.03	0.10	0.27
W width ($\pm$ 0.06 GeV)	0.02	0.03	0.12	0.08	0.12
ISR simulation	< 0.01				
FSR simulation	< 0.01	0.21	0.17	0.08	0.21
Bose-Einstein effects	0.03	< 0.01			—
Colour Reconnection	0.19	—	—	—	—
TOTAL	1.46	1.36	1.43	2.52	2.76

Table 5.10: *The different sources of systematic uncertainty on the cross sect ion measurement. All sources of systematic uncertainty are added in quadrature to obt ain a final systematic uncertainty on the cross section measurement.*

5.8 Conclusions

5.8.1 W-pair production cross section

The L3 measurements are combined with published and priliminary results of the other LEP experiments to increase the statistical sensitivity. A global fit [100] is performed with as inputs, provided by the four LEP experiments: the center-of-mass energies, the corresponding integrated luminosities, the measured total W-pair production cross sections at the eight center-of-mass energies, with their statistical uncertainty and the full breakdown of systematics. From the statistical uncertainties, a 32 X 32 covariance matrix is constructed and used in a single, global χ^2-fit to the 32 measurements. The inter-experiment and inter-energy correlations are properly taken into account. All sources of systematics are taken fully uncorrelated among LEP experiments except the systematics related to the hadronisation modelling of the four-jet QCD background which is treated as fully correlated among LEP experiments and center-of-mass energies.

The LEP combined result for the total WW cross section as function of the center-of-mass energy $\sqrt{s}$ resented in Figure 5.19. The experimental data are compared to the theoretical calculations of the YFSWW3 and RACOONWW programs between 155 and 215 GeV for a $M_W = 80.35$ GeV. The common systematic uncertainty on the cross section is 0.6 %, dominated by the systematics related to the hadronisation modelling. The theoretical accuracy on the cross section calculation of the YFSWW3 and RACOONWW programs, presented by the blue band, is of the order of 0.7% at 170 GeV and decreases to 0.4 % above 200 GeV. In the threshold region a theoretical uncertainty of 2 % is assigned due to the accuracy on the implementation of the Improved Born Appoximation. A good agreement is found with the Standard Model prediction: the LEP combined ratio of the measured WW cross section with respect to the Standard Model expectation calculated with YFSWW3 is consistent with one

$$\mathcal{R}_{WW} = 0.993 \pm 0.009 \ (\chi^2/\mathrm{ndf} = 32.3/31) \tag{5.54}$$

This LEP combined ratio is the average of the ratios measured by the four LEP experiments at the eight center-of-mass energies. Only the 189-209 GeV LEP2 data are used because of the low statistics of the 161 and 172 GeV data samples and the high sensitivity of the cross section on the W mass in this threshold region.

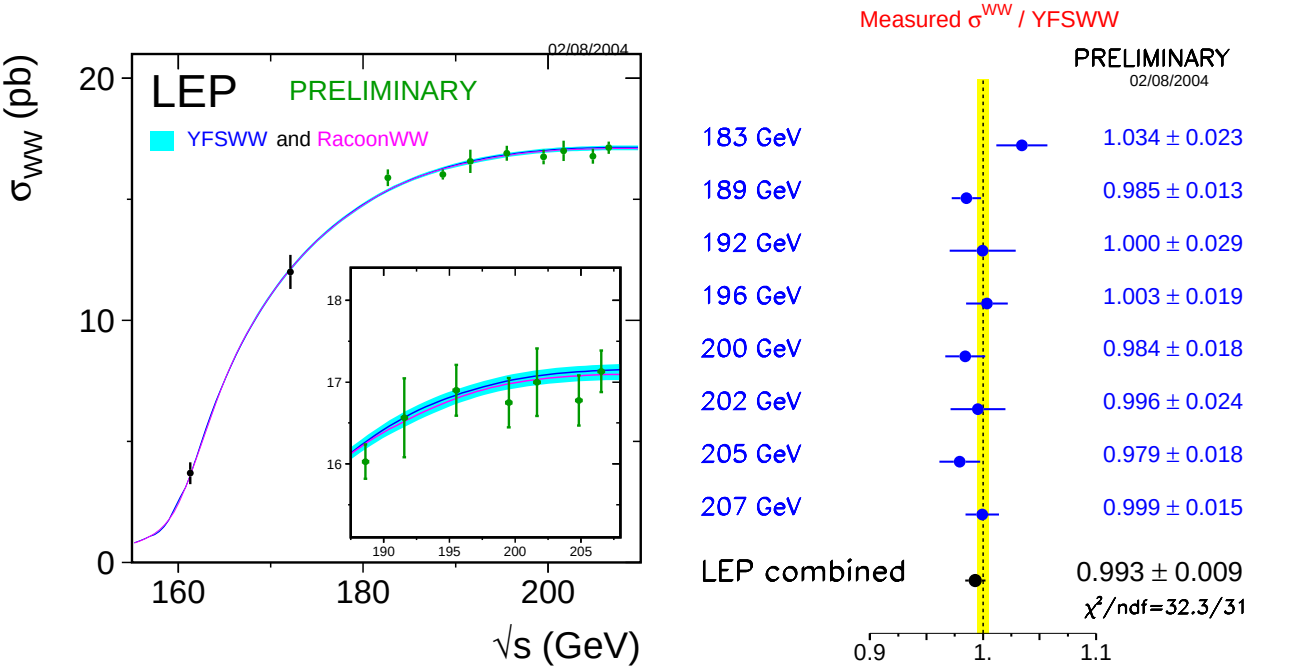

Figure 5.19: *Left: The LEP combined total WW cross section at CCO3 level as function of the center-of-mass energy $\sqrt{s}$. The dots represent the LEP 161-209 GeV data, the solid line represents the Standard Model expectation as calculated with YFSWW3 and RACOONWW programs. The error bars combine the statistical and systematic uncertainty added in quadrature.* Right: *The LEP combined ratio of the measured cross section with respect to the Standard Model expectation calculated with YFSWW3.*

The good agreement between the LEP data and the Standard Model prediction for the total W-pair production cross section gives a direct confirmation of the existence of the γWW- and ZWW vertices, predicted by the Standard Model. Figure 5.20 shows theoretical predictions for the total W pair production cross section as function of the center-of-mass energy $\sqrt{s}$ under different assumptions: the dashed line represents the prediction in absence of the ZWW vertex, while the dotted line shows the contribution for the t-channel ν-exchange process only. The t-channel ν-exchange dominates around the threshold energy. At higher energies, the contribution of the t-channel grows rapidly with increasing energy and would violate unitarity. According to the Standard Model the t-channel growth is compensated by the contribution of the s-channel γ/Z-exchange with such a coefficient that the cross section decreases with increasing center-of-mass energy. The dashed line represents the situation where there is only γ-exchange. In this case there would be unitarity violation too. Hence also the s-channel Z-exchange is necessary to obtain a finite cross section presented by the solid line.

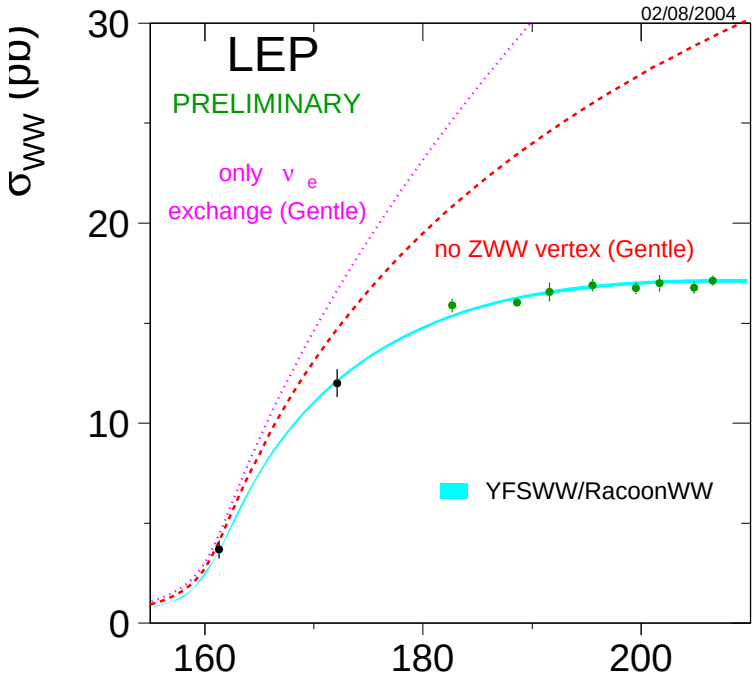

Figure 5.20: *The total W pair production cross section as function of the center-of-mass energy $\sqrt{s}$ for different theoretical predictions. The solid line gives the YFSWW3 and RACOONWW Standard Model expectation, the dashed represents the prediction in absence of the ZWW vertex, while the dotted line shows the contribution for the t-channel ν process for W-pair production only.*

5.8.2 W-decay branching ratios

The measured single-channel cross sections for the $e^+e^- \rightarrow W^+W^- \rightarrow ffff(\gamma)$ reaction of the four LEP experiments above 161 GeV are used to extract the W hadronic and leptonic branching ratios with and without charged-lepton universality. They are presented in Figure 5.21. The measured values for the W leptonic branching ratios agree with the Standard Model (χ^2/ndf = 15/11). The individual leptonic branching ratios are compatible with the averaged leptonic branching ratio within 2.4σ and so, confirm the hypothesis of charged-lepton universality. The branching ratio for the $W \rightarrow \tau\nu$ is about 3σ larger the average of branching ratio for the $W \rightarrow e\nu$ and $W \rightarrow \mu\nu$ decays due to the high cross section measured in the $qq\tau\nu(\gamma)$ channel. The LEP combined result for the W hadronic branching ratios is consistent with the Standard Model prediction.

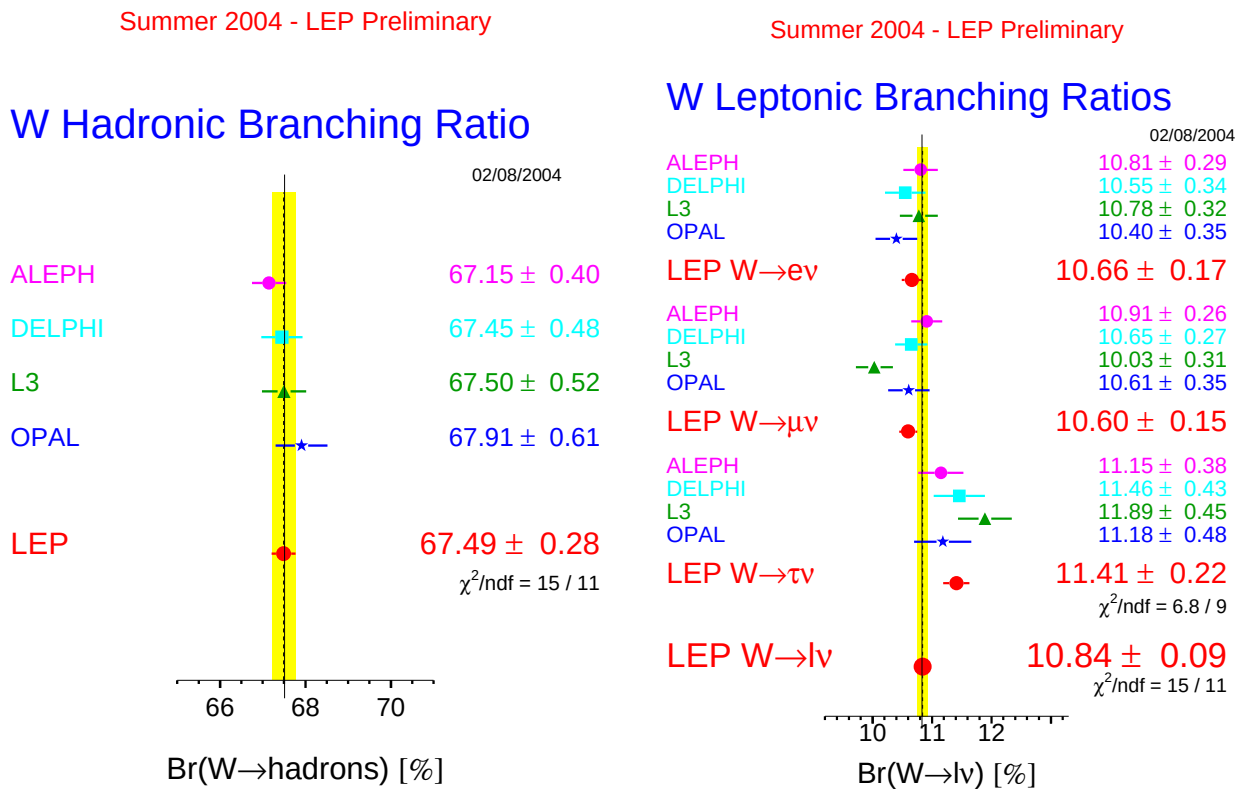

Figure 5.21: *The LEP combined W hadronic and leptonic branching ratio.*

The LEP combined value of V_{cs} is

$$V_{cs} = 0.976 \pm 0.014 \tag{5.55}$$

and is in agreement with the Standard Model. The uncertainty includes the contribution from the uncertainty on α_s and on the other CKM elements but is dominated by the experimental uncertainty on the measured branching ratios.

Chapter 6

Measurement of the W Spin Density Matrix

This chapter reports on the measurement of the single W Spin Density Matrix (SDM) from the L3 data, collected at center-of-mass energies $\sqrt{s} = 189 - 209$ GeV, and corresponding to a total integrated luminosity $\mathcal{L} = 629$ pb^{-1}. The leptonic W-decays from the semi-leptonic $qqe\nu(\gamma)$ and $qq\mu\nu(\gamma)$ W-pair events are considered in the analysis.

The Spin Density Matrix elements for the W boson alone, are called single W SDM elements and calculated for the W bosons produced in W pair production. They are determined as function of the W-boson production angle and are calculated from the angular distributions of the charged W-decay lepton in the restframe of the corresponding W-boson. A projection operator method is used. For direct comparison with theoretical models, a bin-to-bin correction is applied on the measured SDM elements which takes into account the background contamination and the limited detector acceptance and resolution.

First, the signal process and the WW phase space are defined. This is followed by the study of the resolution on the angular variables, used to calculate the SDM elements. Also the angular dependence of the selection efficiency and the purity is analysed.

Second, the SDM elements are defined from the theoretical point of view and the calculation from the experimentally measured angular distributions is explained. The most suitable binning for the bin-to-bin correction factors is searched for.

Finally, the experimental SDM elements are calculated and the $qqe\nu(\gamma)$ and $qq\mu\nu(\gamma)$ final states are combined. Several systematic checks are performed to identify possible sources of bias and the systematic uncertainties are listed. Tests on tree-level CPT- and CP-invariance are performed and the W-boson longitudinal and transverse helicity fractions are derived from the SDM analysis.

6.1 Signal Definition

In principle, one could use the three W-pair decay channels for the SDM analysis: the hadronic channel, the semi-leptonic channel and the purely leptonic channel.

- In the **hadronic channel**, four hadronic jets are produced, which makes the charge determination and hence, the distinction between fermion and antifermion very difficult. Also the assignment of the hadrons to the correct jet, i.e. the jet reconstruction, and the pairing of the jets into a W boson are not 100% efficient.
- The **semi-leptonic channel** is characterised by two hadronic jets and an isolated, high-energy lepton. Here the W charge is identified by the lepton charge. The distinction between quark and antiquark in the hadronic system remains impossible. The missing momentum due to the emission of one or more neutrinos escaping undetected, is derived by a kinematic fit based on the principle of energy-momentum conservation.
- In the **leptonic channel**, two isolated, high energy leptons are detected. Although the charge of the lepton is well measured, the missing momentum of at least two neutrinos leads to a two-fold ambiguity in the reconstruction of the W production angle. If the two leptons are taus this is even more problematic.

From the experimental point of view, the semi-leptonic final states $qqe\nu(\gamma)$ and $qq\mu\nu(\gamma)$ present the fewest ambiguities and are used in the SDM analysis.

Only the CCO3 set of diagrams with the additional restriction on the polar angle of the charged lepton

$$20^\circ < \theta_l^{gen} < 160^\circ \tag{6.1}$$

are considered as signal for the measurement of the single W SDM elements. An extrapolation to the full phase space is performed a posteriori assuming a Standard Model angular distribution for the charged lepton. The Monte Carlo generator used for the SDM analysis is the KandY four-fermion generator.

The selection of the $qqe\nu(\gamma)$ and the $qq\mu\nu(\gamma)$ final state is the same as for the measurement of the W-pair production cross section with two additional cuts. First, MIP muons are discarded. Second, an additional cut is applied on the reconstructed polar angle of the charged lepton: $\mid \cos\theta_l^{rec} \mid < 0.92$ to stay in the central region of the TEC where the track reconstruction quality is highest. Also the contribution of the single W component is reduced by this cut.

$\langle\sqrt{s}\rangle$ (GeV)	$\mathcal{L}$ pb^{-1}	ϵ_{sel} (%)	π (%)	N_{data}	N_{exp}
$qqe\nu(\gamma)$ final state					
188.6	176.8	81.7	95.6	322	334
191.6	29.8	80.7	95.5	68	62
195.5	84.1	81.0	95.4	159	163
199.6	83.3	78.9	95.7	145	159
201.8	37.1	79.9	96.3	68	72
204.8	79.0	78.8	95.7	168	151
206.5	130.5	78.7	95.6	252	249
208.0	8.6	80.2	96.0	14	16
$qq\mu\nu(\gamma)$ final state					
188.6	176.8	76.3	94.2	293	311
191.6	29.8	69.6	94.5	52	53
195.5	84.1	75.5	94.3	131	151
199.6	83.3	74.7	94.0	120	155
201.8	37.1	74.4	94.2	70	68
204.8	79.0	74.3	94.2	123	140
206.5	130.5	73.8	94.3	211	230
208.0	8.6	75.4	94.2	20	15

Table 6.1: *The selection efficiency and purity at each center-of-mass energy from 189 GeV to 209 GeV for the $qqe\nu(\gamma)$ and the $qq\mu\nu(\gamma)$ final state samples. Also the number of selected data events, N_{data}, and the number of expected events, N_{exp}, is mentionned.*

A total of 1205 $qqe\nu(\gamma)$ events and 1020 $qq\mu\nu(\gamma)$ events are selected while 1196 $qqe\nu(\gamma)$ and 1124 $qq\mu\nu(\gamma)$ events are expected from the Monte Carlo signal and background simulation. The selection efficiency at each energy point from 189 GeV to 209 GeV for the $qqe\nu(\gamma)$ and the $qq\mu\nu(\gamma)$ final state are given in Table 6.1. Also the number of observed data events, N_{data}, and the number of expected events, N_{exp}, is mentionned there.

6.2 Generated Angular Distributions

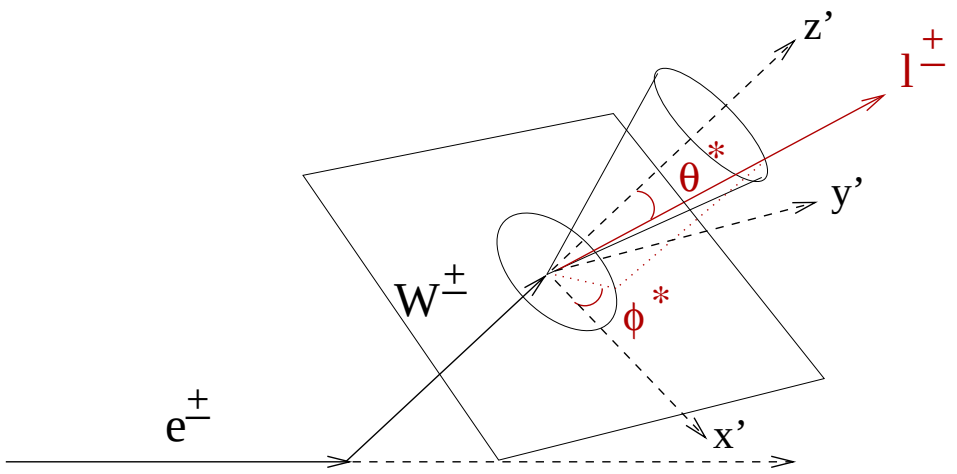

Figure 6.1: *For a given value of $\theta^\star$, the possible $\phi^\star$ values describe a cone with half opening angle $\theta^\star$ around the the direction of the W boson in the laboratory frame (z'-axis).*

Figure 6.2 shows the distribution of the cosine of the W^+ and W^- production angle, $\cos\theta_{W^+}$ and $\cos\theta_{W^-}$, the cosine of the polar, $\cos\theta^\star_{l^+}$ and $\cos\theta^\star_{l^-}$, and the azimutal angle, $\phi^\star_{l^+}$ and $\phi^\star_{l^-}$, of the W^+-decay antilepton and the W^--decay lepton in the corresponding W restframe. The solid line represents Standard Model distributions at $\sqrt{s}$=189 GeV for the $qql\nu(\gamma)$ signal as calculated with the KandY Monte Carlo.

From Figures (a) and (b) we clearly see that the W^- has a forward peaking angular distribution while the W^+ polar angle peaks to the backward region. At the threshold $\sqrt{s} = 2M_W \sim 161$ GeV, the W^- and W^+ bosons are produced almost isotropically, but they get more and more peaked in the forward, respectively backward direction with increasing center-of-mass energy. This is due to the dominant t-channel ν-exchange process which favours the scattering at low angle. The s-channel-exchange processes lead to a W-production angle which is symmetric relative to $\theta_W = \pi/2$.

The $\cos\theta^\star_l$ distributions (c)-(d) result from angular momentum conservation for a spin 1 W boson decaying into two spin 1/2 leptons and from the $V-A$ nature of the coupling of the W boson to the fermions that pushes the lepton in the W direction and the anti-lepton in the opposite direction.

The distributions of the angles $\theta^\star_l$ and $\phi^\star_l$, displayed in (e)-(f), are picturally presented in Figure 6.1. The polar angle $\theta^\star_l$ is defined as the angle between the charged W-decay lepton and the direction of flight of the W boson in the laboratory frame, here represented by the z'-axis. For a given value of $\theta^\star_l$, the spectrum of possible $\phi^\star_l$ values can be visualised as a cone with half opening angle $\theta^\star_l$ centered around the z'-axis. The possible $\phi^\star_l$ values describe a circle given by the projection of the cone on the (x',y')-plane.

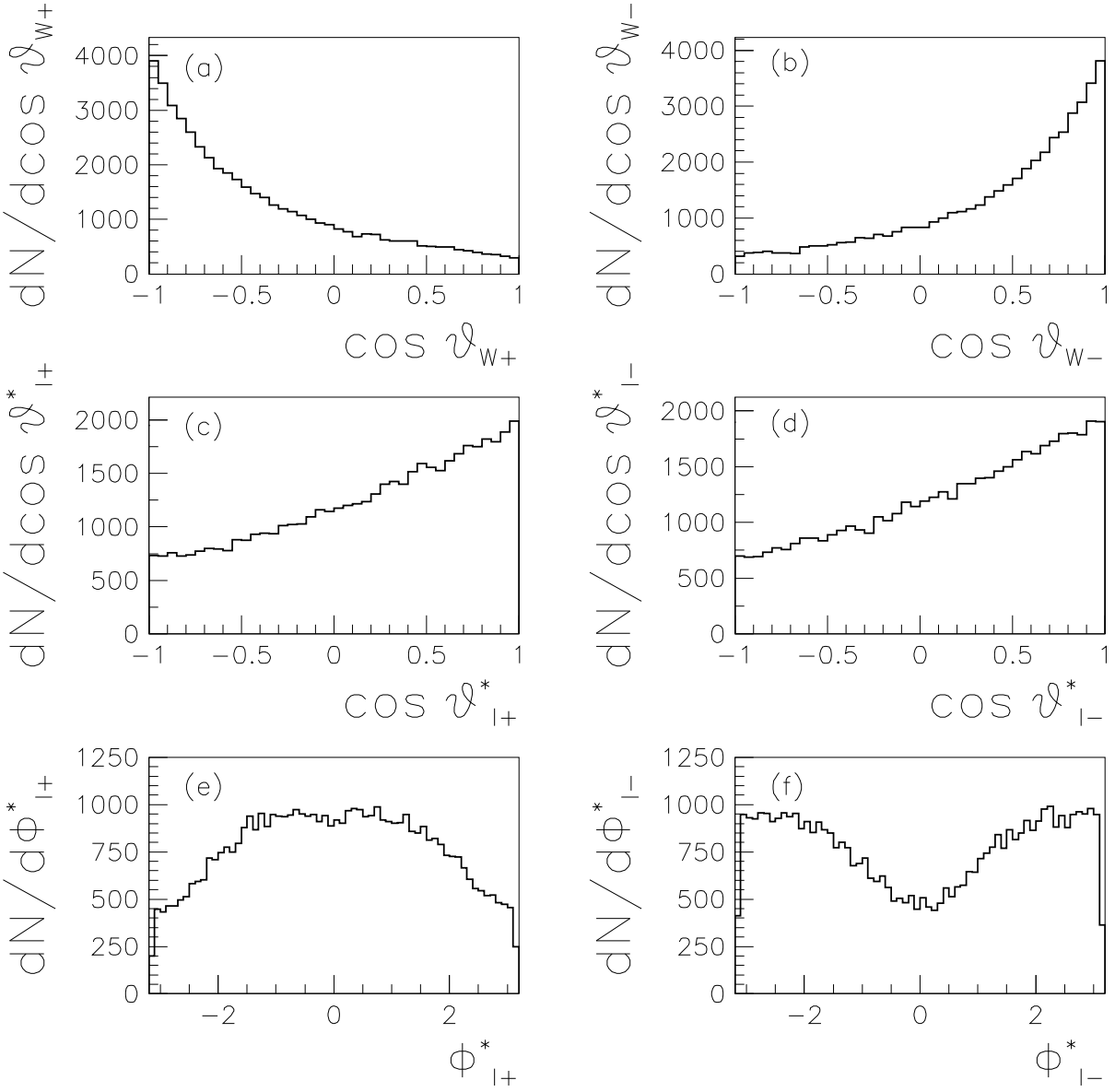

Figure 6.2: *The distribution of the cosine of the W^+ and W^- production angle (a)-(b), the cosine of the polar angle (c)-(d) and the azimutal angle (e)-(f) of the W^--decay lepton and the W^+-decay antilepton in the corresponding W restframe. The solid line represents Standard Model distributions at $\sqrt{s}$=189 GeV for the qql$\nu(\gamma)$ signal as calculated with the KandY Monte Carlo.*

Intuitively $\phi_l^\star$ expresses the angular separation between the lepton and the (e,W)-plane spanned by the x'- and the z'-axis ($\phi^\star$=0). Angular momentum conservation forces the lepton in the (e,W)-plane and so, small azimutal angles $\phi_l^\star$ are favoured. The shift with π between the $\phi_{l^+}^\star$ and $\phi_{l^-}^\star$ distributions is due to the opposite direction of the y'-axis in the W^+ restframe relative to the W^- restframe.

As the W^+ and W^- are emitted back-to-back, their direction of flight is exactly opposite and therefore the $\cos\theta_W$ distributions can be transformed into each other, or more general, the full angular information from W^+ and W^- decays can be combined assuming CPT-invariance: there is no difference between the physics of the W^+ and the W^- boson. By convention, the W^- boson is chosen as reference. The sign of the $\cos\theta_{W^+}$ distribution is changed

$$\cos\theta_{W^+} \rightarrow -\cos\theta_{W^+} \tag{6.2}$$

and, similarly, the $\phi_{l^+}^\star$ and $\phi_{l^-}^\star$ distributions are combined by a shift of π

$$\phi_{l^+}^\star \rightarrow \phi_{l^+}^\star + \pi \quad (\phi_{l^+}^\star < 0) \tag{6.3}$$

$$\phi_{l^+}^\star \rightarrow \phi_{l^+}^\star - \pi \quad (\phi_{l^+}^\star > 0) \tag{6.4}$$

The polar angles of the W^--decay lepton and the W^+-decay antilepton remain unchanged.

6.3 Measured Angular Distributions

Figures 6.3 and 6.4 represent the measured angular distributions for the L3 189-209 GeV data in the $qqe\nu(\gamma)$ and $qq\mu\nu(\gamma)$ final states compared to the corresponding luminosity averaged reconstructed angular distributions as predicted by the Standard Model KandY Monte Carlo . The angular distributions of the leptonic W^+ and W^- decays from different W-pair events are combined as discussed in the previous section and labelled as W^- distributions. A good agreement is obtained with the Standard Model Monte Carlo prediction for the $qqe\nu(\gamma)$ final state: $\chi^2/d.o.f. = 1.4$. For the $qq\mu\nu(\gamma)$ final state the agreement is less: $\chi^2/d.o.f. = 2.1$ This is due to the deficit of $qq\mu\nu(\gamma)$ events already mentionned in the cross section measurement (Chapter 5).

6.3.1 Angular resolution

For the single W SDM measurement, it was agreed within the LEP SDM working group to divide the W production angle distribution into 8 bins of equal size, $\Delta_{bin}(\cos\theta_W) = 0.25$. The resolution of the cosine of the W production angle, determined as

$$(\cos\theta_W)^{rec} - (\cos\theta_W)^{gen} \tag{6.5}$$

is presented in Figure 6.5 for the leptonically decaying W^+ and W^- bosons from the 189 GeV $qqe\nu(\gamma)$ (Left) and the $qq\mu\nu(\gamma)$ (Right) KandY Monte Carlo sample.

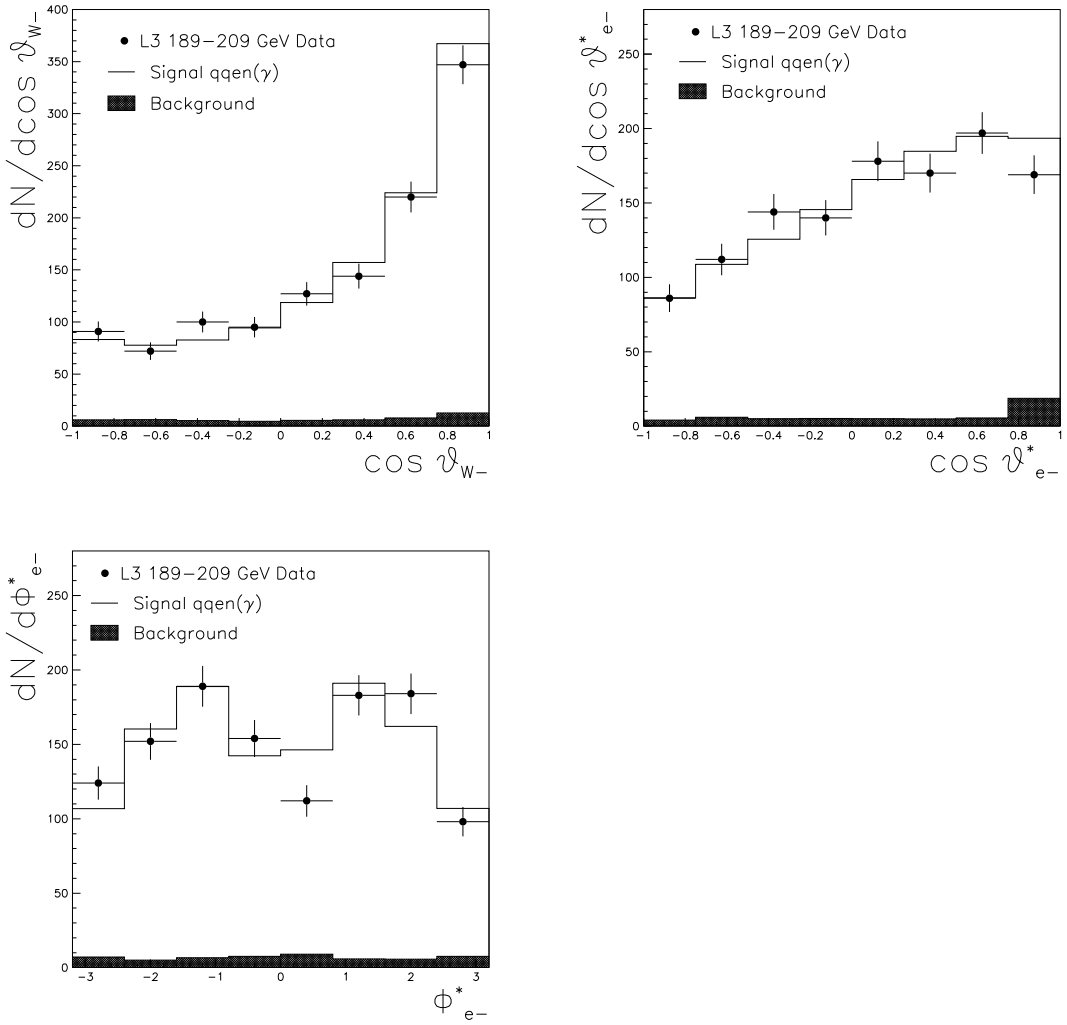

Figure 6.3: *The distributions of cosine of the polar angle of the W boson, the cosine of the polar angle and the azimutal angle of the electron in the W restframe. The dots represent the L3 189-209 GeV $qqe\nu(\gamma)$ data and the solid line the corresponding luminosity averaged reconstructed angular distribution for the $qqe\nu(\gamma)$ final state as predicted by the Standard Model KandY Monte Carlo. The black area gives the background contribution. The uncertainties are statistical only.*

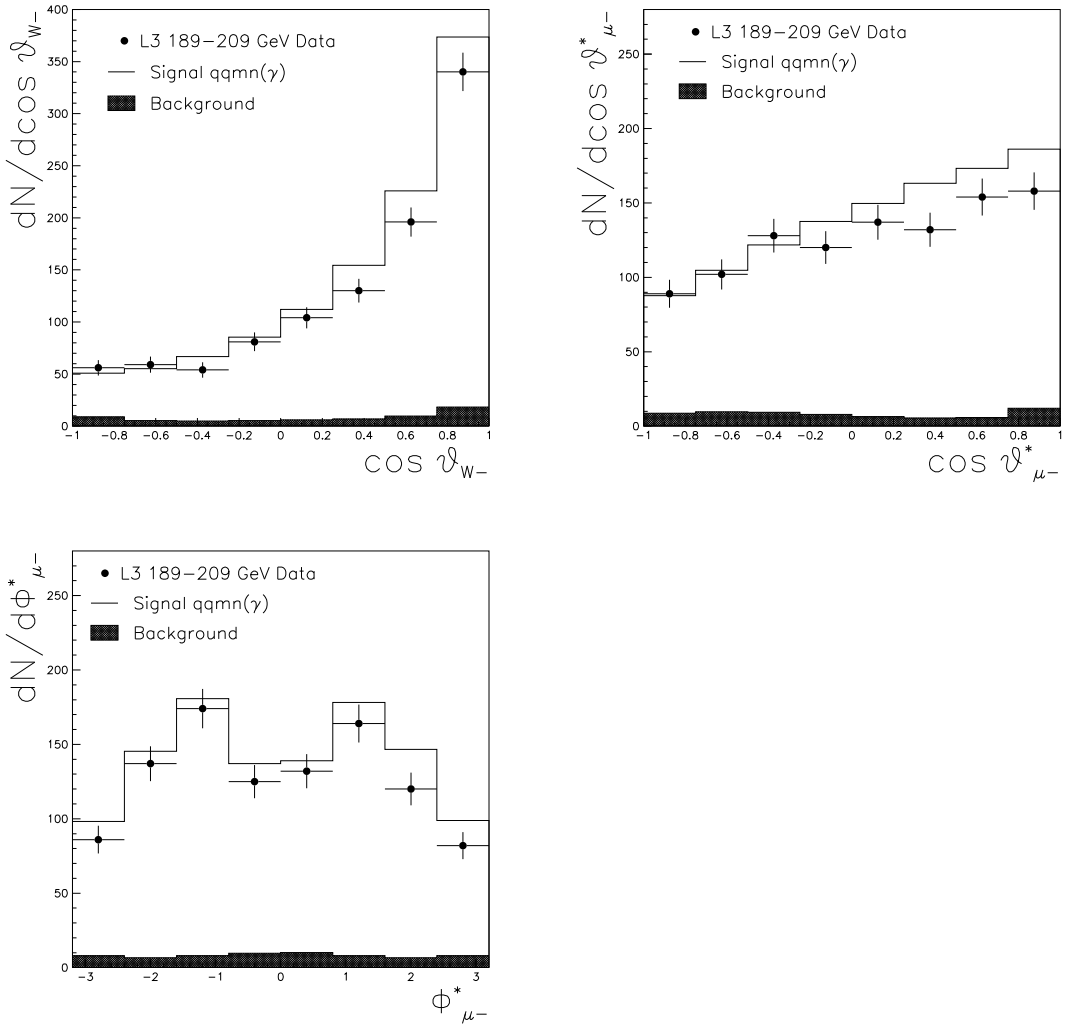

Figure 6.4: *The distributions of cosine of the polar angle of the W boson, the cosine of the polar angle and the azimutal angle of the muon in the W restframe. The dots represent the L3 189-209 GeV $qq\mu\nu(\gamma)$ data and the solid line the corresponding luminosity averaged reconstructed angular distribution for the $qq\mu\nu(\gamma)$ final state as predicted by the Standard Model KandY Monte Carlo. The black area gives the background contribution. The uncertainties are statistical only.*

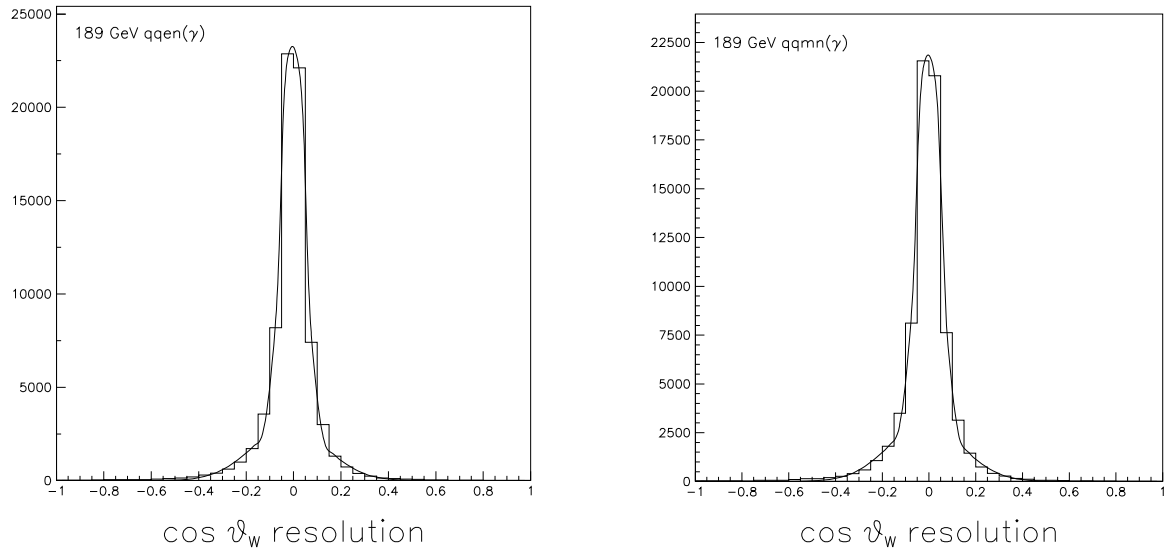

Final state	$qqe\nu(\gamma)$	$qq\mu\nu(\gamma)$
σ (1^{st} Gaussian)	0.05	0.05
σ (2^{nd} Gaussian)	0.16	0.16
χ^2/d.o.f.	40.4/40	39.7/40
σ (68% integral)	0.06	0.06
$R_{ev}([-0.125; 0.125])$	84.5%	84.6%

Figure 6.5: Above: *The resolution on the cosine of the W production angle for the* $qqe\nu(\gamma)$ *(Left) and the* $qq\mu\nu(\gamma)$ *(Right) final state. A fit is performed with a double Gaussian.* Below: *The fit results of the double Gaussian fit. The width of the integrated distribution including 68% of the events and the fraction of events included in the interval of width 0.25 centered on zero are mentionned.*

A fit is performed with a double Gaussian: the first Gaussian represents the peak region, the second Gaussian includes the queues. The width of the Gaussians, the width of the integrated distribution including 68% of the events and the fraction of events included in the interval of width 0.25 centered on zero, are listed in the Figure 6.5. About 84% of the events lie within the bin width of 0.25.

The resolution of $\cos\theta_l^\star$

$$(\cos\theta_l^\star)^{rec} - (\cos\theta_l^\star)^{gen} \tag{6.6}$$

and on $\phi_l^\star$

$$(\phi_l^\star)^{rec} - (\phi_l^\star)^{gen} \tag{6.7}$$

are shown in Figure 6.6 for the $qqe\nu(\gamma)$ final state together with the fit results of a double

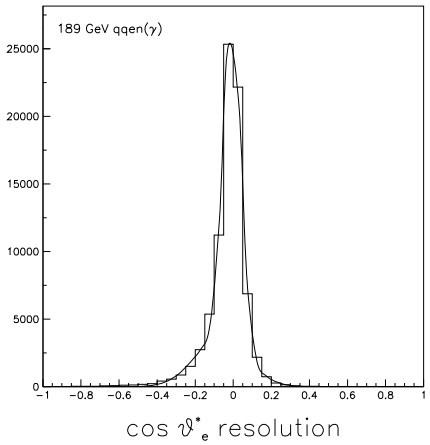

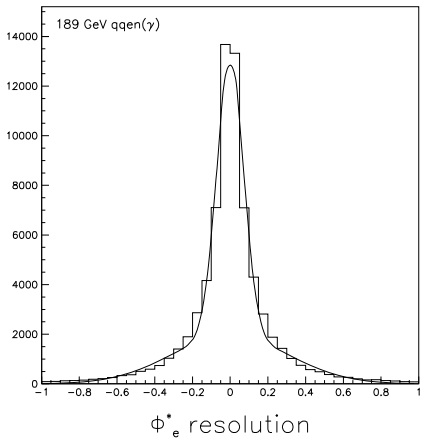

Final state	$qqe\nu(\gamma)$		$qq\mu\nu(\gamma)$	
	$\cos\theta_e^\star$	$\phi_e^\star$	$\cos\theta_\mu^\star$	$\phi_\mu^\star$
σ (1^{st} Gaussian)	0.05	0.07	0.06	0.07
σ (2^{nd} Gaussian)	0.13	0.31	0.17	0.34
χ^2/d.o.f.	39.0/38	54.4/40	31.7/39	47.4/40
σ (68% integral)	0.06	0.2	0.10	0.2
$R_{ev}([-0.125; 0.125])$	85.8%	-	76.3 %	-
$R_{ev}([-0.8$ rad$; 0.8$ rad$])$	-	93.7%	-	92.4%

Figure 6.6: Above: *The resolution on the cosine of the polar angle,* $\cos\theta_l^\star$ *(Left), and the azimutal angle* $\phi_l^\star$ *(Right) for the* $qqe\nu(\gamma)$ *final state.* Below: *The fit results of the double Gaussian fit for the* $qqe\nu(\gamma)$ *and the* $qq\mu\nu(\gamma)$ *final state. The width of the integrated distribution including 68% of the events and the fraction of events included in the interval of width 0.25 centered on zero are mentionned.*

Gaussian fit. When dividing also the $\cos\theta_l^\star$ and $\phi_l^\star$ distribution into 8 equal size bins, more than 68% of the events lie within the bin width of 0.25 and 0.8 rad respectively.

6.3.2 Selection efficiency and bin-to-bin migration

The total efficiency in a particular bin k of the angular distribution is the product of the selection efficiency and the migration in that bin

$$\epsilon_{tot}(k) = \epsilon_{sel}(k) \times M(k) \tag{6.8}$$

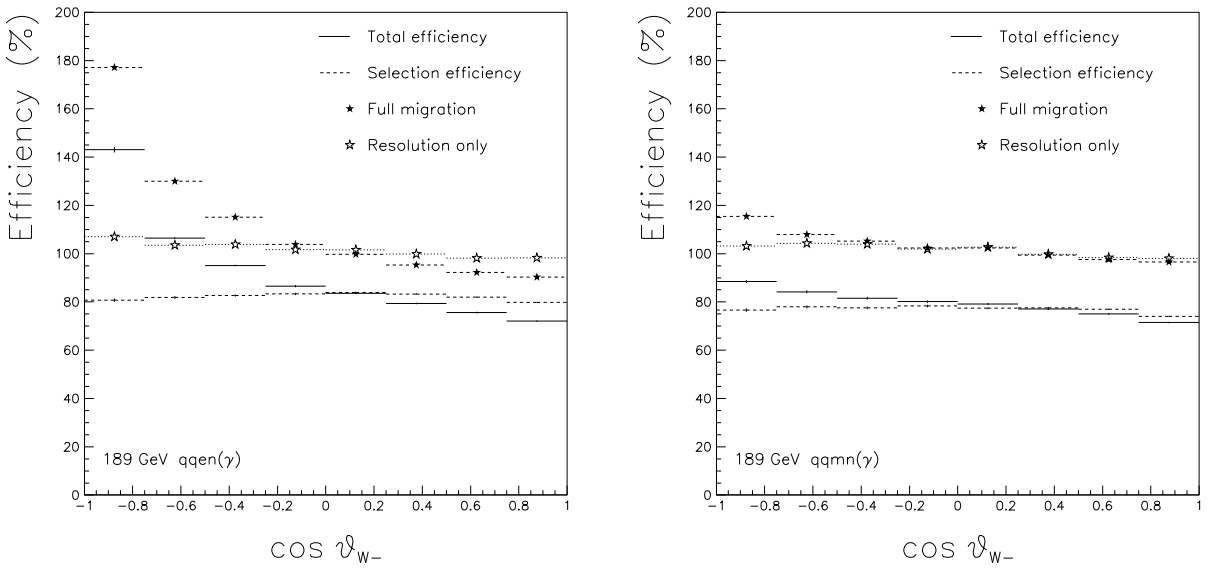

Figure 6.7: *The efficiency ϵ_{tot} (solid line) as function of $\cos\theta_{W^-}$ for the $qqe\nu(\gamma)$ (Left) and the $qq\mu\nu(\gamma)$ (Right) final state. The selection efficiency, ϵ_{sel}, is presented by the dashed line. The migration, M, including resolution effects and charge misreconstructions, and the migration due to resolution effects only, are also displayed as full stars and open stars respectively.*

where the selection efficiency in the bin k of the angular distribution is given by

$$\epsilon_{sel}(k) = \frac{N_{sign}^{gen+sel}(k)}{N_{sign}^{gen}(k)} \tag{6.9}$$

where N_{sign}^{gen} is the number of generated signal events and $N_{sign}^{gen+sel}$ the number of signal events generated and selected in the same bin after reconstruction. The migration in the bin k of the angular distribution is

$$M(k) = \frac{N_{sign}^{sel}(k)}{N_{sign}^{gen+sel}(k)} \tag{6.10}$$

where N_{sign}^{sel} represents the number of reconstructed signal events selected in the bin k, independently from the fact if they were also generated in that bin. The bin-to-bin migration is due to the limited detector resolution and charge misreconstructions. The limited detector resolution makes the reconstructed angles vary within the detector resolution around the lepton's true angle of emission. Consequently, some of the events, generated close to the boarder region of a bin, are reconstructed in a another bin. If the bin size is chosen large enough compared to the detector resolution, the migration concerns principally neighbouring bins.

On the contrary, the charge misreconstruction leads to a cross feed between symmetric bins: a generated W^- is reconstructed as W^+ and vice versa leading to a sign flip in the $\cos\theta_W$ distribution and a shift by π in the $\phi_l^\star$ distribution. A detailled study of the charge confusion is given in Appendix B.

The total efficiency is shown in Figure 6.7 for the $qqe\nu(\gamma)$ final state (Left) and the $qq\mu\nu(\gamma)$ final state (Right). The selection efficiency is constant in $\cos\theta_{W^-}$ except at small angles where the detector acceptance is lower. The variation in the total efficiency distribution is dominated by the migration due to charge misreconstructions. The probability for charge misreconstruction, called charge confusion probability, is much smaller for the $qq\mu\nu(\gamma)$ final state than for $qqe\nu(\gamma)$ final state as both the TEC and the muon chambers are used for the track reconstruction, leading to a better charge determination for muons than for electrons. This is clearly visible from the event migration matrix, presented in Figure 6.8 for the $qqe\nu(\gamma)$ (Left) and the $qq\mu\nu(\gamma)$ (Right) final state. The diagonal of the migration matrix contains all non-migrating events. When dividing the $\cos\theta_{W^-}$ distribution in 8 equal size bins, the percentage of events that are generated and reconstructed in the same $\cos\theta_{W^-}$ bin, is about 77.3% for the $qqe\nu(\gamma)$ final state and 76.4% for the $qq\mu\nu(\gamma)$ final state. The events with a wrongly reconstructed lepton charge are found in the opposite diagonal. The percentage of such events is about 7.7% for the $qqe\nu(\gamma)$ final state and 1% for the $qq\mu\nu(\gamma)$ final state. From Figure 6.7 the charge confusion appears to be largest in the backward direction. This asymmetry reflects the forward peaking of the $\cos\theta_W$ distribution of the W^-. Although the charge confusion probability is symmetric in the forward and backward direction, a relatively larger fraction of events gets affected by the charge misreconstruction and migrates backwards.

The efficiencies as function of $\cos\theta_l^\star$ and $\phi_l^\star$ are shown in Figure 6.9.

6.3.3 Four-fermion correction

A four-fermion correction is necessary to bring the data which has contributions from all four-fermion processes, to the CC03 signal definition used by theoretical predictions. The total 4f-corrected efficiency is given by

$$\epsilon_{tot}^{4f\to cco3}(k) = \frac{N_{sign\ 4f}^{sel}(k)}{N_{sign\ cco3}^{gen}(k)} \tag{6.11}$$

where $N_{sign\ cco3}^{gen}$ stands for the number of generated CC03 signal events and $N_{sign\ 4f}^{sel}$ the number of reconstructed signal four-fermion events selected in bin k. The total efficiency corrects for the detector acceptance through the selection efficiency and for the detector resolution through the inclusion of migration effects. The emission of ISR and FSR photons are corrected for at generator level.

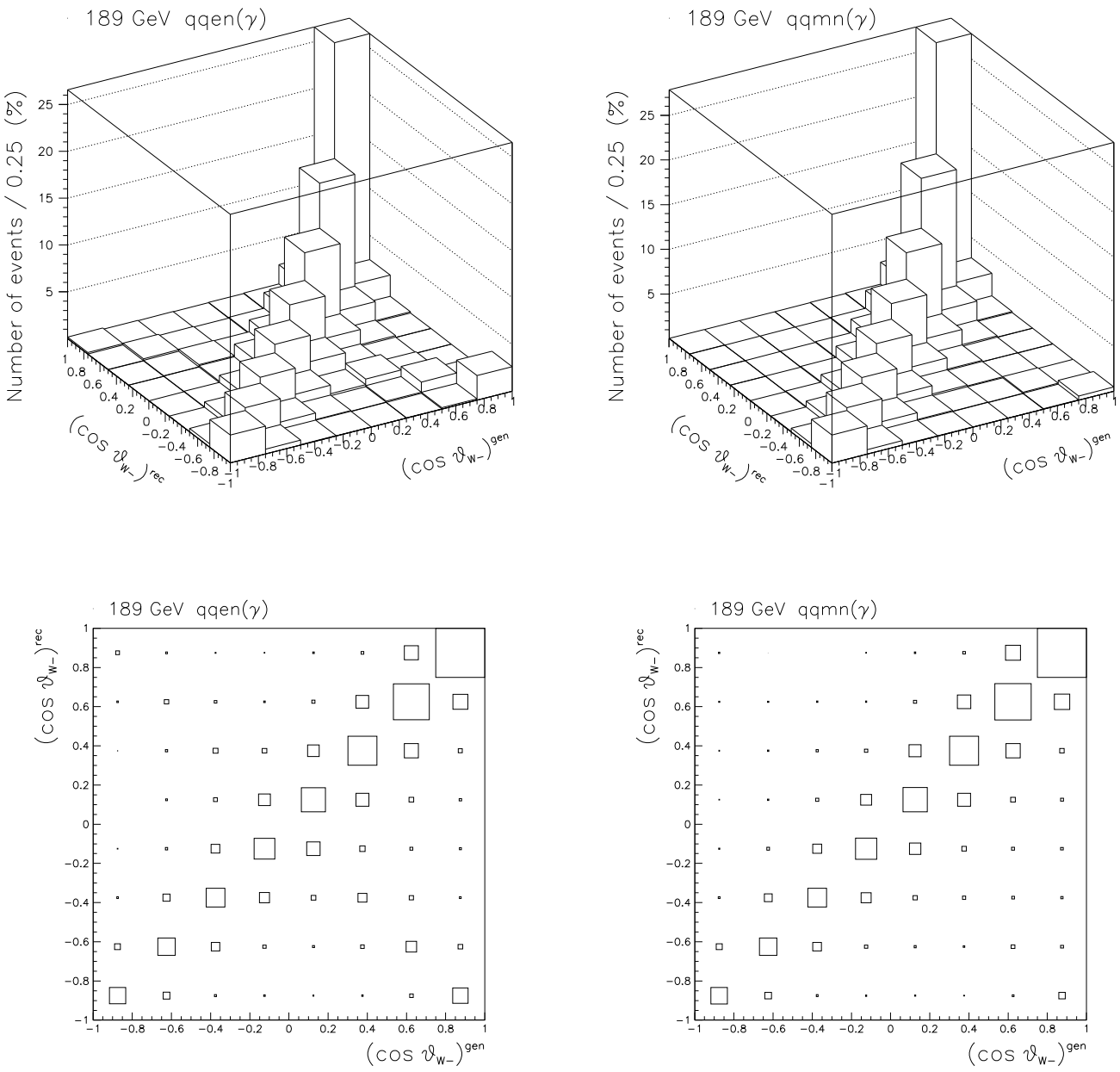

Figure 6.8: *The distribution of the reconstructed* $\cos\theta_{W^-}$ *versus the generated* $\cos\theta_{W^-}$ *and the event occupation in the* $(\cos\theta^{gen}_{W^-}, \cos\theta^{rec}_{W^-})$*-plane for the* $qq e\nu(\gamma)$ *(Left) and the* $qq\mu\nu(\gamma)$ *(Right) final state at* $\sqrt{s} = 189$ *GeV. The distribution is normalised to the total number of generated events.*

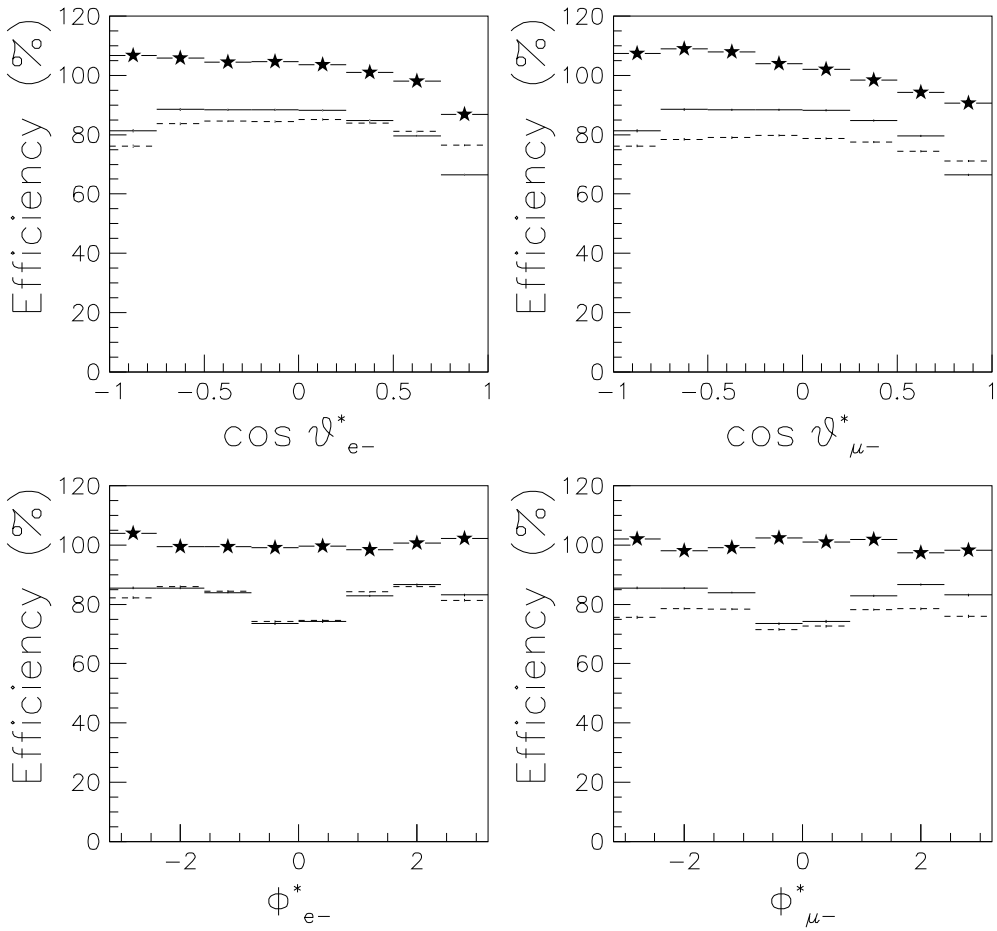

Figure 6.9: *The efficiency ϵ_{tot} (solid line) as function of $\cos\theta^\star_{l^-}$ (Above) and $\phi^\star_{l^-}$ (Below) for the $qqe\nu(\gamma)$ and $qq\mu\nu(\gamma)$ final state at $\sqrt{s} = 189$ GeV. The dashed line represents the selection efficiency. The migration, M, is displayed as full stars.*

ISR photons are recombined with the closest electron or positron and the boost due to ISR emission is properly taken into account to reestablish a e^+e^--center-of-mass system and to calculate the correct W-production angle. The FSR photons are recombined with the closest charged fermion. Both corrections are needed to compare with the theoretical calculations like the Bilenky-Gounaris prediction which do not include the effects of ISR and FSR (see Appendix A).

To increase the statistics, the total efficiency is assumed symmetric in $\phi^\star$

$$\epsilon_{tot}^{4f\to cco3}(\phi^\star) = \epsilon_{tot}^{4f\to cco3}(-\phi^\star) \tag{6.12}$$

which is a good approximation, as seen from Figure 6.9. The $\phi^\star$ distribution is symmetric on generator level for CC03 as well as for non-CC03 SM events.

6.3.4 Purity

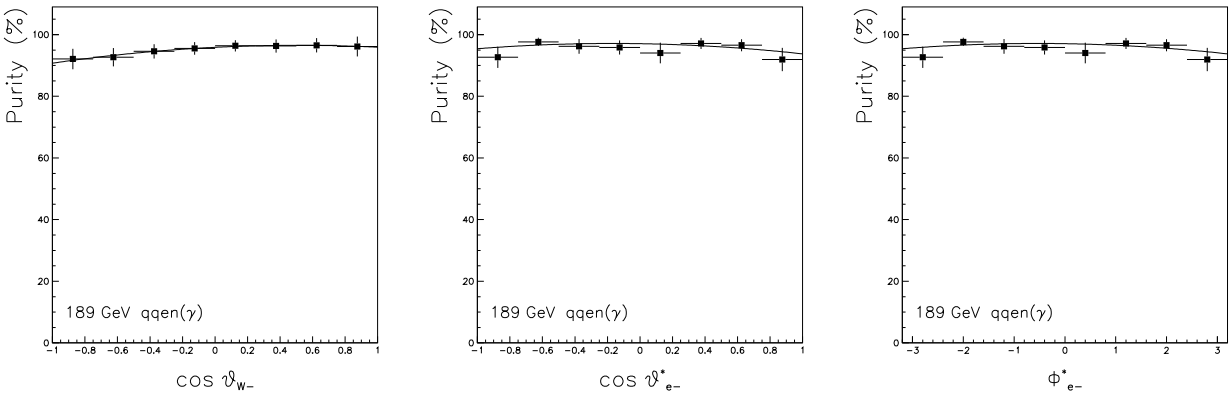

Figure 6.10: *The purity as function of* $\cos\theta_{W^-}$, $\cos\theta^\star_{e^-}$ *and* $\phi^\star_{e^-}$ *for the* $qqe\nu(\gamma)$ *final state at* $\sqrt{s} = 189$ *GeV. A polynomial fit of second order is performed to represent the purity.*

The purity in a particular bin k of the angular distribution is defined as

$$\pi(k) = \frac{N^{exp}_{sign\ 4f}(k)}{N^{exp}_{sign\ 4f}(k) + N^{exp}_{bkg}(k)} \tag{6.13}$$

where $N^{exp}_{sign\ 4f}$ is the number of expected signal events in the bin k and N^{exp}_{bkg} is the number of expected background events in the same bin.

For the $qqe\nu(\gamma)$ final state, the background is dominated by single W boson production and by the production of W-pairs decaying into a $qq\tau\nu(\gamma)$ final state, followed by the decay $\tau \to e\nu_e\nu_\tau$. The non-W background consists of ZZ-, Zee- and $q\bar{q}\gamma$ production. The $qq\mu\nu(\gamma)$ final state is also affected by the production of W-pairs decaying into the $qq\tau\nu(\gamma)$ final state and with $\tau \to \mu\nu_\mu\nu_\tau$. The non-$W$ background consists of ZZ- and $q\bar{q}\gamma$ production. For both channels, the two-photon background was found negligible. Except for the $q\bar{q}\gamma$ background, generated by the KK2f Monte Carlo, all four-fermion backgrounds are generated by the KandY generator.

The purity as function of $\cos\theta_{W^-}$, $\cos\theta^\star_{e^-}$ and $\phi^\star_{e^-}$ is shown in Figure 6.10 for the $qqe\nu(\gamma)$ final state at $\sqrt{s} = 189$ GeV. A fit is performed with a second order polynomial. The purity distribution is uniform over a large range. It decreases in the backward region where the single W background contamination is concentrated.

In contrast to the cross section measurement, the non-CCO3 process is not considered as background in the definition of the purity, but corrected for as a background through the definition of the total efficiency.

A fraction of the particles generated in the very forward-backward direction, are reconstructed but escape into the beampipe. While the purity remains finite, the selection efficiency tends to zero in this region. The restriction to the visible part of the detector, ensured by the signal definition, solves the problem of diverging correction factors.

6.4 The Single W SDM Elements

The two-particle joint SDM elements are defined as [101]

$$\rho_{\tau_1\tau_1'\tau_2\tau_2'}(s,\cos\theta_W) \equiv \frac{\sum_\lambda F^\lambda_{\tau_1\tau_2}\ (F^\lambda_{\tau_1'\tau_2'})^\star}{\sum_{\lambda,\tau_1,\tau_2}|F^\lambda_{\tau_1\tau_2}|^2}\ , \tag{6.14}$$

where $F^\lambda_{\tau_1\tau_2}$ is the helicity amplitude for the production of a W-pair with helicities τ_1 and τ_2. The helicity amplitudes for W-pair production are calculated analytically using the Bilenky-Gounaris formalism [101, 102] and explained in detail in Appendix A.

The single W SDM elements are obtained by summation over all possible helicities of one of the W bosons, by convention the W^+,

$$\rho^{W^-}_{\tau_1\tau_1'}(s,\cos\theta_{W^-}) \equiv \sum_{\tau_2}\rho_{\tau_1\tau_1'\tau_2\tau_2}(s,\cos\theta_{W^-}) \tag{6.15}$$

and constitute a 3 X 3 complex matrix

$$\begin{pmatrix} \rho_{++} & \rho_{+-} & \rho_{+0} \\ \rho_{-+} & \rho_{--} & \rho_{-0} \\ \rho_{0+} & \rho_{0-} & \rho_{00} \end{pmatrix} \tag{6.16}$$

The single W SDM elements are constrained by Hermiticity

$$\rho^{W^-}_{\tau\tau'} = (\rho^{W^-}_{\tau'\tau})^\star \tag{6.17}$$

and are normalised to unity

$$\sum_\tau \rho^{W^-}_{\tau\tau} = 1 \tag{6.18}$$

The diagonal elements of the single W SDM are real and express the probability to produce a W^- with a transverse polarisation (ρ_{++} and ρ_{--}) or with a longitudinal polaristation (ρ_{00}). The off-diagonal elements measure the interference between different W helicity amplitudes. They differ from zero if the W boson is produced in a linear superposition of helicity states, as predicted by the Standard Model, but would be zero for a W boson produced in a definite helicity state. Figure 6.11 shows the tree-level Standard Model prediction for the single W SDM elements as function $\cos\theta_{W^-}$ for the W^- boson at $\sqrt{s} = 189$ GeV.
The SDM elements for the W^+ boson are obtained by CPT-invariance

$$\rho^{W^+}_{\tau\tau'} = (\rho^{W^-}_{-\tau-\tau'})^\star \tag{6.19}$$

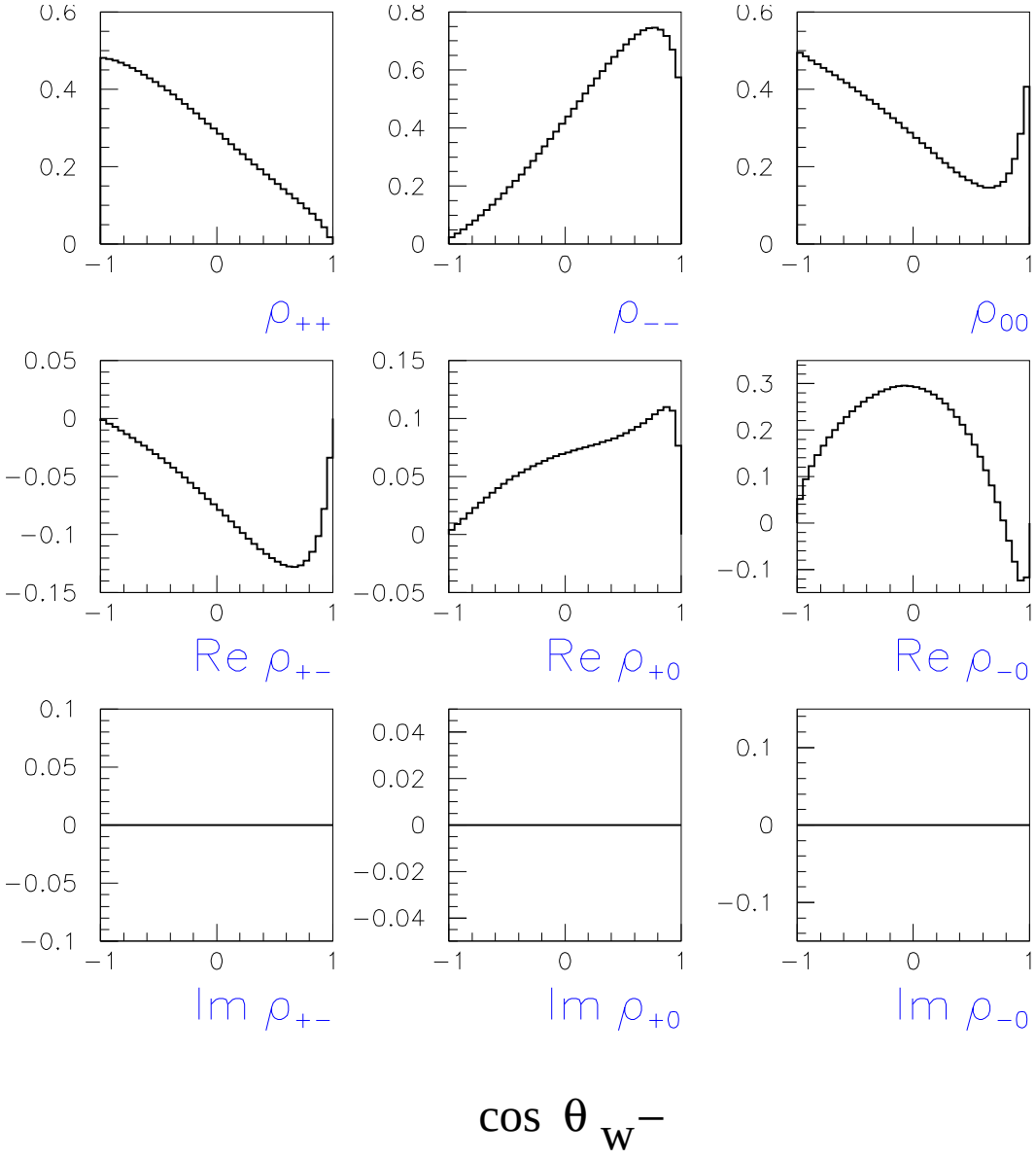

Figure 6.11: *The tree-level Standard Model prediction for the single W SDM elements for the W^- boson as function $\cos\theta_{W^-}$ at $\sqrt{s} = 189$ GeV. The SDM elements are calculated analytically using Bilenky-Gounaris formalism [101, 102].*

6.5 Measurement of the Single W SDM

The single W SDM elements are obtained from the angular distributions of the polar angle of the W boson (θ_W), the polar decay angle of the lepton ($\theta_l^\star$) and its azimuthal decay angle ($\phi_l^\star$) in the restframe of the corresponding W boson.

For the $W^- \to l^-\bar{\nu}_l$ decay, the single W SDM elements are related to the three-fold differential cross section

$$\frac{d^3\sigma(e^+e^- \to W^+W^- \to W^+\ l^-\bar{\nu}_l)}{d\cos\theta_{W^-}\ d\cos\theta^\star_{l^-}\ d\phi^\star_{l^-}} = BR(W^- \to l^-\bar{\nu}_l)(\frac{3}{8\pi})^2\ \frac{d\sigma(e^+e^- \to W^+W^-)}{d\cos\theta_{W^-}}$$
$$\times \sum_{\tau\tau'} \rho^{W^-}_{\tau\tau'}(s, \cos\theta_{W^-})\ D_{\tau\tau'}(\theta^\star_{l^-}, \phi^\star_{l^-}) \tag{6.20}$$

where the D-functions $D_{\tau\tau'}(\theta^\star_{l^-}, \phi^\star_{l^-})$ describes the angular distribution of the lepton for a given W-helicity. As the leptons in the final state are relativistic and the lepton masses are negligible relative to the W mass, the left-and right- handed chiral states originating from the weak interaction can be approximated by the left- and right-handed helicity states. In this approximation, the Wigner-Eckart theorem gives as expression for the decay functions

$$D_{\tau\tau'}(\theta^\star, \phi^\star) = L_\tau(\theta^\star, \phi^\star)\ L^\star_{\tau'}(\theta^\star, \phi^\star) \tag{6.21}$$

with

$$L_{-1}(\theta^\star, \phi^\star) = \frac{1}{\sqrt{2}}(1 + \cos\theta^\star)e^{-i\phi^\star} \tag{6.22}$$

$$L_0(\theta^\star, \phi^\star) = -\sin\theta^\star \tag{6.23}$$

$$L_{+1}(\theta^\star, \phi^\star) = \frac{1}{\sqrt{2}}(1 - \cos\theta^\star)e^{+i\phi^\star} \tag{6.24}$$

and are related to the rotation matrix for a spin 1 particle. The W-decay functions $D_{\tau\tau'}$ can be inverted to isolate an helicity state. The correponding projection operators [102], $\Lambda^{W^-}_{\tau\tau'}$, are applied on the angular distribution of the lepton to project out the information about the helicities of the W boson. The single W SDM element $\rho^{W^-}_{\tau\tau'}$ is given by

$$\rho^{W^-}_{\tau\tau'}(s, \cos\theta_{W^-}) = \frac{1}{BR(W^- \to l^-\bar{\nu}_l)}\ \frac{1}{\frac{d\sigma(e^+e^- \to W^+W^- \to W^+\ l^-\bar{\nu}_l)}{d\cos\theta_{W^-}}}$$
$$\int \frac{d^3\sigma(e^+e^- \to W^+W^- \to W^+\ l^-\bar{\nu}_l)}{d\cos\theta_{W^-}\ d\cos\theta^\star_{l^-}\ d\phi^\star_{l^-}}\ \ \Lambda^{W^-}_{\tau\tau'}(\theta^\star_{l^-}, \phi^\star_{l^-})\ d\cos\theta^\star_{l^-}\ d\phi^\star_{l^-} \tag{6.25}$$

A similar relation is obtained for the $W^+ \to l^+\nu_l$ decay.
The projection operators are

$$\Lambda^{W^-}_{\pm\pm} = \Lambda^{W^+}_{\mp\mp} = \frac{1}{2}(5\cos^2\theta^\star_l \mp 2\cos\theta^\star_l - 1) \tag{6.26}$$

$$\Lambda^{W^-}_{00} = \Lambda^{W^+}_{00} = 2 - 5\cos^2\theta^\star_l \tag{6.27}$$

$$\Lambda^{W^-}_{+-} = \Lambda^{W^+}_{+-} = 2e^{-2i\phi^\star_l} \tag{6.28}$$

$$\Lambda^{W^-}_{\pm 0} = -(\Lambda^{W^+}_{\mp 0})^\star = \frac{-8}{3\pi\sqrt{2}}(1 \mp 4\cos\theta^\star_l)e^{\mp i\phi^\star_l}. \tag{6.29}$$

The diagonal projection operators depend only on the polar angle of the lepton, while the off-diagonal projection operators have also an azimuthal angle dependence.

In this analysis, the single W SDM elements are calculated in bins of $\cos\theta_{W^-}$ as

$$\rho^{W^-}_{\tau\tau'}(k) = < \Lambda^{W^-}_{\tau\tau'}(k) > = \frac{1}{N_k}\sum_{i=1}^{N_k} \Lambda^{W^-}_{\tau\tau'}(\theta^\star_{l^-}, \phi^\star_{l^-})_i \ , \tag{6.30}$$

where N_k is the number of events in the bin k and where $\Lambda^{W^-}_{\tau\tau'}$ is the projection operator calculated from the kinematical variables of the event. To take into account detector acceptance, resolution effects and background contamination, each event i is reweighted with a correction factor $\omega_{cor,i}$

$$\rho^{W^-}_{\tau\tau'}(k) = < \tilde{\Lambda}^{W^-}_{\tau\tau'}(k) > = \frac{1}{\omega_{tot}(k)}\sum_{i=1}^{N_k} \Lambda^{W^-}_{\tau\tau',i} \ . \ \omega_{cor,i} \tag{6.31}$$

where

$$\omega_{tot}(k) = \sum_{i=1}^{N_k} \omega_{cor,i} \tag{6.32}$$

The statistical uncertainty is the Root Mean Squared (RMS) of the event SDM element distribution, rescaled with the square root of the inverse number of equivalent events N_{equiv} to account for the event-by-event reweighting

$$\sigma_{stat}(\rho^{W^-}_{\tau\tau'}(k)) = \sqrt{\frac{\sum_{i=1}^{N_k} (\Lambda^{W^-}_{\tau\tau',i} - < \Lambda^{W^-}_{\tau\tau'}(k) >)^2}{(N_k - 1)}} \ . \ \sqrt{\frac{1}{N_{equiv}}} \tag{6.33}$$

where

$$N_{equiv}(k) = \frac{\omega^2_{tot}(k)}{\sum_{i=1}^{N_k} \omega^2_{cor,i}} \tag{6.34}$$

When no correction is applied, i.e. $\omega_{cor,i} = 1$ for all events, the number of equivalent events becomes N_k and Eq. 6.33 reduces to the expression for the standard deviation of the mean of the unweighted distribution

$$\sigma(< \Lambda^{W^-}_{\tau\tau'}(k) >) = \sqrt{\frac{\sum_{i=1}^{N_k} (\Lambda^{W^-}_{\tau\tau',i} - < \Lambda^{W^-}_{\tau\tau'}(k) >)^2}{N_k(N_k-1)}} \tag{6.35}$$

6.5.1 Bin-to-bin correction factors

As the SDM elements are determined from the measured angular distributions, a direct comparison with theoretical predictions makes sense only after correction for the detector effects and the background contamination. These corrections are determined from Monte Carlo simulation and incorporated in the definition of the bin-to-bin correction factor

$$\omega_{cor}(\Omega_{3D}) = \frac{\pi(\Omega_{3D})}{\epsilon^{4f\to cco3}_{tot}(\Omega_{3D})} \tag{6.36}$$

The correction factor depends on the position occupied by the event in the 3-dimensional phase space Ω_{3D}=($\cos\theta_W$, $\cos\theta^\star_l$, $\phi^\star_l$) which is hereby divided in 3-dimensional boxes.

The full 189-209 GeV statistics is treated simultaneously, but the measured SDM elements are rescaled event-by-event using a $\sqrt{s}$-dependent correction factor.

6.5.2 Optimisation of the binning

The typical resolution on $\cos\theta_W$, $\cos\theta^\star$ and $\phi^\star$ lies within the chosen bin width. For the bin-to-bin correction, a further optimisation of the binning is necessary to avoid potential bias effects. The binning of the 3-dimensional phase space Ω_{3D} for the bin-to-bin correction factor ω_{cor}, is chosen such that a optimal use is made of the available Monte Carlo statistics per bin and deviations due to a coarse binning are reduced as much as possible. On the other hand, the bin size has to be as small as possible to be sensitive to the presence of anomalous couplings, i.e. non-Standard Model couplings, and $CP(T)$-violation.

As the diagonal projection operators Λ_{++}, Λ_{--} and Λ_{00} do only depend on the W production angle and on the lepton's polar decay angle, the bin-to-bin correction uses only these two angles. This increases the box statistics significantly. Similarly, the off-diagonal projection operator Λ_{+-} is only a function of the W production angle and the lepton's azimuthal decay angle and the bin-to-bin correction in two dimensions is performed. The remaining projection operators vary with all three angles and a 3-dimensional parameterisation of the bin-to-bin correction factor is compulsory.

The influence of the binning is studied by comparing the bin-to-bin corrected SDM elements to their corresponding generator level distributions. Because of the binning, a deviation of the SDM elements could arise and introduce a systematic uncertainty. This deviation is exclusively related to the choice of the binning and would also be present for an ideal Monte Carlo with infinite statistics but with the same binning. A bias is introduced if the deviation represents several times the statistical uncertainty and this for several consecutive $\cos\theta_{W^-}$ bins. From the experimental point of view, the bias is only relevant if it represents a large fraction of the expected data statistical uncertainty. For the available KandY Monte Carlo statistics at 189 GeV, the expected data statistical uncertainty is about 20 times larger than the statistical uncertainty obtained from Monte Carlo simulation.

- $\cos\theta_{W^-}$ **binning**

The evolution of the nine single W SDM elements as function of the number of $\cos\theta_{W^-}$ bins is shown in the Figures of Appendix C1 for the $qq\mu\nu(\gamma)$ final state at $\sqrt{s} = 189$ GeV. The solid points with error bar shows the KandY Monte Carlo single W SDM elements on reconstruction level, after bin-to-bin correction , while the dotted line represents the corresponding distribution on generator level. The binning in $\cos\theta^\star$ was fixed to 12 for the diagonal elements and to 8 for the off-diagonal elements ρ_{+0} and ρ_{-0}, while the binning in $\phi^\star$ is 16 for the off-diagonal element ρ_{+-} and 10 for the off-diagonal elements ρ_{+0} and ρ_{-0}. Also the average deviation, defined as

$$\langle\Delta\rangle = \frac{1}{N_{\cos\theta_W}} \sum_{k=1}^{N_{\cos\theta_W}} \frac{(\rho^{rec}(k) - \rho^{gen}(k))^2}{\sigma^2_{stat}(\rho^{rec}(k))} \tag{6.37}$$

is shown as function of the number of bins $N_{\cos\theta_W}$ and gives an idea of the average deviation in unit of statistical uncertainty. For all single W SDM elements a division of the cosine of the W production angle in 8 equal size bins, proposed by the LEP SDM group, is sufficient.

- $\cos\theta^\star$ **binning**

The evolution of the diagonal single W SDM element ρ_{++} as function of the number of $\cos\theta^\star$ bins is displayed in Figure 6.12. The element is shown in each of the 8 $\cos\theta_{W^-}$ bins for the $qq\mu\nu(\gamma)$ final state at $\sqrt{s} = 189$ GeV. Appendix C2 gives the evolution of the other SDM elements. The binning in $\cos\theta_{W^-}$ was fixed to 8, while the binning in $\phi^\star$ to 10 for the off-diagonal elements ρ_{+0} and ρ_{-0}. For the diagonal single W SDM elements a division of the cosine of the lepton's polar decay angle in 12 equal size bins is necessary, for the off-diagonal elements ρ_{+0} and ρ_{-0} 10 equal size bins are sufficient.

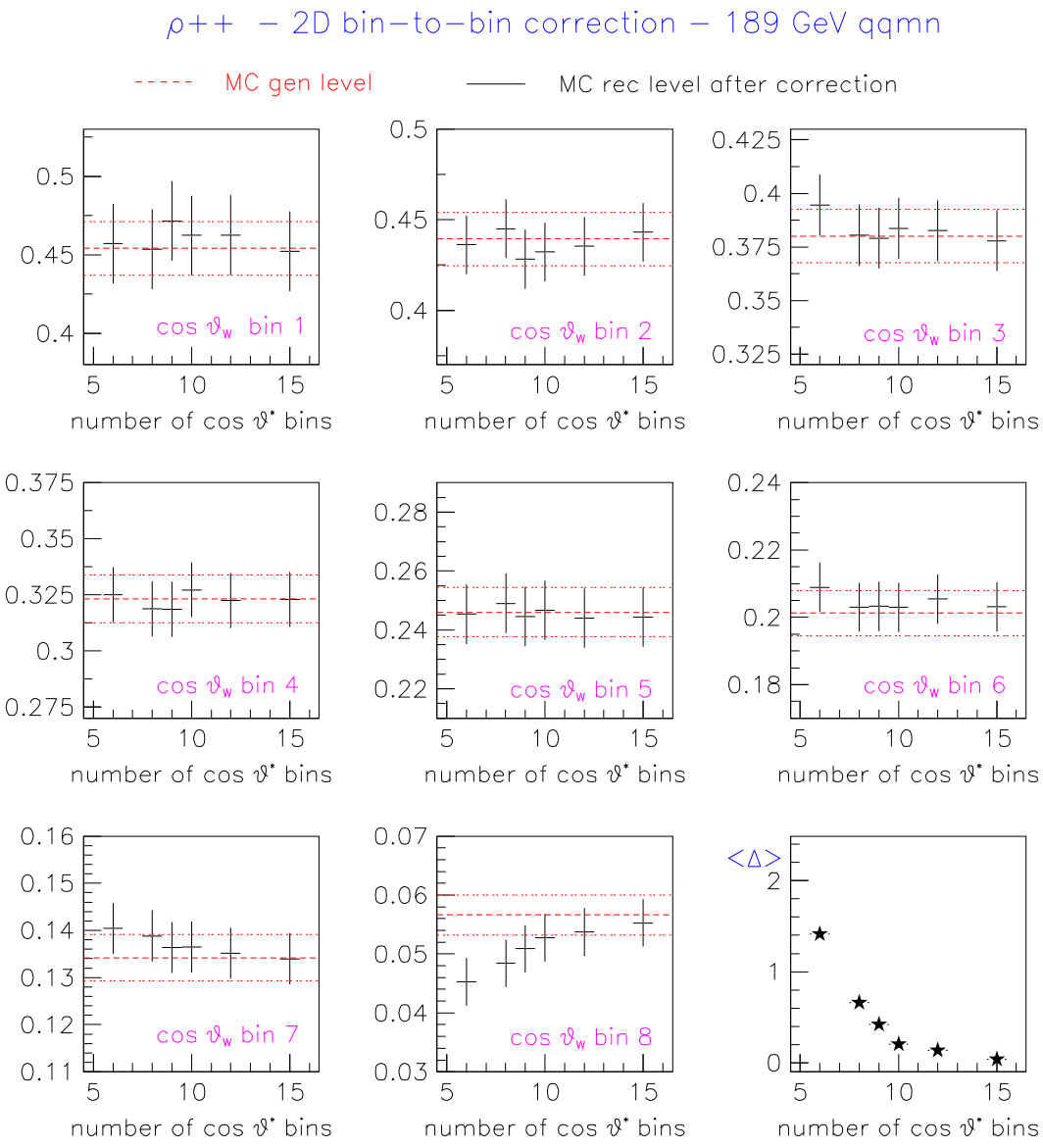

Figure 6.12: *The evolution of the diagonal single W SDM element ρ_{++} as function of the number of $\cos\theta^\star$ bins in each of the 8 $\cos\theta_{W^-}$ bins for the $qq\mu\nu(\gamma)$ final state at $\sqrt{s} = 189$ GeV. The solid points with error bar shows the KandY Monte Carlo single W SDM elements as function of the number of $\cos\theta^\star$ bins, on reconstruction level, after bin-to-bin correction, while the dashed line represents the corresponding distribution on generator level with its corresponding 1σ-band. Also the average deviation is shown as function of the number of $\cos\theta^\star$ bins.*

Binning	$\rho_{++},\ \rho_{--},\ \rho_{00}$	ρ_{+-}	$\rho_{+0},\ \rho_{-0}$
$\cos\theta_{W^-}$	8	8	8
$\cos\theta^\star$	12	-	8
$\phi^\star$	-	16	10

Table 6.2: *The number of bins for the bin-to-bin correction factor ω_{cor} that corrects for the background contamination and the detector acceptance and resolution.*

• **$\phi^\star$ binning**

The evolution of the real part of the off-diagonal single W SDM element ρ_{+-} as function of the number of $\phi^\star$ bins is displayed in Figure 6.13. The element is shown in each of the 8 $\cos\theta_{W^-}$ bins for the $qq\mu\nu\mu(\gamma)$ final state at $\sqrt{s} = 189$ GeV. Appendix C3 gives the evolution of the other SDM elements. The binning in $\cos\theta_{W^-}$ as well as in $\cos\theta^\star$ was fixed to 8. For the single W SDM element ρ_{+-} a $\phi^\star$ binning of 16 equal size bins is necessary,while for the elements ρ_{+0} and ρ_{-0} a division of the lepton's azimuthal decay angle in 10 equal size is sufficient. As the resolution in $\phi^\star$ is typically of the order of 0.1 radians, a $\phi^\star$ binning of 10 or 16, corresponding to a bin width of 0.64 respectively 0.4 keeps the resolution effects sufficiently small.

The number of equal size bins used in the determination of bin-to-bin correction factor ω_{cor} are summarised in Table 6.2.

• **$\sqrt{s}$-dependence**

A $\sqrt{s}$-dependent bin-to-bin correction is applied to follow the detector response and the behaviour of background processes as function of the center-of-mass energies. Figure 6.14 shows the relative difference of the correction factor values at higher center-of-mass energies $\sqrt{s} = 192 - 209$ GeV relative to the 189 GeV values for the 2D and the 3D bin-to-bin correction. A fit with a Gaussian is performed. All distributions are symmetric and centered on zero. The variation of the bin-to-bin correction factors with the center-of-mass energy $\sqrt{s}$ is about 10% for the 2D corrections and 18% for the 3D correction.

Appendix C4 compares the corrected single W SDM elements to the generated level distributions for the SM KandY Monte Carlo in the $qq\mu\nu(\gamma)$ final state at each center-of-mass energy from $\sqrt{s} = 189 - 209$ GeV. All deviations are below 3σ except for the element Im($\rho+-$) in the second $\cos\theta_{W^-}$ bin at $\sqrt{s}$=205 GeV (3.9 σ) and for the element Re($\rho-0$) in the eighth $\cos\theta_{W^-}$ bin at $\sqrt{s}$=206 GeV (3.7 σ). The deviation between the reconstructed and bin-to-bin corrected single W SDM elements and their corresponding generator level distributions are added as systematic uncertainty due to the correction method, as explained in the Section 6.7.2.

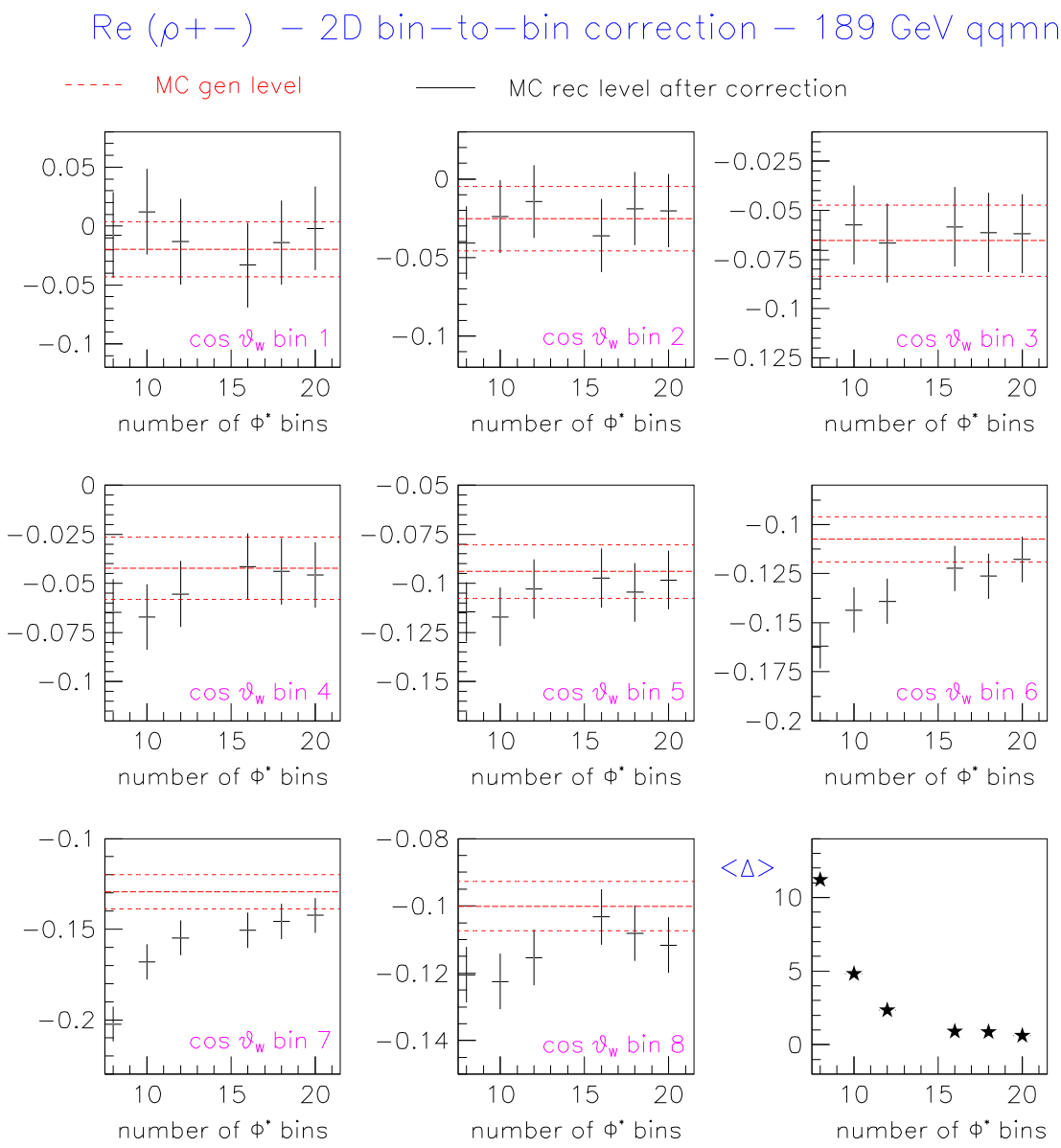

Figure 6.13: *The evolution of the real part of the off-diagonal single W SDM element ρ_{+-} as function of the number of $\phi^\star$ bins in each of the 8 $\cos\theta_{W^-}$ bins for the $qq\mu\nu(\gamma)$ final state at $\sqrt{s} = 189$ GeV. The solid points with error bar shows the KandY Monte Carlo single W SDM elements as function of the number of $\phi^\star$ bins, on reconstruction level after bin-to-bin correction, while the dashed line represents the corresponding distribution on generator level with its corresponding 1σ-band. Also the average deviation is shown as function of the number of $\phi^\star$ bins.*

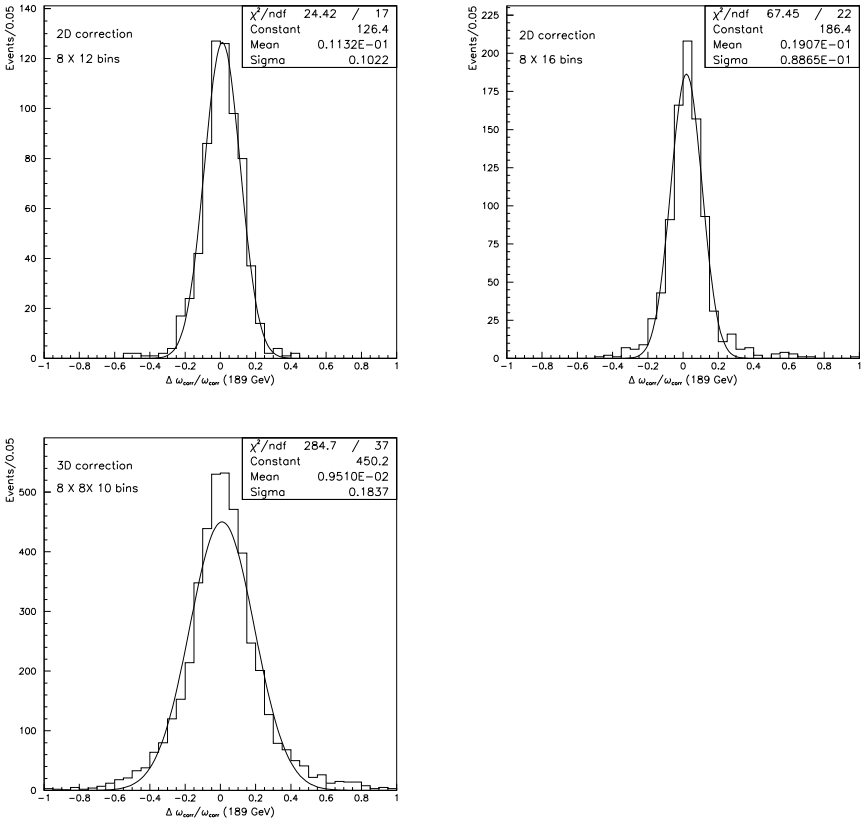

Figure 6.14: *The relative difference of the bin-to-bin correction factor ω_{cor} at the higher center-of-mass energies $\sqrt{s} = 192 - 209$ GeV relative to the 189 GeV values for the 2D and the 3D bin-to-bin correction for the $qq\mu\nu$ final state as obtained with the signal SM KandY Monte Carlo.*

6.6 Experimental Results

The single W SDM elements as a function of $\cos\theta_{W^-}$ are presented in Figures 6.15 and 6.16 for the $qqe\nu(\gamma)$ final state and the $qq\mu\nu(\gamma)$ final state respectively. The dots show the L3 data at the center-of-mass energies $\sqrt{s} = 189 - 209$ GeV. The error bars give the total uncertainty combining statistics and systematics contributions. The Standard Model prediction is shown by the solid line and calculated as the luminosity averaged, generator level SDM distributions using the 189-209 GeV KandY Monte Carlo samples. The agreement with the Standard Model prediction is evaluated by a χ^2-test using the total uncertainty, without taking into account the correlation between $\cos\theta_{W^-}$ bins and between SDM elements. The agreement is marginal: $\chi^2/d.o.f. = 107.0/72(CL = 4.7\ \%)$ for the $qqe\nu(\gamma)$ final state and $\chi^2/d.o.f. = 76.6/72(CL = 33.3\ \%)$ for the $qq\mu\nu(\gamma)$ final state.

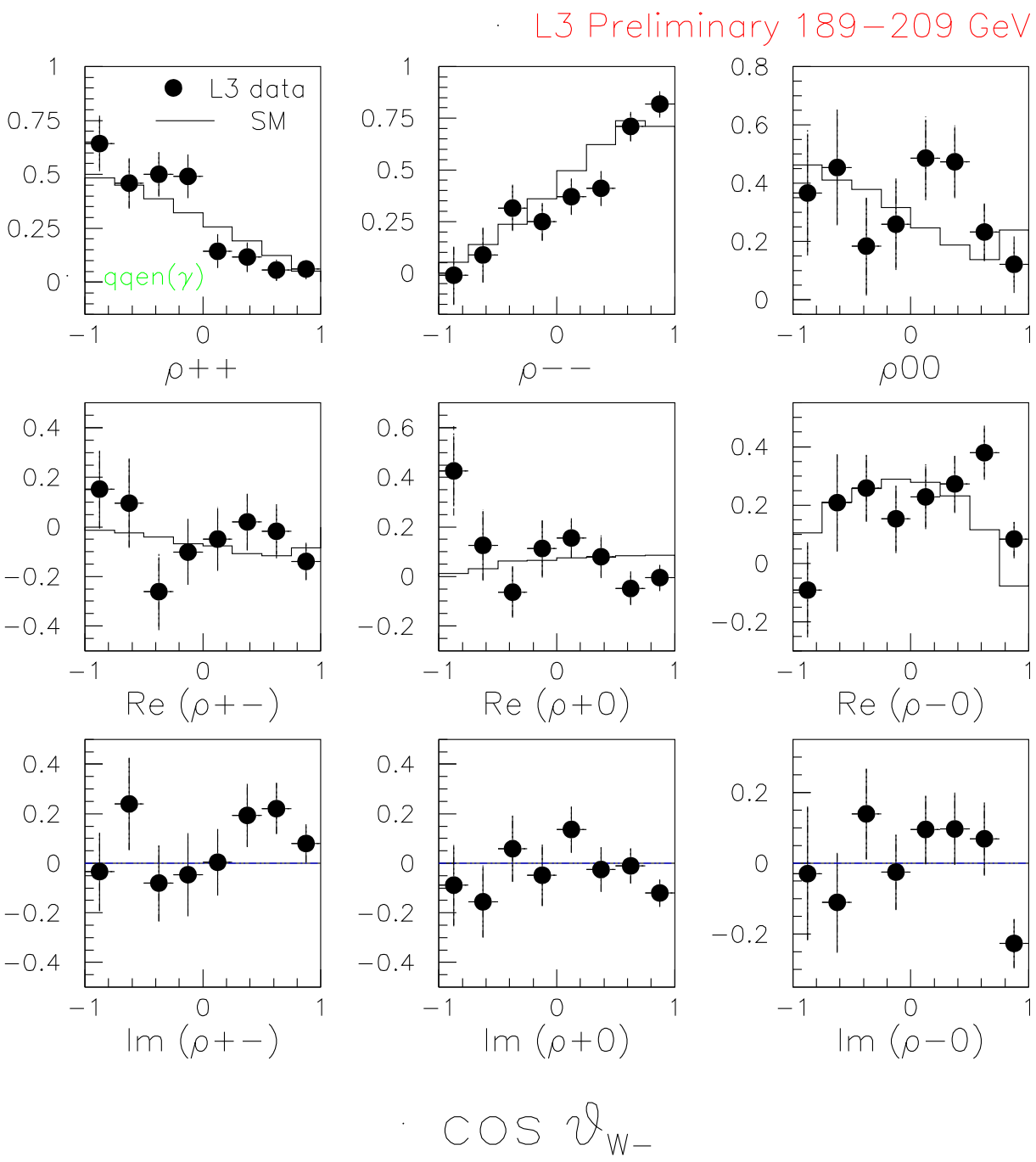

Figure 6.15: *The single SDM elements, as a function of* $\cos\theta_{W^-}$. *The dots represent the L3* $qq e\nu(\gamma)$ *data selected at the center-of-mass energies* $\sqrt{s} = 189 - 209$ *GeV. The error bars show the total uncertainty combining the statistics and the systematics contributions The Standard Model prediction is shown by the solid line.*

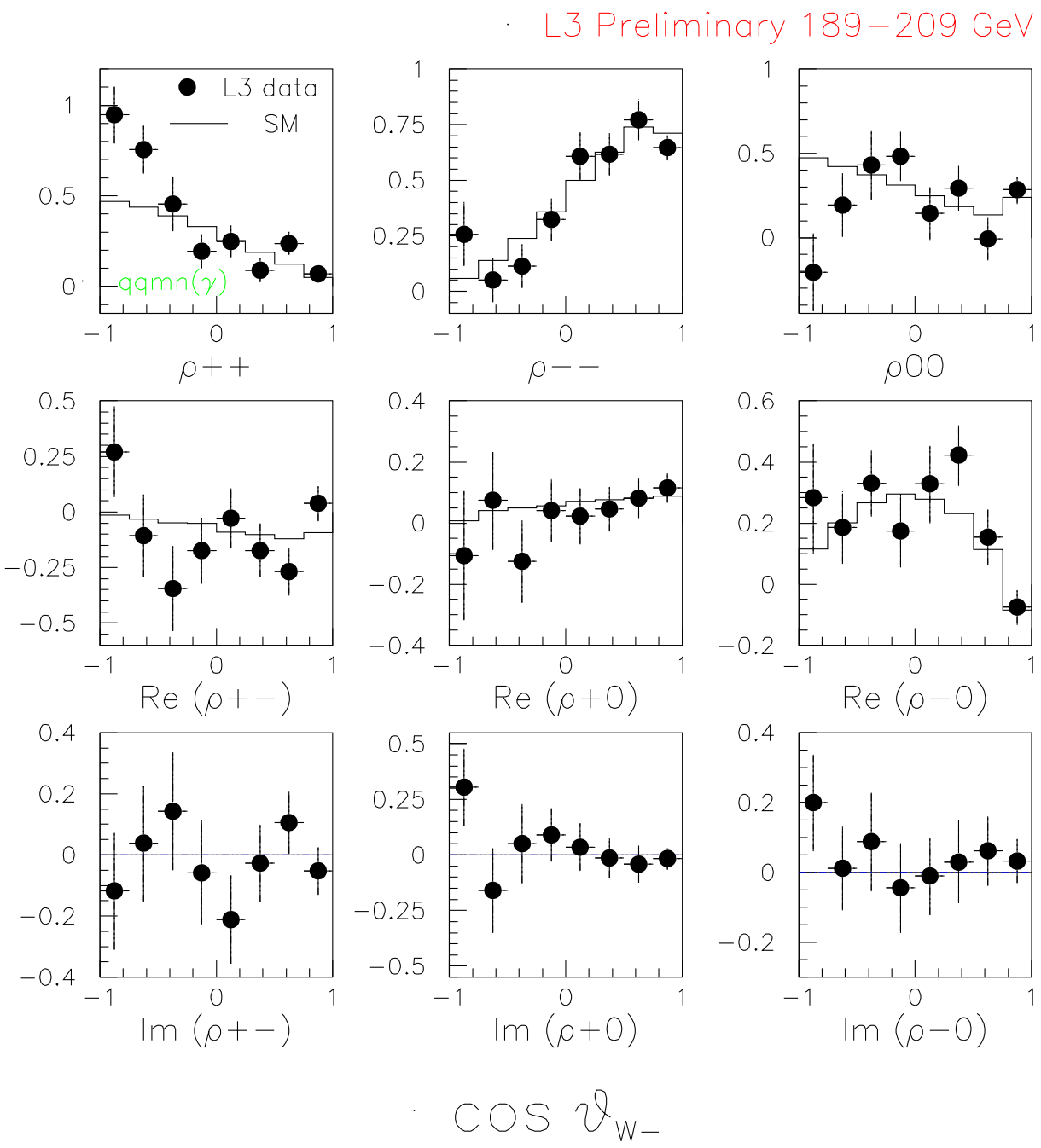

Figure 6.16: *The single SDM elements, as a function of* $\cos\theta_{W^-}$. *The dots represent the L3* $qq\mu\nu(\gamma)$ *data selected at the center-of-mass energies* $\sqrt{s} = 189 - 209$ *GeV. The error bars show the total uncertainty combining the statistics and the systematics contributions The Standard Model prediction is shown by the solid line.*

6.7 Systematic Uncertainties

The measurement of the SDM elements and the measurement of the W-pair production cross section have in common a large number of sources of systematic uncertainty, already discussed in Chapter 5. The main source of systematics for the SDM measurement is the limited Monte Carlo statistics and the charge confusion for the $qqe\nu(\gamma)$ final state.

6.7.1 Limited Monte Carlo statistics

Although the bin size has been optimized, some regions of the lepton phase space remain scarecely populated due to the limited Monte Carlo statistics and are therefore sensitive to statistical fluctuations. The effect of the limited Monte Carlo statistics, both for the signal as for the background, is estimated by smearing the total efficiency and the purity by their statistical uncertainty. The number of selected Monte Carlo events for the signal and the background are changed simultaneously by their statistical uncertainty, thus including the correlations between signal and background. The modified correction factors are then applied on a large number of pseudo data samples and the difference between SDM element value of the pseudo samples with baseline correction factors and these with the efficiency-purity smeared correction factors is taken as systematic uncertainty after substraction of the statistical accuracy, in quadrature. The systematic uncertainty due to limited Monte Carlo statistics is uncorrelated between W-pair decay channels.

6.7.2 Correction method

Due to the binning of the correction, chosen large enough to avoid statistical fluctuations, the angular dependence of the efficiency and the purity is integrated out over the bin and leads to a loss of sensitivity. A source of systematic uncertainty related to binning is introduced. The systematics depends only indirectly on the Monte Carlo statistics through choice of the binning but not directly: a deviation would also be present for an ideal Monte Carlo of infinite statistics with the same coarse binning but would disappear in case of an infinitely small binning. The Monte Carlo difference between corrected SDM elements and the generated distributions is introduced as systematic uncertainty and assumed uncorrelated between W-pair decay channels.

6.7.3 Detector modelling

Jet and lepton reconstruction

A good knowledge of the detector response to hadrons and leptons is crucial for the measurement of the SDM elements. To evaluate the effect, the energy and angular variables of the data are modified according to the maximal observed additional resolution and calibration obtained from the study of Z-peak events summarised in Table 4.2. The maximal effect on the SDM elements is taken as systematic uncertainty which is assumed correlated between W-pair decay channels for the jet reconstruction systematics and uncorrelated for the lepton reconstruction systematics. The good lepton reconstruction quality by the L3 detector, leads to a smaller uncertainty than the jet reconstruction which influences the SDM measurement through the kinematic fit.

Charge confusion

The SDM analysis depends on the charge assignment and therefore the lepton charge confusion has been studied in detail using τ-jets. The analysis is presented in Appendix B. The Monte Carlo charge assignment is corrected to reproduce the measured lepton charge confusion present in the real data. The correction depends on the decay channel, the reconstructed particle and its inverse transverse momentum value $1/P_T$. A correction is applied for electrons, MIP muons and muons reconstructed in the forward and backward muon chambers. No correction is applied for muons reconstructed in the barrel region of the muon chamber where the charge confusion is well modelled by the detector simulation. The relative uncertainty on the ratio of the measured charge confusion in data and in Monte Carlo as function of $1/P_T$ is propagated as a systematic uncertainty: $\delta R/R = \pm 0.096$ for the BGO barrel and $\delta R/R = \pm 0.13$ for the endcaps. This remaining uncertainty in the charge confusion correction is assumed uncorrelated between the W-decay channels.

6.7.4 Theoretical uncertainties

Signal cross section

The data are corrected with the Standard Model KandY Monte Carlo. The underlying theoretical calculations are subject to uncertainties and hence, are a possible source of systematics.

The number of expected signal events depends on the total cross section for W-pair production which has a theoretical uncertainty estimated to be about 0.5%[103]. In order to assign a systematic uncertainty, the normalisation of the expected CCO3 signal is varied by 0.5%. The effect on the single W SDM elements is negligible.

Background cross sections

The expected background, evaluated with the background Monte Carlo generators are subject to uncertainties on theoretical predictions for the total and differential cross section and therefore a possible source of systematics. The normalisation of the expected background is varied with the corresponding theoretical uncertainty on the total cross section, which is $\pm 0.5\%$ for the single W background, $\pm 2\%$ for the W-pair production background (non-CCO3 4f processes and W-pair decays into channels other than signal) and for neutral-current four fermion processes (Zee and ZZ background) and $\pm 1\%$ for the $q\bar{q}(\gamma)$ background. The effect of the background cross sections pointed out to be negligible.

ISR and FSR simulation

The systematic uncertainty due to the ISR modelling in KandY Monte Carlo is evaluated by comparing the results at order $\mathcal{O}(\alpha^3)$ to those when only ISR up to $\mathcal{O}(\alpha^2)$ is considered. The effect is found negligible.

The influence of FSR is evaluated by removing the Monte Carlo events with at least one FSR photon passing an energy cut of 100 MeV. The average observed shift of the SDM elements is taken as systematic uncertainty and uncorrelated is between W-pair channels.

$\mathcal{O}(\alpha)$ corrections

The SDM elements are calculated from the W production angle and the lepton's polar and azimuthal decay angles. As the theoretical uncertainty on the corresponding differential cross section is not available, there is no straightforward way to assess a corresponding systematic uncertainty. It is reasonable to assume that the uncertainty is smaller than the full effect of the inclusion of the $\mathcal{O}(\alpha)$ corrections in the LPA or the DPA approach. Studies performed with the RACOONWW Monte Carlo generator with a different implementation of the DPA, showed a level of agreement of about half the size of the full effect[104]. The difference in SDM element values with and without the inclusion of the $\mathcal{O}(\alpha)$ corrections in the LPA approach is taken as systematic uncertainty, fully correlated between the W-pair channels.

Hadronisation

The discription of the fragmentation and hadronisation process, i.e. the recombination of coloured partons into quarks and finally into colourless jets, represents a possible source of systematic uncertainty. The hadronisation model implemented in the baseline KandY

Monte Carlo is PYTHIA. To estimate the effect of the hadronisation, a comparison is made between the baseline KandY Monte Carlo with PYTHIA hadronisation and KandY Monte Carlo samples with different hadronisation models like HERWIG and ARIADNE which are discussed in detail in Chapter 3. The parameters used in these models are tuned with high statistics $q\bar{q}$ events at the Z peak. The effect of the hadronisation model is assumed 50% correlated among the different models as through the use of common four momenta and 50% uncorrelated due to the different implementation of the hadronisation process. Since no hadronisation model can be favorised a priori, the average of the absolute shift in SDM element value between the different models is quoted as systematic uncertainty. The hadronisation uncertainty is fully correlated between W-pair channel. It is assumed independent of the center-of-mass energy as the dependence with $\sqrt{s}$ is only logarithmic and the average of the systematic uncertainty at 189 GeV and 208 GeV is taken as the systematic uncertainty due to hadronisation modelling.

6.7.5 Total systematic uncertainty

Table 6.3 shows the individual sources of systematic uncertainty on the element ρ_{++} in the 8 $\cos\theta_{W^-}$ for the $qqe\nu(\gamma)$ final state. Also the measured SDM value and its statistical uncertainty are quoted. All systematic uncertainties are assumed uncorrelated among each other and are added in quadrature to get the total systematic uncertainty on the SDM element. The numerical results for all SDM elements, both $qqe\nu(\gamma)$ and $qq\mu\nu(\gamma)$ final states are presented in Appendix D1.1 and D1.2, without repeating negligible contributions. For all measurements, the systematic uncertainty is smaller than the statistical accuracy of the data.

6.8 Systematic Checks

6.8.1 Stability test

Inside a $\cos\theta_{W^-}$ bin, the event SDM element distribution is not Gaussian. This can introduce a bias in the calculation of the SDM elements in case of low statistics. Therefore, a stability test is performed with a large number of toy Monte Carlo samples, N_{toy}, of variable number of events, N_{MC}. The toy samples are constructed by randomly extracting N_{MC} SDM element values out of the luminosity averaged, generator level event SDM element distribution. The full statistics $qq\mu\nu(\gamma)$ KandY Monte Carlo at $\sqrt{s} = 189 - 209$ GeV is hereby used.

L3 189-209 GeV data	$\rho_{++}(\cos\theta_{W^-}\ bin)$							
***qqeν*(γ) final state**	1	2	3	4	5	6	7	8
ρ_{++}	0.644	0.458	0.500	0.491	0.144	0.116	0.056	0.061
$\sigma_{tot}(\rho_{++})$	0.123	0.116	0.103	0.102	0.078	0.070	0.050	0.046
$\sigma_{stat}(\rho_{++})$	0.112	0.113	0.098	0.099	0.076	0.067	0.048	0.039
$\sigma_{sys}(\rho_{++})$	0.049	0.028	0.029	0.024	0.017	0.021	0.015	0.024
Source of systematic uncertainty								
MC statistics	0.036	0.009	0.019	0.007	0.008	0.006	0.004	0.018
Correction method	0.002	0.003	< 0.001	0.004	0.004	0.003	0.003	0.004
Charge confusion	0.024	0.018	0.004	0.006	0.002	0.003	0.002	0.004
Lepton reconstruction	0.002	0.002	0.001	0.002	< 0.001	0.002	< 0.001	0.002
Jet reconstruction	0.017	0.012	0.015	0.017	0.004	0.013	0.004	0.007
Signal cross section	< 0.001							
Background cross sections	< 0.001							
ISR	< 0.001							
FSR	0.001							
$\mathcal{O}(\alpha)$ corrections	0.005	0.004	< 0.001	0.002	< 0.001	< 0.001	< 0.001	< 0.001
Hadronisation	0.013							

Table 6.3: *The individual sources of systematic uncertainty on the element ρ_{++} in the 8 $\cos\theta_{W^-}$ for the $qqe\nu(\gamma)$ final state. The systematic uncertainty on the signal and background cross sections and the ISR simulation are negligible. All systematic uncertainties are assumed uncorrelated among each other and are added in quadrature to get the total systematic uncertainty on the SDM element. Also the measured SDM value and its statistical uncertainty are quoted.*

The mean value of the SDM element distribution obtained with the N_{toy} Monte Carlo samples

$$< \rho_{toy}(N_{MC}) >= \frac{1}{N_{toy}} \sum_{i=1}^{N_{toy}} \rho_{toy}^{i}(N_{MC}) \tag{6.38}$$

where ρ_{toy}^{i} represents the SDM element value measured with the toy Monte Carlo sample i. The corresponding statistical uncertainty is

$$\sigma_{stat}(< \rho_{toy}(N_{MC}) >) = \frac{RMS(\rho_{toy}(N_{MC}))}{\sqrt{N_{toy}}} \tag{6.39}$$

The evolution of both variables is studied for 100 (N_{toy}) toy Monte Carlo samples containing 50, 500, 1000, 10000 and 20000 events (N_{MC}). The results are presented in Table 6.4 for all nine single W SDM elements in the first $\cos\theta_{W^-}$ bin: $-1 \leq \cos\theta_{W^-} < -0.75$ and which is the lowest statistics bin. The corresponding statistics for the data sample is 56. The mean value of the SDM element distribution remains stable and the statistical uncertainty scales correctly with the sample size. No bias is observed on the SDM elements for low statistics samples. The conclusion holds for all $\cos\theta_{W^-}$ bins.

To test the stability of the bin-to-bin correction, the same test is performed using reconstructed Monte Carlo events after bin-to-bin correction. Also here, the results are stable in all $\cos\theta_{W^-}$ bins and, no bias is introduced by the bin-to-bin correction on the calculated SDM elements for low statistics samples.

6.8.2 Test with a large number of pseudo data samples

The level of statistical agreement between the calculated single W SDM element and its Standard Model expectation, as well as the reliability of the statistical uncertainty defined in Eq. 6.33, are evaluated by replacing the data sample by a large number of pseudo data samples i.e. Monte Carlo samples of the same statistics as the data and with a signal and background population as predicted by the Standard Model. A set of 100 and 200 (N_{pseudo}) pseudo data samples, simulating the 189 GeV and the 206 GeV $qq\mu\nu(\gamma)$ data, are used. The number of expected data events in the $qq\mu\nu(\gamma)$ final state is 293 at 189 GeV and 212 at 206.5 GeV.

The SDM elements, ρ_{pseudo}^{i}, and their statistical uncertainty, $\sigma_{stat}(\rho_{pseudo}^{i})$, as defined in Eq. 6.33, are calculated for each pseudo data sample i.

$< \rho_{toy}(N_{MC}) >$			
N_{MC}	$< \rho_{++} >$	$< \rho_{--} >$	$< \rho_{00} >$
50	0.453 ± 0.131	0.021 ± 0.092	0.524 ± 0.181
500	0.442 ± 0.045	0.020 ± 0.0268	0.521 ± 0.052
1000	0.447 ± 0.027	0.019 ± 0.020	0.518 ± 0.045
10000	0.447 ± 0.010	0.020 ± 0.007	0.519 ± 0.013
20000	0.447 ± 0.006	0.020 ± 0.005	0.519 ± 0.010
N_{MC}	$<$ Re $(\rho_{+-})>$	$<$ Re $(\rho_{+0})>$	$<$ Re $(\rho_{-0})>$
50	-0.094 ± 0.206	-0.019 ± 0.152	0.197 ± 0.114
500	-0.076 ± 0.070	-0.057 ± 0.050	0.186 ± 0.039
1000	-0.081 ± 0.043	-0.054 ± 0.035	0.188 ± 0.027
10000	-0.086 ± 0.013	-0.057 ± 0.011	0.190 ± 0.007
20000	-0.086 ± 0.009	-0.057 ± 0.007	0.189 ± 0.006
N_{MC}	$<$ Im $(\rho_{+-})>$	$<$ Im $(\rho_{+0})>$	$<$ Im $(\rho_{-0})>$
50	0.050 ± 0.211	-0.030 ± 0.173	-0.011 ± 0.110
500	0.026 ± 0.064	-0.017 ± 0.053	-0.012 ± 0.040
1000	0.028 ± 0.048	-0.019 ± 0.037	-0.006 ± 0.026
10000	0.022 ± 0.013	-0.018 ± 0.012	-0.010 ± 0.009
20000	0.021 ± 0.010	-0.017 ± 0.008	-0.008 ± 0.006

Table 6.4: *The mean value of the toy Monte Carlo samples SDM element distribution as function of the size of the sample N_{MC}. The results for all nine single W SDM elements are displayed and are obtained using 100 toy Monte Carlo samples constructed by randomly extracting values out of the luminosity averaged, generator level event SDM element distributions. The full statistics $qq\mu\nu(\gamma)$ KandY Monte Carlo at $\sqrt{s} = 189 - 209$ GeV is used. The quoted numbers are for the first $\cos\theta_{W^-}$ bin, $-1 \leq \cos\theta_{W^-} < -0.75$, which is the lowest statistics bin. The corresponding statistics of the data sample is 56. No bias is observed on the SDM elements for low statistics samples.*

The mean value and the RMS of the SDM element distributions obtained with the set of N_{pseudo} pseudo data samples, as well as their respective statistical precision, are evaluated. The mean value of SDM element distribution obtained with the N_{pseudo} pseudo data samples

$$< \rho_{pseudo} >= \frac{1}{N_{pseudo}} \sum_{i=1}^{N_{pseudo}} \rho^{i}_{pseudo} \tag{6.40}$$

represents an estimator for the expected SDM element value [105, 106].

The RMS of the pseudo data samples SDM element distribution

$$RMS(\rho_{pseudo}) = \sqrt{\frac{1}{N_{pseudo}-1} \sum_{i=1}^{N_{pseudo}} (\rho^{i}_{pseudo} - < \rho_{pseudo} >)^2} \tag{6.41}$$

is an estimator for the expected statistical precision on the SDM element.

The statistical uncertainty on the mean SDM value $< \rho_{pseudo} >$ is given by

$$\sigma_{stat}(< \rho_{pseudo} >) = \frac{RMS(\rho_{pseudo})}{\sqrt{N_{pseudo}}} \tag{6.42}$$

For a large number of pseudo data samples, the statistical uncertainty on the RMS is

$$\sigma_{stat}(RMS(\rho_{pseudo})) = \frac{RMS(\rho_{pseudo})}{\sqrt{2N_{pseudo}}} \tag{6.43}$$

As an example, table 6.5 gives the numerical results of the analysis of 200 pseudo data samples at 189 GeV and at 206 GeV for the $qq\mu\nu(\gamma)$ data and for the single W SDM element ρ_{++} in the eight $\cos\theta_{W^-}$ bins. Figure 6.17 shows the pseudo data samples SDM element distribution, ρ_{pseudo}, and the corresponding statistical uncertainty distribution, $\sigma_{stat}(\rho_{pseudo})$, as defined by Eq. 6.33, for the single W SDM element ρ_{++} in the first $\cos\theta_{W^-}$ bin. The results are obtained with the set of 200 pseudo data samples at 189 GeV and at 206 GeV for the $qq\mu\nu(\gamma)$ data. Also shown are the distribution of the 2D and 3D correction factors ω_{cor} of the pseudo data samples. At both center-of-mass energies, the mean value is centered around 1.3 and compatible with the ratio of the purity on the efficiency as seen from Table 6.1.

189 GeV	$\rho_{++}(cos\theta_{W^-})$		
$\cos\theta_{W^-}$ bin	SM prediction	$< \rho_{pseudo} >$	$RMS(\rho_{pseudo})$
1	0.432 ± 0.017	0.452 ± 0.019	0.273 ± 0.014
2	0.414 ± 0.015	0.406 ± 0.018	0.249 ± 0.012
3	0.356 ± 0.013	0.368 ± 0.016	0.231 ± 0.012
4	0.302 ± 0.011	0.306 ± 0.014	0.193 ± 0.010
5	0.243 ± 0.009	0.257 ± 0.012	0.168 ± 0.008
6	0.225 ± 0.007	0.235 ± 0.010	0.137 ± 0.007
7	0.179 ± 0.005	0.184 ± 0.006	0.091 ± 0.005
8	0.034 ± 0.004	0.046 ± 0.005	0.072 ± 0.004

206 GeV	$\rho_{++}(\cos\theta_{W^-})$		
$\cos\theta_{W^-}$ bin	SM prediction	$< \rho_{pseudo} >$	$RMS(\rho_{pseudo})$
1	0.459 ± 0.020	0.530 ± 0.020	0.279 ± 0.014
2	0.439 ± 0.017	0.459 ± 0.018	0.260 ± 0.013
3	0.373 ± 0.014	0.377 ± 0.017	0.235 ± 0.012
4	0.302 ± 0.012	0.301 ± 0.013	0.190 ± 0.010
5	0.232 ± 0.010	0.231 ± 0.010	0.148 ± 0.007
6	0.198 ± 0.007	0.198 ± 0.008	0.115 ± 0.006
7	0.161 ± 0.005	0.162 ± 0.006	0.085 ± 0.004
8	0.019 ± 0.003	0.031 ± 0.004	0.056 ± 0.003

Table 6.5: *The mean value and the RMS of the pseudo data samples SDM element distribution. The results are given for the of single W SDM element ρ_{++} and obtained with the set of 200 pseudo data samples at 189 GeV and at 206 GeV for the $qq\mu\nu(\gamma)$ data. Agreement is found between mean value and the Standard Model prediction as calculated with the full statistics KandY Monte Carlo at the corresponding center-of-mass energy.*

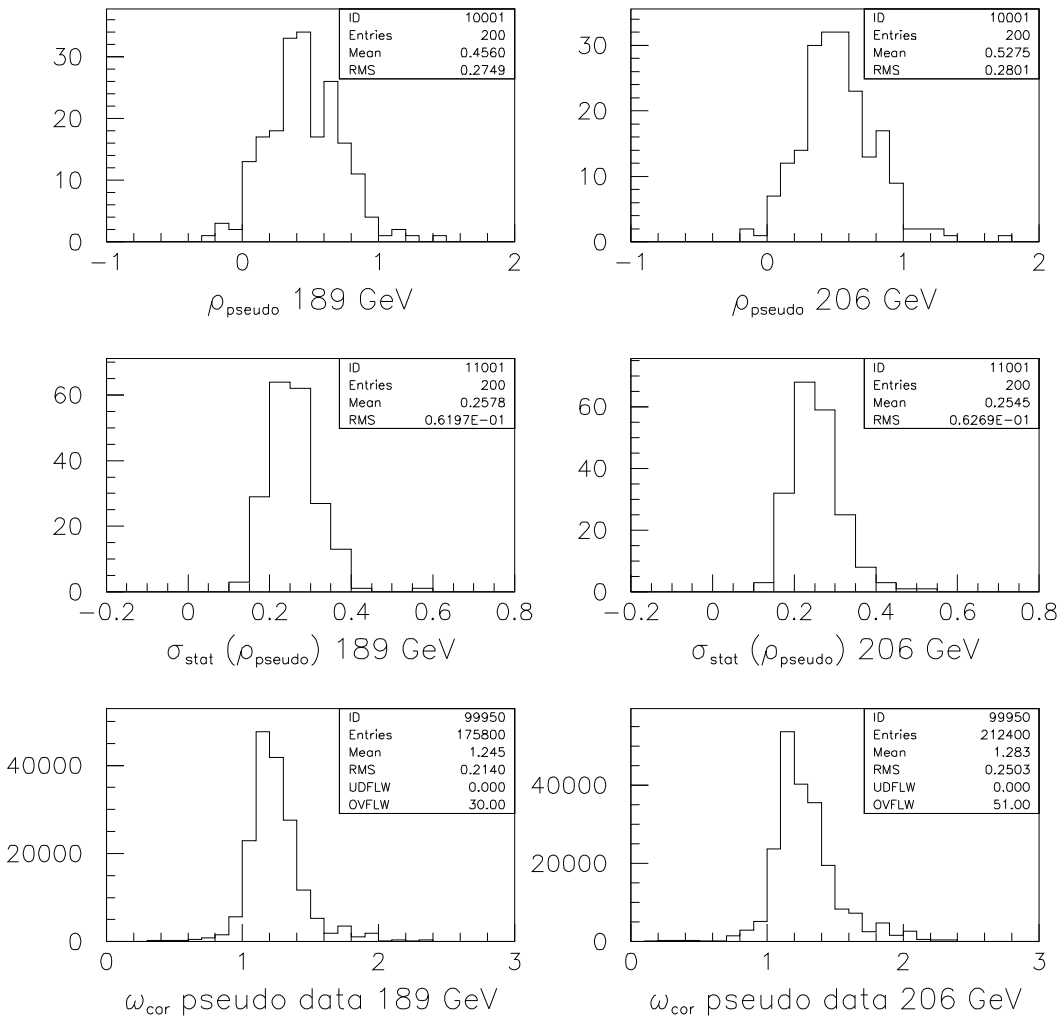

Figure 6.17: *The pseudo data samples SDM element distribution (Top) and the distribution of the statistical uncertainty (Middle), as defined by Eq. 6.33, for the single W SDM element ρ_{++} in the first $\cos\theta_{W^-}$ bin ($-1 \leq \cos\theta_{W^-} < -0.75$) as drawn from 200 pseudo data samples at 189 GeV and at 206 GeV for the $qq\mu\nu(\gamma)$ data. Also shown are the distribution of the 2D and 3D correction factors ω_{cor} of the pseudo data samples (Bottom).*

Pull test of the statistical uncertainty definition

To test if the uncertainty definition of Eq. 6.33 is statistically meanful, the following pull is defined

$$pull^{\,i} = \frac{\rho^{\,i}_{pseudo} - \rho_{SM}}{\sigma_{stat}(\rho^{\,i}_{pseudo})} \tag{6.44}$$

where ρ_{SM} is calculated with the full statistics generator level KandY Monte Carlo and where the index i runs over the pseudo data samples. The pull distribution for all nine single W SDM elements in all eight $\cos\theta_{W^-}$ bins is evaluated in the pull (72 points/sample). The pull distribution for each SDM element in each $\cos\theta_{W^-}$ bin separately (1 point/sample) is given in Appendix C5.

In the limits of the validity of the Central Limit Theorem [107], the pull distributions are normally distributed for a sufficiently large sample size, with a zero central value and an RMS equal to one. If this is realised, the definition Eq. 6.33 provides a good estimator for the statistical uncertainty on the single W SDM element.

The pull distribution for all nine single W SDM elements in all eight $\cos\theta_{W^-}$ bins (72 points), using the set of 200 pseudo data samples at 189 GeV (Left) and at 206 GeV (Right) $qq\mu\nu(\gamma)$ data, are presented in Figure 6.18. The table summarises the results for 100 and 200 pseudo data samples at both center-of-mass energies.

The mean value of the pull distribution, $< pull >$ and its RMS, $RMS(pull)$, are given with their statistical precision. Also the fraction of events beyond 3σ is quoted.
The mean values are compatible with zero, but the RMS of the pull distributions are slightly larger than one. Therefore SDM statistical uncertainty definition (Eq. 6.33) underestimates the statistical uncertainty by about 4%. The deviation is due to to the non-Gaussian shape of the pull distribution at larger pull values, confirmed by the fraction of events within 3σ which is smaller than the expected 99.73 % corresponding to the 3σ interval for a Gaussian distribution. When performing a fit with a Gaussian in the central region of the pull distribution, an standard deviation of one is retrieved.

Pull test of the Standard Model agreement

To test the level of agreement between the mean value of the pseudo data samples SDM element distributions, $< \rho_{pseudo} >$ and the corresponding Standard Model expectation, ρ_{SM}, the following pull is defined

$$pull = \frac{< \rho_{pseudo} > - \rho_{SM}}{\sigma_{stat}(< \rho_{pseudo} >)} \tag{6.45}$$

where the pull is evaluated in in each $\cos\theta_{W^-}$ bin of the nine SDM elements (72 points).

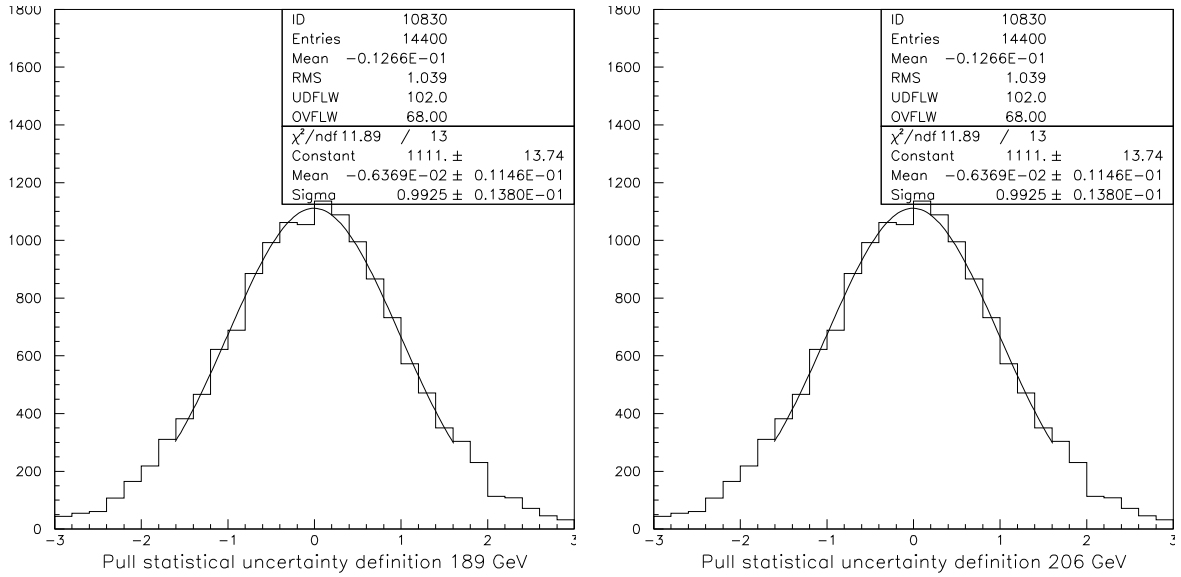

$$pull = \frac{\rho^{i}_{pseudo} - \rho_{SM}}{\sigma_{stat}(\rho^{i}_{pseudo})}$$

$\langle\sqrt{s}\rangle$ (GeV)	N_{pseudo}	$< pull >$	$RMS(pull)$	$< -3\sigma$ (%)	$> 3\sigma$ (%)
189	100	-0.009 ± 0.012	1.033 ± 0.009	0.8	0.5
	200	-0.013 ± 0.009	1.039 ± 0.006	0.7	0.5
206.5	100	-0.012 ± 0.012	1.001 ± 0.008	0.8	0.5
	200	-0.014 ± 0.008	1.019 ± 0.006	0.7	0.4

Figure 6.18: Above: *The pull distribution testing the statistical meaning of the uncertainty definition Eq. 6.33. All nine single W SDM elements in all eight* $\cos\theta_{W^-}$ *bins are included in the pull distribution (72 points/sample). A fit is performed with a Gaussian in the central region of the pull distribution.* Below: *The mean value of the pull distribution,* $< pull >$*, and its RMS,* $RMS(pull)$*, are given with their statistical precision. Also the fraction of events beyond* 3σ *is quoted. A set of 100 and 200 pseudo data samples at 189 GeV and at 206 GeV for the* $qq\mu\nu(\gamma)$ *data is used.*

Figure 6.19 shows the pull distribution using the set of 200 pseudo data samples at 189 GeV (Left) and at 206 GeV (Right) for the $qq\mu\nu(\gamma)$ data. A fit with a Gaussian is performed. The table summarises the results for 100 and 200 pseudo data samples at both center-of-mass energies.

The mean value of the pull distribution, $< pull >$, and its RMS , $RMS(pull)$, are given with their statistical precision. Also the fraction of events beyond 3σ is quoted. As the mean value of the pull distributions are compatible with zero, the SDM element calculation and consequently, the bin-to-bin correction method, reproduce the Standard Model prediction and the analysis is free of bias for finite samples as small as the data sample. The RMS of the pull distribution is about 10 to 20 % larger than one.

6.9 Tests of CPT- and CP-invariance

In the Standard Model, W-pair production is assumed a CPT- and CP- invariant interaction, both at tree-level as at one-loop level. As a direct consequence, the experimentally measured physical quantities like mass, lifetime, branching ratio, are the same for the CPT- and CP-transformed states. Figure 6.20 shows the effect of a CP-transformation on a helicity configuration. The charge conjugation operator C changes the sign of the charge, while the parity operator P reverses the particle's momentum but keeps the particle's spin unchanged.

The azimuthal angular distributions $\phi^\star$ are most sensitive to CP-violating interactions [108]. In the Standard Model, the azimuthal angular distributions are symmetric around zero. An asymmetry is introduced if a CP-violating phase would be present in the WWZ or $WW\gamma$ vertex at tree-level or at one-loop level. Only the off-diagonal elements depend on $\phi^\star$ and provide a test of CPT- and CP-invariance.

The effect on the SDM elements caused by the existence of an anomalous coupling $\Delta\kappa_\gamma = \pm 1$ and $\tilde{\lambda}_\gamma = \pm 1$ is shown in Figures 6.21 and 6.22. As mentionned in Chapter 2, the SDM formalism is sensitive to the existence of anomalous TGC's and can be used as a method to extract TGC's. The Bilenky-Gounaris (BILGOU) analytical calculation was used to simulate the triple gauge coupling dependence.

The effect of CP-conserving couplings is restricted to the diagonal SDM elements and the real part of the off-diagonal SDM elements. The sensitivity of CP-violating couplings is the largest in the imaginary part of the off-diagonal SDM elements. There is no difference between negative and positive CP-violating couplings of the same magnitude. This is true at tree-level but not in presence of loop effects where both CP-conserving as CP-violating couplings will always lead to non-zero imaginary parts of the SDM elements.

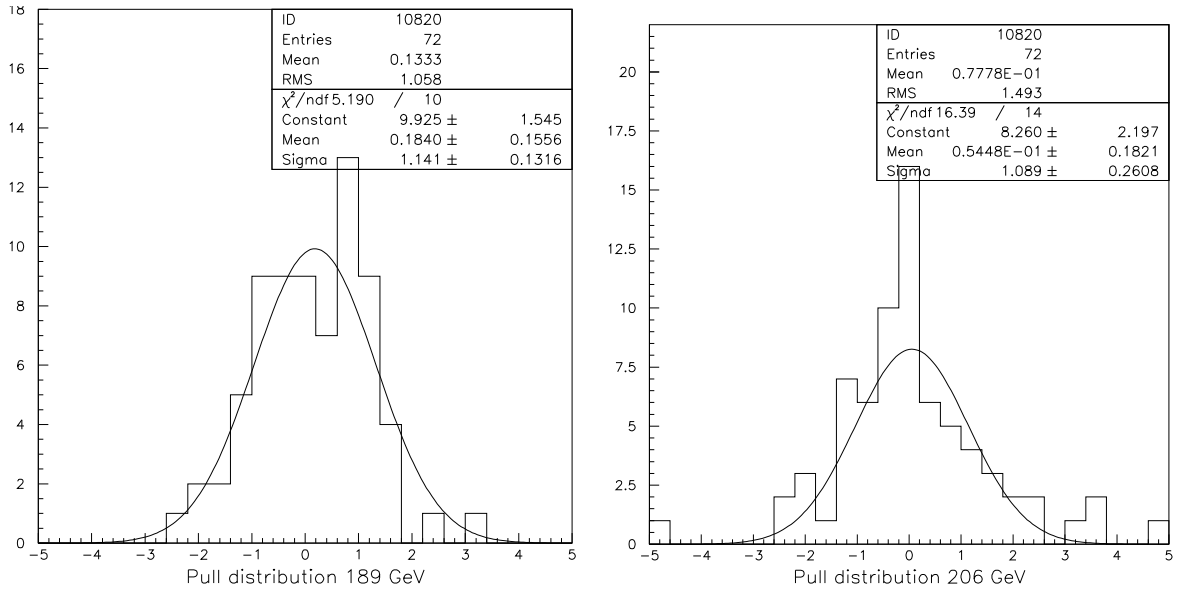

$$pull = \frac{< \rho_{pseudo} > - \rho_{SM}}{\sigma_{stat}(< \rho_{pseudo} >)}$$

$\langle\sqrt{s}\rangle$ (GeV)	N_{pseudo}	$< pull >$	$RMS(pull)$	$< -3\sigma$ (%)	$> 3\sigma$ (%)
189	100	0.017 ± 0.128	1.086 ± 0.091	0.	0.
	200	0.133 ± 0.125	1.058 ± 0.088	0.	1.4%.
206.5	100	0.050 ± 0.139	1.176 ± 0.098	0.	0.
	200	0.078 ± 0.176	1.493 ± 0.124	1.4%	5.5%

Figure 6.19: Above: *The pull distribution testing the level of agreement between the mean SDM value, $< \rho_{pseudo} >$, and the corresponding Standard Model expectation ρ_{SM} as calculated with the full statistics generator level KandY Monte Carlo. All nine single W SDM elements in all eight $\cos\theta_{W^-}$ bins are included in the pull distribution (72 points/sample). A fit with a Gaussian is performed.* Below: *The mean value of the pull distribution, $< pull >$, and its RMS, $RMS(pull)$, are given with their statistical precision. Also the fraction of events beyond 3σ is quoted. A set of 100 and 200 pseudo data samples at 189 GeV and at 206 GeV for the $qq\mu\nu(\gamma)$ data is used.*

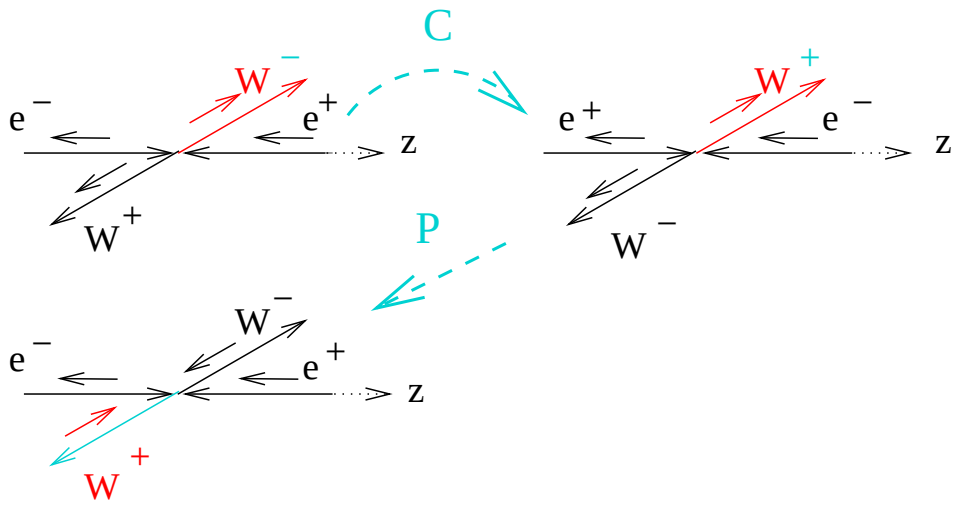

Figure 6.20: *The effect of a CP-transformation on a helicity configuration for the W-pair production process. In the Standard Model, W-pair production is assumed a CP-invariant interaction*

From CPT-invariance follows

$$\rho^{W^-}_{\tau\tau'} = (\rho^{W^+}_{-\tau-\tau'})^\star \tag{6.46}$$

while for CP-invariance

$$\rho^{W^-}_{\tau\tau'} = (\rho^{W^+}_{-\tau-\tau'}) \tag{6.47}$$

When decomposing into real and imaginary parts, Eq. 6.46 leads to

$$\mathrm{Re}(\rho^{\mathrm{W}^-}_{\tau\tau'}) - \mathrm{Re}(\rho^{\mathrm{W}^+}_{-\tau-\tau'}) = 0 \tag{6.48}$$

$$\mathrm{Im}(\rho^{\mathrm{W}^-}_{\tau\tau'}) + \mathrm{Im}(\rho^{\mathrm{W}^+}_{-\tau-\tau'}) = 0 \tag{6.49}$$

and Eq. 6.47 gives

$$\mathrm{Re}(\rho^{\mathrm{W}^-}_{\tau\tau'}) - \mathrm{Re}(\rho^{\mathrm{W}^+}_{-\tau-\tau'}) = 0 \tag{6.50}$$

$$\mathrm{Im}(\rho^{\mathrm{W}^-}_{\tau\tau'}) - \mathrm{Im}(\rho^{\mathrm{W}^+}_{-\tau-\tau'}) = 0 \tag{6.51}$$

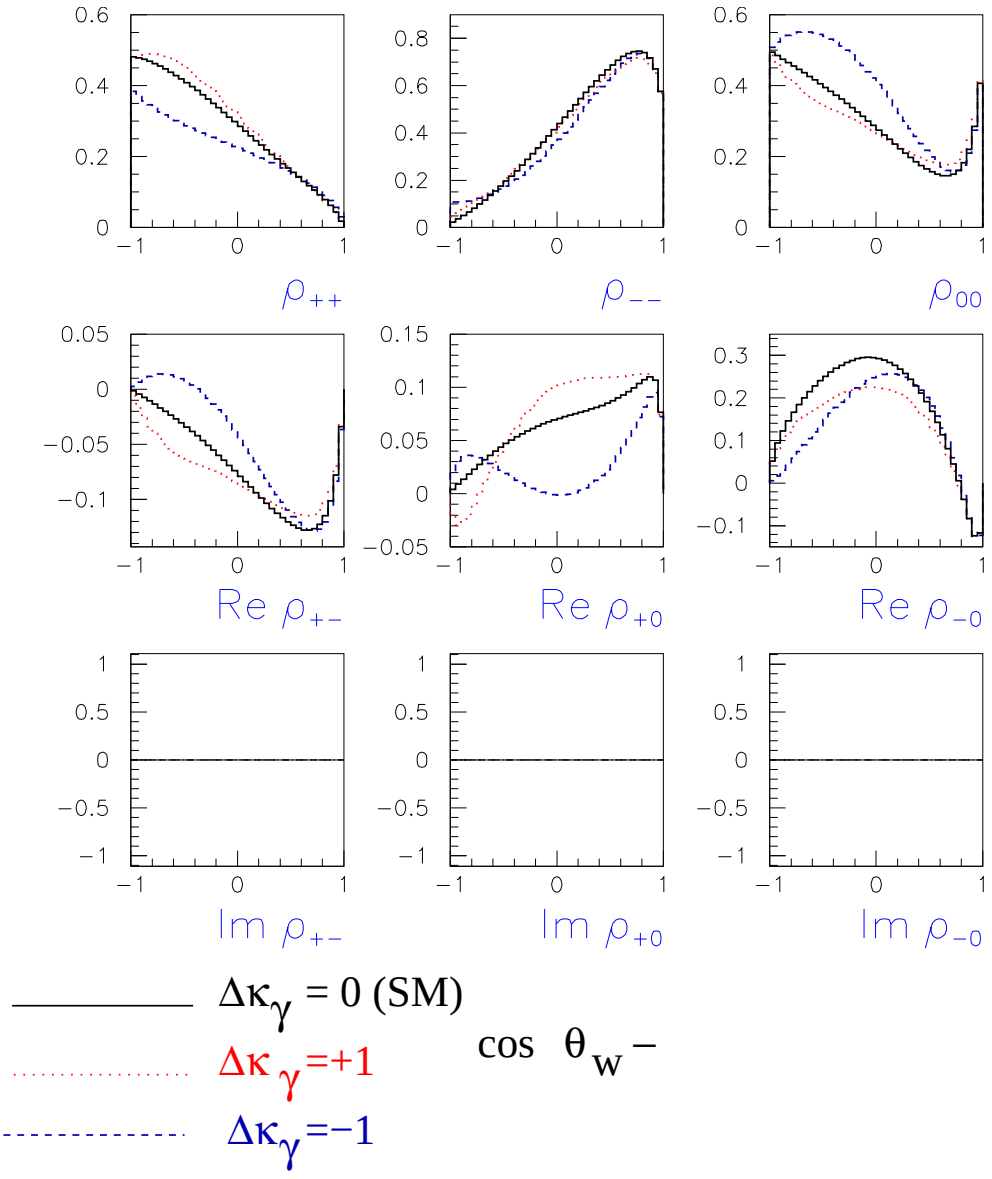

Figure 6.21: *The tree-level Standard Model prediction for the single W SDM elements for the W^- boson as function $\cos\theta_{W^-}$ at $\sqrt{s} = 189$ GeV. The effect on the SDM elements caused by the existence of an anomalous, i.e. non-Standard Model, CP-conserving coupling $\Delta\kappa_\gamma = \pm 1$ is also shown. The Bilenky-Gounaris analytical calculation is used to simulate the coupling-dependence.*

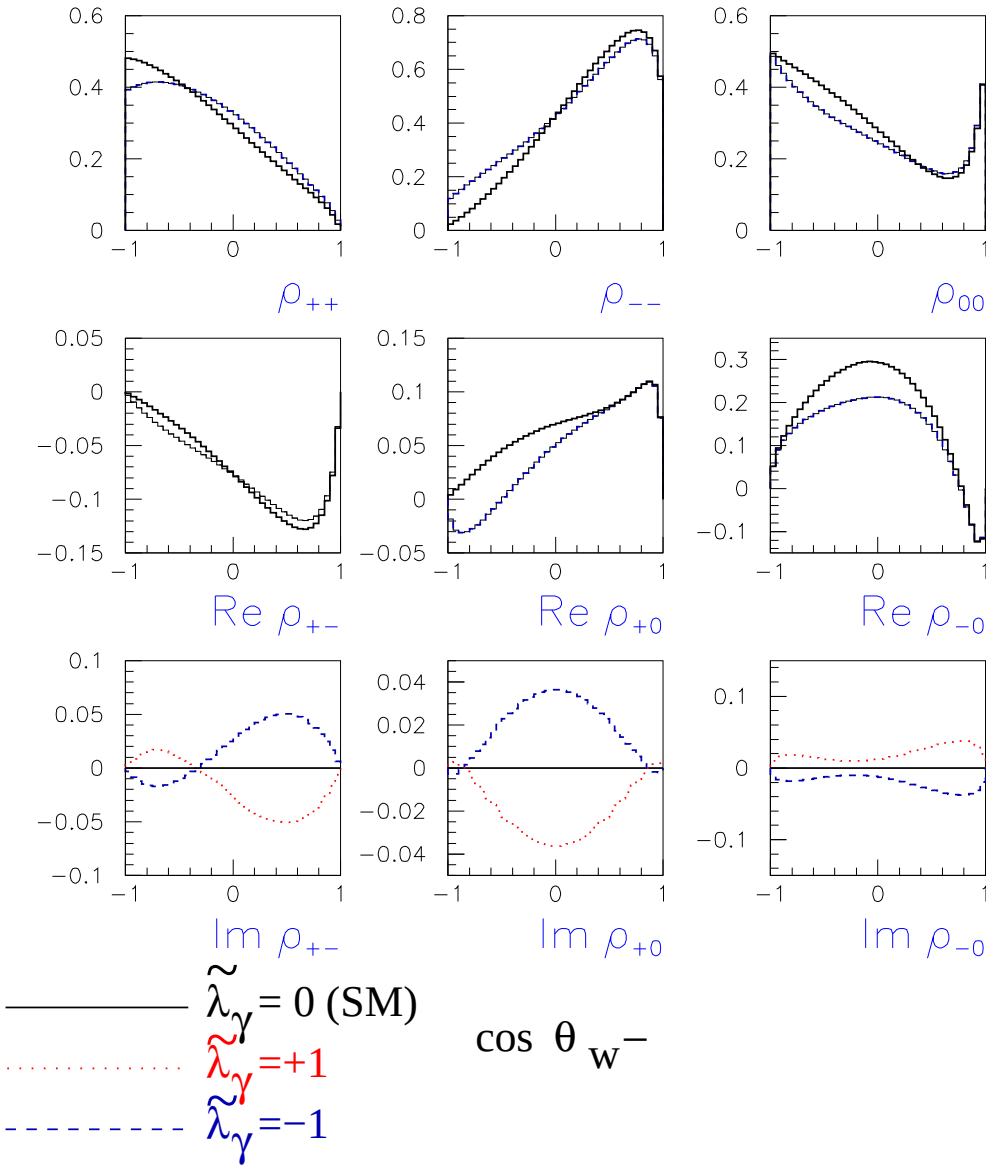

Figure 6.22: *The tree-level Standard Model prediction for the single W SDM elements for the W^- boson as function $\cos\theta_{W^-}$ at $\sqrt{s} = 189$ GeV. The effect on the SDM elements caused by the existence of an anomalous, i.e. non-Standard Model, CP-violating coupling $\tilde{\lambda}_\gamma = \pm 1$ is also shown. The Bilenky-Gounaris analytical calculation is used to simulate the coupling-dependence.*

For the real parts, CPT-invariance and CP-invariance lead to the same relations and they are not sensitive to tree-level CP-violation. The difference of the real parts of the W^- and W^+ SDM elements is zero unless CPT is violated or if the SDM analysis would be sensitive to loop-effects. A non-zero value of the sum of the imaginary parts of the W^- and W^+ SDM elements leads to the same conclusions.

Loop effects make the imaginary parts of the W^- and W^+ SDM elements deviate in a different way. Therefore suitable relations are constructed which cancel these deviations in order to be sensitive to tree-level CP violation only

$$\mathrm{Im}(\rho^{\mathrm{W}^-}_{+-}) - \mathrm{Im}(\rho^{\mathrm{W}^+}_{-+}) = 0 \tag{6.52}$$

$$\mathrm{Im}(\rho^{\mathrm{W}^-}_{+0}) - \mathrm{Im}(\rho^{\mathrm{W}^+}_{-0}) = 0 \tag{6.53}$$

$$\mathrm{Im}(\rho^{\mathrm{W}^-}_{-0}) - \mathrm{Im}(\rho^{\mathrm{W}^+}_{+0}) = 0 \tag{6.54}$$

A non-zero value of these relations points to a CP-violating mechanism at the TGC vertex at tree-level.

Conversely, relations are formed which cancel out the deviations due to tree-level CP-violation and which are exclusively sensitive to effects beyond tree-level or CPT-violation

$$\mathrm{Im}(\rho^{\mathrm{W}^-}_{+-}) + \mathrm{Im}(\rho^{\mathrm{W}^+}_{-+}) = 0 \tag{6.55}$$

$$\mathrm{Im}(\rho^{\mathrm{W}^-}_{+0}) + \mathrm{Im}(\rho^{\mathrm{W}^+}_{-0}) = 0 \tag{6.56}$$

$$\mathrm{Im}(\rho^{\mathrm{W}^-}_{-0}) + \mathrm{Im}(\rho^{\mathrm{W}^+}_{+0}) = 0 \tag{6.57}$$

These two set of equations (6.52-6.54) and (6.55-6.57) provide a completely model-independent test of CP and CPT-violation in the W-pair production process. The tests are presented in Figure 6.23 for the $qqe\nu(\gamma)$ final state and in Figure 6.24 for the $qq\mu\nu(\gamma)$ final state at the center-of-mass energies $\sqrt{s} = 189 - 209$ GeV. Within the total uncertainty, the sum as well as the difference of the imaginary parts are compatible with zero and therefore confirm the absence of CPT- and CP-violation at tree-level as predicted by the Standard Model.

The agreement with CPT- and CP-invariance is evaluated by a χ^2-test using the total uncertainty, without taking into account the correlations between $\cos\theta_{W^-}$ bins. The compatibility with the Standard Model is given in Table 6.6 for each relation separately.

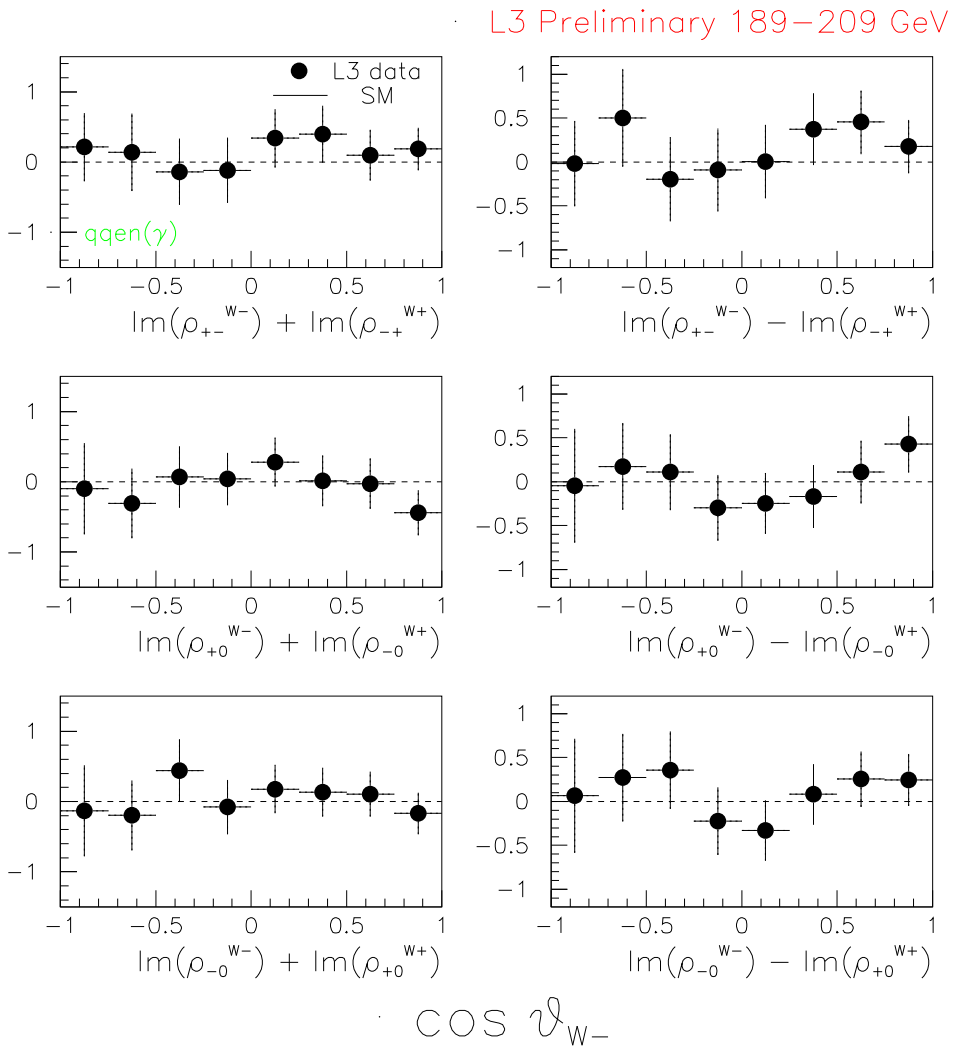

Figure 6.23: *The sum of the imaginary parts of the off-diagonal elements, sensitive to tree-level CPT-violation (Left), and the difference, sensitive to tree-level CP-violation (Right). The dots represent the* $qqe\nu(\gamma)$ *events selected by L3 at at center-of-mass energies* $\sqrt{s} = 189 - 209$ *GeV. The Standard Model prediction is presented by the horizontal line at zero. The errors bars combine statistical and systematic uncertainties.*

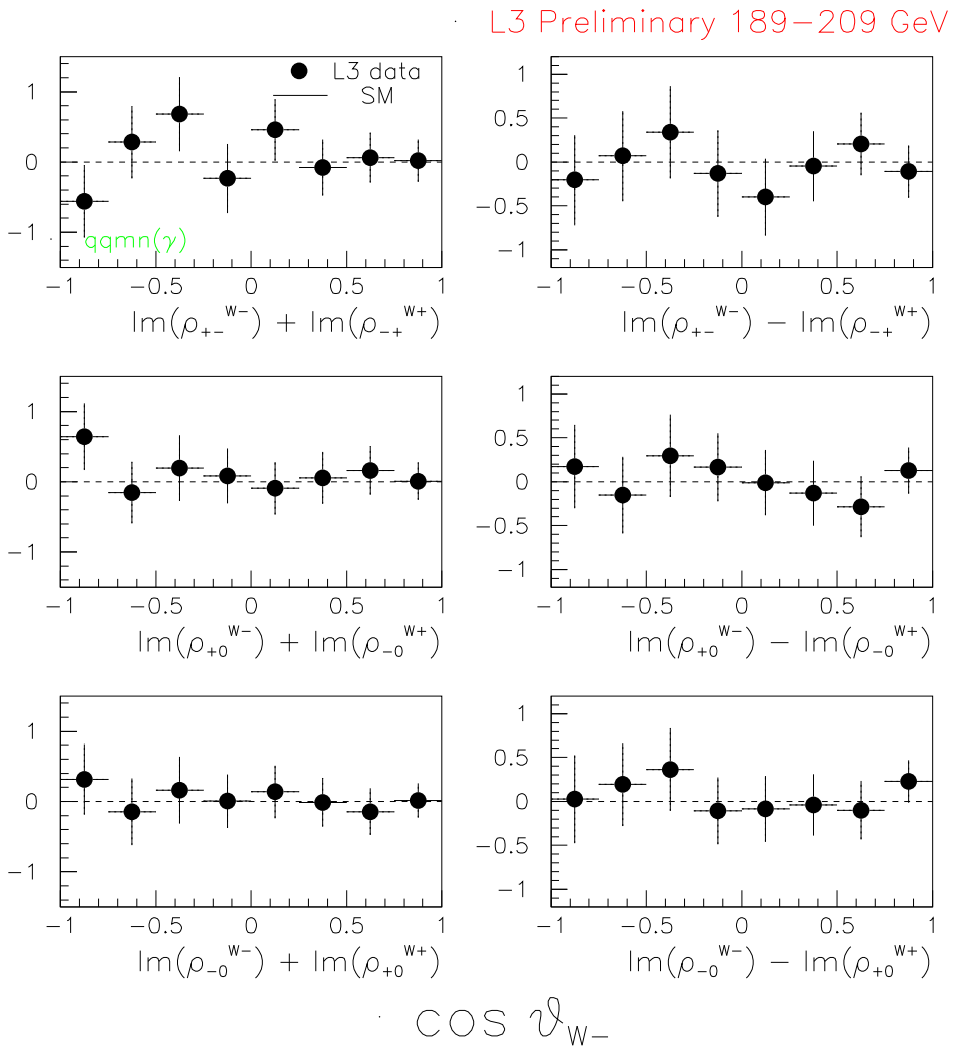

Figure 6.24: *The sum of the imaginary parts of the off-diagonal elements, sensitive to tree-level CPT-violation (Left), and the difference, sensitive to tree-level CP-violation (Right). The dots represent the $qq\mu\nu(\gamma)$ events selected by L3 at at center-of-mass energies $\sqrt{s} = 189 - 209$ GeV. The Standard Model prediction is presented by the horizontal line at zero. The errors bars combine statistical and systematic uncertainties.*

CPT-invariance $\chi^2/d.o.f. - CL$		
Test	$qqe\nu(\gamma)$	$qq\mu\nu(\gamma)$
$\mathrm{Im}(\rho^{\mathrm{W}^-}_{+-}) + \mathrm{Im}(\rho^{\mathrm{W}^+}_{-+})$	2.5/8 (96.2 %)	4.6/8 (79.9 %)
$\mathrm{Im}(\rho^{\mathrm{W}^-}_{+0}) + \mathrm{Im}(\rho^{\mathrm{W}^+}_{-0})$	2.9/8 (94.0 %)	2.4/8 (96.6 %)
$\mathrm{Im}(\rho^{\mathrm{W}^-}_{-0}) + \mathrm{Im}(\rho^{\mathrm{W}^+}_{+0})$	2.1/8 (97.8 %)	0.9/8 (99.9 %)
CP-invariance $\chi^2/d.o.f. - CL$		
Test	$qqe\nu(\gamma)$	$qq\mu\nu(\gamma)$
$\mathrm{Im}(\rho^{\mathrm{W}^-}_{+-}) - \mathrm{Im}(\rho^{\mathrm{W}^+}_{-+})$	3.7/8 (88.3 %)	1.9/8 (99.0 %)
$\mathrm{Im}(\rho^{\mathrm{W}^-}_{+0}) - \mathrm{Im}(\rho^{\mathrm{W}^+}_{-0})$	3.4/8 (90.7 %)	0.9/8 (99.9 %)
$\mathrm{Im}(\rho^{\mathrm{W}^-}_{-0}) - \mathrm{Im}(\rho^{\mathrm{W}^+}_{+0})$	3.6/8 (89.1 %)	1.9/8 (98.4 %)

Table 6.6: *The agreement with CPT- and CP-invariance, is evaluated by a χ^2-test. The $\chi^2/d.o.f.$ for each relation separately is given for the $qqe\nu(\gamma)$ and the $qq\mu\nu(\gamma)$ final state. The L3 189-209 GeV data is included.*

6.10 Combination of single-channel results

Single W SDM elements

The single W SDM elements of the $qqe\nu(\gamma)$ and $qq\mu\nu(\gamma)$ final states are combined bin-to-bin with one another. For a particular $\cos\theta_{W^-}$ bin k, the combined result is obtained as

$$\rho^{comb}(k) = \frac{1}{\omega_{tot}(k)}[\omega^e(k).\rho^e(k) + \omega^\mu(k).\rho^\mu(k)] \tag{6.58}$$

with $\omega_{tot}(k) = \omega^e(k) + \omega^\mu(k)$. The weights $\omega^e(k)$ and $\omega^\mu(k)$ are related to the statistical uncertainty on the SDM element

$$\omega^l_{\mathcal{L}}(k) = \frac{1}{\sigma^2_{stat}(\rho^l(k))} \quad (l = e,\ \mu) \tag{6.59}$$

The statistical uncertainty on the combined single W SDM element, is given by

$$\sigma_{stat}(\rho^{comb}(k)) = \sqrt{\frac{1}{\omega_{tot}(k)}} \tag{6.60}$$

For the combined systematic uncertainty, an equal weight is given to the $qqe\nu(\gamma)$ and $qq\mu\nu(\gamma)$ final states, but the way of combining depends on the type of correlation between the channels systematics [107]:

• **Channel Correlated (CC) systematic uncertainties:**

$$\sigma_{sys}^{CC}(\rho^{comb}) = \frac{\sigma_{sys}(\rho^{e}) + \sigma_{sys}(\rho^{\mu})}{2} \tag{6.61}$$

where both channels are assumed fully correlated. All CC systematic uncertainties are assumed fully positively correlated among both W-decay channels. The CC systematics are the signal cross section, the background cross sections, the hadronisation, the jet reconstruction, the ISR implementation and $\mathcal{O}(\alpha)$ corrections.

• **Channel UnCorrelated (CUC) systematic uncertainties**:

$$\sigma_{sys}^{CUC}(\rho^{comb}) = \frac{1}{2}\sqrt{\sigma_{sys}^{2}(\rho^{e}) + \sigma_{sys}^{2}(\rho^{\mu})} \tag{6.62}$$

The CUC systematics are the Monte Carlo statistics, the systematics associated to the bin-to-bin correction method, the charge confusion, the lepton reconstruction and the FSR implementation.

All systematic uncertainties are assumed uncorrelated among each other and are added in quadrature to get the total systematic uncertainty on the SDM element combining both W-decay channels. The contribution of the individual sources of systematics and the total systematic uncertainty on the combined single W SDM elements in all $\cos\theta_{W^-}$ bins are numerically presented in Appendix D1.3. The combined SDM value and its statistical uncertainty are also quoted.

The single W SDM elements as a function of $\cos\theta_{W^-}$ are presented in Figure 6.25 for the $qqe\nu(\gamma)$ and the $qq\mu\nu(\gamma)$ final states combined. The agreement with the Standard Model prediction, within the available experimental precision, statistical and systematic uncertainty combined is : $\chi^2/d.o.f. = 93.3/72$ ($CL = 4.7$ %). The correlations between $\cos\theta_{W^-}$ bins and between SDM elements are not taken into account. The agreement with anomalous CP-conserving coupling $\Delta\kappa_\gamma = +0.5$ is also evaluated in a χ^2-test and leads to $\chi^2/d.o.f. = 95.0/72$ ($CL = 3.6$ %). For the CP-violating coupling $\tilde{\lambda}_Z = -0.5$, a value $\chi^2/d.o.f. = 109.6/72$ ($CL = 2.9$ %) is obtained. The marginal agreement with the Standard Model does not allow to rule out the existence of such anomalous couplings.

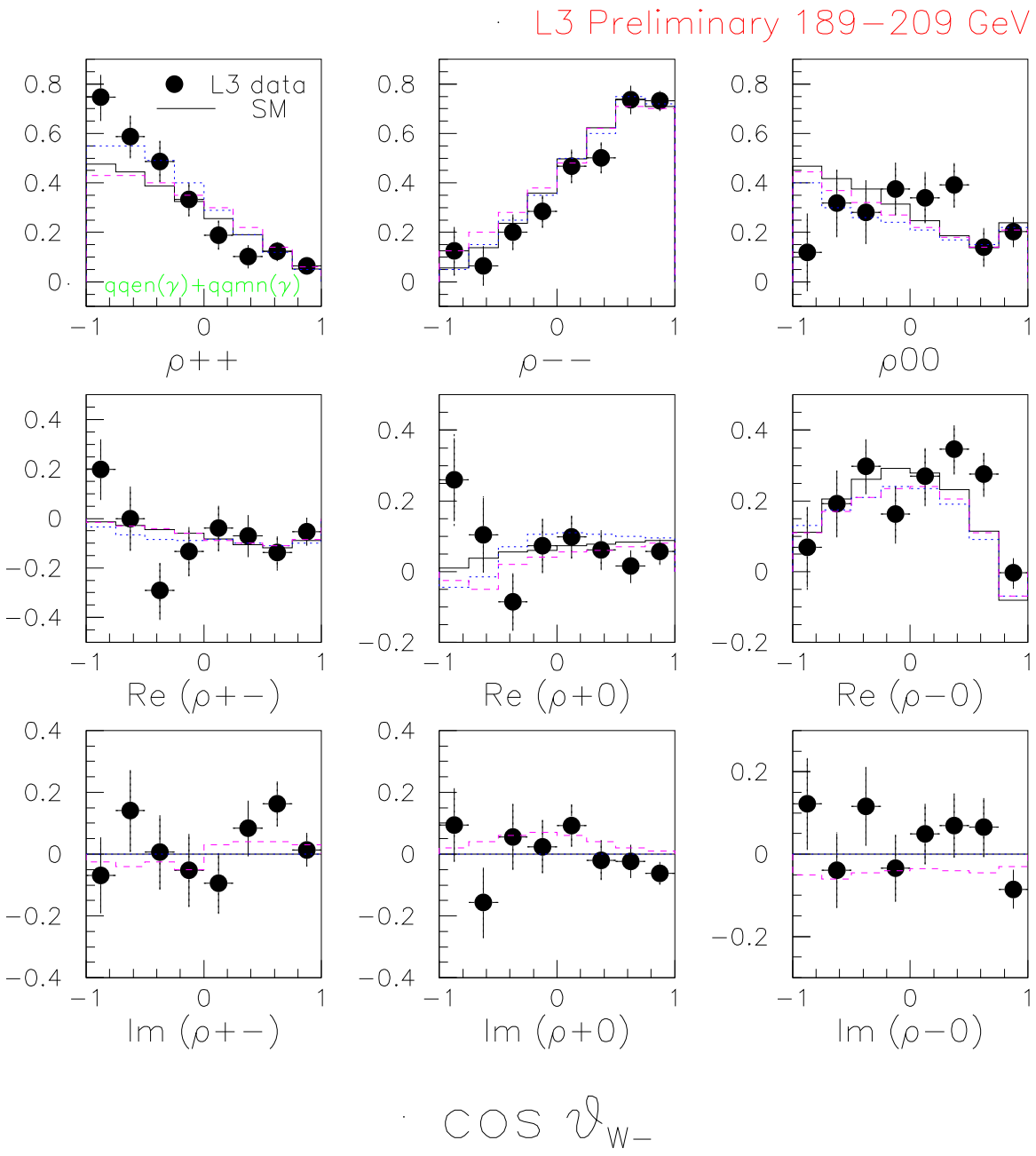

Figure 6.25: *The single SDM elements, as a function of* $\cos\theta_{W^-}$. *The dots represent the results for the L3 combined* $qqe\nu(\gamma)$ *and* $qq\mu\nu(\gamma)$ *data selected at the center-of-mass energies* $\sqrt{s} = 189 - 209$ *GeV. The error bars show the total uncertainty combining statistics and systematics contributions. The Standard Model prediction is shown by the solid line. The distributions in presence of an anomalous CP-conserving coupling* $\Delta\kappa_\gamma = +0.5$ *(blue dotted line) and an CP-violating coupling* $\tilde{\lambda}_Z = -0.5$ *(pink dashed line) are also displayed.*

Tests of CPT- and CP-invariance

The tree-level CPT- and CP-invariance tests are expressed as a sum and a difference of W^+ and W^- SDM element values. Their systematic uncertainty depends on the existence or not of correlations between the systematics for the W^+ and the W^- boson:

- **W^+ and W^- Correlated (WC) systematic uncertainties:**

$$\sigma_{sys}^{CC}(\rho^{W^+} \pm \rho^{W^-}) = \sigma_{sys}(\rho^{W^+}) \pm \sigma_{sys}(\rho^{W^-}) \tag{6.63}$$

The WC systematics are the theoretical uncertainties and the systematics associated to the bin-to-bin correction method, the ISR and FSR simulation, the $\mathcal{O}(\alpha)$ corrections, the signal and background cross sections, the jet and lepton reconstruction, the hadronisation modelling and the charge confusion correction.

- **W^+ and W^- Uncorrelated (WUC) systematic uncertainties:**

$$\sigma_{sys}^{CC}(\rho^{W^+} \pm \rho^{W^-}) = \sqrt{\sigma_{sys}^2(\rho^{W^+}) + \sigma_{sys}^2(\rho^{W^-})} \tag{6.64}$$

The WUC systematics are the statistical uncertainty and the systematics related limited Monte Carlo statistics.

The combination over the W-pair channels $qqe\nu(\gamma)$ and $qq\mu\nu(\gamma)$ proceeds according to the same rules as for the single W SDM elements. The contribution of the individual sources of systematics and the total systematic uncertainty on the CPT- and CP-invariance tests in all $\cos\theta_{W^-}$ bins are numerically presented in Appendix D2. The combined value for the test relations and its statistical uncertainty are also quoted.

The test of CP- and CPT-invariance at tree-level for the $qqe\nu(\gamma)$ and $qq\mu\nu(\gamma)$ final states combined at the center-of-mass energies $\sqrt{s} = 189 - 209$ GeV is presented in Figure 6.26. Within the experimental uncertainty, statistical and systematic uncertainty combined, the sum and the difference of the imaginary parts are compatible with zero, thus confirming the absence of CPT- and CP-violation at tree-level as predicted by the Standard Model. The compatibility with the Standard Model and with the presence of an CP-violating coupling $\tilde{\lambda}_Z = 0.5$ is expressed in Table 6.7 with a χ^2-test. The correlations between $\cos\theta_{W^-}$ bins are not taken into account.

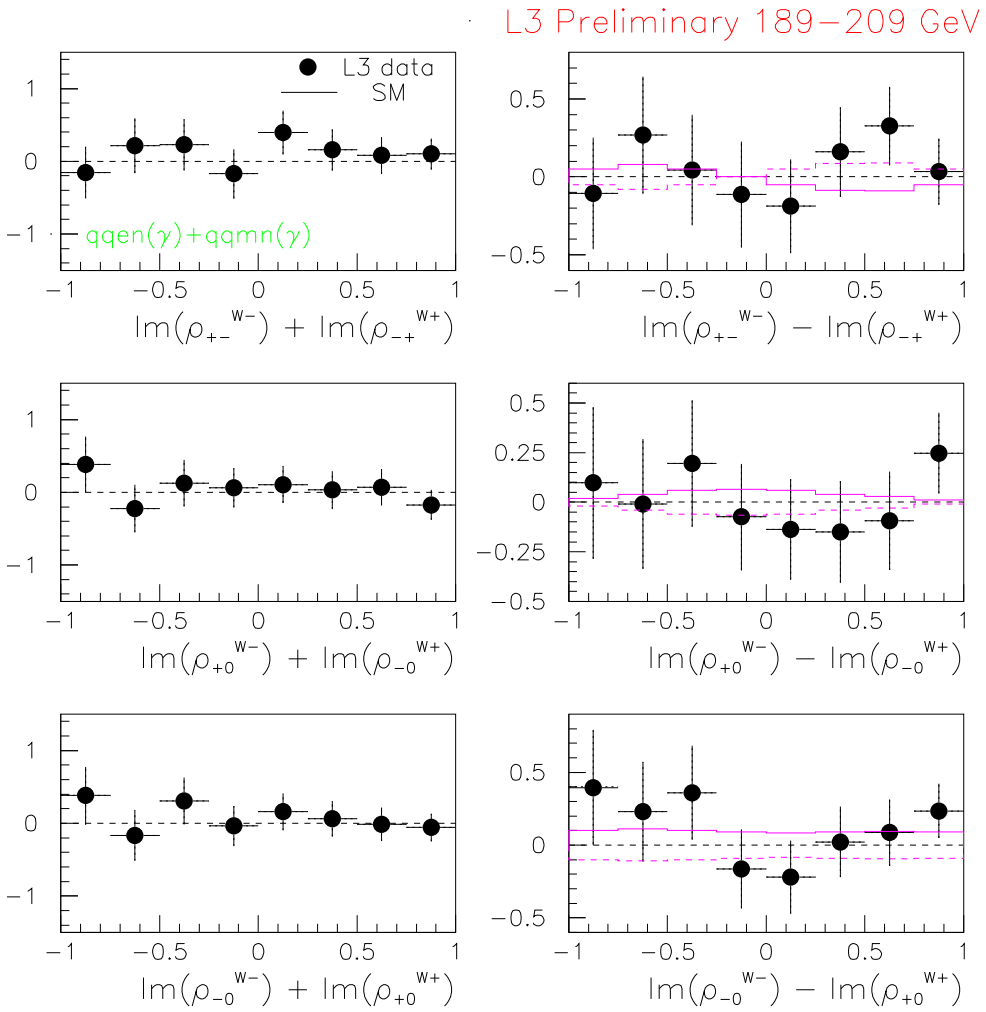

Figure 6.26: *The sum of the imaginary parts of the off-diagonal elements, sensitive to tree-level CPT-violation (Left), and the difference, sensitive to tree-level CP-violation (Right). The dots represent the combined result for the $qq\mu\nu(\gamma)$ and the $qq\mu\nu(\gamma)$ events selected by L3 at at center-of-mass energies $\sqrt{s} = 189 - 209$ GeV. The Standard Model prediction is presented by the horizontal line at zero. The dashed pink line shows the prediction for an anomalous CP-violating coupling $\tilde{\lambda}_Z = -0.5$ while the solid pink line $\tilde{\lambda}_Z = +0.5$ The errors bars combine statistical and systematic uncertainties.*

$\chi^2/d.o.f.$ - CL	
CPT-invariance test	SM
$\mathrm{Im}(\rho^{\mathrm{W}^-}_{+-}) + \mathrm{Im}(\rho^{\mathrm{W}^+}_{-+})$	3.5/8 (89.9 %)
$\mathrm{Im}(\rho^{\mathrm{W}^-}_{+0}) + \mathrm{Im}(\rho^{\mathrm{W}^+}_{-0})$	2.6/8 (95.7 %)
$\mathrm{Im}(\rho^{\mathrm{W}^-}_{-0}) + \mathrm{Im}(\rho^{\mathrm{W}^+}_{+0})$	1.8/8 (98.7 %)

$\chi^2/d.o.f.$ - CL		
CP-invariance test	SM	$\tilde{\lambda}_Z = 0.5$
$\mathrm{Im}(\rho^{\mathrm{W}^-}_{+-}) - \mathrm{Im}(\rho^{\mathrm{W}^+}_{-+})$	3.1/8 (92.8 %)	4.3/8 (82.9 %)
$\mathrm{Im}(\rho^{\mathrm{W}^-}_{+0}) - \mathrm{Im}(\rho^{\mathrm{W}^+}_{-0})$	2.8/8 (94.6 %)	2.7/8 (95.2 %)
$\mathrm{Im}(\rho^{\mathrm{W}^-}_{-0}) - \mathrm{Im}(\rho^{\mathrm{W}^+}_{+0})$	4.6/8 (79.9 %)	5.1/8 (74.7%)

Table 6.7: *The agreement with CPT- and CP-invariance, predicted by the Standard Model, is evaluated by a χ^2-test. The compatibility with the presence of an CP-violating coupling $\tilde{\lambda}_Z = 0.5$ is also evaluated. The $\chi^2/d.o.f.$ and corresponding Confidence Level(CL)is given for each relation separately. The results combine $qqe\nu(\gamma)$ and $qq\mu\nu(\gamma)$ final states and include the L3 189-209 GeV data.*

6.11 Measurement of the W-Polarisation

The first measurement by the L3 collaboration of the W-polarisation was done by fitting the analytical helicity functions to the measured angular distributions of the W-decay products [9]. The analysis is restricted to semi-leptonic W-pair events $qqe\nu(\gamma)$ and $qq\mu\nu(\gamma)$ as they present fewest ambiguities.

Denoting the fractions of helicity -1, +1 and 0 states the W^- boson as f_-, f_+ and f_0, the lepton angular spectrum in the W restframe is given by

$$\frac{1}{N}\frac{dN}{d\cos\theta_l^\star} = f_-\frac{3}{8}(1+\cos\theta_l^\star)^2 + f_+\frac{3}{8}(1-\cos\theta_l^\star)^2 + f_0\frac{3}{4}\sin^2\theta_l^\star \qquad (6.65)$$

for leptonic W^- decays. Assuming CP-invariance, f_-, f_+ and f_0 represent also the helicity fractions of helicity +1, -1 and 0 of the W^+ boson. As seen from Figure 6.27 (Left), a fit without the contribution of the longitudinal helicity state fails to describe the data. Figure 6.27 (Right) shows the angular dependence of the W helicity fractions.

The W polarisation is also obtained through the measurement of the W Spin Density Matrix. The average fraction of longitudinally polarised W bosons is given by

$$f_0 = \frac{1}{N_{ev}^{tot}}\sum_{k=1}^{N_{bins}} \rho_{00}(k) N_{ev}(k) \qquad (6.66)$$

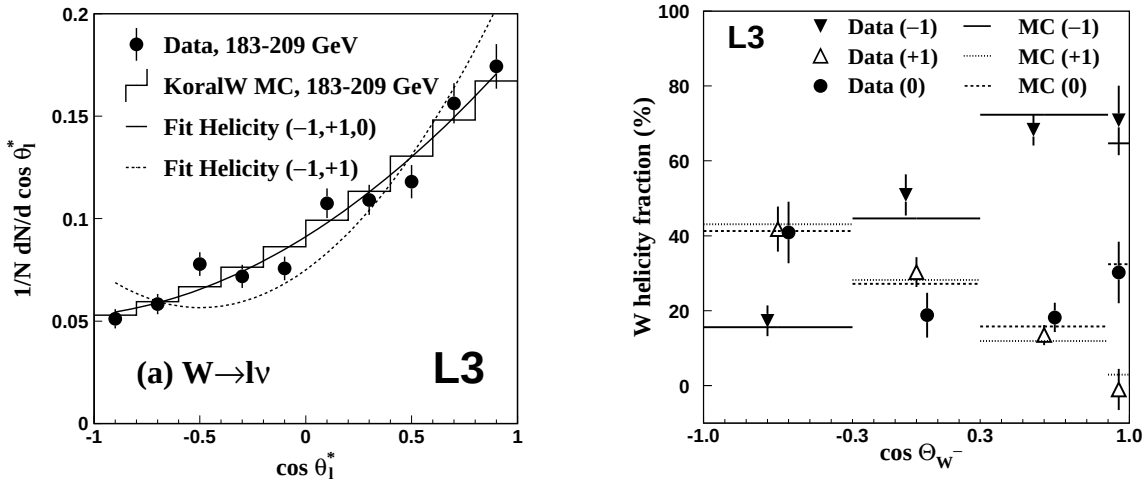

Figure 6.27: Left: *The W-decay lepton angular spectrum in the W restframe for the leptonic W decays measured in the L3 183-209 GeV data. Fits are performed taking into account only transverse helicity states (dotted line) and including both transverse and longitudinal helicity states (solid line). A fit without longitudinal contribution fails to describe the data.* Right: *The W helicity fractions as function of the cosine of the W^- production angle [9].*

where $N_{ev}(k)$ is the number of events in the $\cos\theta_{W^-}$-bin k and $N_{ev}^{tot} = \sum_{k=1}^{N_{bins}} N_{ev}(k)$. Similarly, the average fraction of transversely polarised W bosons is

$$f_+ = \frac{1}{N_{ev}^{tot}} \sum_{k=1}^{N_{bins}} \rho_{++}(k) N_{ev}(k) \tag{6.67}$$

for the helicity +1 state, and

$$f_- = \frac{1}{N_{ev}^{tot}} \sum_{k=1}^{N_{bins}} \rho_{--}(k) N_{ev}(k) \tag{6.68}$$

for the helicity -1 state. The diagonal elements of the single W SDM are normalised to unity by construction

$$\rho_{++} + \rho_{--} + \rho_{00} = 1 \tag{6.69}$$

but are not individually constrained between zero and one. Figure 6.28 shows the W helicity fraction as function of the cosine of the W^- production angle. Also the Standard Model expectation and the previous L3 measurement using a fit method, are shown. The two methods give consistent results. The large value for the longitudinal polarisation in the first $\cos\theta_{W^-}$ bins is mainly due to the contribution of the $qq\mu\nu(\gamma)$ final state.

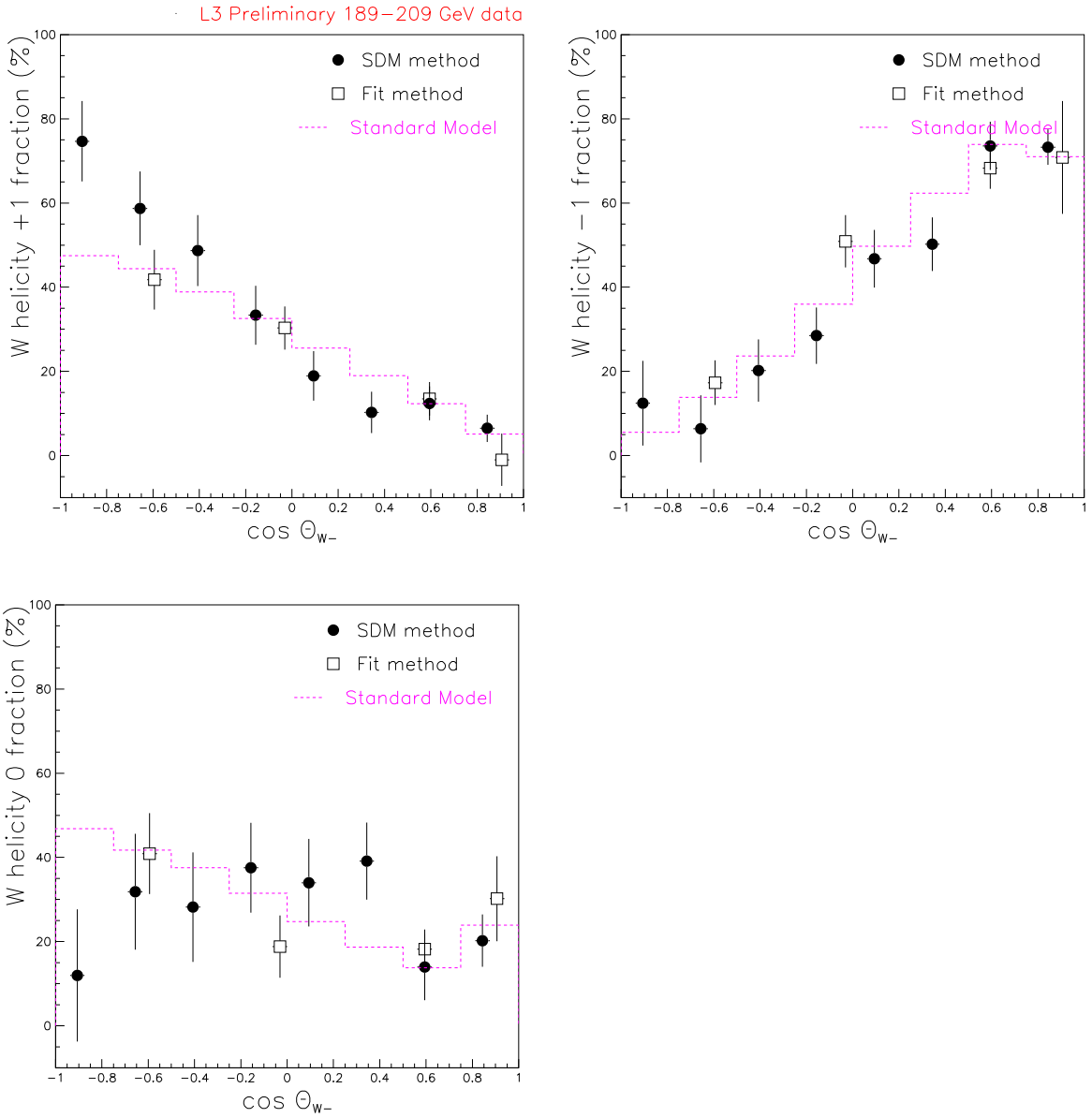

Figure 6.28: *The W transverse and longitudinal helicity fractions as function of the cosine of the W^- production angle for the 189-209 GeV data. The $qqe\nu(\gamma)$ and $qq\mu\nu(\gamma)$ final states are combined. The values obtained with the SDM method are compared to the previous L3 measurement using a fit method [9]. The error bars include statistical and systematic uncertainties. The Standard Model prediction for the W polarisation is represented by the dashed line.*

W helicity fractions			
	SDM method	Fit method	SM prediction
$f_+(\%)$	$22.2 \pm 2.3 \pm 0.7$	$18.9 \pm 1.7 \pm 1.5$	17.4 ± 0.3
$f_-(\%)$	$52.8 \pm 2.4 \pm 0.6$	$58.9 \pm 2.7 \pm 1.6$	58.6 ± 0.3
$f_0(\%)$	$25.0 \pm 3.9 \pm 1.0$	$22.1 \pm 3.6 \pm 1.7$	24.0 ± 0.5

	$\chi^2/d.o.f.$	CL
$f_+(\%)$	17.4/8	2.6 %
$f_-(\%)$	2.7/8	95.2 %
$f_0(\%)$	12.9/8	11.5.2 %

Table 6.8: *The fractions of tranversely polarised W bosons, f_+ and f_+, and the fraction of longitudinally polarised W bosons, f_0, for leptonically decaying W bosons measured from the L3 189-209 GeV data. The results include the $qqe\nu(\gamma)$ and $qq\mu\nu(\gamma)$ final states. The first uncertainty is statistical, the second is systematic. Agreement between the W helicity fractions from the SDM method and the Standard Model prediction is evaluated by a χ^2-test.*

The measured W helicity fractions are presented in Table 6.8 for the 189-209 GeV data and include the $qqe\nu(\gamma)$ and $qq\mu\nu(\gamma)$ final states. The measured values are in agreement with the Standard Model prediction, calculated as the luminosity-weighted average of the generator level KandY distributions at the different center-of-mass energies. The statistical uncertainty on the SM prediction is also given.

Chapter 7

Measurement of the W Triple Gauge Couplings

A direct consequence of the non-Abelian $SU(2)_L \otimes U(1)_Y$ gauge structure of the Standard Model is the appearance of interactions between three and four gauge bosons, the so-called Triple Gauge Couplings (TGC) and Quartic Gauge Couplings (QGC) [109]. The charged TGC's are measured in the vertices $WW\gamma$ and WWZ and are directly observed at LEP2. The QGC's in the vertices $WWWW$ and $WWZZ$ are not observable at LEP energies, while the QGC's in the vertices $WW\gamma\gamma$ and $WWZ\gamma$ are almost negligible and therefore upper limits are derived. The TGC's and QGC's are presented in Figure 7.1.

Although gauge couplings between neutral gauge bosons do not exist in the Standard Model because the Abelian groups $U(1)_Y$ and $U(1)_{em}$ commute which each other, they are searched for at LEP. They are a signature of new physics beyond the Standard Model which can manifest itself in two ways: up to now undiscovered fermions and/or bosons created on-shell and decaying to the same final state as the Standard Model gauge bosons,

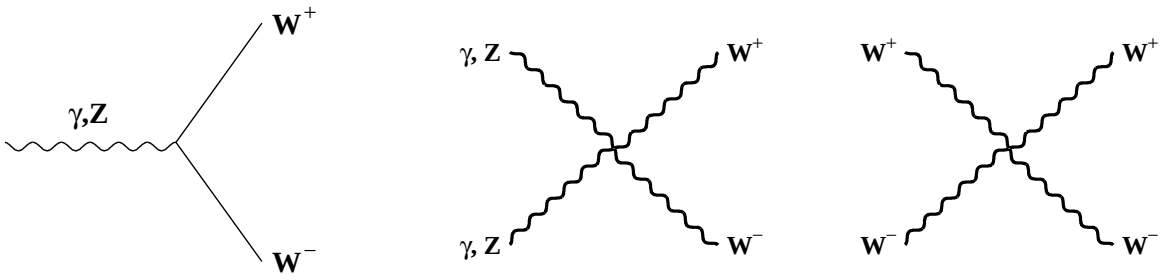

Figure 7.1: *The triple and quartic gauge couplings predicted by the Standard Model. The triple gauge couplings are studied at LEP, while the quartic gauge couplings are negligible or not observable at LEP energies.*

could contribute at tree level or modify the known, existing Standard Model vertices through radiative corrections. The deviations of possible new physics like supersymmetry, technicolor, composite W bosons, etc, are estimated of the same order of the already existing Standard Model radiative corrections i.e. 10^{-3} depending on the coupling parameter. This is smaller than the expected LEP2 sensitivity of the order $10^{-1} - 10^{-2}$ [27]. As the t-channel W-pair production process involves the exchange of a neutrino, W TGC's are only measurable in the ZWW and γWW vertices of the s-channel W-pair production process. Because of the dominance of t-channel process at LEP energies, the LEP2 sensitivity to anomalous TGC's is limited to the coherent interference between the t-channel and s-channel processes.

7.1 Previous Direct and Indirect measurements

The first direct limits [110] were obtained in the eighties at the e^+e^- colliders PEP (SLAC) and PETRA (DESY) where the process, $e^+e^- \to \nu\bar{\nu}\gamma$, was studied. Only a weak bound on the coupling κ_γ could be derived : $-73.5 < \Delta\kappa_\gamma < 37.0$ (90% CL).
A couple of years later, the UA2 experiment made the limit on κ_γ one order of magnitude more stringent [111]: $-3.5 < \kappa_\gamma < 5.9$ (95% CL). They also performed the first measurement of the coupling λ_γ: $-3.6 < \lambda_\gamma < 3.5$ (95% CL).

In the ninties, more precise measurements became possible with the hadron collider TEVATRON. The DØ experiment studied three gauge boson final states in $\bar{p}p$ collisions at $\sqrt{s} = 1.8$ TeV [112]: $\bar{p}p \to W\gamma + X$, $\bar{p}p \to W^+W^- + X \to l^+\nu l^-\bar{\nu} + X$ $(l = e, \mu)$ and $\bar{p}p \to WW/WZ + X \to l\nu jj + X$. The transverse energy distribution of the final state gauge boson or the decay leptons from the gauge boson pair were used in a binned maximum likelihood fit. One coupling was varied at a time while the others were fixed to their Standard Model value. The following 95 %CL limits were obtained by the DØ experiment:

$$-0.30 < \Delta\kappa_\gamma < 0.43$$

$$-0.20 < \lambda_\gamma < 0.20$$

$$-0.29 < \Delta g_1^Z < 0.57$$

assuming the scale of new physics at 2.0 TeV. The couplings κ_γ and λ_γ were also measured by the CDF experiment but only with W-pair production with leptonic W-decay, at $\sqrt{s} = 1.8$ TeV [113] and therefore the bounds are weaker than the ones obtained by the DØ experiment.

The W-γ couplings were also studied at the ep colliders HERA. The ZEUS experiment searched for leptonic W-decays in single W production, $e^+p \to e^+W^\pm + X$, at a center of mass energy $\sqrt{s} = 300$ GeV [114].

They derived at 95% CL

$$-4.7 < \Delta\kappa_\gamma < 1.5$$

$$-3.2 < \lambda_\gamma < 3.2$$

The first indirect limits on TGC's were derived from loop corrections containing VWW ($V = \gamma, Z$) vertices. The most stringent indirect bounds come from the precision measurements at the Z-peak [115] where TGC's were measured through their impact on radiative corrections to fermion pair production in e^+e^- interactions. The following results were obtained when varying one coupling and fixing the other one to its Standard Model value: $\Delta g_1^Z = -0.017 \pm 0.018$ and $\Delta\kappa_\gamma = -0.016 \pm 0.019$. When both couplings are allowed to vary, the limits decrease to $\Delta g_1^Z = -0.013 \pm 0.027$ and $\Delta\kappa_\gamma = -0.005 \pm 0.029$. In both cases there is a good agreement with the Standard Model prediction $\Delta g_1^Z = 0$ and $\Delta\kappa_\gamma = 0$. When restricting the analysis to the $Z \to b\bar{b}$ channel, also the couplings λ and g_5^Z can be measured [116]: $|\lambda_\gamma| = |\lambda_Z| \lesssim 0.81$ and $|g_5^Z| \lesssim 0.23$ while the Standard Model values are $\lambda_\gamma = \lambda_Z = 0$ and $g_5^Z = 0$. Atomic parity violation measurements tighten the bound on the coupling λ to $-0.02 < \lambda < 0.08$ [117].

Much weaker constraints come from the measurement of the muon's anomalous magnetic moment $(g-2)_\mu$ [112], the inclusive radiative penguin decay $b \to s\gamma$ [118] and the flavour-changing neutral current decay of B mesons at hadron colliders [119]. Comparison between the measured muon magnetic dipole moment and the theoretical estimate led to the following estimate: $|\lambda_\gamma| =\lesssim 5$. A non-zero coupling $\tilde{\lambda}_\gamma$ would induce an electric dipole moment for the quark and therefore a sever limit $|\tilde{\lambda}_\gamma| \lesssim 2.5\ 10^{-4}$ was derived using the experimental upper bound on the neutron electric dipole moment.

7.2 Extraction Methods

All the information available for the TGC measurement is contained in the five-fold cross section

$$\frac{d^5\sigma(e^+e^- \to W^+W^- \to f_1\bar{f}_2 f_3\bar{f}_4)}{d\cos\theta_{W^-}\ d\cos\theta^*_{f_1}\ d\phi^*_{f_1}\ d\cos\theta^*_{\bar{f}_4}\ d\phi^*_{\bar{f}_4}} \tag{7.1}$$

However, experimentally one can not distinguish the quark from the antiquark in a hadronic W-decay as charge reconstruction and flavor tagging are very difficult to realise in a single jet. The angular distributions are therefore folded and restricted to $0 < \theta^*_q < \pi/2$ and $0 < \phi^*_q < \pi$. In case of a leptonic W-decay, the presence of undetectable neutrinos reduces the reliability of the reconstruction.

For semi-leptonic W-pair events, the charge of the hadronically decaying W is tagged by the lepton charge. The convention is made to represent the angles of the negative lepton from a W^--decay. This implies that the decay angles of a positive lepton from a W^+-decay are transformed assuming that W^+ and W^- bosons have the same behaviour (CPT-invariance). In practice, the following distributions are taken into account

- $W^+W^- \rightarrow qqqq : \cos\theta_{W^-},\ (\cos\theta^\star_{q_1}, \phi^\star_{q_1})_{fold},\ (\cos\theta^\star_{q_2}, \phi^\star_{q_2})_{fold}$
- $W^+W^- \rightarrow qqe\nu,\ qq\mu\nu,\ qq\tau\nu : \cos\theta_{W^-}, (\cos\theta^\star_l, \phi^\star_l),\ (\cos\theta^\star_q, \phi^\star_q)_{fold}$
- $W^+W^- \rightarrow l\nu l\nu\ :\ \sigma_{tot}$ information

The largest sensitivity comes from the W polar decay angle distribution. A kinematic fit is performed to improve the resolution on the measured energies and angles of the reconstructed leptons and jets.

At LEP, the methods used to extract W TGC's are the Binned Maximum Likelihood method (BML) [120], the Optimal Observable (OO) method [121, 122] and more recently the Spin Density Matrix method (SDM) [123]. All methods extract the couplings directly or indirectly from the above mentionned five-dimensional angular distributions. The main interest of the SDM method is its possibility to extract not only CP-conserving couplings but also to set limits on CP-violating ones, absent in the Standard Model.

The L3 TGC measurement uses the BML method to extract the CP-conserving couplings g_1^Z, κ_γ and λ_γ. The OO method is used as a cross check.

7.2.1 Binned Maximum Likelihood method

The five-dimensional phase space is devided into bins with a size chosen to get an optimal sensitivity for the available Monte Carlo statistics. The coupling dependence is introduced by event-by-event reweighting at generator level of the fully simulated baseline Monte Carlo events and the couplings are extracted by a maximum likelihood fit.
For each decay channel i and at each center-of-mass energy $\sqrt{s}$, a likelihood function is constructed as the product of the Poisson probabilities for the occupation in each bin j of the 5D phase space Ω_{5D}

$$L_i(\alpha, \sqrt{s}) = \prod_j \frac{e^{-\mu_j(\alpha)} \mu_j(\alpha)^{N^j_{data}}}{N^j_{data}!} \tag{7.2}$$

where α represents the set of fitted couplings, N^j_{data} the number of selected data events in the bin j and μ_j the number of expected signal and background events in the j-th bin.

The latter is expressed as

$$\mu_j(\alpha) = \sum_{signal+bkg\ k} \frac{\sigma^k_{gen}\mathcal{L}_{data}}{N^k_{gen}} \sum_{l=1}^{N^j_{acc}} \frac{\mid \mathcal{M}_k(\Omega^l_{5D},\alpha) \mid^2}{\mid \mathcal{M}_k(\Omega^l_{5D},\alpha_{SM}) \mid^2} \tag{7.3}$$

where $\mathcal{M}_k(\Omega^l_{5D},\alpha)$ and $\mathcal{M}_k(\Omega^l_{5D},\alpha_{SM})$ are the matrix elements of the final state of the processus k, for a set of couplings α and α_{SM}, and for an event generated in the phase space Ω^l_{5D}. The first sum extends over all signal and background processes with cross section σ^k_{gen} represented by N^k_{gen} Monte Carlo events. The second sum runs over all the accepted Monte Carlo events N^j_{acc} in the bin j. For the background processes which do not contain the studied TGC vertex $\mid \mathcal{M}_k(\Omega^l_{5D},\alpha) \mid^2 / \mid \mathcal{M}_k(\Omega^l_{5D},\alpha_{SM}) \mid^2 = 1$.

The likelihood functions of the different channels and center-of-mass energies are finally combined

$$L(\alpha) = \prod_{channel\ i} \prod_{\sqrt{s}} L_i(\alpha,\sqrt{s}) \tag{7.4}$$

where i is the channel number and where α represents the couplings allowed to vary in the fit.

7.2.2 Optimal Observable method

In this method, the five-dimensional phase space Ω, is projected onto one or two parameters per TGC, called optimal observables. As the electroweak Lagrangian of Eq. 2.68 is linearly dependent on the TGC's, the coupling-dependent differential cross section for W-pair production is expressed as a polynomial of second order

$$\frac{d\sigma(\alpha)}{d\Omega} = c^0(\Omega) + \sum_i c^1_i(\Omega)\alpha_i + \sum_{i\leq j} c^2_{ij}(\Omega)\alpha_i\alpha_j \tag{7.5}$$

and the optimal observables are defined as

$$\mathcal{O}^1_i = \frac{c^1_i(\Omega)}{c^0(\Omega)} \quad \mathcal{O}^2_{ij} = \frac{c^2_{ij}(\Omega)}{c^0(\Omega)} \tag{7.6}$$

The optimal observable distributions reconstructed in the data are fitted and the couplings are extracted by χ^2-minimisation.

7.2.3 Spin Density Matrix method

The Spin Density Matrix (SDM) method [108] for W TGC extraction consists of three main steps.

First, the angular distributions of the W bosons and the W-decay leptons are measured and used to calculate the SDM elements in bins of $\cos\theta_{W^-}$. No bin-to-bin detector correction is applied and the reconstructed angles are directly used.

In the second step, coupling-dependent SDM elements are constructed using the WW helicity amplitudes, provided by the Bilenky-Gounaris formalism (Appendix A), which depend on the 14 W TGC's. The event SDM elements, ρ_{ev}^{PO}, are calculated by applying the projection operators on the reconstructed Standard Model Monte Carlo events, and they are modified event-by-event to include the coupling dependence ρ_{ev}^{bilgou}. Hereby, there are two possible approaches: an additive approach, where the coupling-dependence is added to ρ_{ev}^{PO},

$$\rho_{ev}(\vec{\alpha}) = \rho_{ev}^{PO} + (\rho_{ev}^{bilgou}(\vec{\alpha}) - \rho_{ev}^{bilgou}(\vec{\alpha}_{SM})) \tag{7.7}$$

and a multiplicative approach, where ρ_{ev}^{PO} is multiplied by a coupling-dependent factor,

$$\rho_{ev}(\vec{\alpha}) = \rho_{ev}^{PO} \times \frac{\rho_{ev}^{bilgou}(\vec{\alpha})}{\rho_{ev}^{bilgou}(\vec{\alpha}_{SM})} \tag{7.8}$$

where $\vec{\alpha}$ represents a general set of triple gauge couplings $\vec{\alpha}$ and $\vec{\alpha}_{SM}$ the set of Standard Model couplings. The explicite form of $\rho^{bilgou}(\vec{\alpha})$ is found in Appendix A (Eq. A.7). As the imaginiary part of the off-diagonal elements are zero in the Standard Model, the multiplicative approach is not usable for the imaginary part of the SDM, and the additive approach is chosen. However, consistent results were found between both approaches for the diagonal elements and the real parts of the off-diagonal elements.

The coupling-dependent SDM element in a particular bin k of the $\cos\theta_{W^-}$ distribution is given by

$$\rho(k, \vec{\alpha}) = \frac{1}{N_k} \sum_{i=1}^{N_k} \rho_{ev}(k, \vec{\alpha}) \tag{7.9}$$

where N_k is the number of events in the bin k.

Finally, the obtained coupling-dependent SDM elements are fitted to experimental distributions and the couplings are extracted by χ^2-minimisation.

The χ^2 of the SDM-fit is defined as

$$\chi^2_{SDM} = \sum_{k=1}^{N_{bins}} \sum_{element\ i} \sum_{element\ j} [\rho_i^{data}(k) - \rho_i(k,\vec{\alpha})]\ M^{-1}_{cov}(i,j)\ [\rho_j^{data}(k) - \rho_j(k,\vec{\alpha})] \quad (7.10)$$

The SDM elements covariance matrix, $M_{cov}(i,j)$, includes the correlations between the elements and the physical constraint

$$\rho_{++}(k) + \rho_{--}(k) + \rho_{00}(k) = 1 \quad (7.11)$$

for each $\cos\theta_{W^-}$-bin k. The first sum is made over the $\cos\theta_{W^-}$-bins, N_{bins}, and the second and third sum over the SDM elements. As off-diagonal SDM elements are not sensitive to CP-conserving couplings, the sum over the SDM elements is restricted to the diagonal elements and the real parts of the off-diagonal elements when a CP-conserving coupling is studied, leading to 40 degrees of freedom taking into account Eq. 7.11. For the CP-violating coupling, all 9 SDM elements are used, resulting in 72 degrees of freedom. To increase the sensitivity, also the $\cos\theta_{W^-}$ distribution is fitted in parallel.

The next subsections show the results of some preliminary tests to investigate the the feasibility of the SDM method for the extraction of CP-violating couplings.

Sensitivity of the SDM TGC-analysis

As explained in Appendix A, several approximations are made in the Bilenky-Gounaris prediction. Consequently, the additive approach might introduce a potential source of bias. Therefore, the agreement between the projection operator method and the Bilenky-Gounaris prediction is studied with the Standard Model. The generator level CC03 Standard Model KandY at $\sqrt{s} = 189$ GeV is used as test sample in the fit. The results are presented in Table 7.2. A good agreement is found between the fitted values and their Standard Model prediction which is zero for all 14 couplings. For CP-conserving couplings, the main sensitivity is found in the $\cos\theta_{W^-}$ distribution, but for CP-violating couplings, the SDM distributions are most sensitive.

Linearity test

To test if the coupling-dependence is well simulated by the Bilenky-Gounaris prediction in the additive approach, the 189 GeV KandY Monte Carlo samples generated with non-Standard Model CP-conserving couplings $\Delta\kappa_\gamma = 0, \pm 1 \pm 2$ and CP-violating couplings $g_5^Z = 0, \pm 1 \pm 2$ are used as test samples in the fit. The result is presented in Figure 7.3. An excellent linearity is obtained.

CP-conserving couplings

	SDM elements		$\cos\theta_{W^-}$ distribution	
Coupling	Fitted Value	χ^2/ndf	Fitted Value	χ^2/ndf
$\Delta\kappa_\gamma$	$-0.030^{+.034}_{-.033}$	33.6/40	$-0.021^{+.022}_{-.022}$	19.4/8
$\Delta\kappa_Z$	$-0.004^{+.012}_{-.013}$	34.2/40	$-0.008^{+.008}_{-.008}$	19.2/8
Δg_1^γ	$-0.026^{+.023}_{-.023}$	33.0/40	$-0.008^{+.009}_{-.008}$	19.4/8
Δg_1^Z	$-0.011^{+.010}_{-.010}$	33.2/40	$-0.004^{+.004}_{-.004}$	19.2/8
λ_γ	$-0.006^{+.015}_{-.016}$	34.2/40	$-0.007^{+.008}_{-.008}$	19.6/8
λ_Z	$-0.006^{+.015}_{-.016}$	34.2/40	$-0.007^{+.008}_{-.008}$	19.6/8
g_5^γ	$+0.006^{+.023}_{-.024}$	34.7/40	$+0.045^{+.011}_{-.011}$	3.3/8
g_5^Z	$-0.018^{+.017}_{-.017}$	33.2/40	$+0.024^{+.006}_{-.006}$	5.3/8

CP-violating couplings

	SDM elements		$\cos\theta_{W^-}$ distribution	
Coupling	Fitted Value	χ^2/ndf	Fitted Value	χ^2/ndf
g_4^γ	$+0.032^{+.054}_{-.054}$	80.1/64	$+0.000^{+.253}_{-.253}$	20.2/8
g_4^Z	$+0.027^{+.024}_{-.024}$	79.8/64	$+0.000^{+.177}_{-.177}$	20.2/8
$\tilde{\kappa}_\gamma$	$+0.089^{+.056}_{-.087}$	79.4/64	$-0.056^{+.193}_{-.081}$	20.2/8
$\tilde{\kappa}_Z$	$-0.027^{+.026}_{-.017}$	79.4/64	$-0.017^{+.058}_{-.024}$	20.2/8
$\tilde{\lambda}_\gamma$	$-0.009^{+.016}_{-.016}$	80.2/64	$+0.000^{+.076}_{-.076}$	20.2/8
$\tilde{\lambda}_Z$	$-0.009^{+.016}_{-.016}$	80.2/64	$+0.000^{+.076}_{-.076}$	20.2/8

Figure 7.2: *The agreement between the projection operator method and the Bilenky-Gounaris prediction for the Standard Model. The generator level CC03 Standard Model KandY at $\sqrt{s} = 189$ GeV is used as test sample in the fit. All fitted couplings are zero in the Standard Model.*

Since the SDM method with a Bilenky-Gounaris prediction for the coupling-dependence, is proven to work properly, it can be applied to the data to extract the W triple gauge couplings.

7.3 Results

In the L3 data analysis using the binned maximum likelihood method, a fit is performed to each of the three couplings κ_γ, λ_γ and g_1^Z individually but also simultaneous fits to two or three of these couplings are performed [120]. The fits are presented in Figure 7.4. The Standard Model coupling values are represented with a star.

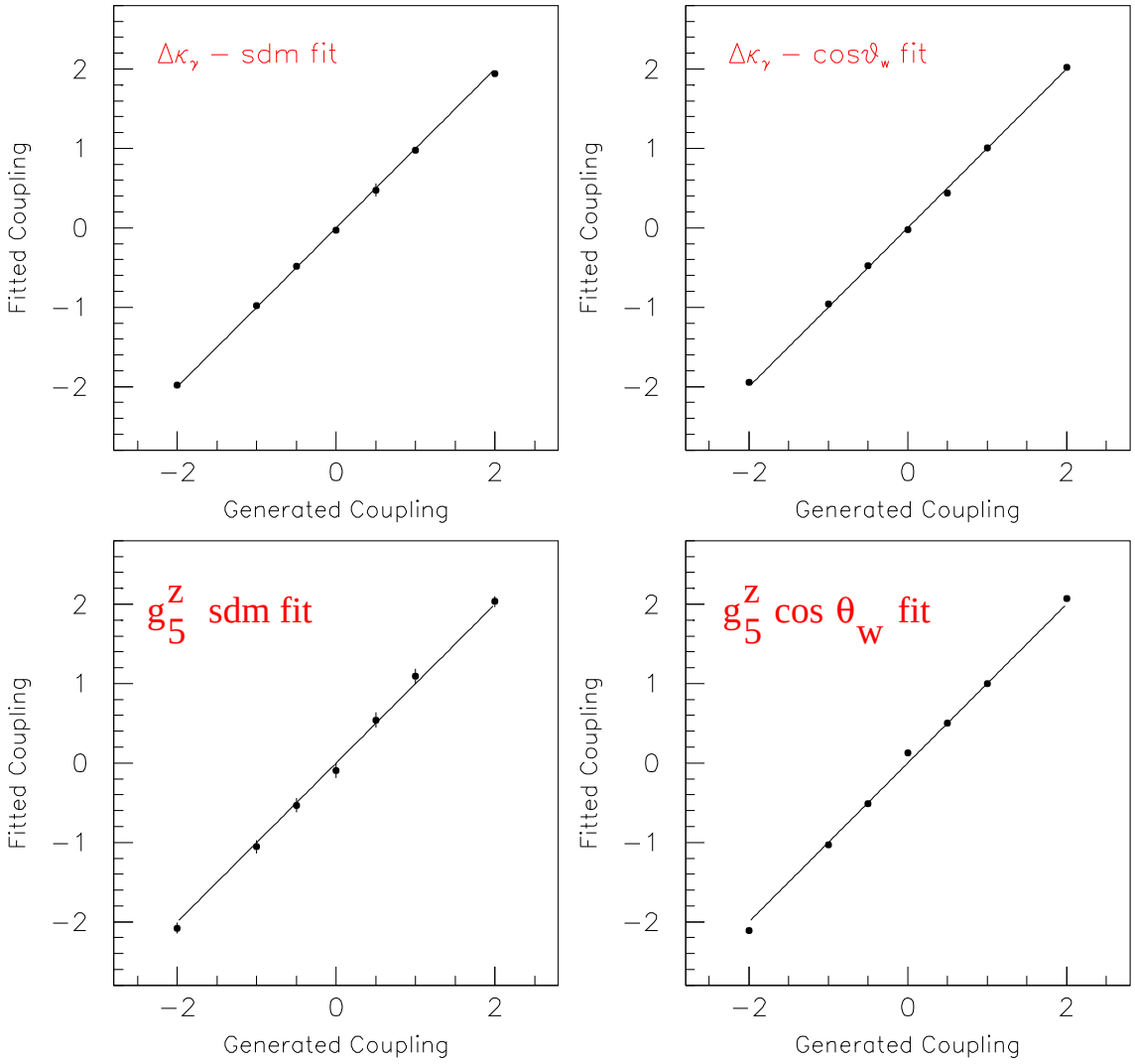

Figure 7.3: *The linearity test for the coupling-dependence simulated by the Bilenky-Gounaris prediction in the additive approach. The fitted coupling is compared to the generated coupling for the SDM and the* $\cos\theta_W$*- χ^2-fit. The solid line represents the exact linearity.*

The horizontal and vertical solid lines represent the 68 % confidence level intervals when all couplings are fixed to their Standard Model value. The shaded and white areas represent the results of the 68 % and 95 % confidence level regions for the two-parameter fit: (a) g_1^Z and κ_γ with $\lambda_\gamma = 0$, (b) λ_γ and κ_γ with $g_1^Z = 1$, and (c) g_1^Z and λ_γ with $\kappa_\gamma = 1$. The two-dimensional projections of the three-parameter log-likelihoods are represented by the dashed line.

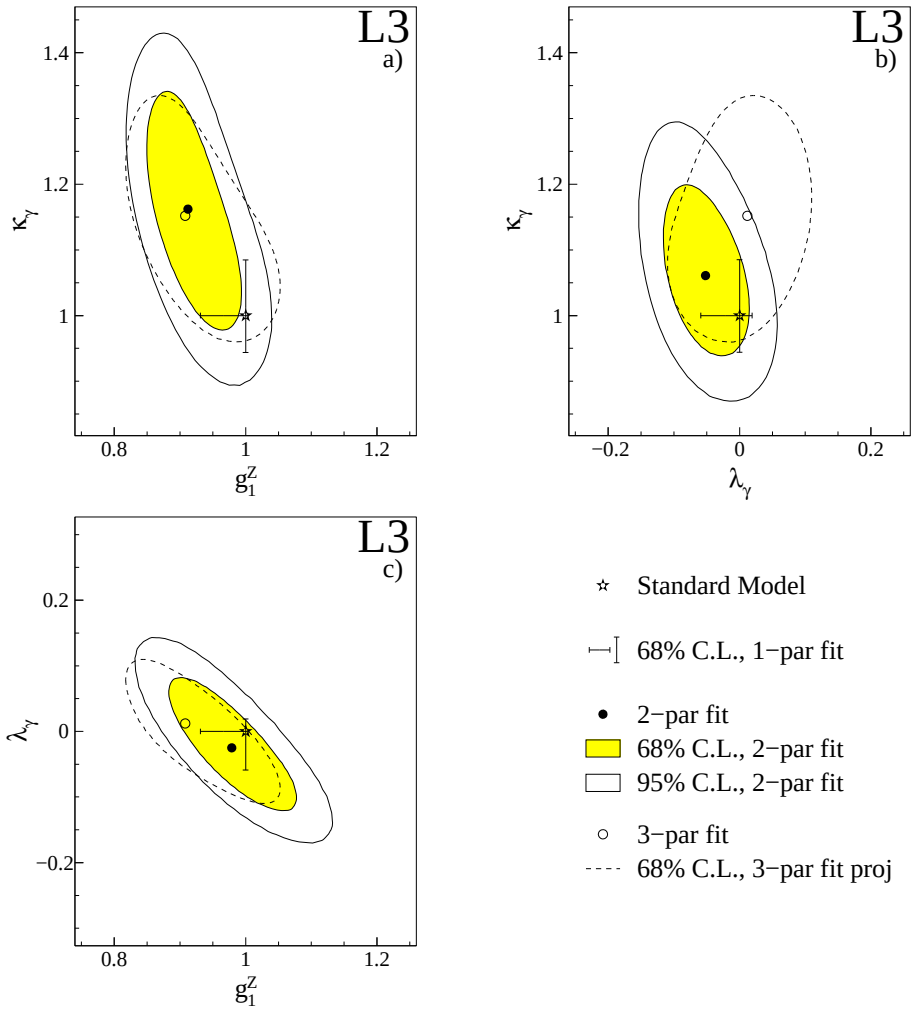

Figure 7.4: *The one-, two- and three-dimensional TGC fits of the couplings (a): g_1^Z and κ_γ, (b): λ_γ-κ_γ (b) and (c): g_1^Z-λ_γ.*

The L3 results are consistent with the ose from the other LEP collaborations and with the Standard Model predictions. A prelimary combination [100] gives

$$g_1^Z = 0.991^{+0.022}_{-0.021} \tag{7.12}$$

$$\kappa_\gamma = 0.984^{+0.042}_{-0.047} \tag{7.13}$$

$$\lambda_\gamma = -0.016^{+0.021}_{-0.023} \tag{7.14}$$

The uncertainty is dominated by the statistical component. The theoretical uncertainty on the differential cross section as function of the W production angle is the most important source of systematics.

Conclusions

The LEP high energy runs have produced large statistics samples of W-pair events. The L3 data of the reaction $e^+e^- \to W^+W^-$ allows precise measurements of the cross section and the angular distributions.

The cross section for W-pair production has been measured from 161 GeV up to 209 GeV. The excellent agreement with the Standard Model prediction confirms the existence of the triple gauge boson vertices $WW\gamma$ and WWZ and consequently, the non-Abelian nature of the electroweak interactions.

The Spin Density Matrix (SDM) of the W boson has been studied as function of the W-production angle in the center-of-mass energy range $\sqrt{s} = 189 - 209$ GeV. Within the statistical precision, a good agreement was found with the Standard Model distributions.

The SDM analysis was also used to perform tests on CPT- and CP-invariance in W-pair production at tree level. No evidence was found for CPT- or CP-violation in the electroweak sector of the W boson, but the statistical precision of the analysis does not allow a sensitivity to loop effects beyond tree-level.

The fraction of longitudinally polarised W bosons was found in agreement with the Standard Model prediction. The measurement is complementary to the W-polarisation studies by the CDF and the DO collaborations at the Tevatron collider at Fermilab [124, 125] in the $t \to Wb$ decay where the W is not created in an interaction between electroweak gauge bosons.

The SDM analysis offers a model independent way to study the W boson polarisation and to extract triple gauge couplings. The SDM technique will gain importance with the future Linear Collider (LC) [126]. For polarised beams, the accuracy on the coupling measurement with the TESLA LC, is estimated of the order of few 10^{-4}, a sensitivity that allows tests at loop level [127].

The LEP measurements increased the credibility of the Standard Model as a theory that provides an accurate description of matter and forces. However, the validity of Standard Model is believed to break down at center-of-mass energies beyond those accessible at LEP. The next step in the understanding of the Standard Model will be taken by the LHC, under construction at CERN and whose first data taking is planned for summer 2007.

Appendix A

Helicity Amplitudes for W-pair Production

A.1 Bilenky-Gounaris formalism

The helicity amplitude for the production of a W-pair with helicities τ and τ', in the $e^+e^- \to W^+W^-$ reaction, is written as the sum of contributions of the t-channel ν-exchange process and the s-channel γ and Z-exchange processes [101, 102, 109])

$$F^{\lambda}_{\tau\tau'}(s, \cos\theta_W, \vec{\alpha}) = -\frac{e^2\lambda}{2} s \; [C^{(\nu)}(\lambda, t) \; \mathcal{M}^{(\nu)}_{\lambda\tau\tau'}(s, \cos\theta_W) + \sum_{i=1}^{7} (C_i^{(\gamma)}(\lambda, s, \vec{\alpha}) + C_i^{(Z)}(\lambda, s, \vec{\alpha})) \; \mathcal{M}_{i,\lambda\tau\tau'}(s, \cos\theta_W)] \tag{A.1}$$

where s is the squared center-of-mass energy, $\cos\theta_W$ the cosine of the W boson production angle and $\vec{\alpha}$ the set of 14 triple gauge couplings (see section 2.4.). The four-momentum transfer t is given by

$$t = M_W^2 - \frac{1}{2}s(1 - \beta\cos\theta_W) \tag{A.2}$$

where β is the velocity of the W boson

$$\beta = \sqrt{(1 - 4M_W^2/s)} \tag{A.3}$$

Only the coupling coefficients $C_i^{(\gamma)}$ and $C_i^{(Z)}$ introduce the triple gauge coupling dependence as the t-channel process does not contain any TGC vertex. The amplitudes $\mathcal{M}_i$ give the helicity composition and the W-decay angle dependence for the different coupling terms.

The explicit expressions C_i and $\mathcal{M}_i$ calculated by "Bilenky-Gounaris" [101, 102]), from the Feynmann diagrams for tree-level W-pair production, are presented in Table A.1. The Z propagator D_Z is approximated at $s > 4M_W^2$ as

$$D_Z \simeq s - M_Z^2 \tag{A.4}$$

and the constants a and b are

$$a = \frac{-1 + 4\sin^2\theta_w}{4\sin\theta_w\cos\theta_w},\ b = \frac{-1}{4\sin\theta_w\cos\theta_w} \tag{A.5}$$

where θ_w represents the electroweak mixing angle.
The first column of the Table gives the coupling coefficients C_i, the following colums give the amplitudes $\mathcal{M}_i$ for a given helicity configuration of the W-pair. The helicity amplitude $F^{\lambda}_{\tau\tau'}$ for a definite electron helicity λ and definite helicities $\tau(\tau')$ for the W^- (W^+) are obtained by first multiplying the elements of the corresponding column with those in the first column and summing them up. Then, the result is multiplied with the common factor on the top of the corresponding column. For the helicity amplitudes with τ'=0 and $\tau = \pm 1$, the last column can be used with the following transformations $\tau \to \tau'$, $\tau' \to \tau$ and $\epsilon \to -\epsilon$. As an example, the W-pair helicity amplitude for a W pair with helicities $\tau, \tau' = +1$ and for an initial electron spin $\lambda = -1/2$ is given by

$$F^{-1/2}_{+1,+1} = \frac{e^2 s}{4}\sin\theta_W[(\frac{-2}{4t\sin^2\theta_w})(\cos\theta_W - \beta) + (\frac{-2}{s} + \frac{2\cot\theta_w}{D_Z}(a+b))(-\beta)] \tag{A.6}$$

while

$$F^{+1/2}_{+1,+1} = \frac{-e^2 s}{4}\sin\theta_W[(\frac{-2}{s} + \frac{2\cot\theta_w}{D_Z}(a-b))(-\beta)] \tag{A.7}$$

for an initial electron spin $\lambda = +1/2$.

Only the first row concerns the ν-echange process, the other rows describe the Z-and γ-exchange processes. Due to the standard $V-A$ property of weak currents, the first row vanishes for right-handed electrons ($\lambda = 1/2$). From Table A.1 it's clear that the W-pair helicity combination $\tau = -\tau' = \pm 1$ can only be produced via the $t-$channel ν-exchange process.

The differential cross section for W-pair production due to both s- as t-channel processes is expressed in terms of the helicity amplitudes

$$\frac{d\sigma(e^+e^- \to W^+W^-)}{d\cos\theta_W} = \frac{|\vec{P}|}{16\pi s\sqrt{s}}\sum_{\lambda\tau\tau'}|F^{\lambda}_{\tau\tau'}|^2 \tag{A.8}$$

where the center-of-mass momentum of the W-boson is given by $|\vec{P}| = \sqrt{s/4 - M_W^2}$.

	Helicity amplitudes $F^{\lambda}_{\tau\tau'}$			
	$\tau=\tau'=\pm1$	$\tau=-\tau'=\pm1$	$\tau=\tau'=0$	$\tau=0,\ \tau'=\pm1,\ \epsilon=+1$
	$\frac{-e^2s\lambda}{2}\sin\theta_W$	$\frac{-e^2s\lambda}{2}\sin\theta_W$	$\frac{-e^2s\lambda}{2}\sin\theta_W$	$\frac{-e^2s\lambda}{2\sqrt{2}}(\tau'\cos\theta_W-2\lambda)$
$\frac{2\lambda-1}{4t\sin^2\theta_w}$	$\cos\theta_W-\beta$	$-\cos\theta_W-2\tau\lambda$	$\frac{s}{2M_W^2}(\cos\theta_W-\beta(1+\frac{2M_W^2}{s})]$	$\frac{\sqrt{s}[\cos\theta_W(1+\beta^2)-2\beta]}{2M_W}-\frac{2M_W\tau'\sin^2}{\sqrt{s}(\tau'\cos\theta_W}$
$\frac{-2(1+\Delta g_1^\gamma)}{s}+\frac{2\cot\theta_w(1+\Delta g_1^Z)}{D_Z}(a-2b\lambda)$	$-\beta$	0	$-\beta(1+\frac{s}{2M_W^2})$	$-\beta\frac{\sqrt{s}}{M_W}$
$\frac{-\Delta\kappa_\gamma}{s}+\frac{\cot\theta_w(\Delta\kappa_Z-\Delta g_1^Z)}{D_Z}(a-2b\lambda)$	0	0	$-\beta\frac{s}{M_W^2}$	$-\beta\frac{\sqrt{s}}{M_W}$
$\frac{-\lambda_\gamma}{s}+\frac{\cot\theta_w\lambda_Z}{D_Z}(a-2b\lambda)$	$-\beta\frac{s}{M_W^2}$	0	0	$-\beta\frac{\sqrt{s}}{M_W}$
$\frac{g_5^\gamma}{s}+\frac{\cot\theta_w g_5^Z}{D_Z}(a-2b\lambda)$	0	0	0	$\beta^2\tau'(\frac{\sqrt{s}}{M_W})^3$
$\frac{-ig_4^\gamma}{s}+\frac{i\cot\theta_w g_4^Z}{D_Z}(a-2b\lambda)$	0	0	0	-$\beta\epsilon\frac{\sqrt{s}}{M_W}$
$\frac{-i(\tilde{\kappa_\gamma}-\tilde{\lambda_\gamma})}{s}+\frac{i\cot\theta_w(\tilde{\kappa_Z}-\tilde{\lambda_Z})}{D_Z}(a-2b\lambda)$	2τ	0	0	$\tau'\epsilon\frac{\sqrt{s}}{M_W}$
$\frac{i\tilde{\lambda_\gamma}}{2s}-\frac{i\cot\theta_w\tilde{\lambda_Z}}{2D_Z}(a-2b\lambda)$	$2\tau\beta^2\frac{s}{M_W^2}$	0	0	0

Table A.1: *The helicity amplitude $F^{\lambda}_{\tau\tau'}$ for a definite electron helicity λ and definite helicities $\tau(\tau')$ for the $W^-(W^+)$ are obtained by first multiplying the elements of the corresponding column with these in the first column and summing them up. Second the result is multiplied with the common factor on the top of the corresponding column.*

A.2 Approximations

The analytical expression for the triple gauge coupling dependent single W SDM element is

$$\rho^{W^-\ bilgou}_{\tau_1\tau_1'}(s,\cos\theta_{W^-},\vec{\alpha}) = \sum_{\tau}\rho_{\tau_1\tau_1'\tau\tau}(s,\cos\theta_{W^-},\vec{\alpha}) \equiv \frac{\sum_\lambda F^\lambda_{\tau_1\tau}\ (F^\lambda_{\tau_1\tau})^\star}{\sum_{\lambda\tau_{1'}\tau}\mid F^\lambda_{\tau_1\tau}\mid^2}(s,\cos\theta_{W^-},\vec{\alpha}) \tag{A.9}$$

where the WW helicity amplitudes are calculated using the Bilenky-Gounaris (BILGOU) formalism. As the $\cos\theta_{W^-}$ distristribution is binned, the prediction for the SDM element in a particular bin k with width Δ_{bin} is given by the integral

$$\frac{1}{\Delta_{bin}}\int \rho^{W^-\ bilgou}_{\tau\tau'}(s,\cos\theta_{W^-},\vec{\alpha})\ d\cos\theta_{W^-} \tag{A.10}$$

Several assumptions concerning the description of the underlying physics process are made in the Bilenky-Gounaris formalism

- only the CC03 diagrams for W-pair production and without radiative corrections are considered, so s is the squared center-of-mass energy without inclusion of ISR radiation
- FSR emission is not considered
- W bosons are on-shell (zero width approximation)
- fermions are massless

As ISR and FSR are implemented in the KandY Monte Carlo, a direct comparison between the projection operator results and the analytical prediction, is only possible under the same assumptions. In order to evaluate the Bilenky-Gounaris prediction for the SDM elements, in the prescribed binning, the WW helicity amplitudes are calculated for each generated KandY Monte Carlo event. The generator level center-of-mass energy and $\cos\theta_{W^-}$, after correction for ISR and FSR emission, are used as input for the analytical expression: ISR and FSR photons are recombined with the closest charged fermion and the boost due to ISR emission is properply taken into account. The Bilenky-Gounaris prediction for the the coupling-dependent SDM element in a particular $\cos\theta_{W^-}$ bin k is then given by

$$<\rho^{W^-\ bilgou}_{\tau\tau'}>(k) = \frac{1}{N_k}\sum_{i=1}^{N_k}\frac{\sum_\lambda F^\lambda_{\tau_1\tau}\ (F^\lambda_{\tau_1\tau})^\star}{\sum_{\lambda\tau_1\tau}\mid F^\lambda_{\tau_1\tau}\mid^2}(s,\cos\theta_{W^-},\vec{\alpha}) \tag{A.11}$$

where N_k is the number of events in the bin k.

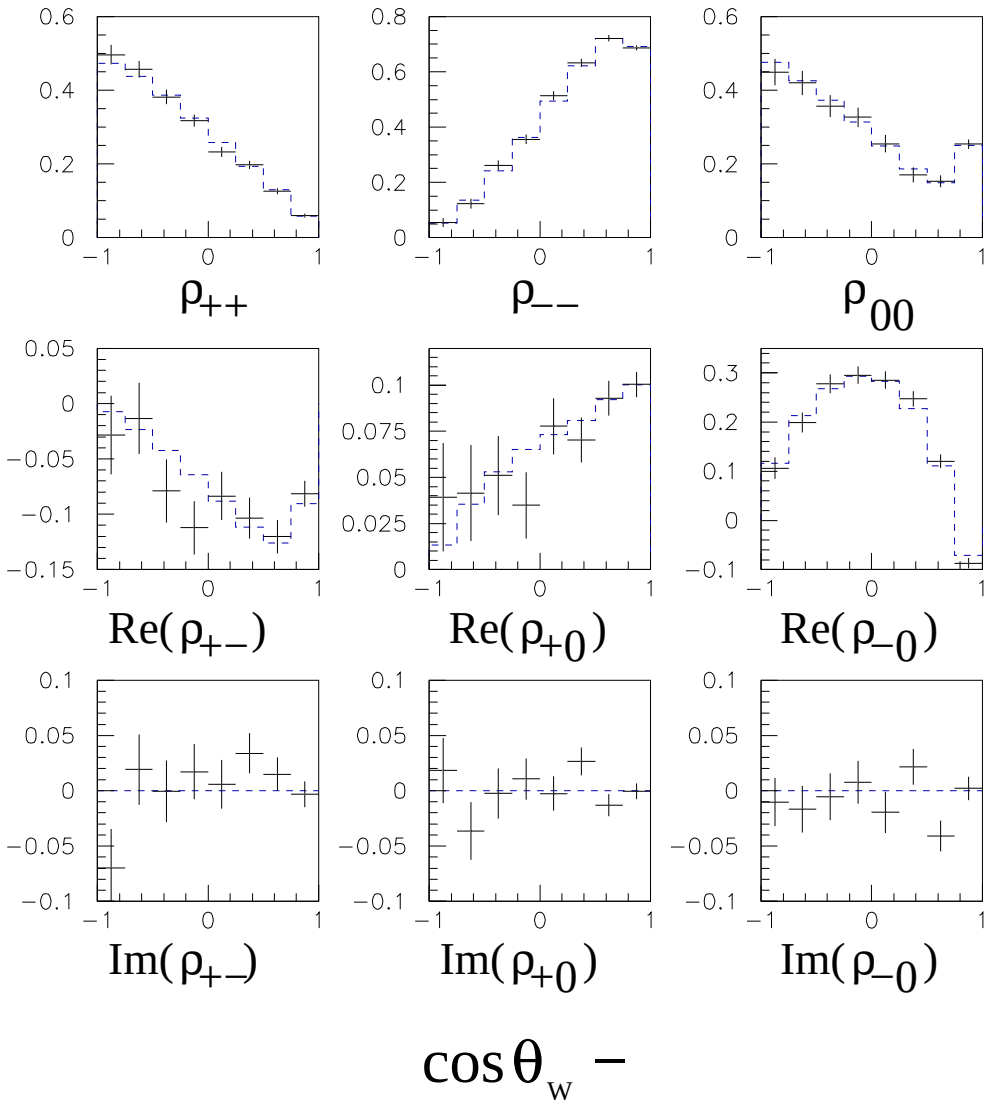

Figure A.1: *Comparison on CCO3 level between the Standard Model Bilenky-Gounaris prediction for the SDM elements (dashed line) and the projection operator SDM results obtained with the generator level KoralW Monte Carlo (solid line) for the qqeν(γ) final state at* $\sqrt{s}$*= 189 GeV. A good agreement is found.*

The comparison between the Standard Model Bilenky-Gounaris prediction for the SDM elements and the projection operator SDM results obtained with the generator level KoralW CC03 Monte Carlo, is shown in Figure A.1 for the $qqe\nu(\gamma)$ final state at $\sqrt{s}$= 189 GeV. A good agreement is found.

Appendix B

Charge Confusion in τ-jets

This Appendix presents the study of the charge confusion(CC),i.e. the probability for charge misreconstruction, in τ-jets using the 1998, 1999 and 2000 calibration data collected at the Z-peak ($\sqrt{s} \cong 90$ GeV), corresponding to a total integrated luminosity of 11 pb^{-1}.

A clean sample of $e^+e^- \to Z \to \tau^+\tau^-$ events, caracterized by a low background contamination and a high signal acceptance, is selected. Only one-prong τ-decays are used in the charge confusion analysis.

The charge confusion was first studied with Bhabha events ($e^+e^- \to Z \to e^+e^-$) but the use of Bhabha events has the drawback that the electron is monoenergetic and so the transverse momentum fixed. Using τ-pair events at the Z-peak ($e^+e^- \to Z \to \tau^+\tau^-$), the transverse momentum dependence of the charge confusion can be studied as the τ-jet energy varies from several GeV to 45 GeV due to the emission of at least one neutrino. This is of particular interest for the measurement of gauge couplings and polarisation studies in the semi-leptonic channels where the lepton is produced in a large energy range. The W charge is derived from the leptonically decaying W and a wrong charge assignment leads to a sign flip in the W angular distribution from which triple gauge coupling values are extracted. Therefore the charge confusion contributes largely to the systematic uncertainty in the measurement of W gauge couplings and the W SDM.

A charge confusion analysis performed on Bhabha events at the 1998, 1999 and 2000 Z-peak has shown a difference in charge confusion in the data compared to the Monte Carlo(MC): $CC_{data}/CC_{MC} = 1.535 \pm 0.060$ in the barrel region of the TEC while $CC_{data}/CC_{MC} = 1.282 \pm 0.040$ in the end caps [104]. To avoid a bias in the gauge couplings measurement, the charge confusion in the MC must be corrected to the value measured in the data sample.

Decay Mode	Branching ratio
$\tau \rightarrow e\nu_e\nu_\tau$	17.8 %
$\tau \rightarrow \mu\nu_\mu\nu_\tau$	17.4%
$\tau \rightarrow hadrons\ \nu_\tau$ where $hadrons = \pi, \rho, a_1, \omega, K, \ldots$	64.8%

Table B.1: *The decay modes of the τ-lepton and the corresponding branching ratios.*

B.1 Selection of $e^+e^- \rightarrow Z \rightarrow \tau^+\tau^-$ events

As the τ-lepton has a lifetime of 0.3 ps, it decays near the interaction region before it escapes from the beampipe. Many decay modes can be distinguished and are presented in Table B.1. All decays are caracterized by a missing energy and momentum, carried away by one or more neutrinos which escape undetected.

B.1.1 Selection criteria

The typical topology of $e^+e^- \rightarrow Z \rightarrow \tau^+\tau^-$ events consists of

- 2 narrow, back-to-back τ-jets
- low track multiplicity : 1 or 3 tracks per τ-jet
- missing energy due to the emission of at least one neutrino

The seletion cuts are chosen in order to get a high purity sample. As we are not interested in a cross section measurement, the signal efficiency is subordinate to the high purity needed for a correct determination of the CC.

The selection of the τ-pair events has three parts. In the first part, the fiducial volume is defined. The analysis is restricted to the TEC region ($|\cos\ \theta_{\tau-jet}| <\ 0.91$) where $\theta_{\tau-jet}$ is the polar angle of the τ-jet, given by the thrust axis of the event. The information from the barrel and end cap BGO calorimeters is also used. The EGAP region ($0.73\ <|\cos\ \theta_{\tau-jet}| <\ 0.81$) is excluded because of its poor energy resolution. In the second part, minimal requirements are imposed to extract the Z-decay events :

- The most energetic τ-jet needs to have an energy

$$E_{\tau-jet} > 9 \text{ GeV}$$

This variable is presented in Figure B.1 (Left).

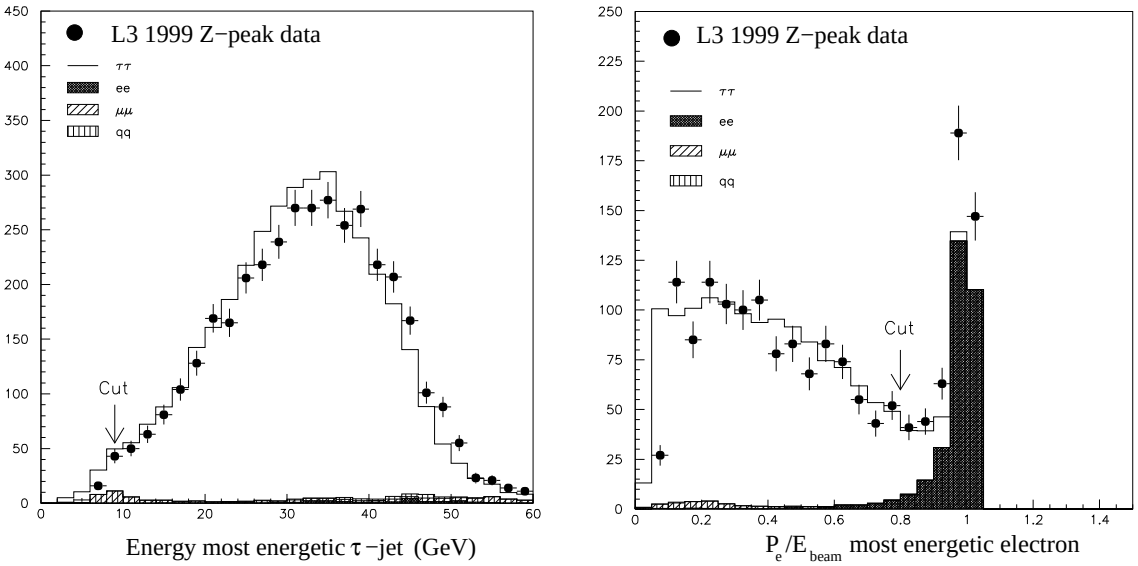

Figure B.1: Left : *The energy of the most energetic τ-jet measured for the selected τ-pair events in the 1999 Z-peak data. Only τ-jets with an energy larger than 9 GeV are selected.* Right : *The electron momentum rescaled to the beam energy for the most energetic electron. Events with a ratio smaller than 0.8 are rejected.*

- The minimal accolinearity, $\cos\alpha_{jets}$, where α_{jets} is the minimum angle between the τ-jet and the hadronic jet in the three-dimensional space, has to be larger than $180° - 11°$

$$\cos\ \alpha_{jets}\ < -\ 0.982$$

- The best scintillator time must lie within the 5 ns after beam crossing ($t = 0$) to reduce cosmic ray events,

$$|t_{best}| < 5 \text{ ns}$$

  This time is recorded by a scintillator and corrected for the time of flight.

The third part aims to reject the background from Z-decays into electron pairs (Bhabha events), muon pairs (dimuon events) or 2 jets of hadrons (hadronic dijet events). In **Bhabha-events**, the scattered electrons have the same energy as the beam and depose almost all their energy in the BGO calorimeter where they form electromagnetic showers.

In order to reject this type of events, we require that

- the total energy deposit in the BGO, rescaled to the beam energy, satisfies

$$E_{BGO}/E_{beam} < 1.8$$

- the momentum of the most energetic electron, rescaled to the beam energy, passes the following requirement

$$P_e/E_{beam} < 0.8$$

  This ratio is shown in Figure B.1 (Right).

- when both an electron and a positron are present in the end caps and two particles are classified as an electron by the particle identification program, these events are rejected by

$$N_{\text{"}electrons\text{"}} < 2$$

In the **dimuon events**, the scattered muons have the same energy as the beam and transverse both the electromagnetic and the hadronic calorimeter with a negligible energy loss. They are finally detected in the muon chambers. Therefore we require that

- if the number of tracks in each τ-jet is smaller than three, the energy deposit in the BGO is at least 1 GeV

$$E_{BGO}^{\tau-jet} > 1 \text{ GeV, if } N_{tracks}^{\tau-jet} < 3$$

  The number of dimuon events where both particles are minimum-ionizing, are reduced. The cut also removes events with a single purely minimum-ionizing track from cosmic rays traversing the detector. The $\tau \to \pi\nu$ decay is supressed while the $\tau \to \pi\pi^0\nu$ decays passes the cut.

- the total momentum of the muons in the event satisfies

$$\sum_\mu P_\mu/E_{beam} < 0.8$$

  This ratio is presented in Figure B.2 (Left).

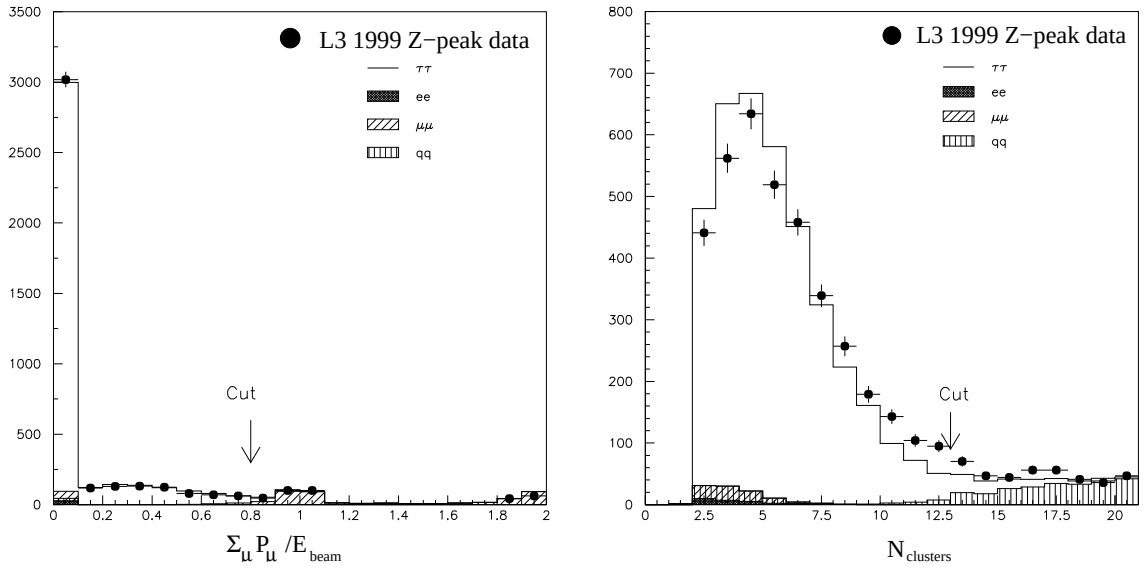

Figure B.2: Left : *The total momentum of the muons in the event, rescaled to the beam energy, measured for the selected τ-pair events in the 1999 Z-peak data. A cut is performed at 0.8 to reduce the number of dimuon events.* Right : *The number of clusters in the τ-pair event. The hadronic events are reduced requiring the presence of at most 13 clusters.*

Hadronic dijet events have a similar topology as the $\tau^+\tau^-$-events. The difference lies in the jet structure. While τ-jets are highly boosted and form narrow jets, hadronic jets are less boosted and hence much broader. The hadronic jets are also caracterized by a much higher track and cluster multplicity than τ-jets.

- To reduce the hadronic events, we ask

$$\begin{aligned} N_{clusters} &< 13 \\ N_{tracks} &\leq 7 \end{aligned}$$

The number of clusters is shown in Figure B.2 (Right).

At the end we restrict the analysis to events where both τ-jets decay into one charged particle (one-prong events) by requiring

$$N_{tracks}^{\tau-jet} < 3$$

B.1.2 Track selection

As the aim of this analysis is to measure the CC to be applied in gauge coupling and polarisation studies, the same track selection are used

- hits/span > 0.5
- DCA < 10 mm
- $P_T > 0.2$ GeV

B.1.3 Selection of the charge confusion analysis sample

A particular topology is asked

- $N_{tracks} \geq 2$
- all tracks are in 15° cones around the thrust-axis of the τ-jet
- the sum of the charges within the cone is non-zero

B.2 The τ-jet Charge Confusion

The charge confusion is defined as the probability to measure the charge of a particle opposite to its real charge. For a real detector, this quantity is not zero because of the finite spacial resolution of the detector, in this case the Time Expansion Chamber (TEC). As the charge of a particle is deduced from its curvature in the magnetic field, wrong charge assignments, due to a wrong track reconstruction, occur [128, 129].

The hits on the TEC-wires, induced by the passage of the charged particle, form a helix in the homogeneous magnetic field. The trajectory of the charged particle is described by the distance of closest approach to the primary vertex (DCA), its polar angle, θ, and its curvature, ρ, obtained from a fit through the coordinates of the track.
The charge q, measured in units of e, is then derived from

$$\rho = \frac{0.3\ qB}{P_T} \tag{B.1}$$

where B is the strength of the magnetic field and $P_T = P \sin\theta$ the momentum in the plane transverse to the magnetic field .
The error on the curvature of the trajectory has a Gaussian distribution and is given by

$$\Delta\rho = \sqrt{(\Delta\rho_{res})^2 + (\Delta\rho_{MCS})^2} \tag{B.2}$$

where $\Delta\rho_{res}$ is the uncertainty due to the finite detector resolution and $\Delta\rho_{MCS}$ the uncertainty related to the uncertainties in the description of multiple scattering on the nuclei of the detector material.
For a large number of hits, $N_{hits} \geq 10$, $\Delta\rho_{res}$ behaves as

$$\Delta\rho_{res} \;\propto\; \frac{\sigma_x}{L^2}.\frac{1}{\sqrt{N_{hits}}} \tag{B.3}$$

with σ_x the spacial resolution ~ 50 μm for the TEC, and L the length of the trajectory in the bending plane.
The uncertainty due to multiple scattering is expressed as

$$\Delta\rho_{MCS} \;\propto\; \frac{q}{P_T^2}.\frac{1}{\sqrt{L_{tot}X_0}} \tag{B.4}$$

with L_{tot} the total length of the trajectory and X_0 the radiation length of the scattering medium. Multiple scattering is mainly contributing at low transverse momentum where it competes with the uncertainty due to the limited detector resolution.

The sign of the charge is derived from the direction of the trajectory's curvature in the magnetic field and the uncertainty on the fitted curvature can lead to a sign flip in the charge assignment. Particles with a high transverse momentum move almost straight through the detector and present almost no curvature. Therefore they have a higher CC than low transverse momentum particles. Hence, we expect the CC to increase with increasing transverse momentum. On the other hand, particles with very low momentum are mainly affected by multiple scattering resulting also in a high CC.

The charge of a τ-jet is obtained from the sum of the charges of its decay products and the single jet charge confusion, $CC_{single\ jet}$, is the probability to measure the charge of a given τ-jet with an opposite sign. This quantity is calculated from the event charge confusion, P_{event}, which represents the percentage of events with a wrong charge assignment for one of the τ-jets or equivalently with both jet charges of same sign

$$P_{event} = \frac{N_{ev}(Q_{\tau^+} = \; Q_{\tau^-})}{N_{tot}} \equiv \frac{N_{equal}}{N_{tot}} \tag{B.5}$$

The event charge confusion depends quadratically on the single jet charge confusion. For a $e^+e^- \rightarrow Z \rightarrow \tau^+\tau^-$ generated event, the following configurations are possible after reconstruction :

Generation		**Reconstruction**		**Probability**
$+\ -$	$\rightarrow$	$+\ +$	(a)	$(1 - CC_{single\ jet})\ CC_{single\ jet}$
		$+\ -$	(b)	$(1 - CC_{single\ jet})^2$
		$-\ -$	(c)	$CC_{single\ jet}\ (1 - CC_{single\ jet})$
		$-\ +$	(d)	$CC^2_{single\ jet}$

For the single jet charge confusion, only the contributions (a) and (c) have to be considered.
For the corresponding event charge confusion, we have

$$P_{event} = \ 2\ (1 - CC_{single\ jet})\ CC_{single\ jet} \tag{B.6}$$

or

$$CC^2_{single\ jet} - CC_{single\ jet} + \frac{P_{event}}{2} = \ 0 \tag{B.7}$$

This quadratic equation has the following solution

$$CC_{single\ jet} = \ \frac{1}{2}(1 - \sqrt{1 - 2P_{event}}) \tag{B.8}$$

with corresponding statistical error

$$\delta_{stat}(CC_{single\ jet}) = \frac{1}{2N_{tot}}\sqrt{\frac{(N_{tot} - N_{equal})N_{equal}}{N_{tot} - 2N_{equal}}} \tag{B.9}$$

A cross check is possible using the MC sample as the reconstructed charge can be directly compared to its generated value. As each jet can be considered as an independent event, statistics is doubled. The single jet charge confusion is given by

$$CC^{MC}_{single\ jet} = \frac{N_{ev}(Q^{rec}_\tau = -Q^{gen}_\tau)}{2N_{tot}} \tag{B.10}$$

B.3 Data and Monte Carlo Samples

Z-peak data	$\mathcal{L}$ (nb^{-1})	N_{sel}
1998	3005	2561
1999	3982	3337
2000	4025	3377

Table B.2: *The data samples used in the charge confusion analysis with their corresponding total integrated luminosity and number of selected events.*

Channel	Monte Carlo	$\sigma(nb)$
Signal		
$e^+e^- \to \tau^+\tau^-$	KK2F [130]	1.48
Background		
$e^+e^- \to e^+e^-$	BHWIDE [46]	8.12
$e^+e^- \to \mu^+\mu^-$	KK2F [130]	1.49
$e^+e^- \to q\bar{q}(\gamma)$	JETSET [40]	25.28

Table B.3: *The Monte Carlo samples for the different channels and their cross section.*

Combining the 1998, 1999 and 2000 data, a total integrated luminosity of 11 pb^{-1} and a total number of selected events of 9725 is obtained (Table B.2). The Monte Carlo samples used in this analysis are summarised in Table B.3. An efficiency of 62 ± 0.1 % and a purity of 86.7 ± 0.1% was obtained. The total reconstructed energy of the event is shown in Figure B.3 (Left). Figure B.3 (Right) presents the polar angle distribution of the selected τ-jets. The EGAP is responsible for the deficits around 0.7 and 2.4 radians.

B.4 Measurement of the Charge Confusion

B.4.1 Barrel and end caps

The τ-jet CC in the barrel and the end caps separately for 1998, 1999 and 2000 Z-peak data is presented in Figure B.4. In the end caps, the CC is about three times larger than in the barrel region. This is explained by the fact that the number of available TEC-wires to determine the trajectory's curvature is 62 in the barrel but decreases with decreasing polar angle in the end caps. The results for the different years agree within the statistical uncertainty. The CC measured in the data is significantly larger than the one simulated in the MC but in agreement for the different years as can be seen in Figure B.4 (Right).

	$\lvert\cos\theta_\tau\rvert$	CC_{data} (%)	CC_{MC}(%)	$R = CC_{data}/CC_{MC}$
1998 Z-peak data				
Barrel	[0.;0.25[	3.86 ± 0.56	1.99 ± 0.09	1.94 ± 0.30
	[0.25;0.5[	2.74 ± 0.49	1.41 ± 0.06	1.95 ± 0.35
	[0.5;0.73[	2.52 ± 0.40	1.30 ± 0.06	1.94 ± 0.32
End caps	[0.81;0.86[	7.74 ± 1.36	4.38 ± 0.25	1.77 ± 0.33
	[0.86;0.91[	23.27 ± 8.47	18.90 ± 2.61	1.23 ± 0.48
1999 Z-peak data				
Barrel	[0.;0.25[	3.13 ± 0.45	1.99 ± 0.09	1.57 ± 0.24
	[0.25;0.5[	2.34 ± 0.37	1.41 ± 0.06	1.66 ± 0.27
	[0.5;0.73[	1.81 ± 0.31	1.30 ± 0.06	1.39 ± 0.24
End caps	[0.81;0.86[	7.17 ± 1.10	4.38 ± 0.25	1.64 ± 0.27
	[0.86;0.91[	26.57 ± 8.13	18.90 ± 2.61	1.41 ± 0.47
2000 Z-peak data				
Barrel	[0.;0.25[	3.43 ±0.46	1.99 ± 0.09	1.72 ± 0.25
	[0.25;0.5[	2.55 ± 0.40	1.41 ± 0.06	1.81 ± 0.29
	[0.5;0.73[	2.53 ± 0.36	1.30 ± 0.06	1.94 ± 0.29
End caps	[0.81;0.86[	8.22 ± 1.20	4.38 ± 0.25	1.88 ± 0.29
	[0.86;0.91[	27.22 ± 7.37	18.90 ± 2.61	1.44 ± 0.44

Table B.4: *The τ-jet charge confusion results in the barrel and end cap regions for 1998, 1999 and 2000 Z-peak data. The level of agreement between the data and the Monte Carlo charge confusion is indicated in the last column. The errors are statistical only.*

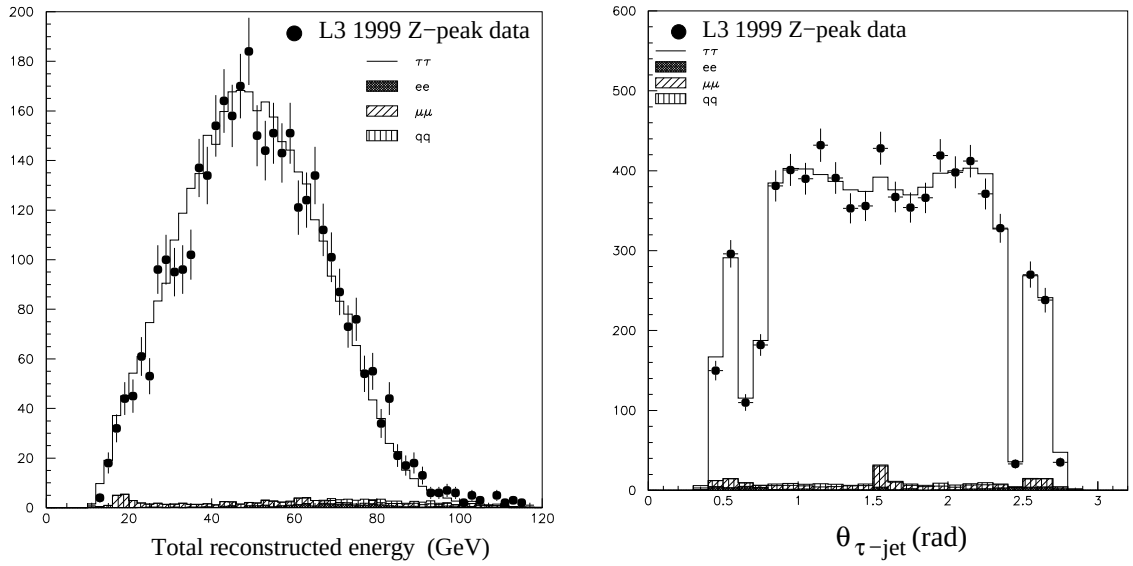

Figure B.3: Left : *The total reconstructed energy measured for the selected τ-pair events in the 1999 Z-peak data.* Right : *The polar angle distribution of the selected τ-jets.*

B.4.2 Angular dependence

Figure B.5 (Left) shows the CC as a function of the absolute value of the cosine of the polar angle of the τ-jet. The CC appears to be constant in the barrel region, while it increases with the decreasing number of wires in the end caps.

The angular dependence of the ratio between the τ-jet CC in the data and in the MC, CC_{data}/CC_{MC}, is presented in Figure B.5 (Right) and is compatible with an angular independent distribution. The ratios are in agreement with the values obtained with Bhabha events. The numeric results are given in Table B.4.

B.5 Transverse Momentum Dependence

The *tau*-pair events are particularly interesting to probe the momentum dependence of the CC. For this purpose, the inverse transverse momentum of the τ-jet track, $1/ < P_T >$, will be used since it follows a Gaussian distribution. As for the data the single jet charge confusion is obtained from the event charge confusion, it can not be expressed as a function of the inverse transverse momentum for each τ-jet separately, but as a function of the average inverse transverse momentum of the τ-jet track.

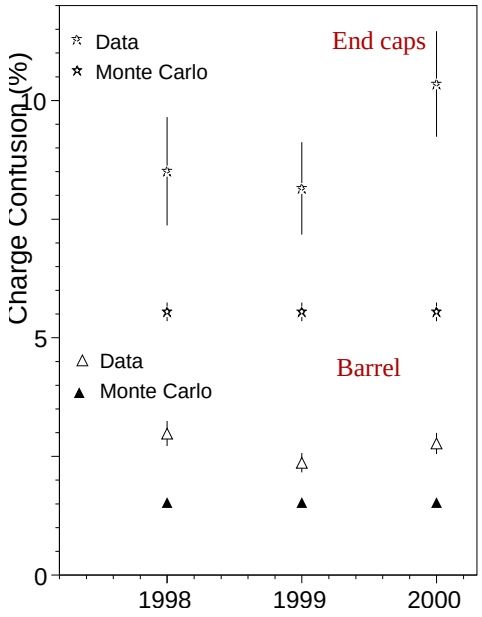

Barrel	CC_{data} (%)	CC_{MC} (%)
1998	2.98±.27	1.53±.04
1999	2.37±.21	1.53±.04
2000	2.77±.22	1.53±.04
End caps	CC_{data} (%)	CC_{MC} (%)
1998	8.51±1.14	5.55±.20
1999	8.15±0.97	5.55±.20
2000	10.35±1.11	5.55±.20

Figure B.4: *The τ-jet charge confusion in barrel and end caps for the 1998, 1999 and 2000 Z-peak data is compared to the Monte Carlo. The errors are statistical only.*

In Figure B.6 (Left) we observe, as expected, the highest CC values at high P_T where the particles describe almost straightline trajectories and where the probability to reconstruct the mirror image of the track is the largest. This is followed by a steep decrease towards a minimum at lower P_T. In this P_T-range, the trajectories are more and more curved and the sign of the charge is more accurately determined. At low P_T (100 MeV-4 GeV) occurs a small increase. This is due to phenomena like multiple scattering and energy loss due to interactions with the detector material which are difficult to simulate in the MC. As the transverse momentum of the lepton in W-pair events is always larger than 4 GeV [104], the P_T-region below 4 GeV can be omitted.

The P_T-dependence of the ratio of the CC measured in the data and in the MC is shown in Figure B.6 (Right) for the 1998, 1999 and 2000 Z-peak data. The results combining 1998, 1999 and 2000 Z-peak data are presented in Table B.5. The ratio between the CC measured in the data and in the MC is presented in Figure B.7 for the barrel region (Left) and the end caps (Right). The ratios obtained from a fit with a constant are $R_{barrel} = 1.46 \pm 0.14$ and $R_{end\ caps} = 1.70 \pm 0.22$.

The results of this charge confusion analysis on τ-pair events can be used to evaluate the charge confusion systematics in gauge couplings and polarisation studies in semi-leptonic channels for which the TEC is used to determine the lepton charge. The correction factors are applied to the baseline MC events in order to include the measured data CC. The uncertainty corresponding to this correction is then propagated as a systematic.

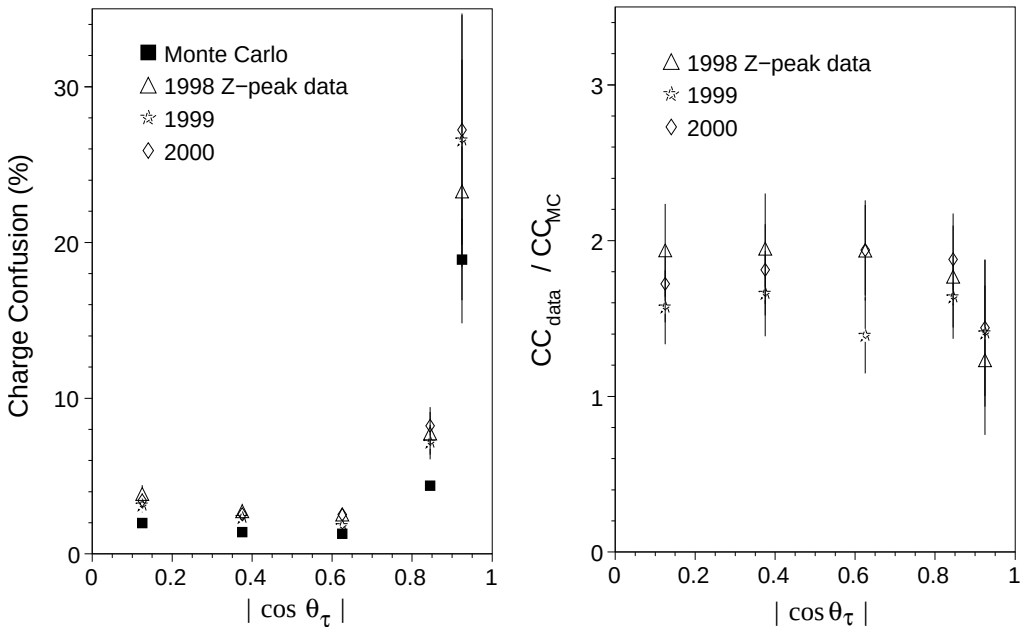

Figure B.5: Left : *The dependence of the τ-jet charge confusion on the absolute value of the cosine of the polar angle of the τ-jet for 1998, 1999 and 2000 Z-peak data.* Right : *The corresponding ratio between the charge confusion measured in τ-pair events in the data and in the Monte Carlo. The errors are statistical only.*

Also the CC for the muons reconstructed in the forward and in the backward muon chambers and for the muons classified as a MIP is determined from the TEC information, needs this correction. The muons reconstructed in the barrel region of the muon chamber have a much smaller CC and is well modelled by the detector simulation. A cross check with dimuon in events at the 1998, 1999 and 2000 Z-peak gives $CC_{data} = 0.47 \pm 0.06$ % and $CC_{MC} = 0.49 \pm 0.02$ % [104].

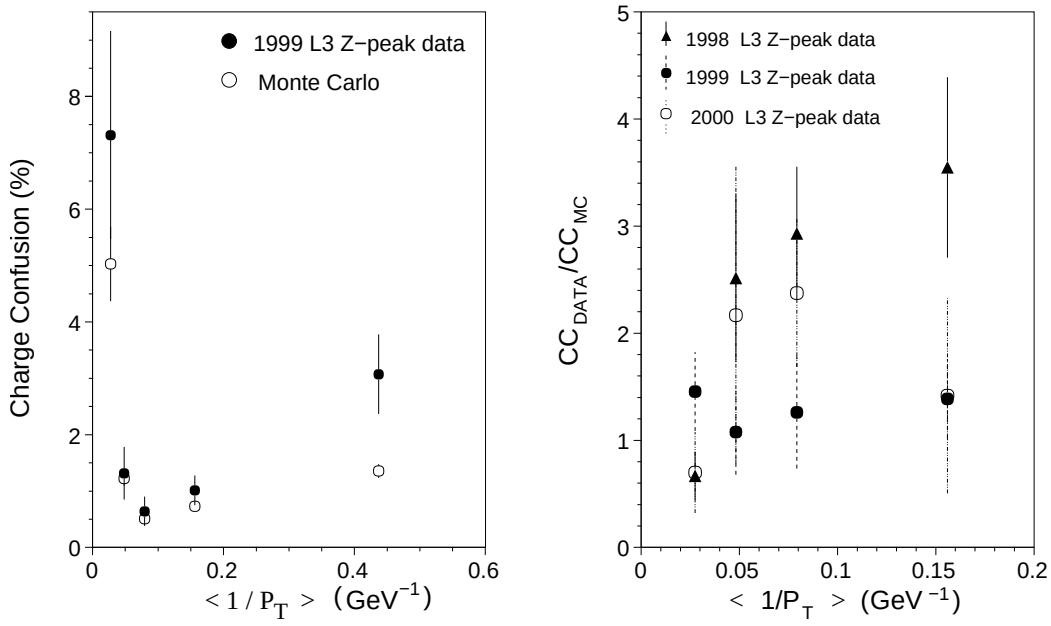

Figure B.6: Left : *The charge confusion as a function of the average inverse transverse momentum of the τ-jet track for the 1999 Z-peak data.* Right : *The ratio between the τ-jet charge confusion measured in the data and the Monte Carlo as a function of average inverse transverse momentum for the 1998, 1999 and 2000 Z-peak data. Only the results for tracks with a P_T larger than 4 GeV are shown. The errors are statistical only.*

$\mathbf{1/P_T}$ $(\mathbf{GeV^{-1}})$	$\boldsymbol{CC_{data}}$ (%)	$\boldsymbol{CC_{MC}}$ (%)	$\boldsymbol{CC_{data}}$ (%)	$\boldsymbol{CC_{MC}}$ (%)
	Barrel		**End caps**	
[0. : 0.035]	4.80 ± 0.88	5.14 ± 0.64	31.7 ± 12.4	14.2 ± 3.40
[0.035 : 0.060]	2.36 ± 0.38	1.24 ± 0.13	7.74 ± 1.74	5.31 ± 1.37
[0.060 : 0.1]	1.05 ± 0.19	0.50 ± 0.04	7.23 ± 1.74	5.30 ± 0.80
[0.1 : 0.25]	1.33 ± 0.18	0.73 ± 0.04	6.45 ± 0.93	3.33 ± 0.22

Table B.5: *The charge confusion as a function of the average inverse transverse momentum of τ-jet track for the barrel and the end caps separately. The results combine 1998, 1999 and 2000 Z-peak data. Only tracks with a P_T larger than 4 GeV are used. The errors are statistical only.*

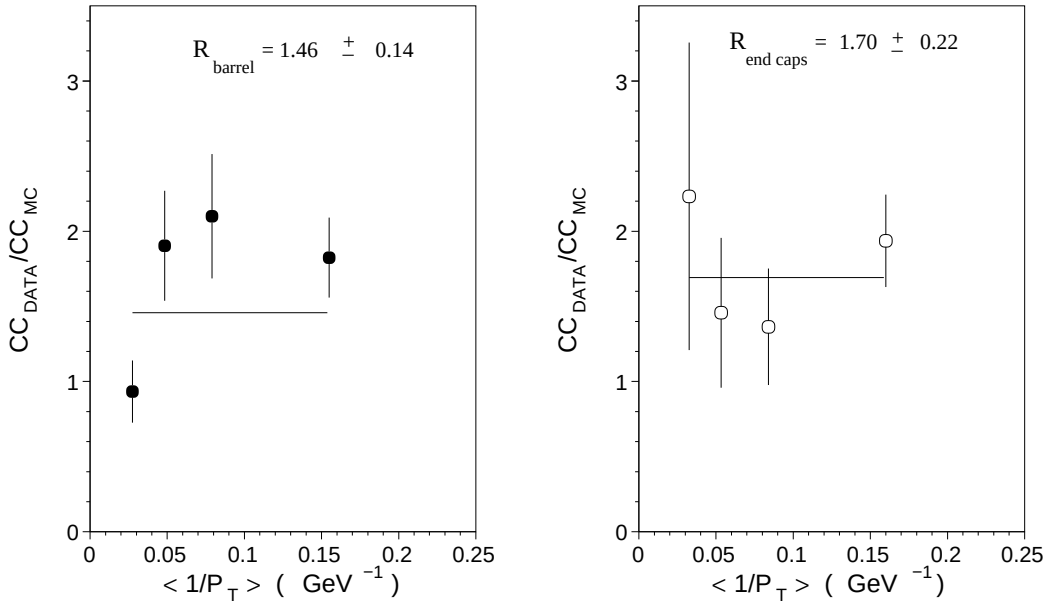

Figure B.7: *The ratio between the charge confusion measured in the data and in the Monte Carlo in the barrel region* (Left) *and the end caps* (Right). *The solid line represents a constant fit through the ratio values. Only tracks with P_T larger than 4 GeV are used. The errors are statistical only.*

Appendix C

Technical tests

C.1 $\cos\theta_W$ binning

The evolution of the nine single W SDM elements as function of the number of $\cos\theta_W$ bins is shown for the $qq\mu\nu(\gamma)$ final state at $\sqrt{s} = 189$ GeV. The solid line shows the KandY Monte Carlo single W SDM elements on reconstruction level, after bin-to-bin correction, while the dotted line represents the corresponding distribution on generator level. The binning in $\cos\theta^\star$ was fixed to 12 for the diagonal elements and to 8 for the off-diagonal elements ρ_{+0} and ρ_{-0}, while the binning in $\phi^\star$ is 16 for the off-diagonal element ρ_{+-} and 10 for the off-diagonal elements ρ_{+0} and ρ_{-0}. Also the average deviation, defined as

$$\langle\Delta\rangle = \frac{1}{N_{\cos\theta_W}} \sum_{k=1}^{N_{\cos\theta_W}} \frac{(\rho^{rec}(k) - \rho^{gen}(k))^2}{\sigma^2_{stat}(\rho^{rec}(k))} \tag{C.1}$$

is shown as function of the number of bins $N_{\cos\theta_W}$.

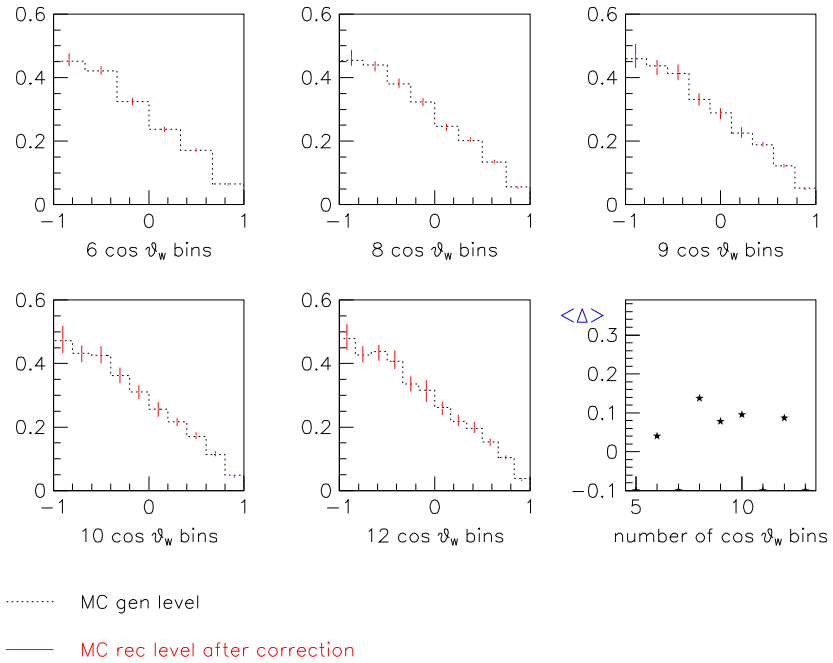
ρ++ (cos ϑw) – 2D bin–to–bin correction – 189 GeV qqmn
6 cos ϑw bins
8 cos ϑw bins
9 cos ϑw bins
10 cos ϑw bins
12 cos ϑw bins
<Δ>
number of cos ϑw bins
MC gen level
MC rec level after correction

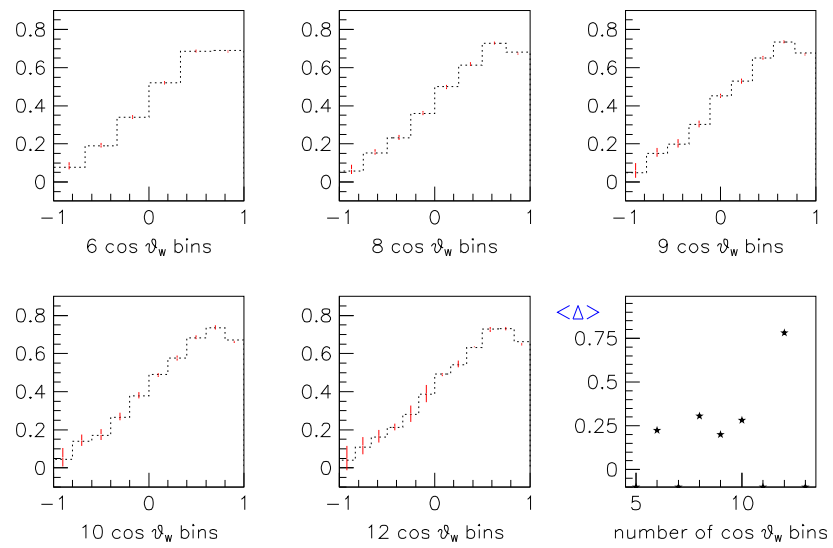
ρ–– (cos ϑw) – 2D bin–to–bin correction – 189 GeV qqmn
6 cos ϑw bins
8 cos ϑw bins
9 cos ϑw bins
10 cos ϑw bins
12 cos ϑw bins
<Δ>
number of cos ϑw bins

ρ00 (cos ϑ$_w$) – 2D bin–to–bin correction – 189 GeV qqmn

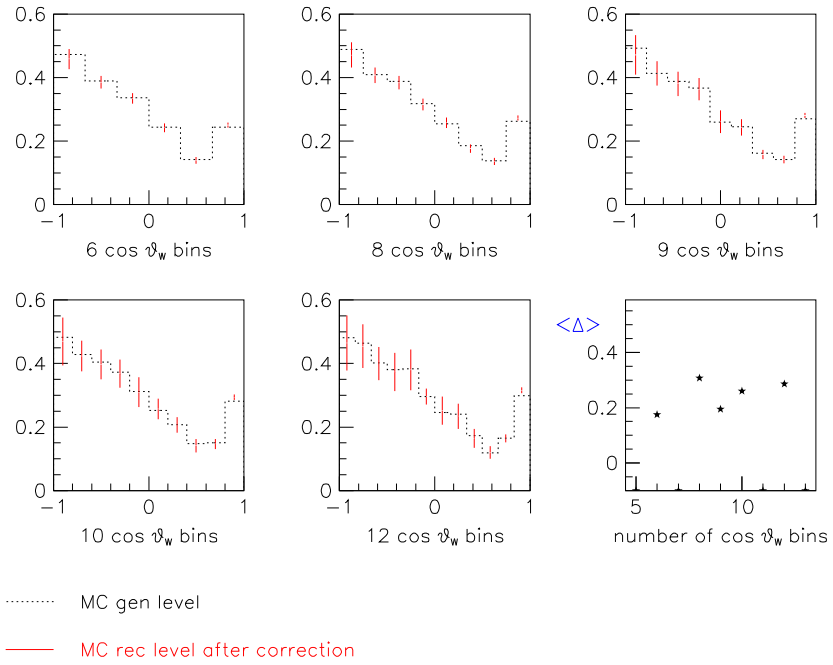

Re (ρ+–) (cos ϑ$_w$) – 2D bin–to–bin correction – 189 GeV qqmn

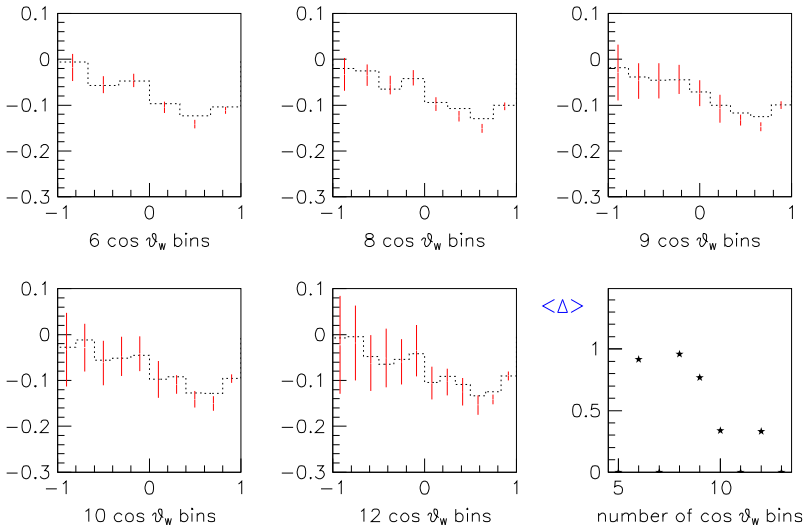

Im (ρ+−) (cos ϑ_W) − 2D bin−to−bin correction − 189 GeV qqmn

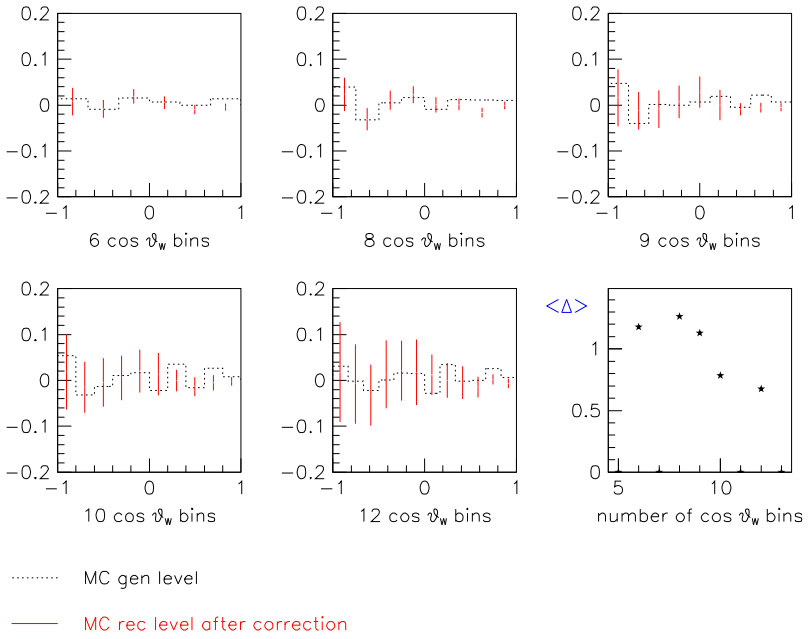

Re (ρ+0) (cos ϑ_W) − 3D bin−to−bin correction − 189 GeV qqmn

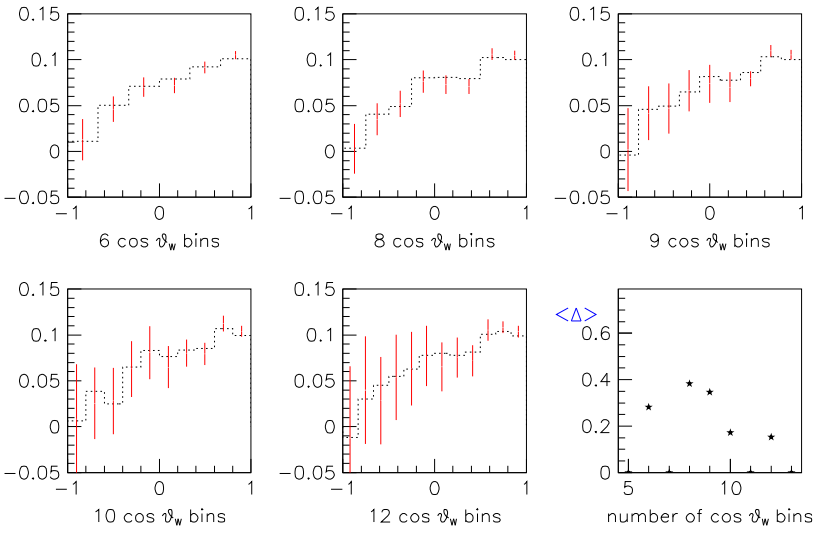

Im $(\rho+0)$ $(\cos\vartheta_w)$ – 3D bin–to–bin correction – 189 GeV qqmn

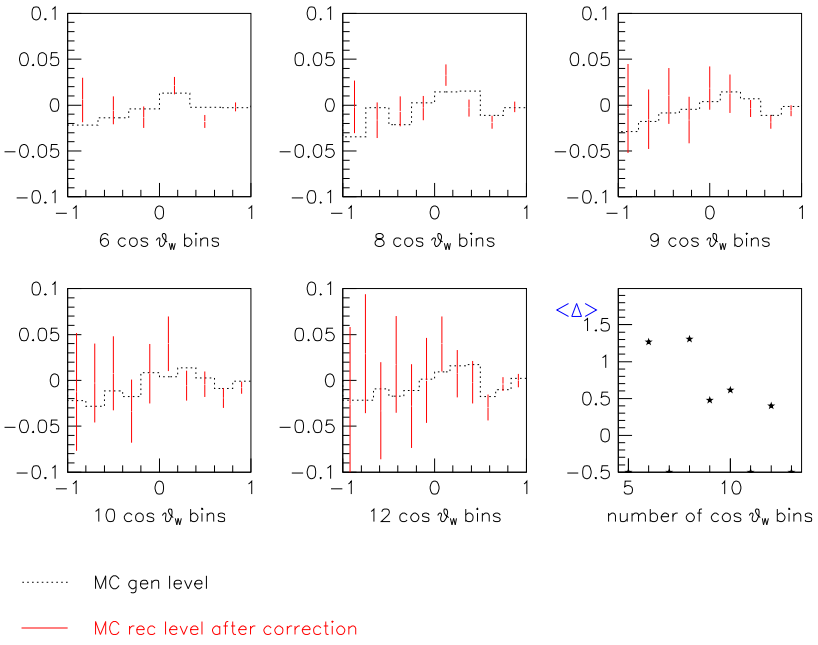

Re $(\rho-0)$ $(\cos\vartheta_w)$ – 3D bin–to–bin correction – 189 GeV qqmn

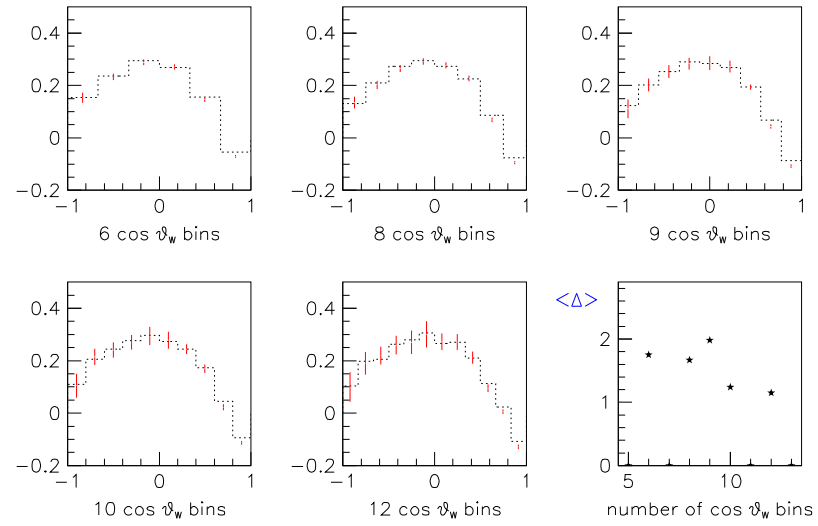

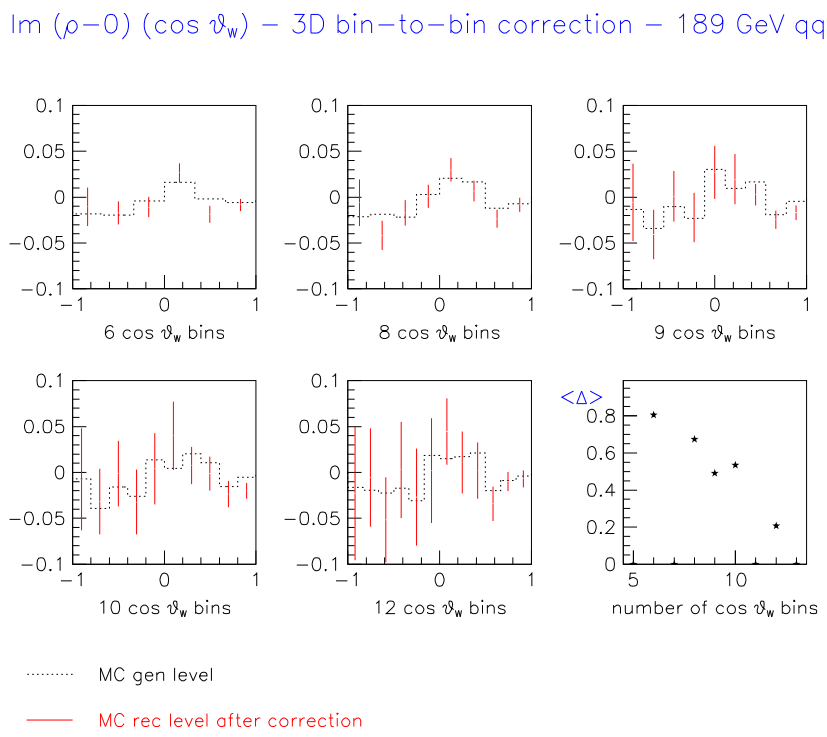

C.2 $\cos\theta^\star$ binning

The evolution of the three diagonal single W SDM elements ρ_{++}, ρ_{--} and ρ_{00}, and the real and the imaginary parts of the off-diagonal single W SDM elements ρ_{+0} and ρ_{-0} as function of the number of $\cos\theta^\star$ bins is shown in each of the 8 $\cos\theta_W$ bins for the $qq\mu\nu(\gamma)$ final state at $\sqrt{s} = 189$ GeV. The solid line shows the KandY Monte Carlo single W SDM elements as function of the number of $\cos\theta^\star$ bins, on reconstruction level, after bin-to-bin correction, while the dashed line represents the corresponding distribution on generator level with its corresponding 1σ-band. The binning in $\cos\theta_W$ was fixed to 8, while the binning in $\phi^\star$ to 10 for the off-diagonal elements ρ_{+0} and ρ_{-0}. Also the average deviation is shown as function of the number of $\cos\theta^\star$ bins.

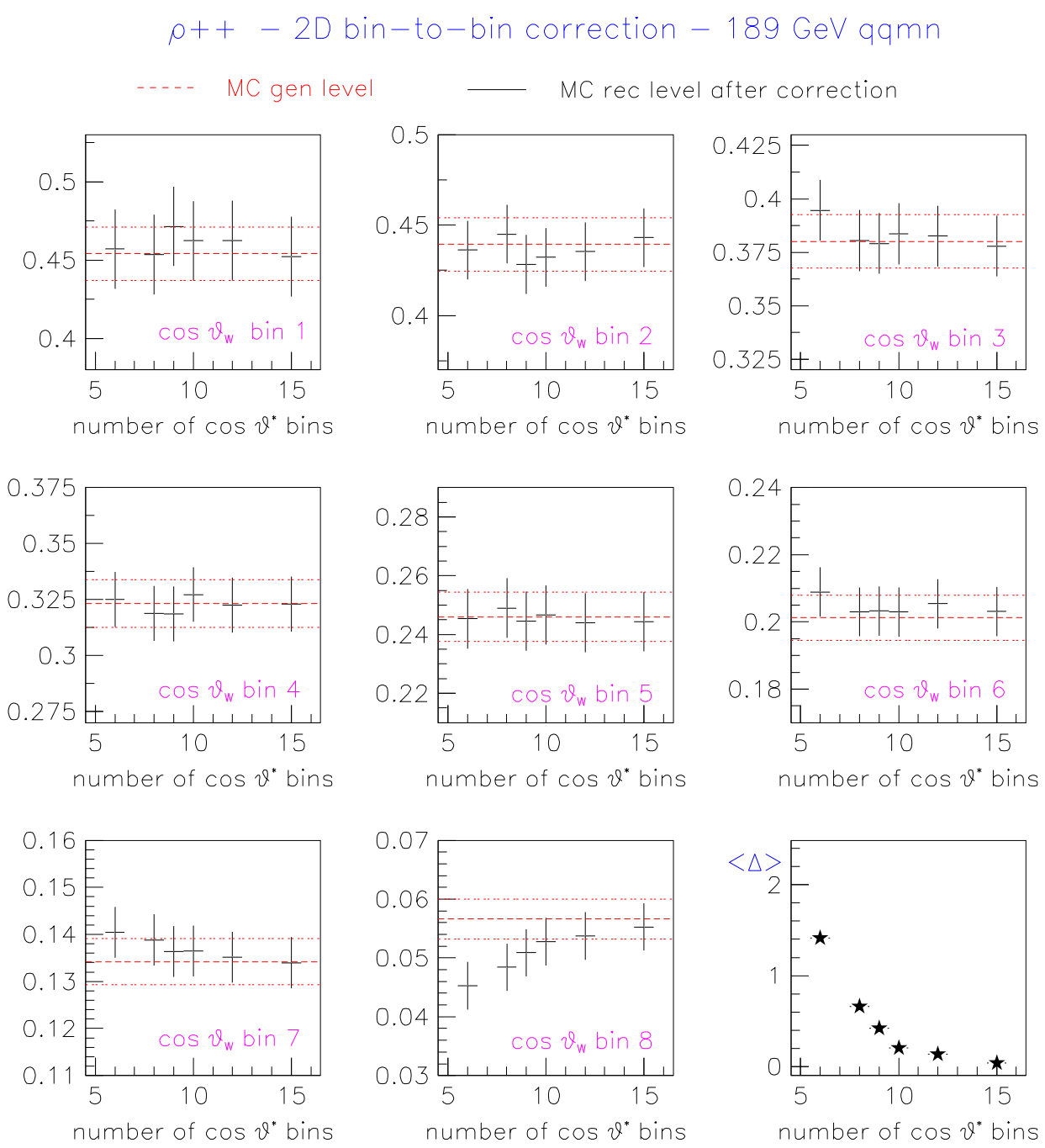
ρ++ – 2D bin–to–bin correction – 189 GeV qqmn
MC gen level
MC rec level after correction
cos ϑw bin 1
cos ϑw bin 2
cos ϑw bin 3
cos ϑw bin 4
cos ϑw bin 5
cos ϑw bin 6
cos ϑw bin 7
cos ϑw bin 8
<Δ>
number of cos ϑ* bins

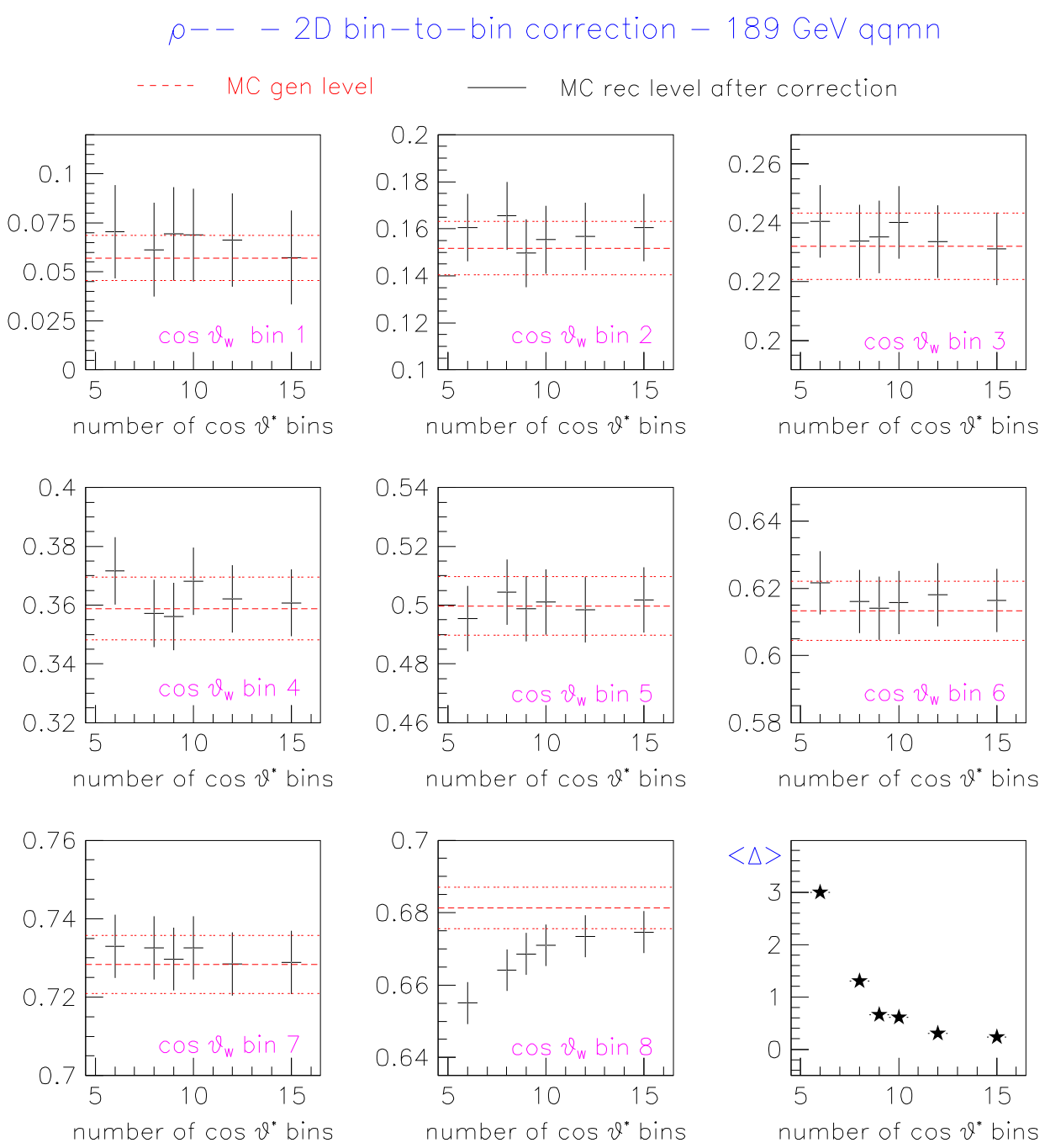
ρ−− − 2D bin−to−bin correction − 189 GeV qqmn
MC gen level
MC rec level after correction
cos ϑw bin 1
cos ϑw bin 2
cos ϑw bin 3
cos ϑw bin 4
cos ϑw bin 5
cos ϑw bin 6
cos ϑw bin 7
cos ϑw bin 8
<Δ>
number of cos ϑ* bins

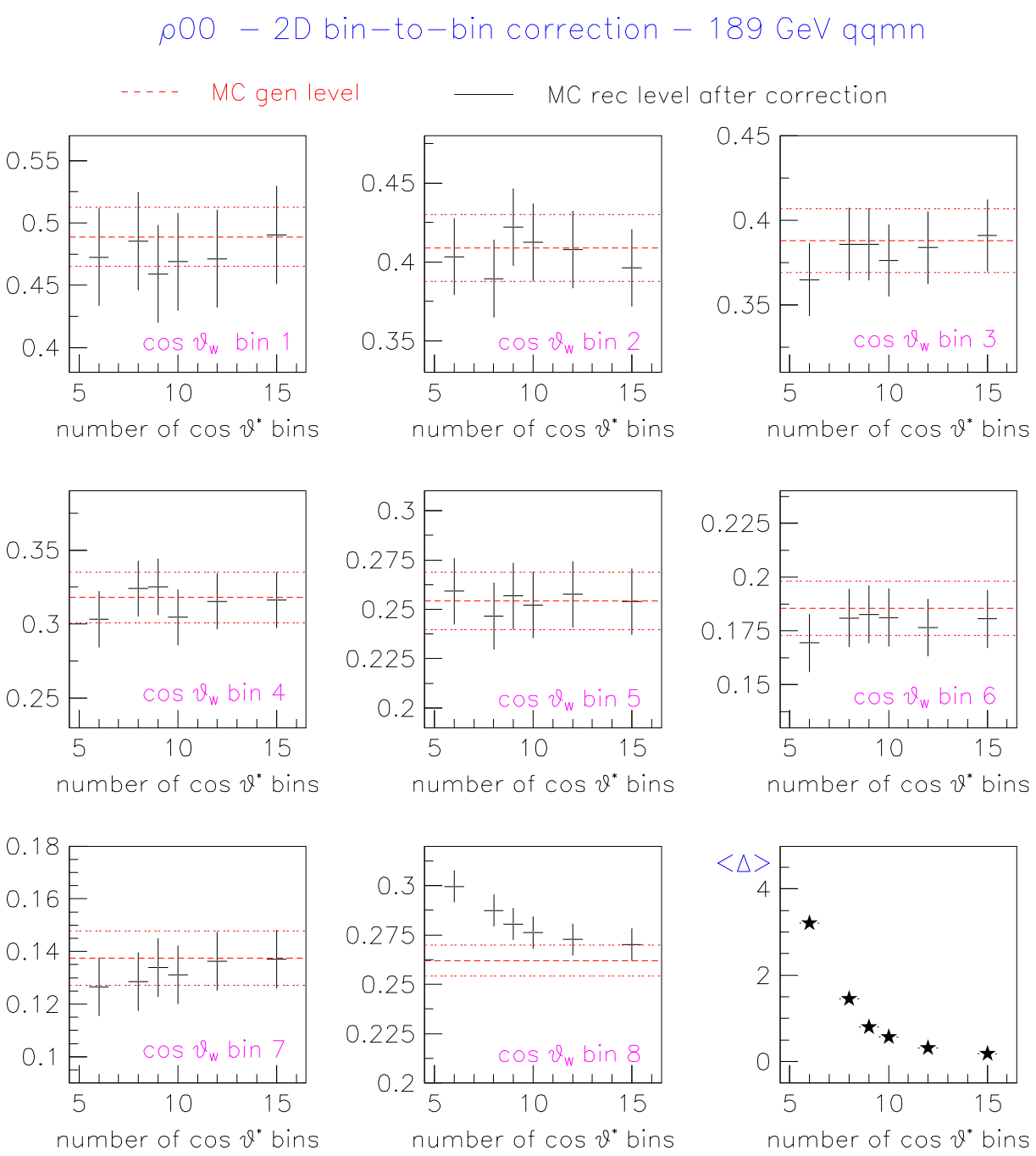
ρ00 – 2D bin–to–bin correction – 189 GeV qqmn
MC gen level
MC rec level after correction
cos ϑw bin 1
cos ϑw bin 2
cos ϑw bin 3
cos ϑw bin 4
cos ϑw bin 5
cos ϑw bin 6
cos ϑw bin 7
cos ϑw bin 8
<Δ>
number of cos ϑ* bins

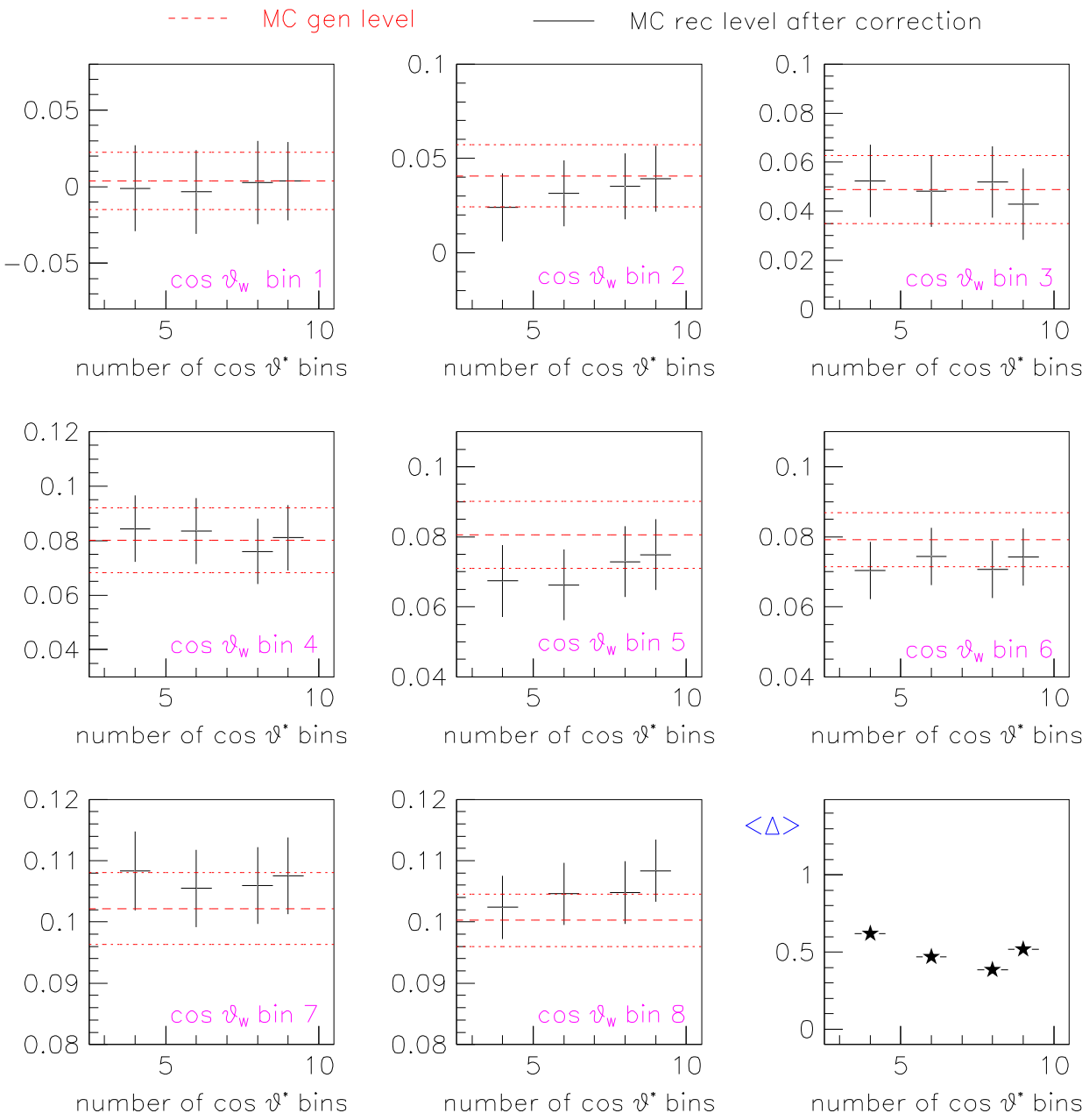
Re (ρ+0) – 3D bin–to–bin correction – 189 GeV qqmn
MC gen level
MC rec level after correction
cos ϑw bin 1
cos ϑw bin 2
cos ϑw bin 3
cos ϑw bin 4
cos ϑw bin 5
cos ϑw bin 6
cos ϑw bin 7
cos ϑw bin 8
<Δ>
number of cos ϑ* bins

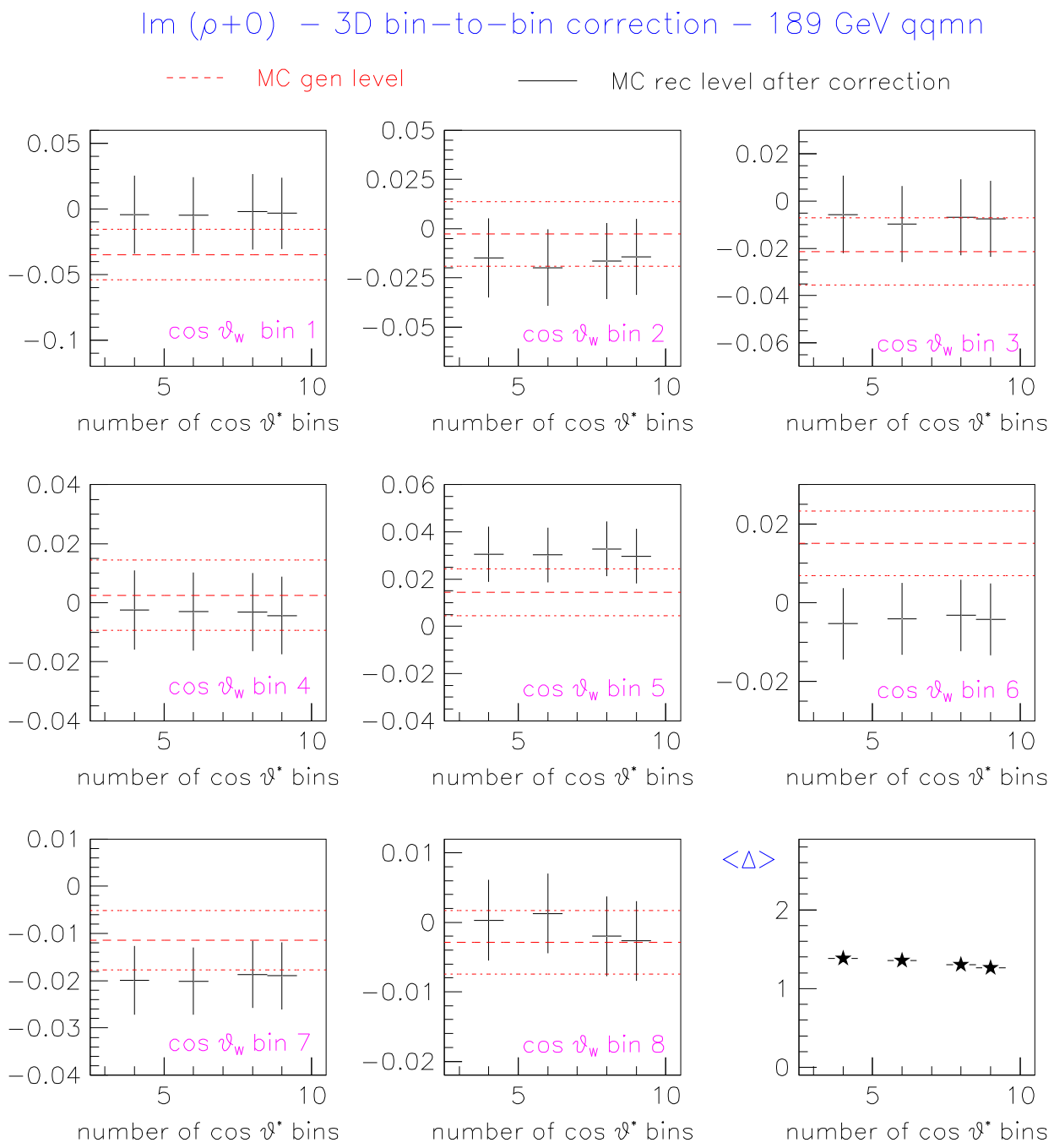
Im (ρ+0) – 3D bin–to–bin correction – 189 GeV qqmn
MC gen level
MC rec level after correction
cos ϑw bin 1
cos ϑw bin 2
cos ϑw bin 3
cos ϑw bin 4
cos ϑw bin 5
cos ϑw bin 6
cos ϑw bin 7
cos ϑw bin 8
<Δ>
number of cos ϑ* bins

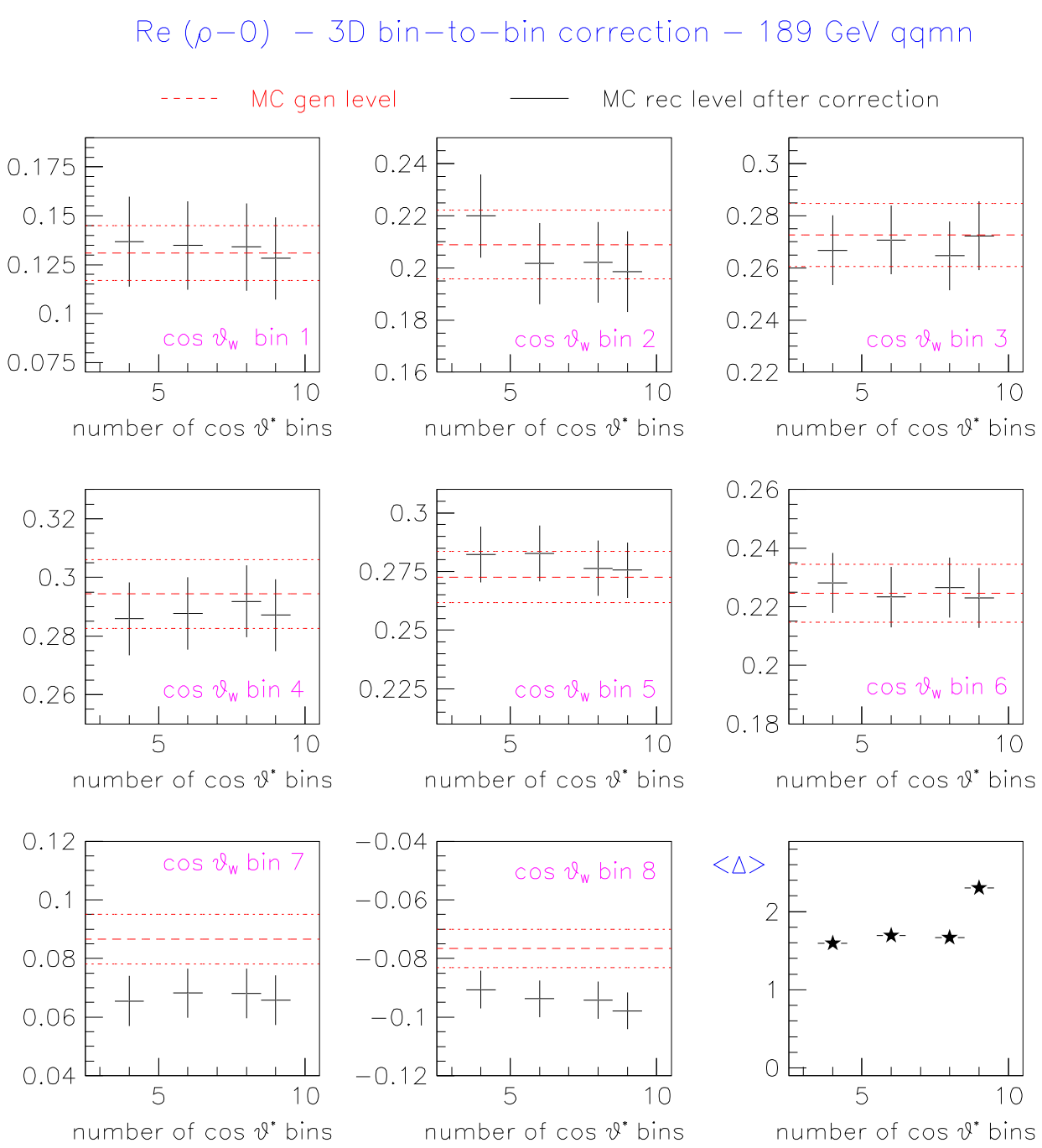
Re (ρ−0) − 3D bin−to−bin correction − 189 GeV qqmn
MC gen level
MC rec level after correction
cos ϑw bin 1
cos ϑw bin 2
cos ϑw bin 3
cos ϑw bin 4
cos ϑw bin 5
cos ϑw bin 6
cos ϑw bin 7
cos ϑw bin 8
<Δ>
number of cos ϑ* bins

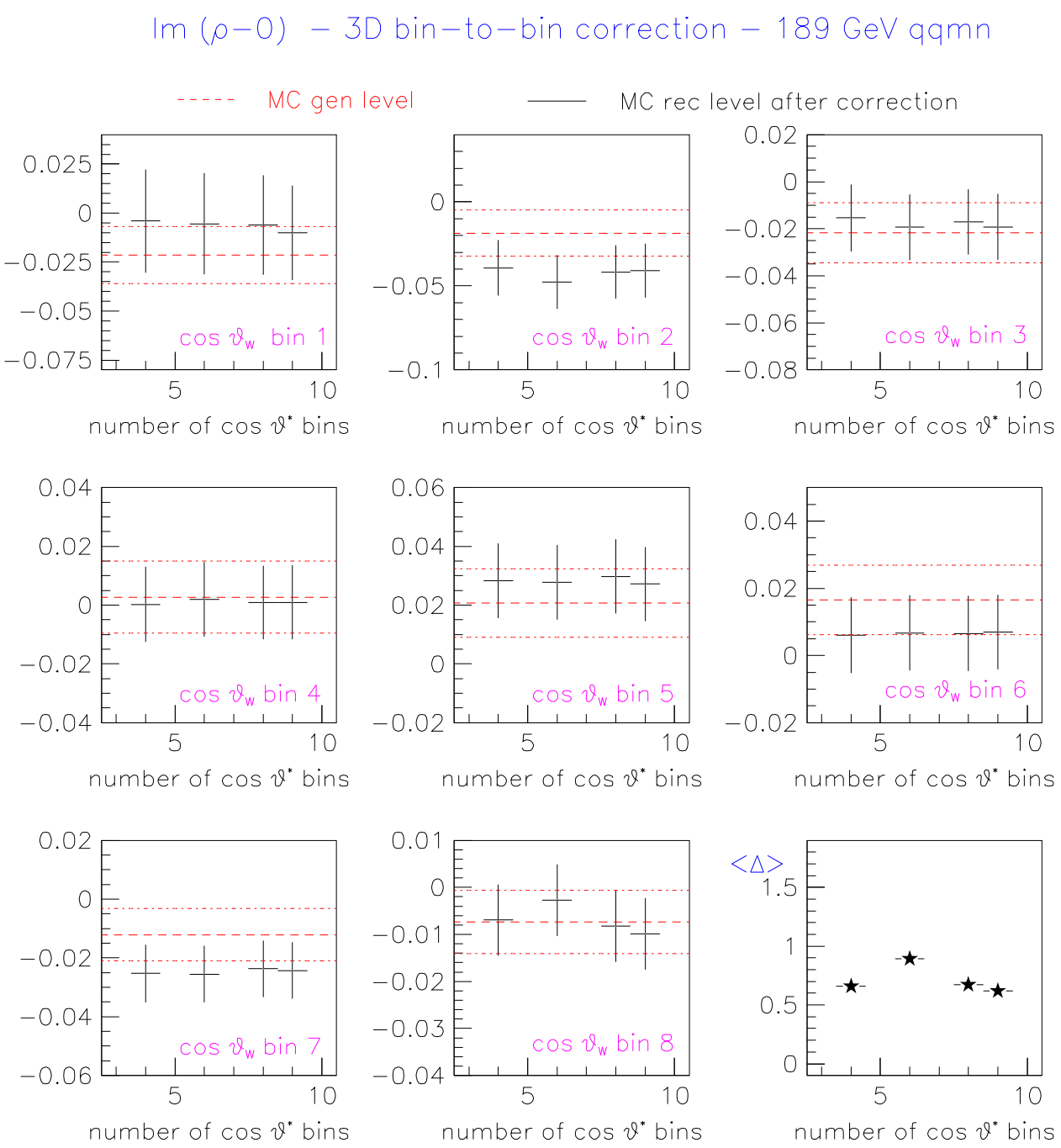
Im (ρ−0) − 3D bin−to−bin correction − 189 GeV qqmn
MC gen level
MC rec level after correction
cos ϑw bin 1
cos ϑw bin 2
cos ϑw bin 3
cos ϑw bin 4
cos ϑw bin 5
cos ϑw bin 6
cos ϑw bin 7
cos ϑw bin 8
<Δ>
number of cos ϑ* bins

C.3 $\phi^\star$ binning

The evolution of the off-diagonal single W SDM elements as function of the number of $\phi^\star$ bins is shown in each of the 8 $\cos\theta_W$ bins for the $qq\mu\nu_\mu(\gamma)$ final state at $\sqrt{s} = 189$ GeV. The solid line shows the KandY Monte Carlo single W SDM elements as function of the number of $\phi^\star$ bins, on reconstruction level, after bin-to-bin correction, while the dashed line represents the corresponding distribution on generator level with its corresponding 1σ-band. The binning in $\cos\theta_W$ as well as in $\cos\theta^\star$ was fixed to 8. Also the average deviation is shown as function of the number of $\phi^\star$ bins.

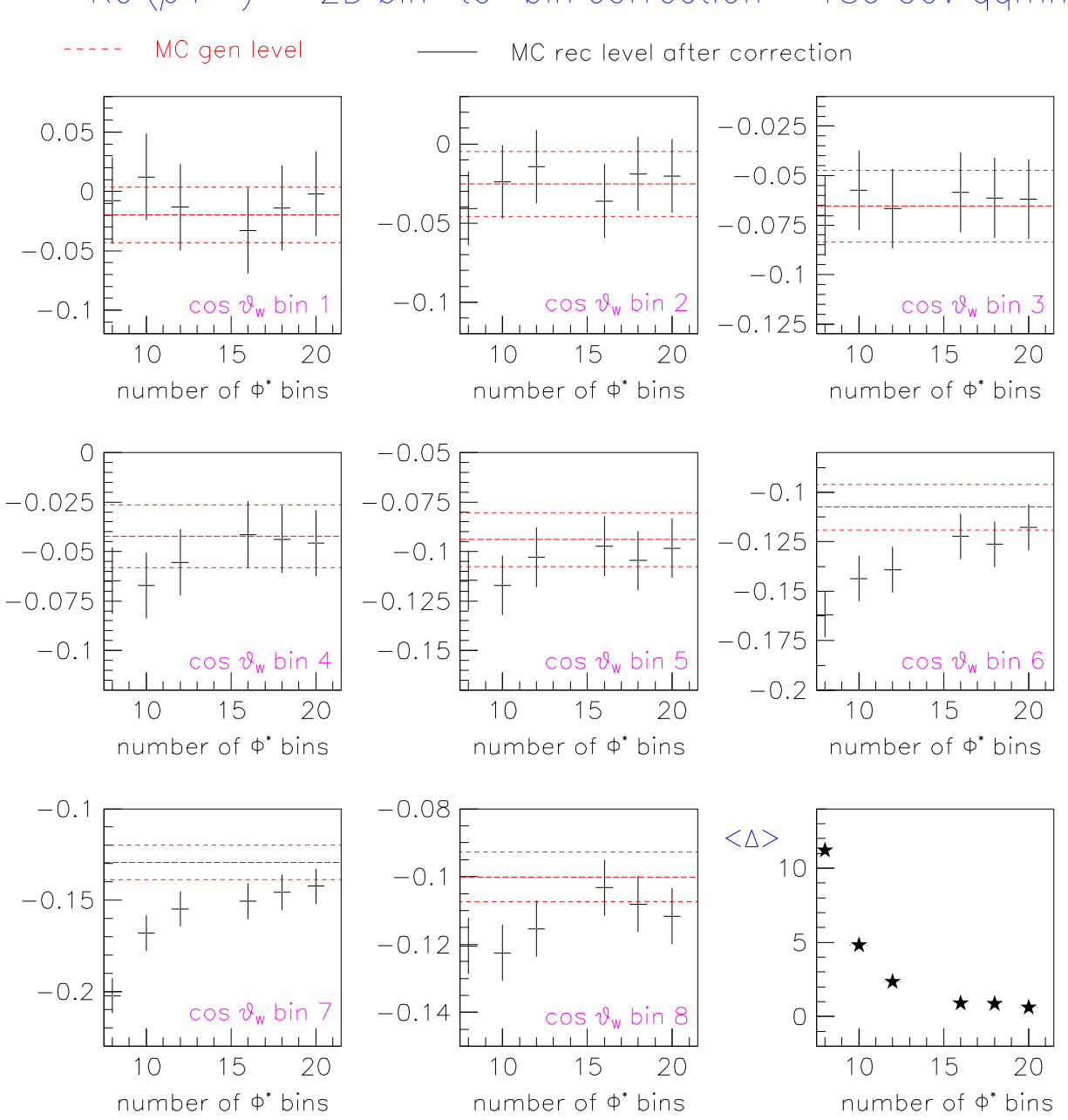
Re (ρ+−) − 2D bin−to−bin correction − 189 GeV qqmn
MC gen level
MC rec level after correction
cos ϑw bin 1
cos ϑw bin 2
cos ϑw bin 3
cos ϑw bin 4
cos ϑw bin 5
cos ϑw bin 6
cos ϑw bin 7
cos ϑw bin 8
<Δ>
number of Φ* bins

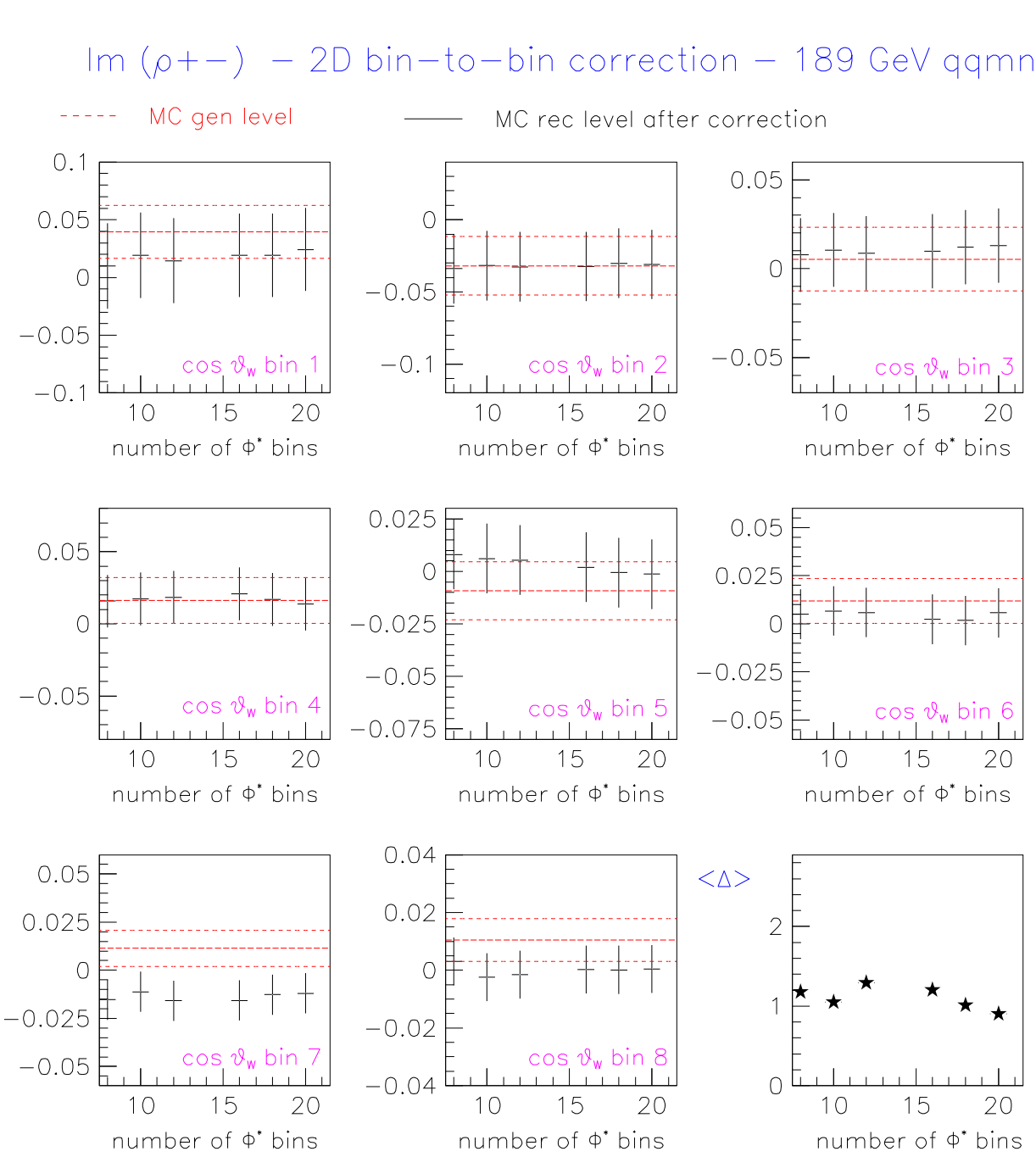
Im (ρ+−) − 2D bin−to−bin correction − 189 GeV qqmn
MC gen level
MC rec level after correction
cos ϑw bin 1
cos ϑw bin 2
cos ϑw bin 3
cos ϑw bin 4
cos ϑw bin 5
cos ϑw bin 6
cos ϑw bin 7
cos ϑw bin 8
number of Φ* bins
<Δ>

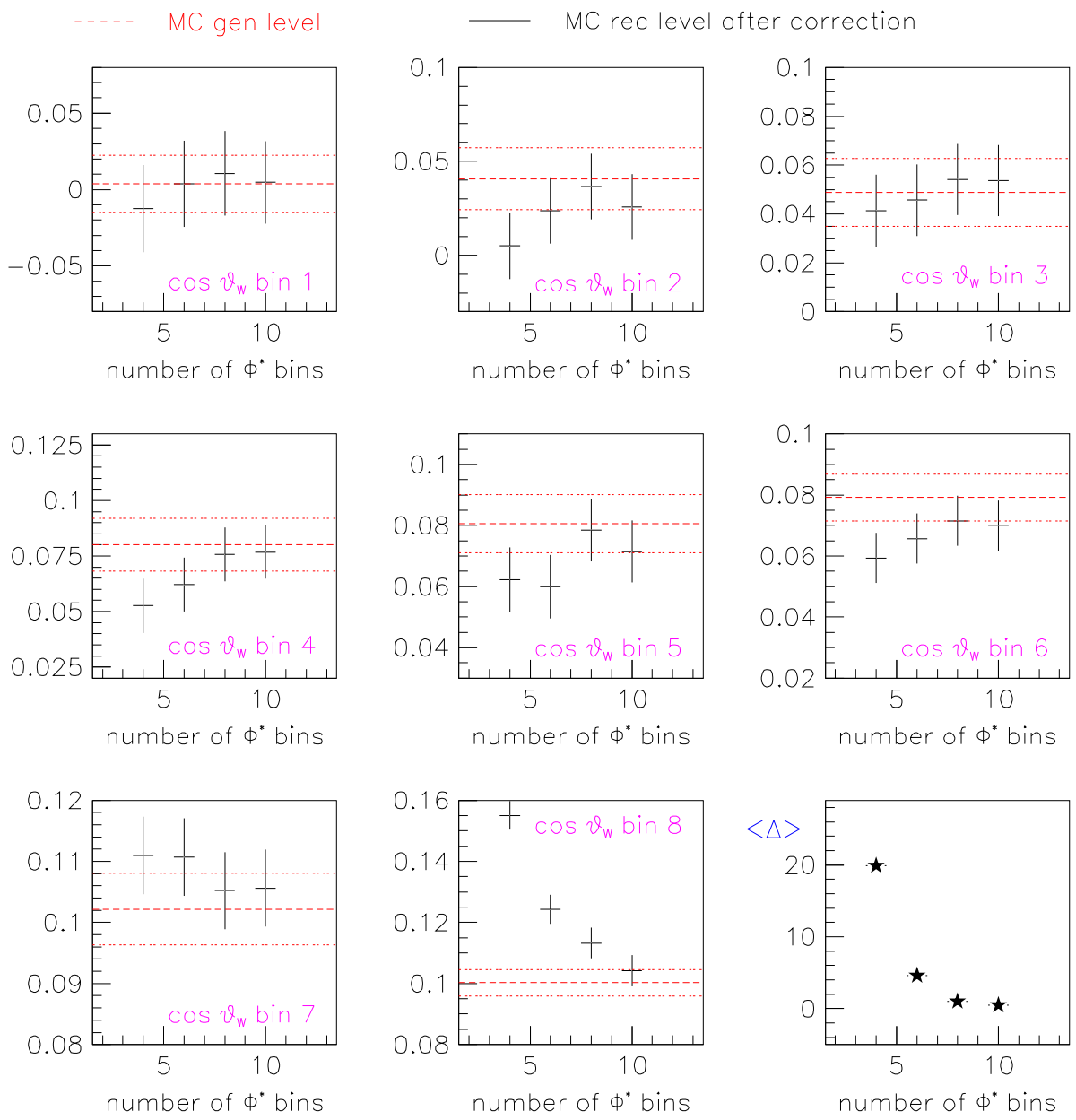
Re (ρ+0) – 3D bin–to–bin correction – 189 GeV qqmn
MC gen level
MC rec level after correction
cos ϑw bin 1
cos ϑw bin 2
cos ϑw bin 3
cos ϑw bin 4
cos ϑw bin 5
cos ϑw bin 6
cos ϑw bin 7
cos ϑw bin 8
<Δ>
number of Φ* bins

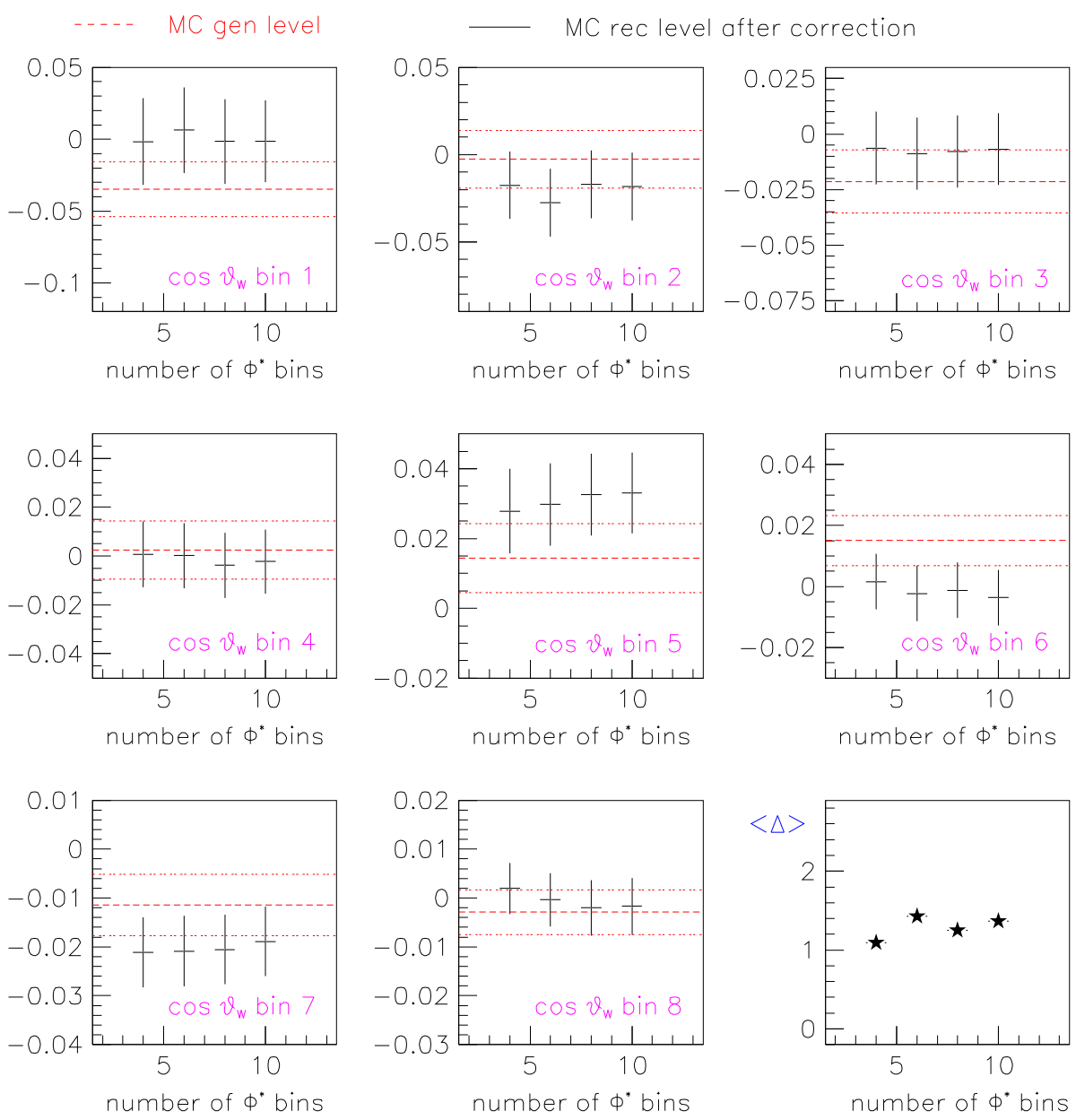
Im (ρ+0) – 3D bin–to–bin correction – 189 GeV qqmn
MC gen level
MC rec level after correction
cos ϑw bin 1
cos ϑw bin 2
cos ϑw bin 3
cos ϑw bin 4
cos ϑw bin 5
cos ϑw bin 6
cos ϑw bin 7
cos ϑw bin 8
<Δ>
number of Φ* bins

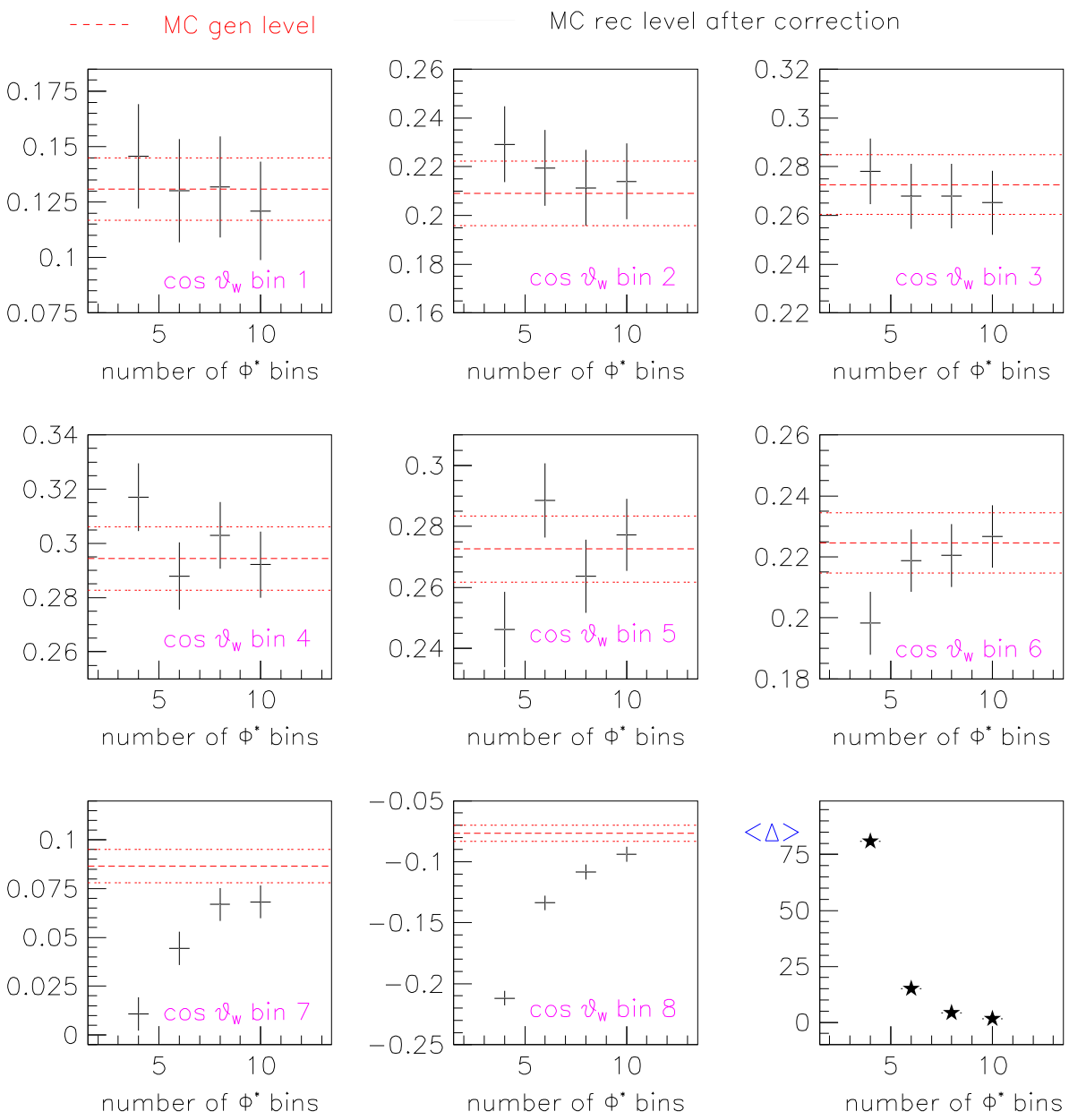
Re (ρ−0) − 3D bin−to−bin correction − 189 GeV qqmn
MC gen level
MC rec level after correction
cos ϑw bin 1
cos ϑw bin 2
cos ϑw bin 3
cos ϑw bin 4
cos ϑw bin 5
cos ϑw bin 6
cos ϑw bin 7
cos ϑw bin 8
<Δ>
number of Φ* bins

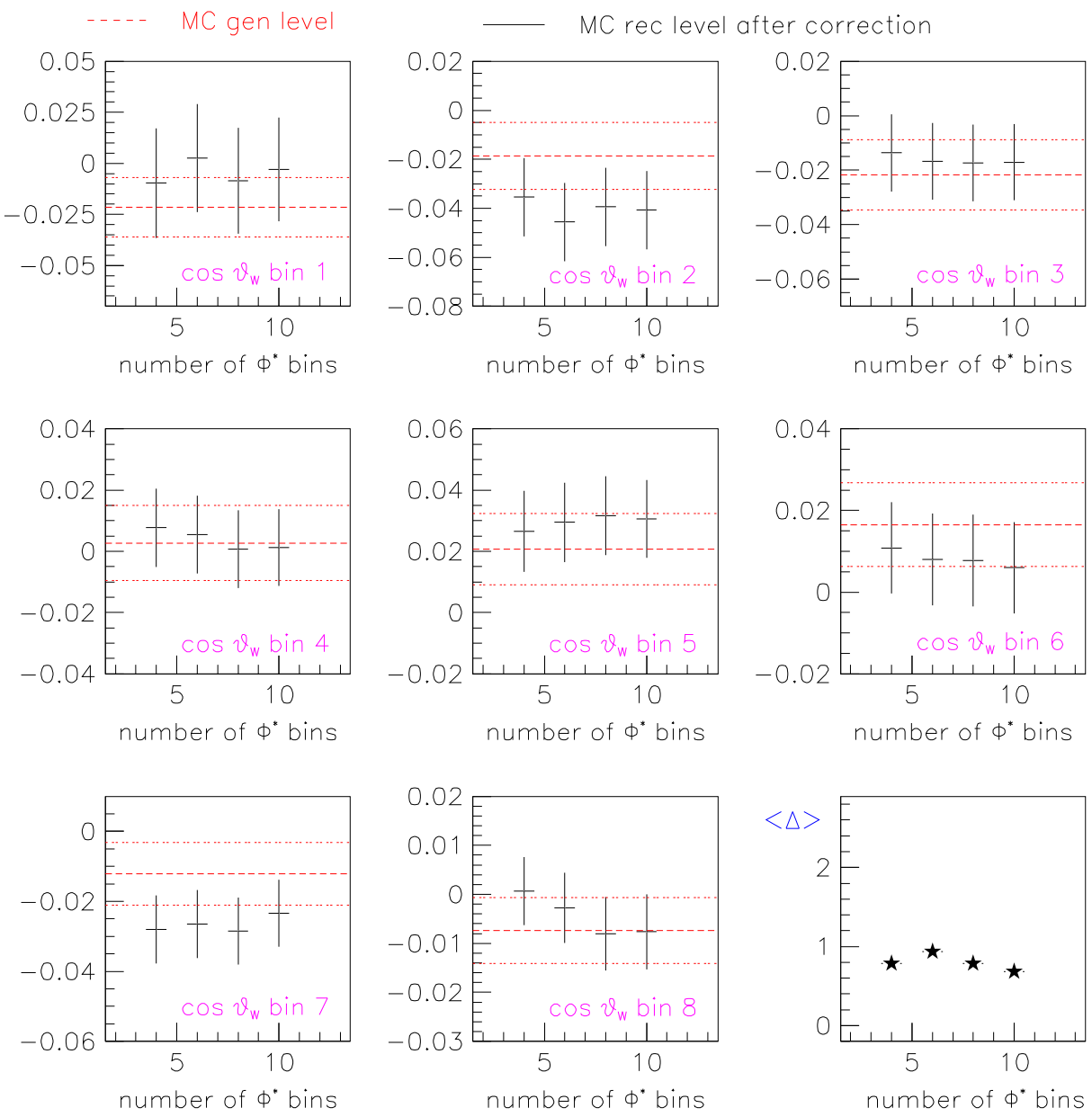
Im (ρ−0) − 3D bin−to−bin correction − 189 GeV qqmn
MC gen level
MC rec level after correction
cos ϑw bin 1
cos ϑw bin 2
cos ϑw bin 3
cos ϑw bin 4
cos ϑw bin 5
cos ϑw bin 6
cos ϑw bin 7
cos ϑw bin 8
<Δ>
number of Φ* bins

C.4 $\sqrt{s}$ dependence

A comparison is shown between the corrected single W SDM elements and the generated level distributions for the SM KandY Monte Carlo in the $qq\mu\nu$ final state at each center-of-mass energy from $\sqrt{s} = 189 - 209$ GeV.

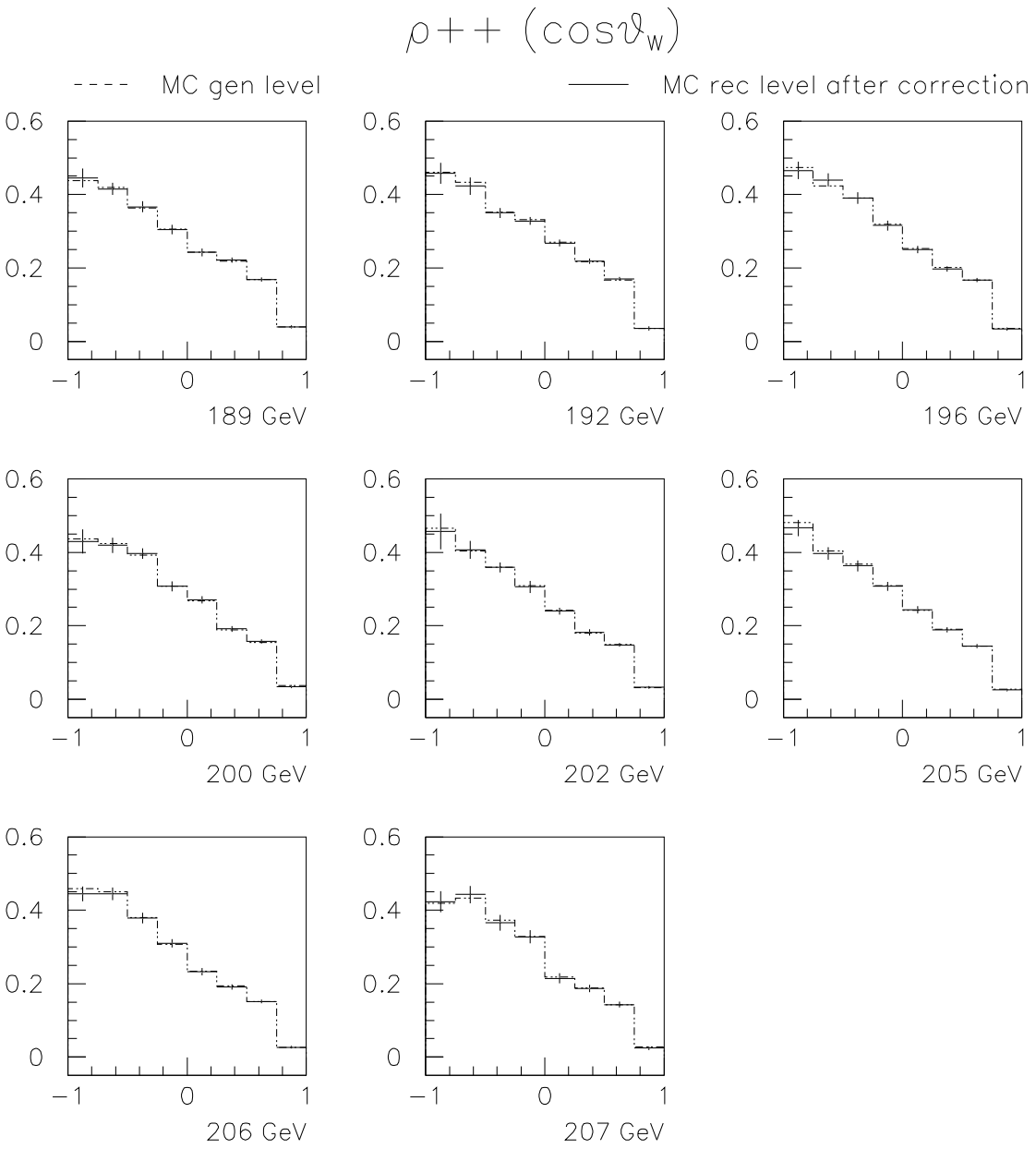

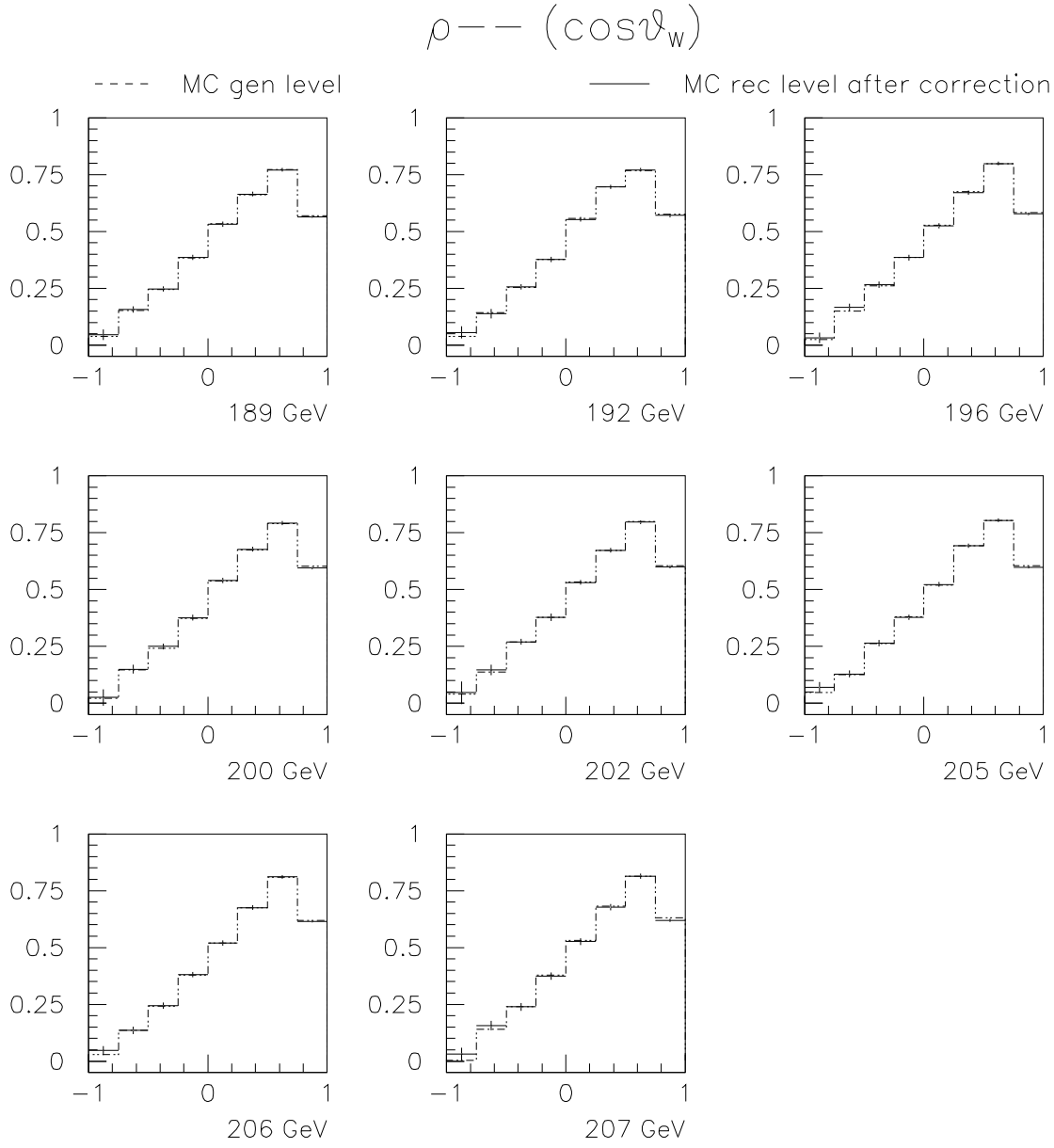
$\rho_{--}(\cos\vartheta_W)$
MC gen level
MC rec level after correction
189 GeV
192 GeV
196 GeV
200 GeV
202 GeV
205 GeV
206 GeV
207 GeV

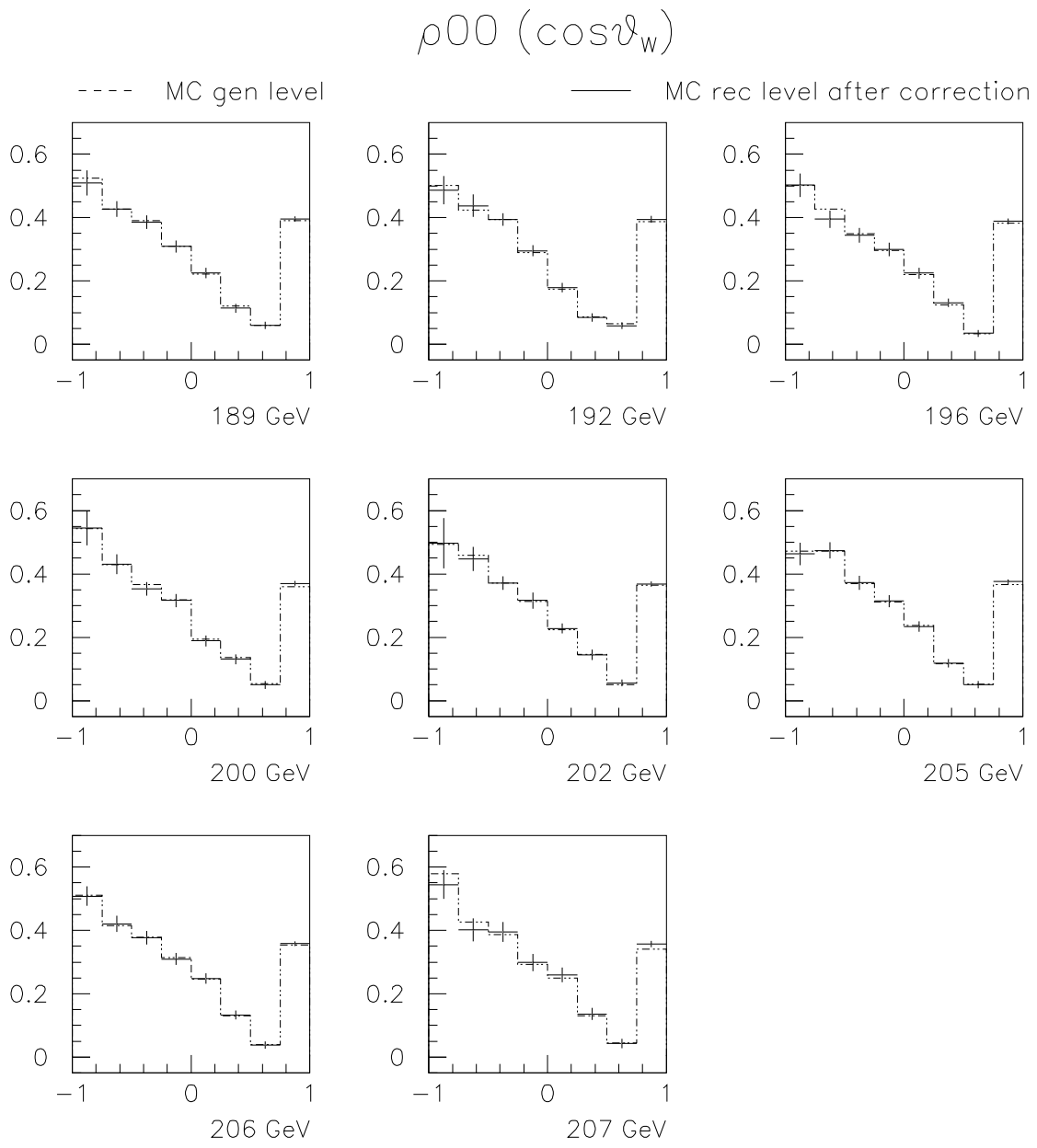
ρ00 (cosϑ_W)
MC gen level
MC rec level after correction
189 GeV
192 GeV
196 GeV
200 GeV
202 GeV
205 GeV
206 GeV
207 GeV

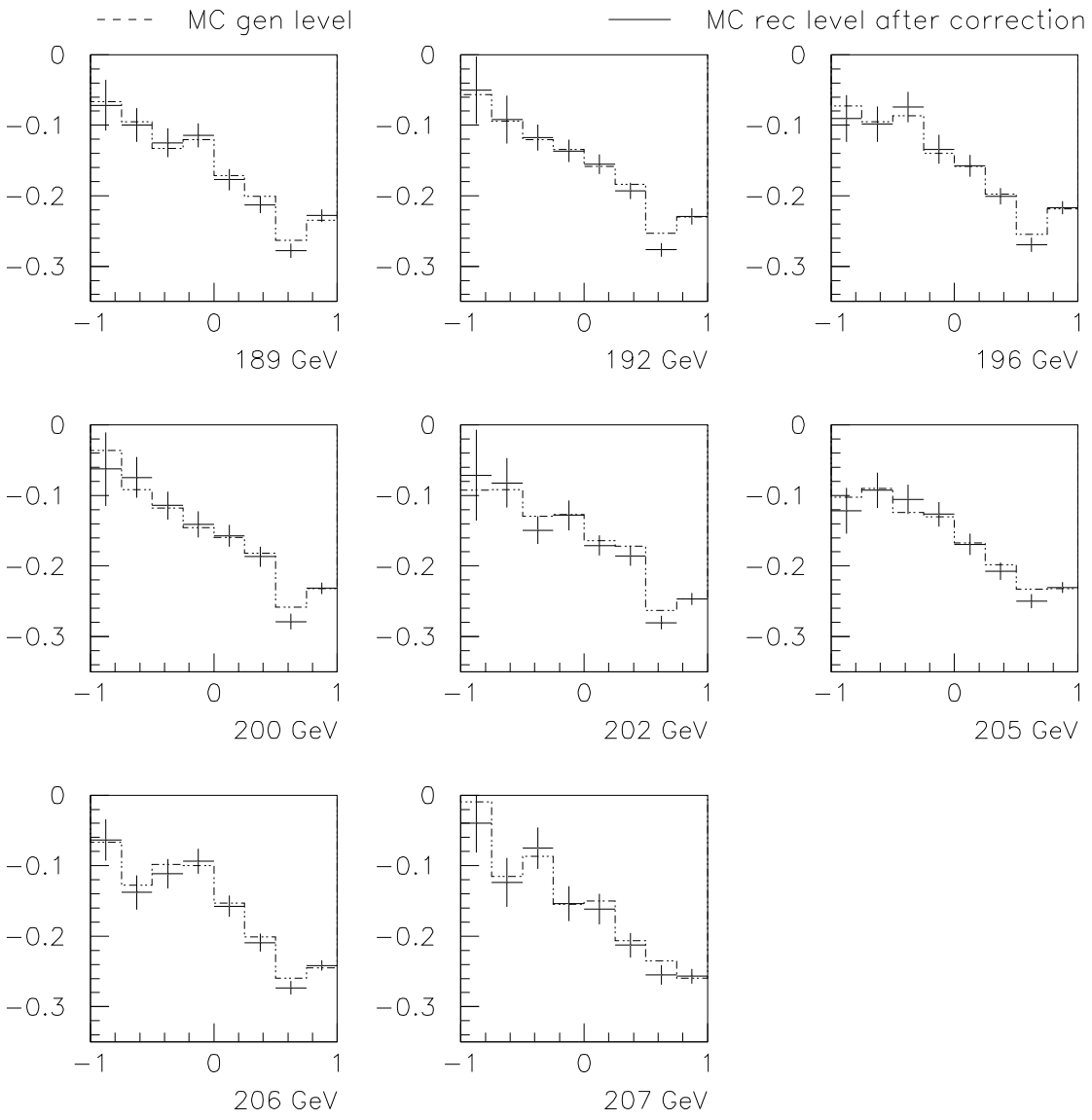
Re (ρ+−) (cosϑ_W)
MC gen level
MC rec level after correction
189 GeV
192 GeV
196 GeV
200 GeV
202 GeV
205 GeV
206 GeV
207 GeV

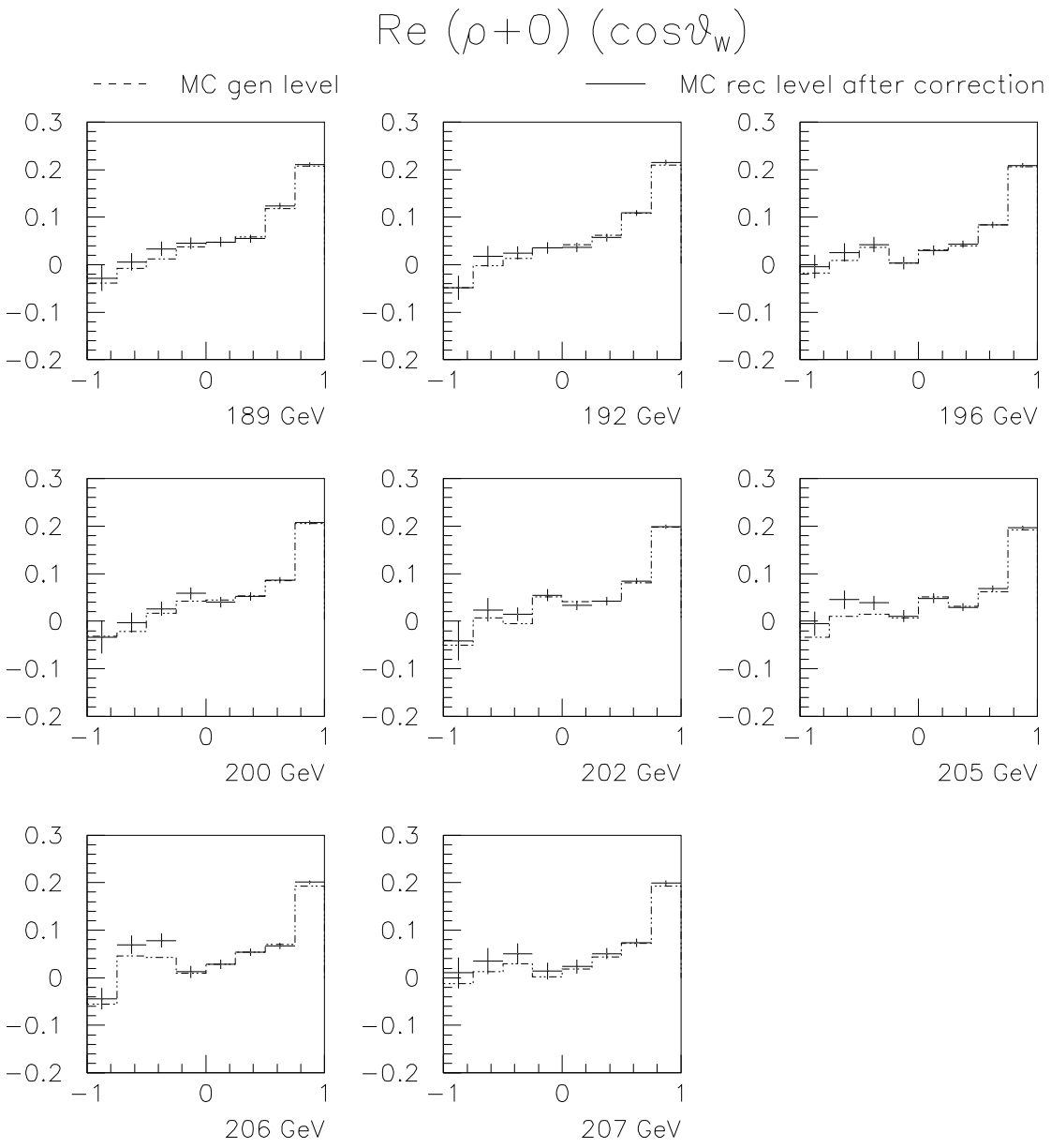
Re (ρ+0) (cosϑW)
MC gen level
MC rec level after correction
189 GeV
192 GeV
196 GeV
200 GeV
202 GeV
205 GeV
206 GeV
207 GeV

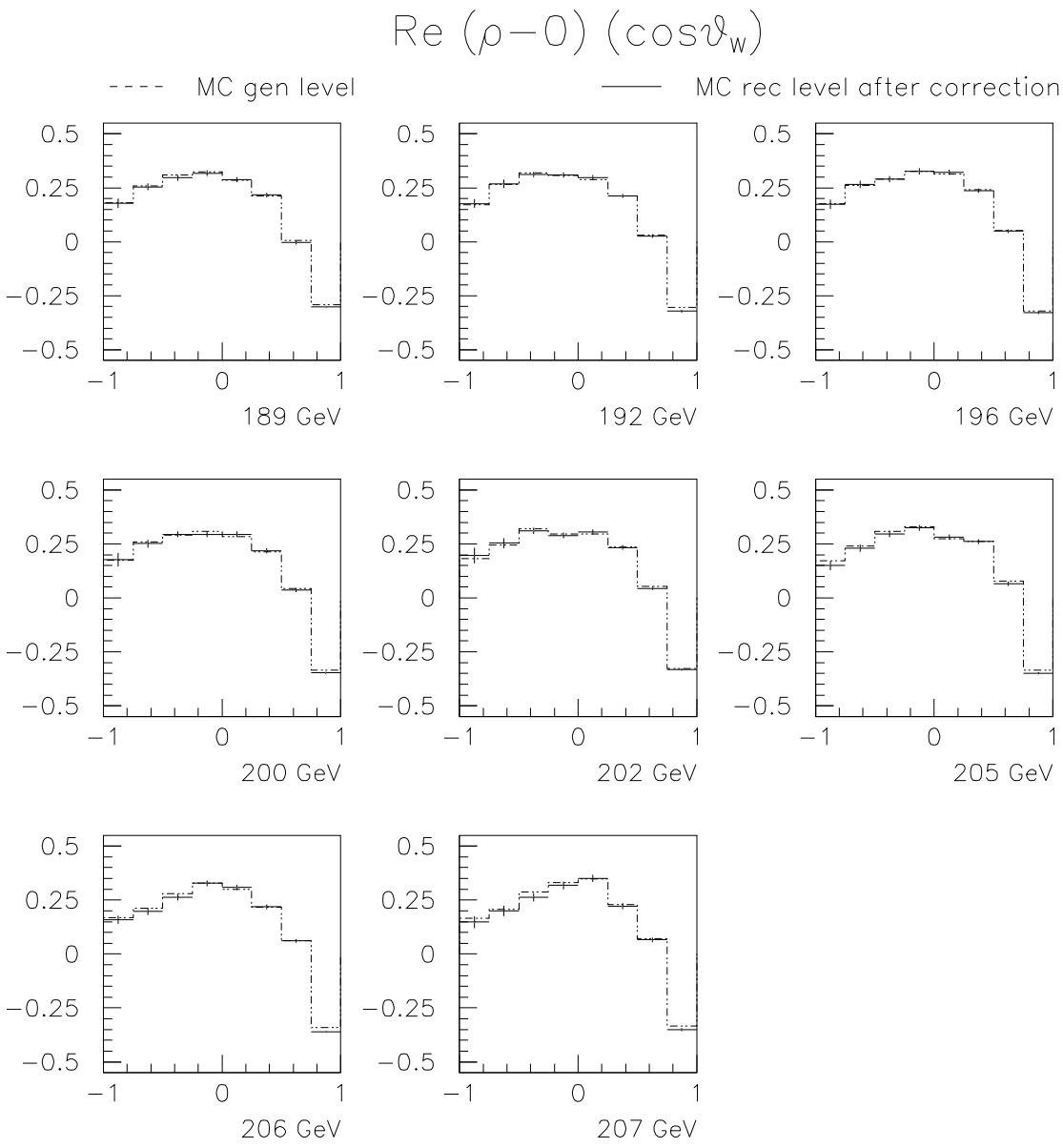
Re (ρ−0) (cosϑ_W)
MC gen level
MC rec level after correction
189 GeV
192 GeV
196 GeV
200 GeV
202 GeV
205 GeV
206 GeV
207 GeV

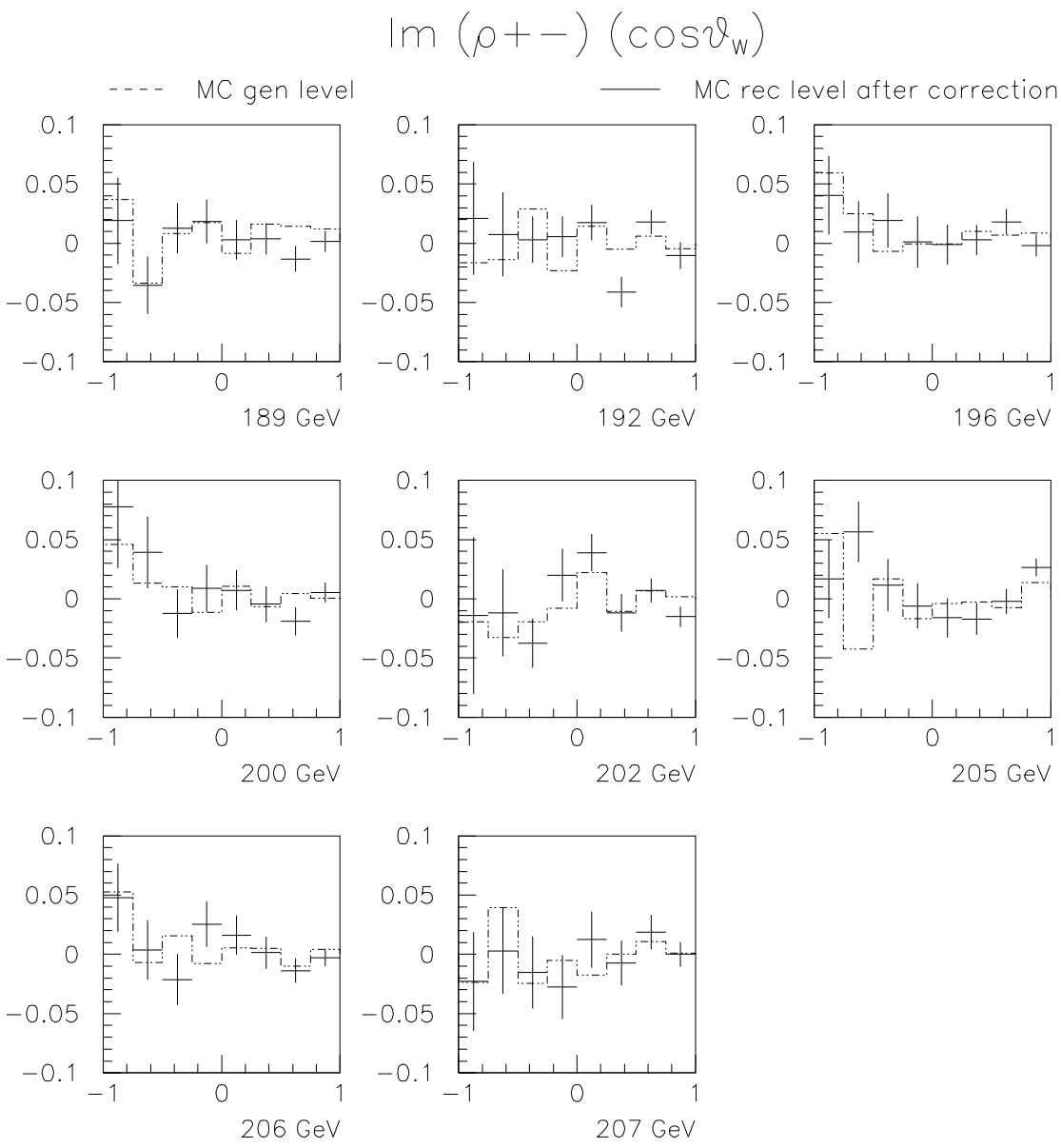
Im (ρ+−) (cosϑW)
MC gen level
MC rec level after correction
189 GeV
192 GeV
196 GeV
200 GeV
202 GeV
205 GeV
206 GeV
207 GeV

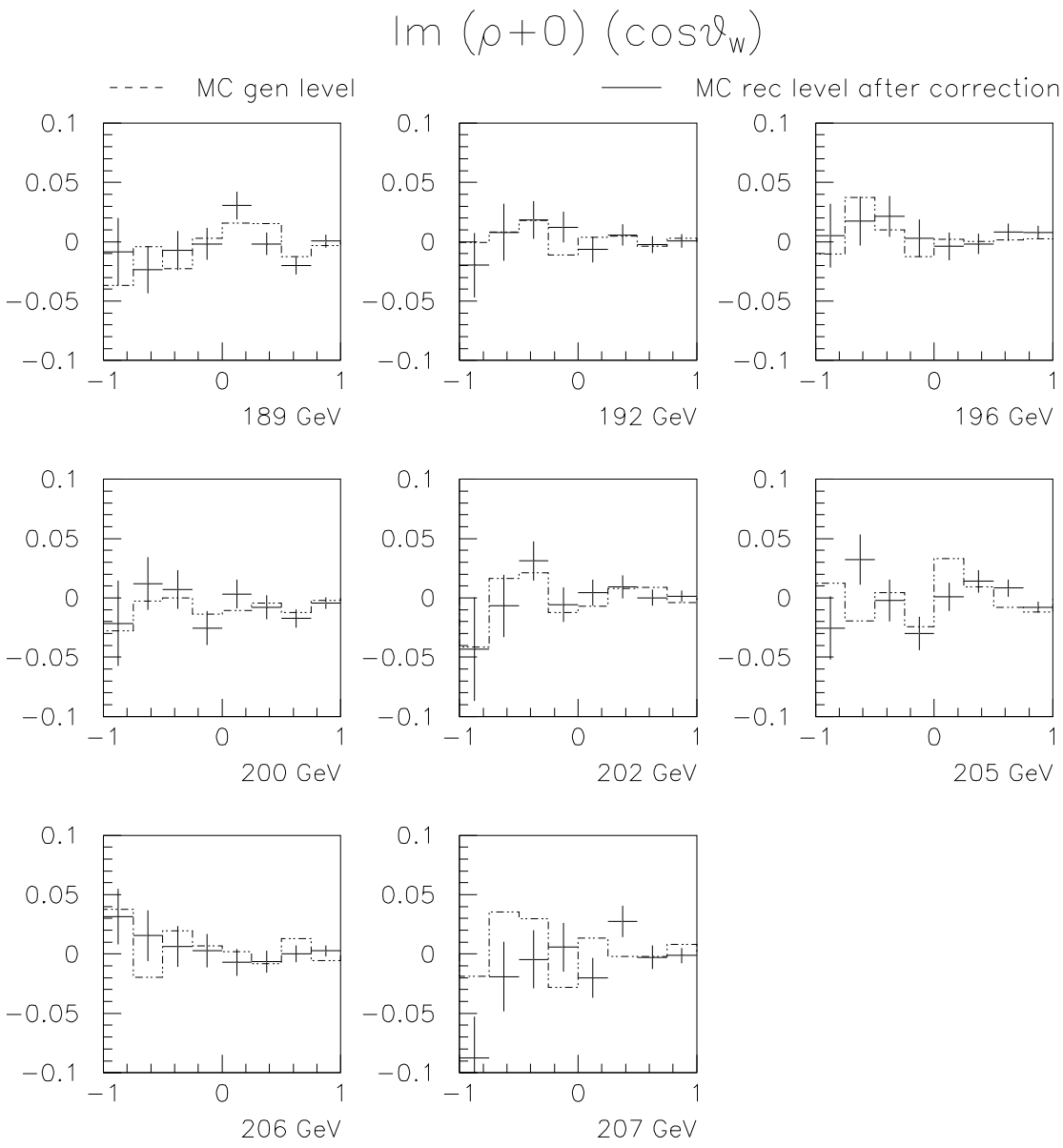
Im (ρ+0) (cosϑ_W)
MC gen level
MC rec level after correction
189 GeV
192 GeV
196 GeV
200 GeV
202 GeV
205 GeV
206 GeV
207 GeV

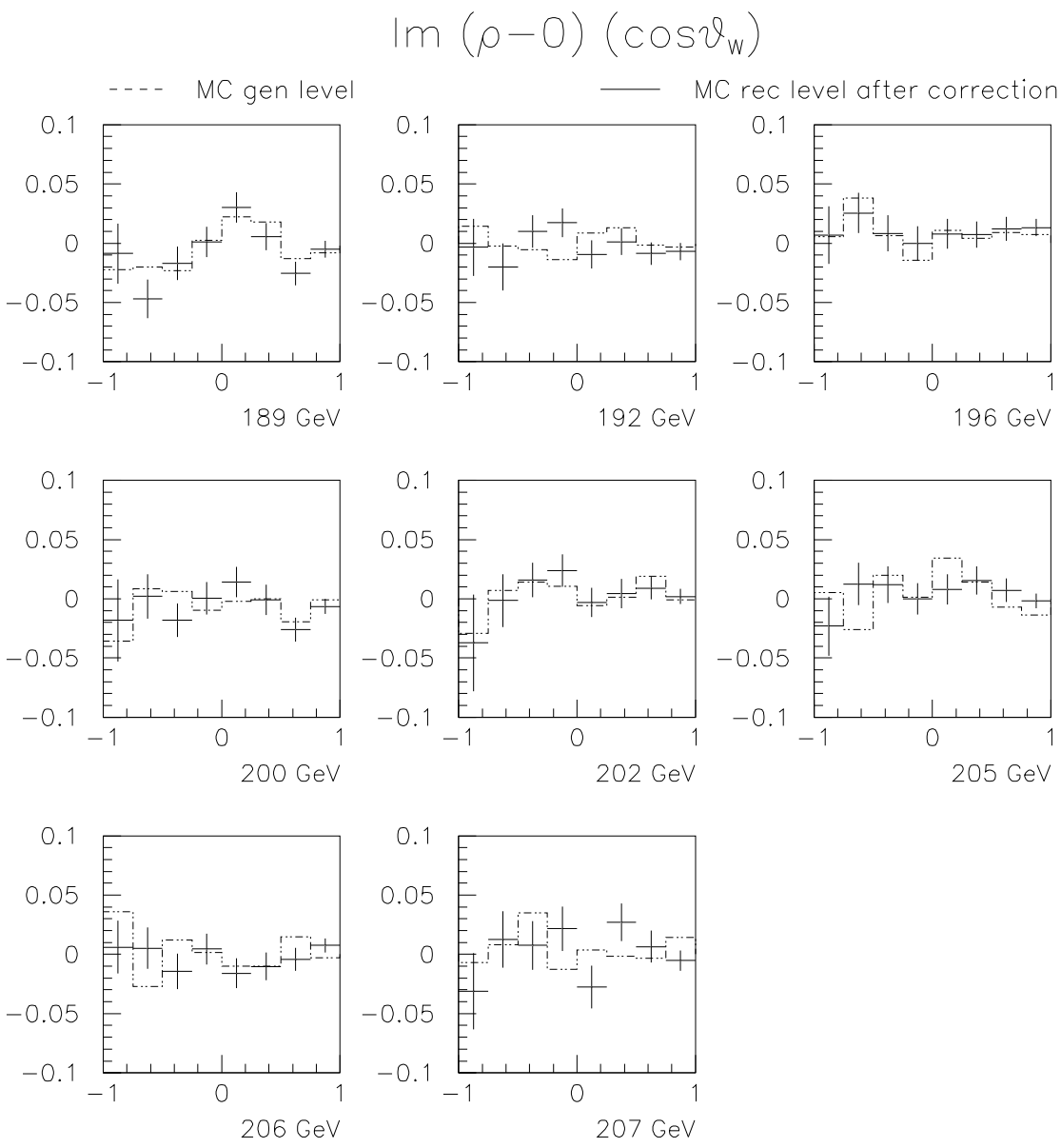
Im (ρ−0) (cosϑ_W)
MC gen level
MC rec level after correction
189 GeV
192 GeV
196 GeV
200 GeV
202 GeV
205 GeV
206 GeV
207 GeV

C.5 Pull distributions

To test if the definition of the statistical uncertainty on the SDM element (Eq. 6.33) is meanful, the following pull is defined

$$pull^{\,i} = \frac{\rho^{\,i}_{pseudo} - \rho_{SM}}{\sigma_{stat}(\rho^{\,i}_{pseudo})} \tag{C.2}$$

where ρ_{SM} is calculated with the full statistics generator level KandY Monte Carlo and where the index i runs over the pseudo data samples. The pull distribution for each SDM elements in the $\cos\theta_{W^-}$ bin separately (1 point/sample) is shown.

Pull distributions $\rho++$

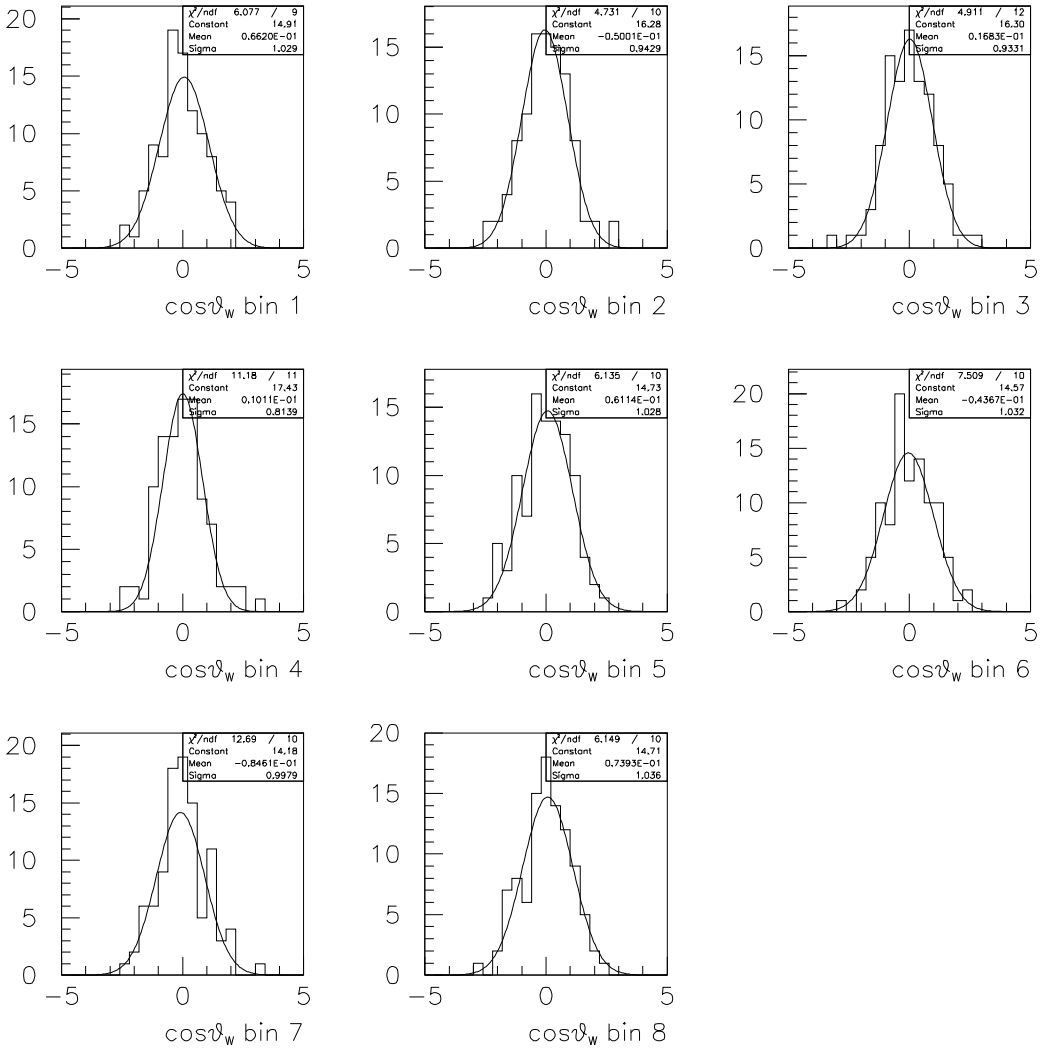

Pull distributions $\rho--$

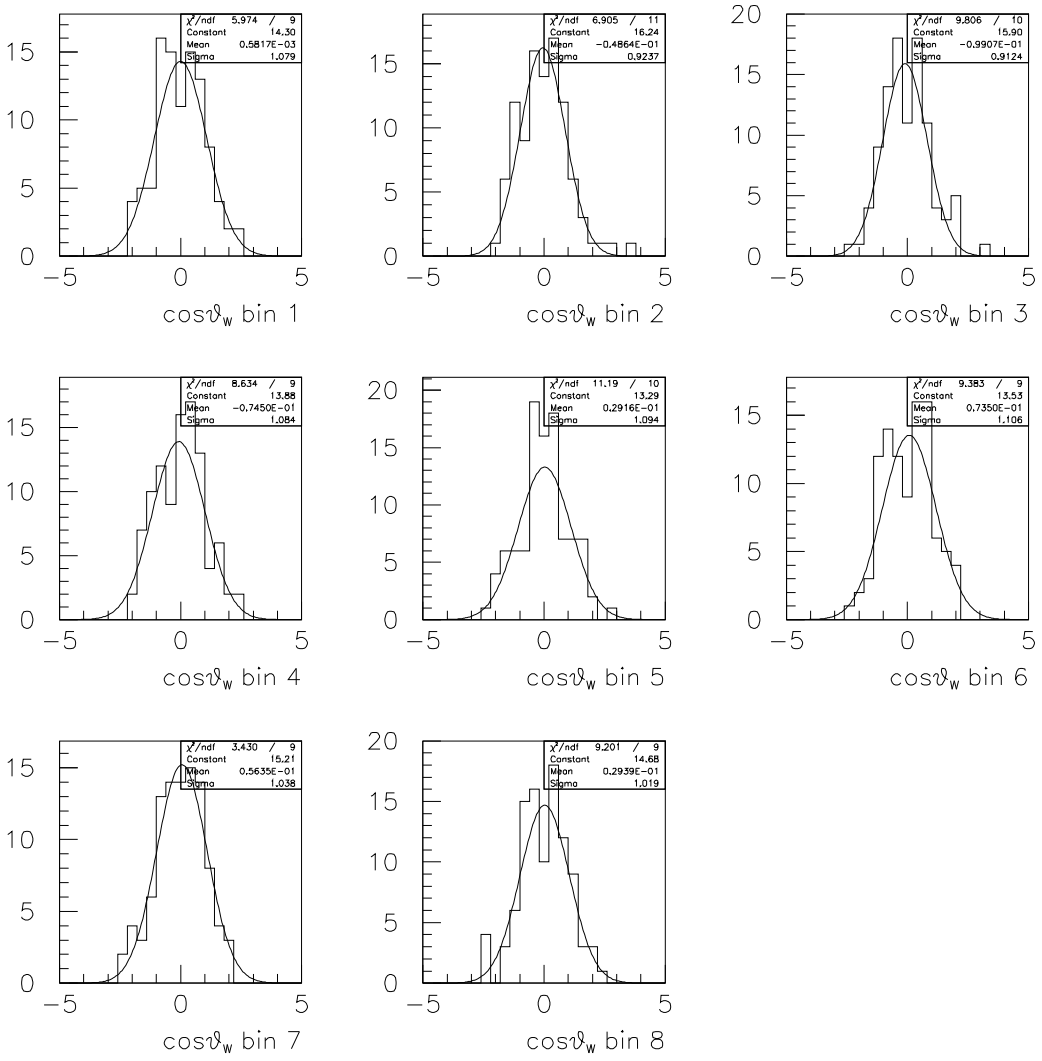

Pull distributions $\rho 00$

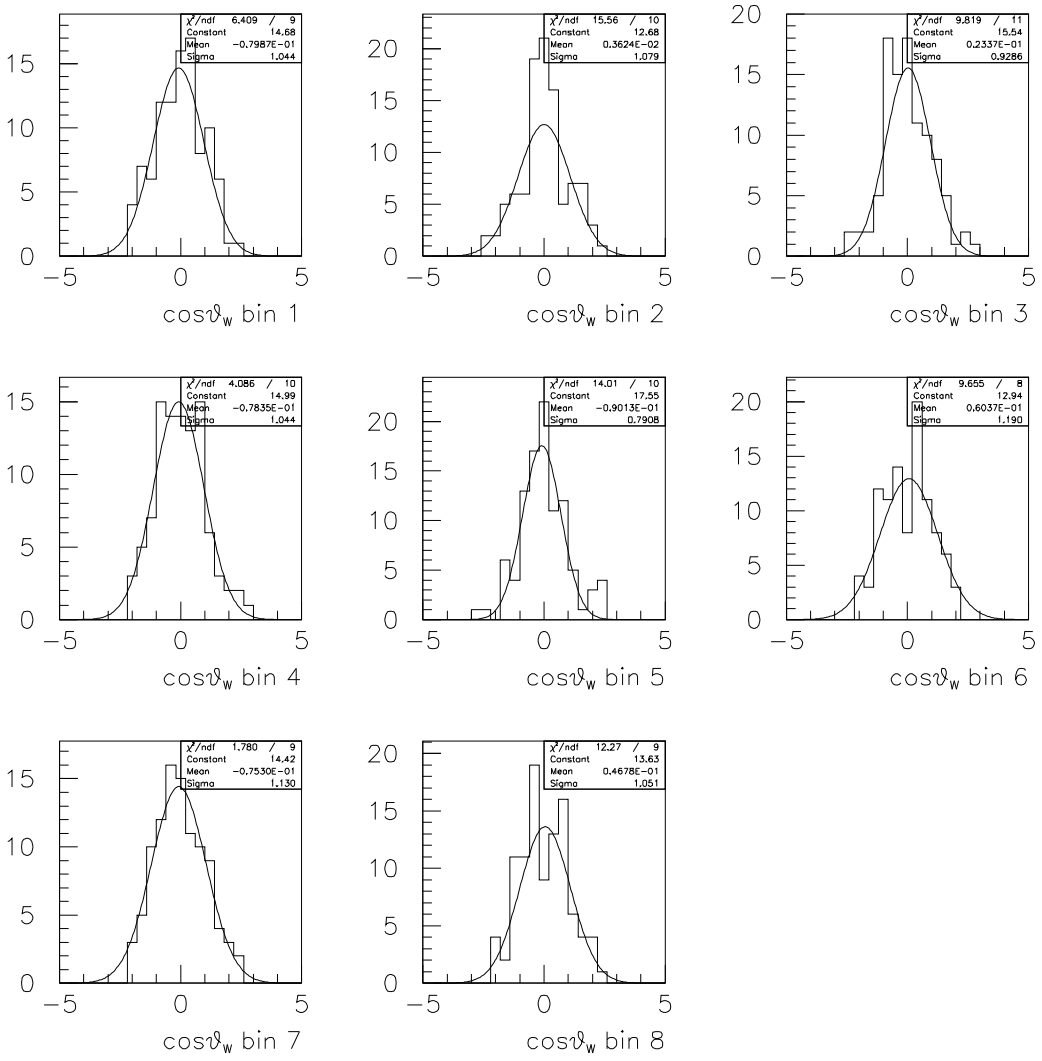

Pull distributions Re $(\rho+-)$

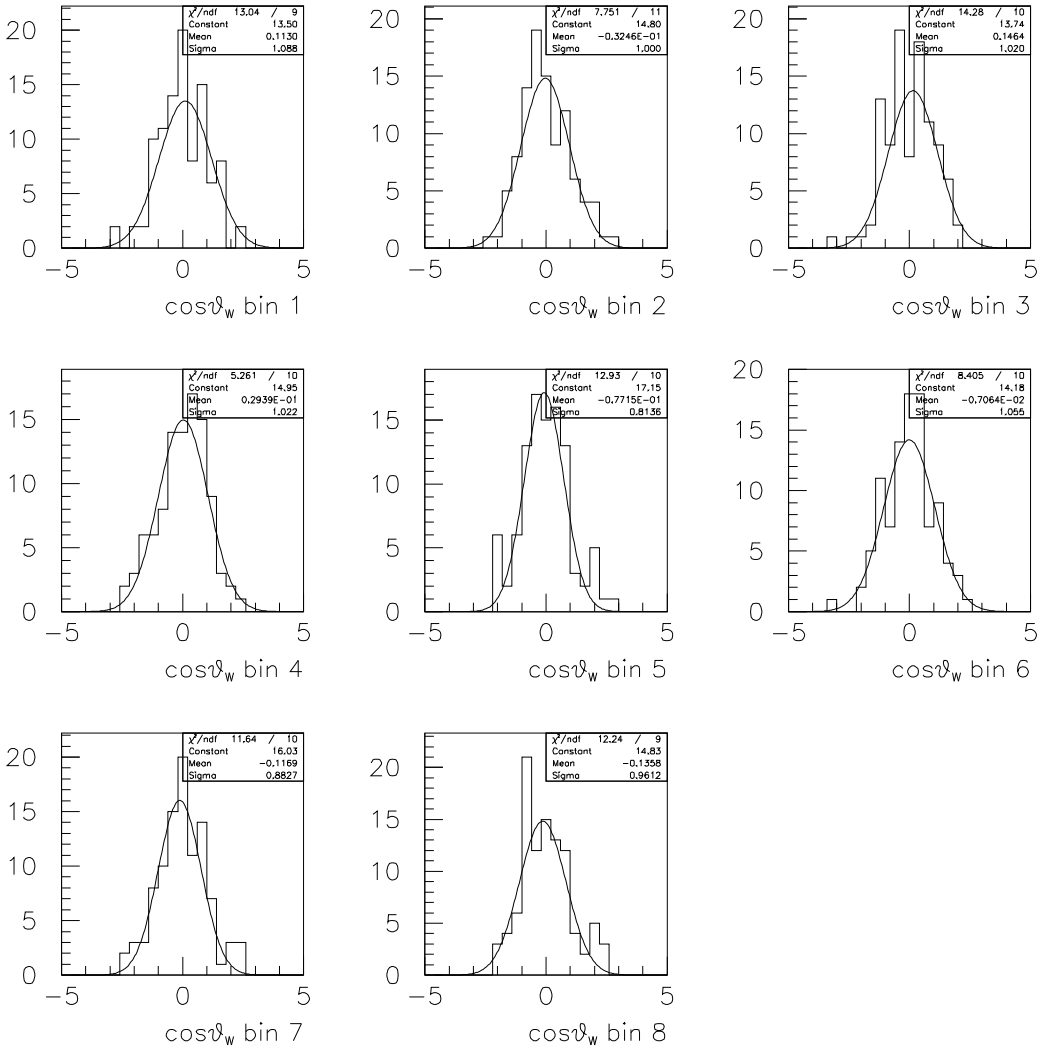

Pull distributions Re $(\rho+0)$

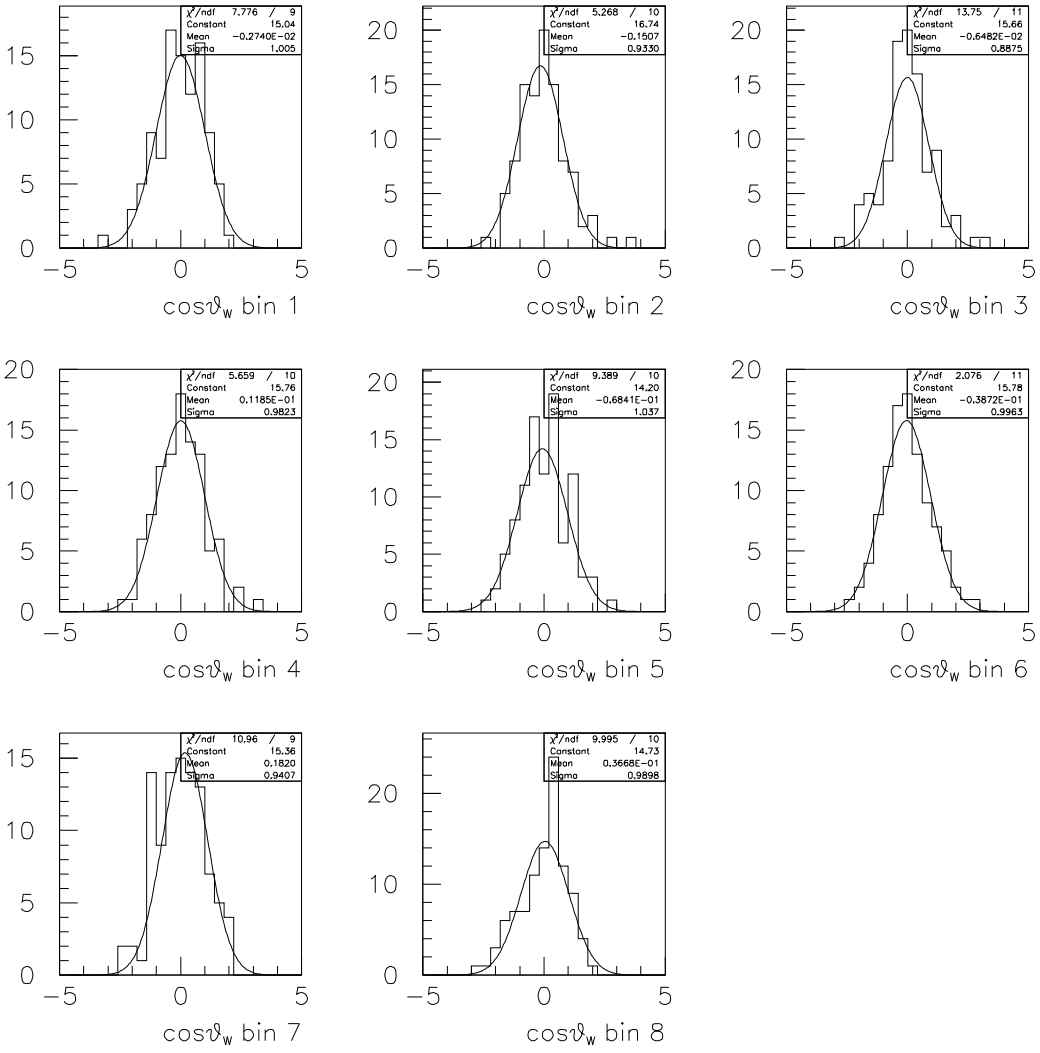

Pull distributions Re $(\rho - 0)$

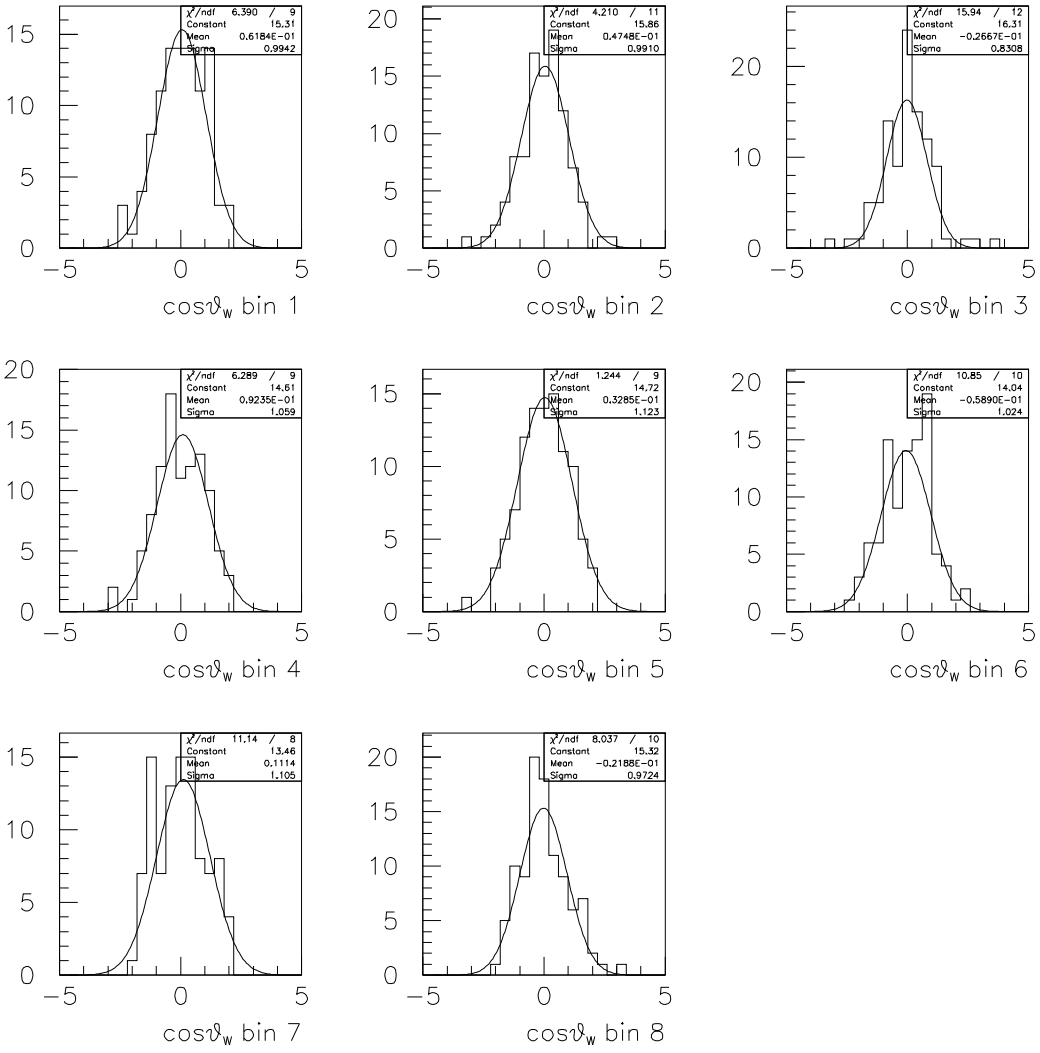

Pull distributions Im $(\rho+-)$

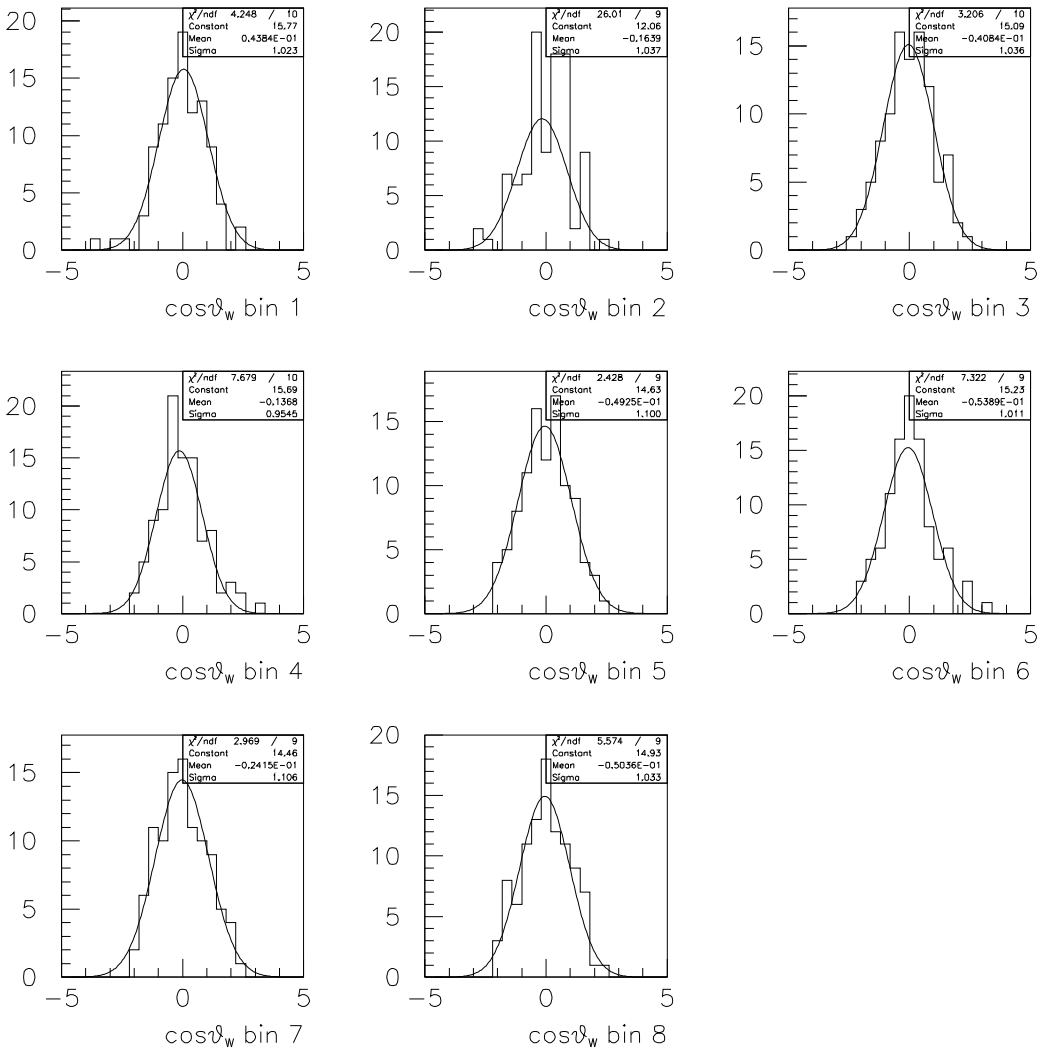

Pull distributions Im (ρ+0)

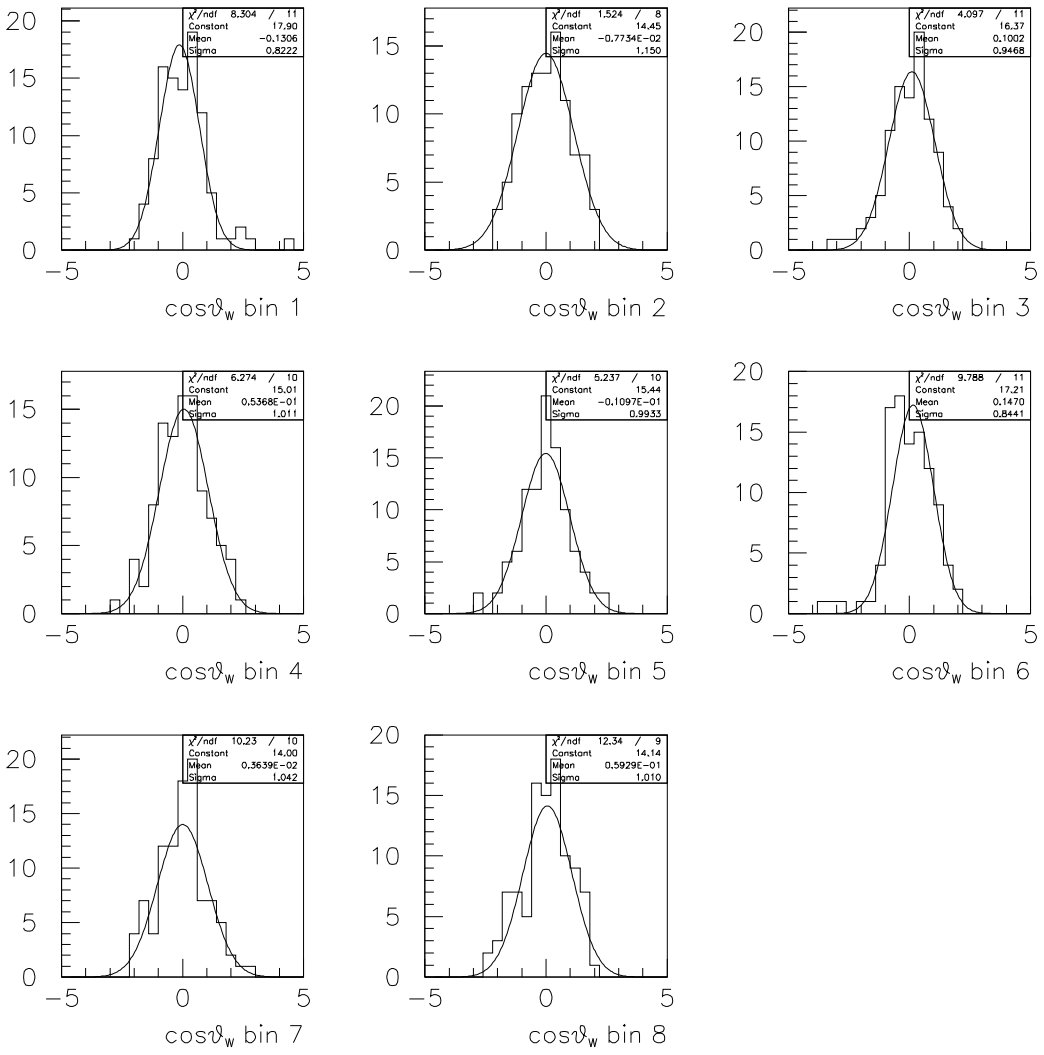

Appendix D

Summary SDM statistical and systematic uncertainties

D.1 Single W SDM elements

D.1.1 $qqe\nu(\gamma)$ final state

L3 189-209 GeV data	$\rho_{++}(\cos\theta_{W^-}\ bin)$							
***qqeν*(γ) final state**	1	2	3	4	5	6	7	8
ρ_{++}	0.644	0.458	0.500	0.491	0.144	0.116	0.056	0.061
$\sigma_{tot}(\rho_{++})$	0.123	0.116	0.103	0.102	0.078	0.070	0.050	0.046
$\sigma_{stat}(\rho_{++})$	0.112	0.113	0.098	0.099	0.076	0.067	0.048	0.039
$\sigma_{sys}(\rho_{++})$	0.049	0.028	0.029	0.024	0.017	0.021	0.015	0.024
Source of systematic uncertainty								
MC statistics	0.036	0.009	0.019	0.007	0.008	0.006	0.004	0.018
Correction method	0.002	0.003	< 0.001	0.004	0.004	0.003	0.003	0.004
Charge confusion	0.024	0.018	0.004	0.006	0.002	0.003	0.002	0.004
Lepton reconstruction	0.002	0.002	0.001	0.002	< 0.001	0.002	< 0.001	0.002
Jet reconstruction	0.017	0.012	0.015	0.017	0.004	0.013	0.004	0.007
FSR	0.001							
$\mathcal{O}(\alpha)$ corrections	0.005	0.004	< 0.001	0.002	< 0.001	< 0.001	< 0.001	< 0.001
Hadronisation	0.013							

L3 189-209 GeV data	$\rho_{--}(\cos\theta_{W^-}\ bin)$							
***qqeν*(γ) final state**	1	2	3	4	5	6	7	8
ρ_{--}	-0.011	0.088	0.315	0.249	0.371	0.411	0.711	0.818
$\sigma_{tot}(\rho_{--})$	0.142	0.133	0.112	0.093	0.088	0.085	0.073	0.061
$\sigma_{stat}(\rho_{--})$	0.140	0.132	0.107	0.090	0.086	0.084	0.071	0.054
$\sigma_{sys}(\rho_{--})$	0.025	0.014	0.032	0.024	0.016	0.014	0.016	0.027
Source of systematic uncertainty								
MC statistics	0.005	0.006	0.010	0.008	0.009	0.004	0.006	0.022
Correction method	0.006	0.007	0.002	0.003	0.004	0.001	< 0.001	0.004
Charge confusion	0.021	0.003	0.028	0.007	0.007	0.005	0.002	0.012
Lepton reconstruction	< 0.001	< 0.001	0.003	0.003	0.003	0.002	< 0.001	< 0.001
Jet reconstruction	0.006	0.006	0.004	0.020	0.006	0.009	0.012	0.003
FSR	0.001							
$\mathcal{O}(\alpha)$ corrections	< 0.001	0.002	< 0.001	< 0.001	< 0.001	0.002	< 0.001	0.001
Hadronisation	0.008							

L3 189-209 GeV data	$\rho_{00}(\cos\theta_{W^-}\ bin)$							
***qqeν*(γ) final state**	1	2	3	4	5	6	7	8
ρ_{00}	0.367	0.454	0.184	0.260	0.485	0.474	0.233	0.121
$\sigma_{tot}(\rho_{00})$	0.213	0.198	0.169	0.155	0.139	0.124	0.100	0.089
$\sigma_{stat}(\rho_{00})$	0.202	0.195	0.164	0.148	0.132	0.120	0.097	0.075
$\sigma_{sys}(\rho_{00})$	0.066	0.036	0.038	0.046	0.043	0.031	0.026	0.047
Source of systematic uncertainty								
MC statistics	0.037	0.017	0.019	0.020	0.036	0.014	0.009	0.038
Correction method	0.008	0.010	< 0.001	0.006	0.009	0.004	0.004	0.008
Charge confusion	0.045	0.021	0.024	0.001	0.004	0.003	< 0.001	0.016
Lepton reconstruction	0.003	0.001	0.001	< 0.001	0.004	0.004	< 0.001	0.003
Jet reconstruction	0.022	0.008	0.011	0.036	0.009	0.019	0.015	0.009
FSR	0.001							
$\mathcal{O}(\alpha)$ corrections	0.006	0.006	0.001	0.002	< 0.001	0.003	< 0.001	0.002
Hadronisation	0.019							

L3 189-209 GeV data	$\mathrm{Re}(\rho_{+-})(\cos\theta_{W^-}\ bin)$							
***qqeν(γ)* final state**	1	2	3	4	5	6	7	8
$\mathrm{Re}(\rho_{+-})$	0.153	0.096	-0.262	-0.101	-0.049	0.021	-0.018	-0.139
$\sigma_{tot}(\mathrm{Re}(\rho_{+-}))$	0.161	0.180	0.153	0.133	0.127	0.115	0.102	0.077
$\sigma_{stat}(\mathrm{Re}(\rho_{+-}))$	0.154	0.176	0.140	0.131	0.124	0.113	0.091	0.075
$\sigma_{sys}(\mathrm{Re}(\rho_{+-}))$	0.046	0.037	0.063	0.025	0.028	0.022	0.046	0.015
Source of systematic uncertainty								
MC statistics	0.006	0.015	0.013	0.007	0.016	0.016	0.041	0.004
Correction method	0.009	0.003	0.004	< 0.001	0.003	< 0.001	0.006	0.001
Charge confusion	0.040	0.016	0.050	0.017	0.016	0.003	0.009	0.003
Lepton reconstruction	< 0.001	0.008	0.009	0.004	0.005	0.003	0.003	< 0.001
Jet reconstruction	0.015	0.023	0.031	0.010	0.005	0.004	0.009	0.002
FSR	0.002							
$\mathcal{O}(\alpha)$ corrections	< 0.001	< 0.001	< 0.001	< 0.001	< 0.001	< 0.001	< 0.001	< 0.001
Hadronisation	0.014							

L3 189-209 GeV data	$\mathrm{Re}(\rho_{+0})(\cos\theta_{W^-}\ bin)$							
***qqeν(γ)* final state**	1	2	3	4	5	6	7	8
$\mathrm{Re}(\rho_{+0})$	0.426	0.127	-0.062	0.114	0.156	0.080	-0.048	-0.004
$\sigma_{tot}(\mathrm{Re}(\rho_{+0}))$	0.178	0.144	0.105	0.119	0.081	0.086	0.068	0.054
$\sigma_{stat}(\mathrm{Re}(\rho_{+0}))$	0.142	0.139	0.100	0.112	0.080	0.080	0.063	0.048
$\sigma_{sys}(\mathrm{Re}(\rho_{+0}))$	0.108	0.039	0.032	0.038	0.015	0.031	0.026	0.023
Source of systematic uncertainty								
MC statistics	0.031	0.009	0.006	0.009	0.003	0.003	0.005	0.012
Correction method	0.004	0.001	< 0.001	< 0.001	0.001	< 0.001	0.001	0.002
Charge confusion	0.102	0.035	0.027	0.019	0.001	0.016	0.014	0.012
Lepton reconstruction	0.001	0.002	0.002	0.012	< 0.001	0.002	0.001	0.002
Jet reconstruction	0.009	0.005	0.003	0.026	0.001	0.023	0.017	0.008
FSR	0.002							
$\mathcal{O}(\alpha)$ corrections	0.006	0.003	0.003	< 0.001	< 0.001	0.002	0.001	< 0.001
Hadronisation	0.013							

L3 189-209 GeV data	$\mathrm{Re}(\rho_{-0})(\cos\theta_{W^-}\ bin)$							
***qqeν(γ)* final state**	1	2	3	4	5	6	7	8
$\mathrm{Re}(\rho_{-0})$	-0.091	0.207	0.258	0.153	0.228	0.272	0.379	0.083
$\sigma_{tot}(\mathrm{Re}(\rho_{-0}))$	0.163	0.167	0.115	0.118	0.111	0.100	0.091	0.066
$\sigma_{stat}(\mathrm{Re}(\rho_{-0}))$	0.151	0.165	0.113	0.110	0.105	0.096	0.082	0.059
$\sigma_{sys}(\mathrm{Re}(\rho_{-0}))$	0.061	0.027	0.022	0.042	0.039	0.029	0.039	0.028
Source of systematic uncertainty								
MC statistics	0.008	0.010	0.009	0.012	0.012	0.002	0.021	0.013
Correction method	0.004	0.008	0.004	0.003	< 0.001	0.004	0.002	0.002
Charge confusion	0.059	0.018	0.010	0.024	0.026	0.016	0.010	0.015
Lepton reconstruction	< 0.001	0.006	0.001	0.006	0.005	0.002	< 0.001	0.003
Jet reconstruction	0.005	0.007	0.004	0.030	0.021	0.020	0.029	0.013
FSR	0.002							
$\mathcal{O}(\alpha)$ corrections	0.003	< 0.001	0.002	< 0.001	< 0.001	0.002	< 0.001	< 0.001
Hadronisation	0.013							

L3 189-209 GeV data	$\mathrm{Im}(\rho_{+-})(\cos\theta_{W^-}\ bin)$							
***qqeν(γ)* final state**	1	2	3	4	5	6	7	8
$\mathrm{Im}(\rho_{+-})$	-0.034	0.239	-0.081	-0.047	0.005	0.193	0.221	0.081
$\sigma_{tot}(\mathrm{Im}(\rho_{+-}))$	0.159	0.186	0.154	0.167	0.134	0.128	0.104	0.077
$\sigma_{stat}(\mathrm{Im}(\rho_{+-}))$	0.158	0.185	0.152	0.166	0.132	0.126	0.102	0.076
$\sigma_{sys}(\mathrm{Im}(\rho_{+-}))$	0.020	0.022	0.025	0.019	0.020	0.021	0.021	0.012
Source of systematic uncertainty								
MC statistics	0.007	0.017	0.014	0.007	0.015	0.011	0.002	0.007
Correction method	0.006	0.005	0.007	0.011	< 0.001	0.005	0.007	0.002
Charge confusion	0.012	0.004	0.011	0.009	0.005	0.012	0.015	0.003
Lepton reconstruction	< 0.001	0.002	0.002	< 0.001	0.004	0.001	< 0.001	0.002
Jet reconstruction	0.007	0.004	0.012	0.003	0.008	0.007	0.005	0.004
FSR	0.002							
$\mathcal{O}(\alpha)$ corrections	< 0.001	< 0.001	< 0.001	< 0.001	< 0.001	< 0.001	< 0.001	< 0.001
Hadronisation	0.008							

L3 189-209 GeV data	$\mathrm{Im}(\rho_{+0})(\cos\theta_{W^-}\ bin)$							
***qqeν*(γ) final state**	1	2	3	4	5	6	7	8
$\mathrm{Im}(\rho_{+0})$	-0.088	-0.155	0.059	-0.048	0.136	-0.025	-0.010	-0.119
$\sigma_{tot}(\mathrm{Im}(\rho_{+0}))$	0.166	0.145	0.133	0.125	0.093	0.091	0.072	0.057
$\sigma_{stat}(\mathrm{Im}(\rho_{+0}))$	0.162	0.143	0.131	0.123	0.091	0.089	0.070	0.055
$\sigma_{sys}(\mathrm{Im}(\rho_{+0}))$	0.037	0.027	0.022	0.018	0.019	0.018	0.012	0.013
Source of systematic uncertainty								
MC statistics	0.012	0.014	0.010	0.009	0.012	0.007	< 0.001	0.004
Correction method	0.006	0.016	< 0.001	0.002	0.002	0.005	< 0.001	< 0.001
Charge confusion	0.026	0.003	< 0.001	0.004	0.005	0.010	0.001	0.002
Lepton reconstruction	0.002	< 0.001	0.005	0.001	0.004	0.002	< 0.001	< 0.001
Jet reconstruction	0.013	0.010	0.015	0.010	0.008	0.005	0.002	0.006
FSR	0.001							
$\mathcal{O}(\alpha)$ corrections	0.012	0.002	0.005	< 0.001	< 0.001	< 0.001	< 0.001	< 0.001
Hadronisation	0.011							

L3 189-209 GeV data	$\mathrm{Im}(\rho_{-0})(\cos\theta_{W^-}\ bin)$							
***qqeν*(γ) final state**	1	2	3	4	5	6	7	8
$\mathrm{Im}(\rho_{-0})$	-0.029	-0.111	0.139	-0.025	0.095	0.098	0.069	-0.227
$\sigma_{tot}(\mathrm{Im}(\rho_{-0}))$	0.189	0.141	0.129	0.107	0.097	0.102	0.104	0.069
$\sigma_{stat}(\mathrm{Im}(\rho_{-0}))$	0.187	0.140	0.128	0.105	0.097	0.100	0.101	0.068
$\sigma_{sys}(\mathrm{Im}(\rho_{-0}))$	0.029	0.022	0.018	0.017	0.013	0.018	0.021	0.014
Source of systematic uncertainty								
MC statistics	0.013	0.011	0.008	0.010	0.002	0.011	0.009	0.006
Correction method	0.006	0.008	0.004	0.002	< 0.001	0.010	0.003	0.001
Charge confusion	0.022	0.007	0.003	0.007	0.001	0.002	0.005	0.006
Lepton reconstruction	< 0.001	0.006	0.002	< 0.001	0.001	0.002	< 0.001	< 0.001
Jet reconstruction	0.004	0.012	0.011	0.004	0.006	0.002	0.014	0.006
FSR	0.001							
$\mathcal{O}(\alpha)$ corrections	0.005	< 0.001	0.003	0.003	0.003	< 0.001	0.002	0.002
Hadronisation	0.009							

D.1.2 $qq\mu\nu(\gamma)$ final state

L3 189-209 GeV data	$\rho_{++}(\cos\theta_{W^-}\ bin)$							
$\boldsymbol{qq\mu\nu(\gamma)}$ **final state**	1	2	3	4	5	6	7	8
ρ_{++}	0.947	0.756	0.456	0.194	0.248	0.090	0.237	0.068
$\sigma_{tot}(\rho_{++})$	0.158	0.132	0.150	0.094	0.087	0.066	0.063	0.043
$\sigma_{stat}(\rho_{++})$	0.157	0.129	0.149	0.093	0.086	0.065	0.061	0.038
$\sigma_{sys}(\rho_{++})$	0.016	0.027	0.019	0.016	0.014	0.012	0.014	0.019
Source of systematic uncertainty								
MC statistics	0.010	0.021	0.013	0.010	0.008	0.001	0.009	0.015
Correction method	0.005	< 0.001	0.004	0.003	0.002	0.003	0.002	0.002
Charge confusion	0.002	< 0.001	< 0.001	< 0.001	< 0.001	< 0.001	< 0.001	< 0.001
Lepton reconstruction	< 0.001	0.002	< 0.001	0.001	< 0.001	< 0.001	0.001	< 0.001
Jet reconstruction	0.003	0.009	0.007	0.005	0.002	< 0.001	0.002	< 0.001
FSR	< 0.001							
$\mathcal{O}(\alpha)$ corrections	0.003	0.006	0.002	0.002	0.002	< 0.001	< 0.001	< 0.001
Hadronisation	0.011							

L3 189-209 GeV data	$\rho_{--}(\cos\theta_{W^-}\ bin)$							
$\boldsymbol{qq\mu\nu(\gamma)}$ **final state**	1	2	3	4	5	6	7	8
ρ_{--}	0.257	0.050	0.114	0.323	0.607	0.616	0.771	0.646
$\sigma_{tot}(\rho_{--})$	0.142	0.100	0.098	0.095	0.107	0.095	0.089	0.056
$\sigma_{stat}(\rho_{--})$	0.138	0.098	0.094	0.094	0.104	0.094	0.086	0.055
$\sigma_{sys}(\rho_{--})$	0.031	0.018	0.027	0.017	0.025	0.014	0.025	0.013
Source of systematic uncertainty								
MC statistics	0.026	0.007	0.019	0.010	0.021	0.006	0.021	0.004
Correction method	0.009	0.002	0.002	0.002	0.005	0.003	0.003	0.001
Charge confusion	0.001	< 0.001	< 0.001	< 0.001	< 0.001	< 0.001	< 0.001	< 0.001
Lepton reconstruction	< 0.001	0.001	< 0.001	0.001	< 0.001	< 0.001	< 0.001	< 0.001
Jet reconstruction	0.003	0.010	0.015	0.004	< 0.001	0.002	0.002	0.001
FSR	< 0.001							
$\mathcal{O}(\alpha)$ corrections	0.002	0.004	< 0.001	< 0.001	< 0.001	< 0.001	< 0.001	< 0.001
Hadronisation	0.012							

L3 189-209 GeV data	$\rho_{00}(\cos\theta_{W^-}\ bin)$							
$\boldsymbol{qq\mu\nu(\gamma)}$ **final state**	1	2	3	4	5	6	7	8
ρ_{00}	-0.204	0.194	0.430	0.483	0.144	0.294	-0.009	0.286
$\sigma_{tot}(\rho_{00})$	0.233	0.189	0.204	0.144	0.156	0.132	0.124	0.083
$\sigma_{stat}(\rho_{00})$	0.231	0.187	0.203	0.142	0.153	0.131	0.122	0.076
$\sigma_{sys}(\rho_{00})$	0.031	0.027	0.020	0.024	0.029	0.019	0.024	0.032
Source of systematic uncertainty								
MC statistics	0.022	0.016	0.006	0.017	0.022	0.010	0.017	0.028
Correction method	0.014	0.002	0.006	0.002	0.008	< 0.001	< 0.001	< 0.001
Charge confusion	0.001	< 0.001	< 0.001	< 0.001	< 0.001	< 0.001	< 0.001	< 0.001
Lepton reconstruction	< 0.001	< 0.001	0.001	0.002	< 0.001	< 0.001	0.002	< 0.001
Jet reconstruction	0.002	0.008	0.008	0.003	0.003	0.003	0.002	0.002
FSR	0.001							
$\mathcal{O}(\alpha)$ corrections	< 0.001	0.010	0.001	0.002	0.003	0.002	0.001	0.001
Hadronisation	0.016							

L3 189-209 GeV data	$\mathrm{Re}(\rho_{+-})(\cos\theta_{W^-}\ bin)$							
$\boldsymbol{qq\mu\nu(\gamma)}$ **final state**	1	2	3	4	5	6	7	8
$\mathrm{Re}(\rho_{+-})$	0.271	-0.107	-0.345	-0.174	-0.028	-0.173	-0.269	0.038
$\sigma_{tot}(\mathrm{Re}(\rho_{+-}))$	0.198	0.186	0.190	0.150	0.136	0.121	0.102	0.080
$\sigma_{stat}(\mathrm{Re}(\rho_{+-}))$	0.190	0.184	0.188	0.148	0.134	0.119	0.095	0.077
$\sigma_{sys}(\mathrm{Re}(\rho_{+-}))$	0.057	0.024	0.027	0.023	0.023	0.021	0.037	0.020
Source of systematic uncertainty								
MC statistics	0.051	0.008	0.018	0.013	0.010	0.010	0.030	0.009
Correction method	0.003	0.010	0.003	< 0.001	0.005	0.003	0.007	< 0.001
Charge confusion	< 0.001	< 0.001	0.001	< 0.001	< 0.001	< 0.001	< 0.001	< 0.001
Lepton reconstruction	< 0.001	0.004	0.004	0.002	0.006	0.001	< 0.001	< 0.001
Jet reconstruction	0.017	0.007	0.007	0.004	0.007	0.005	0.011	0.003
FSR	< 0.001							
$\mathcal{O}(\alpha)$ corrections	< 0.001	< 0.001	< 0.001	< 0.001	< 0.001	< 0.001	< 0.001	< 0.001
Hadronisation	0.018							

L3 189-209 GeV data	$\mathrm{Re}(\rho_{+0})(\cos\theta_{W^-}\ bin)$							
$\boldsymbol{qq\mu\nu(\gamma)}$ **final state**	1	2	3	4	5	6	7	8
$\mathrm{Re}(\rho_{+0})$	-0.107	0.075	-0.126	0.041	0.023	0.046	0.081	0.116
$\sigma_{tot}(\mathrm{Re}(\rho_{+0}))$	0.211	0.162	0.135	0.102	0.093	0.072	0.065	0.049
$\sigma_{stat}(\mathrm{Re}(\rho_{+0}))$	0.210	0.159	0.133	0.101	0.091	0.071	0.064	0.048
$\sigma_{sys}(\mathrm{Re}(\rho_{+0}))$	0.021	0.034	0.021	0.013	0.018	0.014	0.014	0.012
Source of systematic uncertainty								
MC statistics	0.011	0.010	0.015	0.005	0.009	0.006	0.005	0.002
Correction method	0.004	0.003	0.002	0.004	0.003	0.004	0.006	< 0.001
Charge confusion	0.006	< 0.001	< 0.001	< 0.001	< 0.001	< 0.001	< 0.001	< 0.001
Lepton reconstruction	0.006	0.003	< 0.001	0.003	< 0.001	0.002	0.002	0.001
Jet reconstruction	0.008	0.030	0.007	0.001	0.010	0.002	0.001	0.003
FSR	0.001							
$\mathcal{O}(\alpha)$ corrections	0.005	0.002	0.003	< 0.001	0.004	0.002	< 0.001	< 0.001
Hadronisation	0.012							

L3 189-209 GeV data	$\mathrm{Re}(\rho_{-0})(\cos\theta_{W^-}\ bin)$							
$\boldsymbol{qq\mu\nu(\gamma)}$ **final state**	1	2	3	4	5	6	7	8
$\mathrm{Re}(\rho_{-0})$	0.283	0.185	0.330	0.174	0.328	0.422	0.154	-0.074
$\sigma_{tot}(\mathrm{Re}(\rho_{-0}))$	0.181	0.116	0.107	0.117	0.128	0.100	0.091	0.058
$\sigma_{stat}(\mathrm{Re}(\rho_{-0}))$	0.175	0.111	0.102	0.113	0.124	0.098	0.089	0.053
$\sigma_{sys}(\mathrm{Re}(\rho_{-0}))$	0.046	0.032	0.031	0.032	0.031	0.020	0.019	0.024
Source of systematic uncertainty								
MC statistics	0.025	0.024	0.024	0.025	0.009	0.008	0.008	0.011
Correction method	0.005	0.010	0.007	0.009	0.010	0.004	0.002	0.012
Charge confusion	0.003	< 0.001	< 0.001	< 0.001	< 0.001	< 0.001	< 0.001	< 0.001
Lepton reconstruction	0.003	0.006	0.001	< 0.001	0.007	0.002	0.002	< 0.001
Jet reconstruction	0.034	0.005	0.007	0.002	0.021	0.005	0.004	< 0.001
FSR	< 0.001							
$\mathcal{O}(\alpha)$ corrections	0.002	< 0.001	0.002	0.002	0.002	0.004	< 0.001	0.002
Hadronisation	0.017							

L3 189-209 GeV data	$\mathrm{Im}(\rho_{+-})(\cos\theta_{W^-}\ bin)$							
***qqμν*(γ) final state**	1	2	3	4	5	6	7	8
$\mathrm{Im}(\rho_{+-})$	-0.118	0.038	0.144	-0.058	-0.212	-0.027	0.105	-0.052
$\sigma_{tot}(\mathrm{Im}(\rho_{+-}))$	0.192	0.191	0.194	0.169	0.145	0.127	0.102	0.078
$\sigma_{stat}(\mathrm{Im}(\rho_{+-}))$	0.191	0.189	0.192	0.167	0.144	0.126	0.101	0.077
$\sigma_{sys}(\mathrm{Im}(\rho_{+-}))$	0.020	0.031	0.023	0.026	0.015	0.016	0.014	0.015
Source of systematic uncertainty								
MC statistics	0.009	0.014	0.014	0.020	0.006	0.002	0.009	0.007
Correction method	0.004	0.026	0.014	0.013	0.007	0.012	< 0.001	0.005
Charge confusion	< 0.001	< 0.001	< 0.001	< 0.001	< 0.001	< 0.001	< 0.001	< 0.001
Lepton reconstruction	0.003	0.002	0.002	0.002	< 0.001	0.001	< 0.001	0.001
Jet reconstruction	0.014	0.004	0.002	0.003	0.004	0.001	< 0.001	0.003
FSR	< 0.001							
$\mathcal{O}(\alpha)$ corrections	< 0.001	< 0.001	< 0.001	< 0.001	< 0.001	< 0.001	< 0.001	< 0.001
Hadronisation	0.011							

L3 189-209 GeV data	$\mathrm{Im}(\rho_{+0})(\cos\theta_{W^-}\ bin)$							
***qqμν*(γ) final state**	1	2	3	4	5	6	7	8
$\mathrm{Im}(\rho_{+0})$	0.305	-0.160	0.051	0.090	0.036	-0.014	-0.041	-0.017
$\sigma_{tot}(\mathrm{Im}(\rho_{+0}))$	0.175	0.190	0.178	0.119	0.107	0.091	0.083	0.050
$\sigma_{stat}(\mathrm{Im}(\rho_{+0}))$	0.173	0.188	0.178	0.118	0.106	0.090	0.083	0.048
$\sigma_{sys}(\mathrm{Im}(\rho_{+0}))$	0.025	0.025	0.017	0.016	0.017	0.014	0.011	0.012
Source of systematic uncertainty								
MC statistics	0.013	0.014	0.006	0.006	0.010	0.010	0.005	0.003
Correction method	0.007	0.006	0.004	0.001	0.008	0.002	< 0.001	< 0.001
Charge confusion	0.002	< 0.001	< 0.001	< 0.001	< 0.001	< 0.001	< 0.001	< 0.001
Lepton reconstruction	0.004	0.008	0.003	0.002	0.001	< 0.001	0.002	0.001
Jet reconstruction	0.017	0.014	0.010	0.011	0.001	< 0.001	0.002	0.006
FSR	< 0.001							
$\mathcal{O}(\alpha)$ corrections	0.002	0.001	0.003	0.001	0.002	< 0.001	0.001	< 0.001
Hadronisation	0.010							

L3 189-209 GeV data	$\mathrm{Im}(\rho_{-0})(\cos\theta_{W^-}\ bin)$							
$\boldsymbol{qq\mu\nu(\gamma)}$ **final state**	1	2	3	4	5	6	7	8
$\mathrm{Im}(\rho_{-0})$	0.199	0.011	0.089	-0.045	-0.011	0.030	0.061	0.032
$\sigma_{tot}(\mathrm{Im}(\rho_{-0}))$	0.139	0.119	0.143	0.126	0.112	0.119	0.100	0.063
$\sigma_{stat}(\mathrm{Im}(\rho_{-0}))$	0.134	0.117	0.140	0.122	0.110	0.118	0.099	0.062
$\sigma_{sys}(\mathrm{Im}(\rho_{-0}))$	0.038	0.021	0.029	0.033	0.016	0.016	0.015	0.013
Source of systematic uncertainty								
MC statistics	0.014	0.013	0.008	0.022	0.003	0.008	0.007	0.002
Correction method	0.008	0.007	0.003	0.011	0.009	< 0.001	0.003	< 0.001
Charge confusion	0.001	< 0.001	< 0.001	< 0.001	< 0.001	< 0.001	< 0.001	< 0.001
Lepton reconstruction	< 0.001	0.008	< 0.001	< 0.001	0.002	0.003	< 0.001	< 0.001
Jet reconstruction	0.032	0.004	0.025	0.018	< 0.001	0.005	0.003	0.004
FSR	< 0.001							
$\mathcal{O}(\alpha)$ corrections	< 0.001	0.001	0.003	0.002	< 0.001	< 0.001	0.001	0.001
Hadronisation	0.012							

D.1.3 Combination

L3 189-209 GeV data	$\rho_{++}(\cos\theta_{W^-}\ bin)$							
$\boldsymbol{qqe\nu(\gamma)}$ **+** $\boldsymbol{qq\mu\nu(\gamma)}$ **final states**	1	2	3	4	5	6	7	8
ρ_{++}	0.747	0.587	0.487	0.333	0.189	0.102	0.124	0.065
$\sigma_{tot}(\rho_{++})$	0.096	0.087	0.084	0.070	0.059	0.049	0.040	0.033
$\sigma_{stat}(\rho_{++})$	0.091	0.085	0.082	0.068	0.057	0.047	0.038	0.027
$\sigma_{sys}(\rho_{++})$	0.028	0.021	0.019	0.017	0.014	0.015	0.014	0.018
Source of systematic uncertainty								
MC statistics	0.019	0.012	0.012	0.006	0.006	0.003	0.005	0.012
Correction method	0.003	0.002	0.002	0.003	0.003	0.002	0.002	0.002
Charge confusion	0.012	0.009	0.002	0.003	0.001	0.001	0.001	0.002
Lepton reconstruction	0.001	0.002	< 0.001	0.001	< 0.001	0.001	< 0.001	< 0.001
Jet reconstruction	0.009	0.007	0.008	0.009	0.002	0.007	0.002	0.003
FSR	0.004							
$\mathcal{O}(\alpha)$ corrections	0.004	0.005	0.001	0.002	0.001	< 0.001	< 0.001	< 0.001
Hadronisation	0.012							

L3 189-209 GeV data	$\rho_{--}(\cos\theta_{W^-}\ bin)$							
$\boldsymbol{qqe\nu(\gamma)}$ **+**$\boldsymbol{qq\mu\nu(\gamma)}$ **final states**	1	2	3	4	5	6	7	8
ρ_{--}	0.124	0.064	0.202	0.285	0.468	0.502	0.736	0.733
$\sigma_{tot}(\rho_{--})$	0.101	0.080	0.074	0.067	0.069	0.064	0.057	0.042
$\sigma_{stat}(\rho_{--})$	0.098	0.079	0.071	0.065	0.066	0.062	0.055	0.039
$\sigma_{sys}(\rho_{--})$	0.021	0.014	0.022	0.016	0.017	0.012	0.016	0.017
Source of systematic uncertainty								
MC statistics	0.013	0.005	0.011	0.006	0.012	0.003	0.011	0.011
Correction method	0.006	0.004	0.001	0.002	0.003	0.002	0.002	0.002
Charge confusion	0.011	0.001	0.014	0.004	0.003	0.003	0.001	0.006
Lepton reconstruction	< 0.001	< 0.001	0.001	0.002	0.002	< 0.001	< 0.001	< 0.001
Jet reconstruction	0.003	0.006	0.008	0.010	0.003	0.004	0.006	0.001
FSR	0.003							
$\mathcal{O}(\alpha)$ corrections	0.002	0.003	< 0.001	< 0.001	< 0.001	0.002	< 0.001	< 0.001
Hadronisation	0.010							

L3 189-209 GeV data	$\rho_{00}(\cos\theta_{W^-}\ bin)$							
$\boldsymbol{qqe\nu(\gamma)}$ **+**$\boldsymbol{qq\mu\nu(\gamma)}$ **final states**	1	2	3	4	5	6	7	8
ρ_{00}	0.119	0.318	0.282	0.376	0.340	0.391	0.140	0.202
$\sigma_{tot}(\rho_{00})$	0.157	0.138	0.130	0.107	0.104	0.091	0.079	0.062
$\sigma_{stat}(\rho_{00})$	0.152	0.135	0.128	0.103	0.100	0.089	0.076	0.054
$\sigma_{sys}(\rho_{00})$	0.039	0.027	0.025	0.029	0.029	0.023	0.022	0.032
Source of systematic uncertainty								
MC statistics	0.022	0.012	0.010	0.013	0.021	0.009	0.010	0.024
Correction method	0.008	0.005	0.003	0.003	0.006	0.002	0.002	0.004
Charge confusion	0.023	0.011	0.012	< 0.001	0.002	0.001	< 0.001	0.008
Lepton reconstruction	0.001	< 0.001	< 0.001	0.001	0.002	0.002	0.001	0.001
Jet reconstruction	0.011	0.006	0.007	0.018	0.005	0.009	0.008	0.005
FSR	0.006							
$\mathcal{O}(\alpha)$ corrections	0.003	0.008	0.001	0.002	0.002	0.002	< 0.001	0.002
Hadronisation	0.017							

L3 189-209 GeV data	Re ρ_{+-} ($\cos\theta_{W^-}$ *bin*)							
***qqeν*(γ) +*qqμν*(γ) final states**	1	2	3	4	5	6	7	8
Re ρ_{+-}	0.200	-0.001	-0.291	-0.133	-0.039	-0.071	-0.138	-0.052
σ_{tot}(Re ρ_{+-})	0.126	0.130	0.118	0.100	0.094	0.084	0.073	0.057
σ_{stat}(Re ρ_{+-})	0.120	0.127	0.112	0.098	0.091	0.082	0.066	0.054
σ_{sys}(Re ρ_{+-})	0.038	0.025	0.036	0.021	0.022	0.020	0.032	0.017
Source of systematic uncertainty								
MC statistics	0.026	0.009	0.011	0.008	0.009	0.009	0.025	0.005
Correction method	0.005	0.005	0.003	< 0.001	0.003	0.002	0.005	< 0.001
Charge confusion	0.020	0.008	0.025	0.009	0.008	0.001	0.004	0.001
Lepton reconstruction	< 0.001	0.005	0.005	0.002	0.004	0.002	0.001	< 0.001
Jet reconstruction	0.011	0.012	0.016	0.005	0.004	0.003	0.007	0.002
FSR	0.005							
$\mathcal{O}(\alpha)$ corrections	< 0.001	< 0.001	< 0.001	< 0.001	< 0.001	< 0.001	< 0.001	< 0.001
Hadronisation	0.016							

L3 189-209 GeV data	Re ρ_{+0} ($\cos\theta_{W^-}$ *bin*)							
***qqeν*(γ) +*qqμν*(γ) final states**	1	2	3	4	5	6	7	8
Re ρ_{+0}	0.259	0.104	-0.085	0.073	0.098	0.061	0.016	0.057
σ_{tot}(Re ρ_{+0})	0.130	0.108	0.082	0.078	0.062	0.056	0.048	0.037
σ_{stat}(Re ρ_{+0})	0.117	0.104	0.080	0.075	0.060	0.053	0.045	0.034
σ_{sys}(Re ρ_{+0})	0.056	0.027	0.021	0.022	0.014	0.019	0.017	0.016
Source of systematic uncertainty								
MC statistics	0.016	0.007	0.008	0.005	0.005	0.003	0.003	0.006
Correction method	0.003	0.001	< 0.001	0.002	0.001	0.002	0.003	< 0.001
Charge confusion	0.051	0.018	0.013	0.009	< 0.001	0.008	0.007	0.006
Lepton reconstruction	0.003	0.002	< 0.001	0.006	< 0.001	0.001	0.001	0.001
Jet reconstruction	0.006	0.015	0.004	0.013	0.005	0.011	0.009	0.004
FSR	0.003							
$\mathcal{O}(\alpha)$ corrections	0.005	0.002	0.003	< 0.001	0.002	0.002	0.001	< 0.001
Hadronisation	0.012							

L3 189-209 GeV data	Re ρ_{+0} ($\cos\theta_{W^-}$ *bin*)							
$\boldsymbol{qq e\nu(\gamma)}$ **+** $\boldsymbol{qq\mu\nu(\gamma)}$ **final states**	1	2	3	4	5	6	7	8
Re ρ_{+0}	0.259	0.104	-0.085	0.073	0.098	0.061	0.016	0.057
σ_{tot}(Re ρ_{+0})	0.130	0.108	0.082	0.078	0.062	0.056	0.048	0.037
σ_{stat}(Re ρ_{+0})	0.117	0.104	0.080	0.075	0.060	0.053	0.045	0.034
σ_{sys}(Re ρ_{+0})	0.056	0.027	0.021	0.022	0.014	0.019	0.017	0.016
Source of systematic uncertainty								
MC statistics	0.016	0.007	0.008	0.005	0.005	0.003	0.003	0.006
Correction method	0.003	0.001	< 0.001	0.002	0.001	0.002	0.003	< 0.001
Charge confusion	0.051	0.018	0.013	0.009	< 0.001	0.008	0.007	0.006
Lepton reconstruction	0.003	0.002	< 0.001	0.006	< 0.001	0.001	0.001	0.001
Jet reconstruction	0.006	0.015	0.004	0.013	0.005	0.011	0.009	0.004
FSR	0.003							
$\mathcal{O}(\alpha)$ corrections	0.005	0.002	0.003	< 0.001	0.002	0.002	0.001	< 0.001
Hadronisation	0.012							

L3 189-209 GeV data	Im ρ_{+-} ($\cos\theta_{W^-}$ *bin*)							
$\boldsymbol{qq e\nu(\gamma)}$ **+** $\boldsymbol{qq\mu\nu(\gamma)}$ **final states**	1	2	3	4	5	6	7	8
Im ρ_{+-}	-0.068	0.141	0.006	-0.052	-0.094	0.083	0.163	0.014
σ_{tot}(Im ρ_{+-})	0.123	0.134	0.121	0.119	0.098	0.090	0.073	0.055
σ_{stat}(Im ρ_{+-})	0.122	0.132	0.119	0.118	0.097	0.089	0.072	0.054
σ_{sys}(Im ρ_{+-})	0.016	0.020	0.018	0.018	0.014	0.015	0.014	0.012
Source of systematic uncertainty								
MC statistics	0.005	0.011	0.010	0.010	0.008	0.006	0.005	0.005
Correction method	0.004	0.013	0.008	0.008	0.004	0.006	0.003	0.003
Charge confusion	0.006	0.002	0.006	0.005	0.003	0.006	0.007	0.001
Lepton reconstruction	0.002	0.001	0.001	0.001	0.002	< 0.001	< 0.001	0.001
Jet reconstruction	0.008	0.003	0.006	0.002	0.004	0.003	0.003	0.002
FSR	0.003							
$\mathcal{O}(\alpha)$ corrections	< 0.001	< 0.001	< 0.001	< 0.001	< 0.001	< 0.001	< 0.001	< 0.001
Hadronisation	0.010							

L3 189-209 GeV data	Im ρ_{+0} ($\cos\theta_{W^-}$ *bin*)							
$\boldsymbol{qq e\nu(\gamma)}$ **+** $\boldsymbol{qq\mu\nu(\gamma)}$ **final states**	1	2	3	4	5	6	7	8
Im ρ_{+0}	0.095	-0.157	0.056	0.024	0.093	-0.019	-0.023	-0.062
σ_{tot}(Im ρ_{+0})	0.121	0.115	0.107	0.087	0.070	0.065	0.055	0.038
σ_{stat}(Im ρ_{+0})	0.118	0.114	0.106	0.085	0.069	0.063	0.054	0.036
σ_{sys}(Im ρ_{+0})	0.024	0.020	0.016	0.014	0.015	0.014	0.011	0.012
Source of systematic uncertainty								
MC statistics	0.009	0.010	0.006	0.005	0.008	0.006	0.002	0.003
Correction method	0.005	0.009	0.002	0.001	0.004	0.003	< 0.001	< 0.001
Charge confusion	0.013	0.001	< 0.001	0.002	0.002	0.005	< 0.001	0.001
Lepton reconstruction	0.002	0.004	0.003	0.001	0.002	0.001	0.001	< 0.001
Jet reconstruction	0.011	0.008	0.009	0.007	0.004	0.003	0.001	0.004
FSR	0.002							
$\mathcal{O}(\alpha)$ corrections	0.007	0.002	0.004	< 0.001	0.001	< 0.001	< 0.001	< 0.001
Hadronisation	0.011							

L3 189-209 GeV data	Im ρ_{-0} ($\cos\theta_{W^-}$ *bin*)							
$\boldsymbol{qq e\nu(\gamma)}$ **+** $\boldsymbol{qq\mu\nu(\gamma)}$ **final states**	1	2	3	4	5	6	7	8
Im ρ_{-0}	0.122	-0.039	0.116	-0.034	0.049	0.069	0.065	-0.085
σ_{tot}(Im ρ_{-0})	0.112	0.091	0.096	0.082	0.074	0.078	0.072	0.047
σ_{stat}(Im ρ_{-0})	0.109	0.090	0.094	0.080	0.073	0.076	0.071	0.046
σ_{sys}(Im ρ_{-0})	0.025	0.017	0.019	0.020	0.013	0.014	0.015	0.013
Source of systematic uncertainty								
MC statistics	0.010	0.008	0.006	0.012	0.002	0.007	0.006	0.003
Correction method	0.005	0.006	0.002	0.006	0.005	0.005	0.002	< 0.001
Charge confusion	0.011	0.004	0.001	0.004	< 0.001	0.001	0.002	0.003
Lepton reconstruction	< 0.001	0.005	0.001	< 0.001	0.001	0.002	< 0.001	< 0.001
Jet reconstruction	0.016	0.006	0.014	0.009	0.003	0.003	0.007	0.003
FSR	0.003							
$\mathcal{O}(\alpha)$ corrections	0.003	< 0.001	0.003	0.003	0.002	< 0.001	0.002	0.002
Hadronisation	0.011							

D.2 Tests of CPT- and CP-invariance

L3 189-209 GeV data	*CPT-invariance test*: $Im(\rho^{W^-}_{+-}) + Im(\rho^{W^+}_{-+})$ ($\cos\theta_{W^-}$ *bin*)							
$\boldsymbol{qq e\nu(\gamma)}$ and $\boldsymbol{qq\mu\nu(\gamma)}$ **final states**	1	2	3	4	5	6	7	8
$Im(\rho^{W^-}_{+-}) + Im(\rho^{W^+}_{-+})$	-0.155	0.215	0.228	-0.172	0.395	0.156	0.080	0.101
σ_{tot}	0.353	0.376	0.352	0.338	0.301	0.285	0.253	0.212
σ_{stat}	0.350	0.374	0.350	0.337	0.301	0.284	0.250	0.211
σ_{sys}	0.044	0.039	0.029	0.030	0.023	0.022	0.039	0.015
Source of systematic uncertainty								
MC statistics	0.039	0.015	0.018	0.021	0.019	0.018	0.037	0.009
Correction method	0.013	0.033	0.017	0.013	0.005	0.008	0.002	0.003
Charge confusion	0.008	0.001	0.009	0.008	0.003	< 0.001	0.001	0.003
Lepton reconstruction	< 0.001	0.002	< 0.001	0.001	< 0.001	0.002	< 0.001	< 0.001
Jet reconstruction	0.002	0.005	0.002	0.008	0.003	0.002	0.003	0.002
FSR	0.004							
$\mathcal{O}(\alpha)$ corrections	0.002	< 0.001	0.001	0.002	0.001	< 0.001	< 0.001	< 0.001
Hadronisation	0.011							

L3 189-209 GeV data	*CPT-invariance test*: $Im(\rho^{W^-}_{+0}) + Im(\rho^{W^+}_{-0})$ ($\cos\theta_{W^-}$ *bin*)							
$\boldsymbol{qq e\nu(\gamma)}$ and $\boldsymbol{qq\mu\nu(\gamma)}$ **final states**	1	2	3	4	5	6	7	8
$Im(\rho^{W^-}_{+0}) + Im(\rho^{W^+}_{-0})$	0.386	-0.221	0.126	0.061	0.106	0.032	0.070	-0.173
σ_{tot}	0.386	0.332	0.322	0.274	0.257	0.260	0.251	0.208
σ_{stat}	0.382	0.327	0.317	0.268	0.253	0.255	0.247	0.203
σ_{sys}	0.059	0.059	0.058	0.057	0.044	0.051	0.043	0.043
Source of systematic uncertainty								
MC statistics	0.020	0.021	0.020	0.021	0.015	0.013	0.016	0.014
Correction method	0.031	0.024	0.025	0.021	0.017	0.027	0.014	0.010
Charge confusion	0.014	0.004	0.008	0.007	0.006	0.008	0.003	0.010
Lepton reconstruction	0.004	0.013	0.005	0.004	0.004	0.004	0.002	0.004
Jet reconstruction	0.026	0.029	0.033	0.033	0.017	0.024	0.017	0.019
FSR	0.006							
$\mathcal{O}(\alpha)$ corrections	0.012	0.009	0.005	0.005	0.004	0.003	0.002	0.001
Hadronisation	0.033							

L3 189-209 GeV data	*CPT-invariance test*: $Im(\rho^{W^-}_{-0}) + Im(\rho^{W^+}_{+0})$ ($\cos\theta_{W^-}$ *bin*)							
$\boldsymbol{qqe\nu(\gamma)}$ and $\boldsymbol{qq\mu\nu(\gamma)}$ **final states**	1	2	3	4	5	6	7	8
$Im(\rho^{W^-}_{-0}) + Im(\rho^{W^+}_{+0})$	0.151	-0.168	0.309	-0.036	0.159	0.061	-0.014	-0.059
σ_{tot}	0.403	0.347	0.326	0.275	0.255	0.247	0.233	0.191
σ_{stat}	0.394	0.342	0.322	0.271	0.252	0.242	0.229	0.186
σ_{sys}	0.082	0.057	0.055	0.049	0.041	0.045	0.045	0.041
Source of systematic uncertainty								
MC statistics	0.030	0.015	0.014	0.019	0.010	0.007	0.007	0.010
Correction method	0.032	0.024	0.017	0.010	0.019	0.026	0.012	0.010
Charge confusion	0.029	0.013	0.009	0.003	0.002	0.003	0.003	0.007
Lepton reconstruction	0.008	0.005	0.005	0.004	0.003	0.004	0.002	0.004
Jet reconstruction	0.052	0.031	0.035	0.028	0.009	0.015	0.028	0.018
FSR	0.011							
$\mathcal{O}(\alpha)$ corrections	0.010	0.006	0.009	0.004	0.008	0.003	0.002	0.003
Hadronisation	0.032							

L3 189-209 GeV data	*CP-invariance test*: $Im(\rho^{W^-}_{+-})$ - $Im(\rho^{W^+}_{-+})$ ($\cos\theta_{W^-}$ *bin*)							
$\boldsymbol{qqe\nu(\gamma)}$ and $\boldsymbol{qq\mu\nu(\gamma)}$ **final states**	1	2	3	4	5	6	7	8
$Im(\rho^{W^-}_{+-})$ - $Im(\rho^{W^+}_{-+})$	-0.105	0.270	0.044	-0.111	-0.188	0.160	0.329	0.033
σ_{tot}	0.358	0.380	0.355	0.343	0.304	0.289	0.257	0.214
σ_{stat}	0.350	0.374	0.350	0.337	0.301	0.284	0.250	0.211
σ_{sys}	0.077	0.070	0.056	0.064	0.047	0.050	0.058	0.036
Source of systematic uncertainty								
MC statistics	0.039	0.015	0.018	0.021	0.019	0.018	0.037	0.009
Correction method	0.050	0.055	0.034	0.046	0.022	0.030	0.024	0.011
Charge confusion	0.016	0.015	0.017	0.012	0.009	0.010	0.015	0.003
Lepton reconstruction	0.004	0.003	0.003	0.003	0.003	0.002	< 0.001	0.002
Jet reconstruction	0.021	0.016	0.013	0.017	0.013	0.013	0.007	0.007
FSR	0.007							
$\mathcal{O}(\alpha)$ corrections	0.002	< 0.001	0.001	0.002	0.001	< 0.001	< 0.001	< 0.001
Hadronisation	0.032							

L3 189-209 GeV data	*CP-invariance test*: $Im(\rho_{+0}^{W^-})$ - $Im(\rho_{-0}^{W^+})$ ($\cos\theta_{W^-}$ *bin*)							
$\boldsymbol{qqe\nu}(\boldsymbol{\gamma})$ and $\boldsymbol{qq\mu\nu}(\boldsymbol{\gamma})$ **final states**	1	2	3	4	5	6	7	8
$Im(\rho_{+0}^{W^-})$ - $Im(\rho_{-0}W^+)$	0.097	-0.009	0.195	-0.074	-0.137	-0.150	-0.094	0.248
σ_{tot}	0.383	0.328	0.319	0.270	0.254	0.256	0.248	0.204
σ_{stat}	0.382	0.327	0.317	0.268	0.253	0.255	0.247	0.203
σ_{sys}	0.027	0.026	0.031	0.028	0.019	0.020	0.021	0.017
Source of systematic uncertainty								
MC statistics	0.020	0.021	0.020	0.021	0.015	0.013	0.016	0.014
Correction method	0.009	0.010	0.004	0.002	0.009	0.005	0.012	0.005
Charge confusion	0.010	0.002	< 0.001	0.002	0.003	0.006	< 0.001	0.004
Lepton reconstruction	0.002	0.003	0.002	< 0.001	0.003	0.002	0.001	< 0.001
Jet reconstruction	0.006	0.010	0.022	0.017	0.002	0.011	0.002	0.006
FSR	0.003							
$\mathcal{O}(\alpha)$ corrections	0.007	0.002	< 0.001	0.003	0.002	0.001	< 0.001	< 0.001
Hadronisation	0.005							

L3 189-209 GeV data	*CP-invariance test*: $Im(\rho_{-0}^{W^-})$ - $Im(\rho_{+0}^{W^+})$ ($\cos\theta_{W^-}$ *bin*)							
$\boldsymbol{qqe\nu}(\boldsymbol{\gamma})$ and $\boldsymbol{qq\mu\nu}(\boldsymbol{\gamma})$ **final states**	1	2	3	4	5	6	7	8
$Im(\rho_{-0}^{W^-})$ - $Im(\rho_{+0}^{W^+})$	0.040	0.230	0.361	-0.163	-0.220	0.022	0.085	0.234
σ_{tot}	0.396	0.343	0.323	0.272	0.252	0.243	0.229	0.187
σ_{stat}	0.394	0.342	0.322	0.271	0.252	0.242	0.229	0.186
σ_{sys}	0.038	0.023	0.025	0.022	0.016	0.012	0.016	0.013
Source of systematic uncertainty								
MC statistics	0.030	0.015	0.014	0.019	0.010	0.007	0.007	0.010
Correction method	0.018	0.011	0.012	0.006	0.011	0.009	0.003	0.005
Charge confusion	0.010	0.007	0.004	< 0.001	< 0.001	< 0.001	0.002	0.001
Lepton reconstruction	0.004	0.004	0.001	0.002	0.002	0.002	0.001	0.001
Jet reconstruction	0.009	0.008	0.016	0.008	0.005	0.002	0.013	0.005
FSR	0.009							
$\mathcal{O}(\alpha)$ corrections	0.002	0.003	0.001	0.002	0.004	0.001	0.001	0.001
Hadronisation	0.001							

List of Figures

List of Tables

Bibliography

[1] UA1 Collaboration, G.Arnison *et al. Experimental Observation of Isolated Large Transverse Energy Electrons with Associated Missing Energy at* $\sqrt{s} = 540$ *GeV*, Phys. Lett. **B 122** (1983) 103
UA1 Collaboration, G.Arnison *et al. Experimental Observation of Lepton Pairs of Invariant Mass Around 95 GeV/*c^2 *at the CERN SPS Collider*,
Phys. Lett. **B 126** (1983) 398.

[2] UA2 Collaboration, M.Banner *et al. Observation of Single Isolated Electrons pf High Transverse Momentum in Events with Missing Transverse Energy at the CERN anti-p p Collider*, Phys. Lett. **B 122** (1983) 476;
UA2 Collaboration, P.Bagnaia *et al. Evidence for the* $Z^0 \to e^+e^-$ *at the CERN anti-p p Collider*, Phys. Lett. **B 129** (1983) 130.

[3] K. Hagiwara *et al.*, Phys. Rev. **D 66**, 010001 (2002).

[4] ALEPH Collaboration, D.Buskulic *et al.*, Nucl. Instr. Meth. **A 294** (1990) 121.

[5] DELPHI Collaboration, P.Aarnio *et al.*, Nucl. Instr. Meth. **A 303** (1991) 233.

[6] L3 Collaboration, B.Adeva *et al.*, Nucl. Instr. Meth. **A 289** (1990) 35.

[7] OPAL Collaboration, K.Ahmet *et al.*, Nucl. Instr. Meth. **A 305** (1991) 275.

[8] N. Cabibbo, Phys. Rev. Lett. **10** (1963) 531;
M. Kobayashi and T. Maskawa, Prog. Theor. Phys. **49** (1973) 652.

[9] L3 Collaboration, P.Achard *et al.*, Phys. Lett. **B 557** (2003) 147.

[10] Feynman, Leighton and Sands, *The Feynman Lectures on Physics*,
Addison-Wesley Publ.Comp. (1963).

[11] W.Pauli, *Open Letter to Radioactive Persons* (1930).

[12] E.Fermi, *An Attempt of a Theory of Beta Radiation*, Z. Phys. **88** (1934) 161.

[13] T.D.Lee and C.-N.Yang, *Question of Parity Conservation in Weak Interactions*, Phys. Rev. **104** (1956) 254.

[14] C.S.Wu *et Al.*, *Experimental Test of Parity Conservation in Beta Decay*, Phys. Rev. **105** (1957) 1413.

[15] R.P.Feynman and M.Gell-Mann, *Theory of the Fermi Interaction*, Phys. Rev. **109** (1958) 193.

[16] J.S.Schwinger, *A Theory of Fundamental Interactions*, Ann. Phys. **2** (1957) 407.

[17] T.D.Lee and C.-N.Yang, *Possible Nonlocal Effects in μ Decay*, Phys. Rev. **D 108** (1957) 1611.

[18] S.L.Glashow, *Partial Symmetries of Weak Interactions*, Nucl. Phys. **22** (1961) 579.

[19] S.Weinberg, *A Model of Leptons*, Phys. Lett. **19** (1967) 1264.

[20] A.Salam, *Weak and Electromagnetic Interactions* in Elementary Particle Theory, proceedings of the Nobel Symposium held in 1968 at Lerum, Stockholm (Sweden) edited by N.Svartholm (Stockholm, 1968).

[21] G.'t Hooft, *Renormalizable Lagrangians for Massive Yang-Mills Fields*, Nucl. Phys. **B 35** (1971) 167;
G.'t Hooft and M.J.G.Veltman, *Regularization and Renormalization of Gauge Fields*, Nucl. Phys. **B 44** (1972) 189.

[22] P.W.Higgs, *Broken Symmetries, Massless Particles and Gauge Fields*, Phys. Lett. **12** (1964) 132.

[23] S.L.Glashow, Nucl. Phys. **22** (1961) 579;
S.Weinberg, Phys. Rev.Lett. **19** (1967) 1264;
A.Salam, in *Elementary Particles Theory*. ed. N.Svartholm, Stockholm, Almquist and Wiksell (1968) 367.

[24] LEP Collaborations ALEPH, DELPHI, L3, OPAL and LEP Working Group for the Higgs boson searches, *Search for the Standard Model Higgs boson at LEP*, Phys. Lett. **B 565** (2003) 61.

[25] Gargamelle Collaboration, F.J.Hasert *et al.*, *Search for Elastic Muon Neutrino Electron Scattering*, Phys. Lett. **B 46** (1973) 121;
Gargamelle Collaboration, F.J.Hasert *et al.*, *Observation of Neutrino-like Interactions without Muon or Electron in the Gargamelle Neutrino Experiment*, Phys. Lett. **B 46** (1973) 138.

[26] *Physics at LEP1*, G.Burgers, F.Jegerlehner, Report CERN 89-08 (1989).

[27] G. Altarelli, T. Sjöstrand, F. Zwirner, *Physics at LEP2*,
Report CERN 96-01 (1996), Vol.1.

[28] Y.K.Kim, Contribution to the Lepton-Photon Symposium 1997, Hamburg, Auguts 1997.

[29] LEPEWWG/MW/98-02,*LEP WW cross section and W Mass for the 1998 Summer conferences* (1998).

[30] R.Barate *et al.*, ALEPH Collaboration, Phys. Lett. **B 401** (1997) 347;
P.Abreu*et al.*, DELPHI Collaboration, Phys. Lett. **B 397** (1997) 158;
M.Acciarri *et al.*, L3 Collaboration, Phys. Lett. **B 398** (1997) 223;
K.Ackerstaff *et al.*, OPAL Collaboration, Phys. Lett. **B 389** (1996) 416.

[31] LEP Collaborations ALEPH, DELPHI, L3, OPAL and LEP Electroweak Working Group, the SLD Heavy Flavour and Electroweak Groups, *A Combination of Preliminary Electroweak Measurements and Constraints on the Standard Model*, CERN-EP/2003-091, December 2003.

[32] F.Halzen and A.D.Martin, *Quarks and Leptons*, John Wiley Sons, Inc.

[33] GENTLE version 2.00: *A Program for the Semi-Analytic Calculation of Predictions for the Process* $e^+e^- \to 4f$, Comput. Phys. Commun. **104** (1997) 161-187.

[34] K.Hagiwara *et al.*, Nucl. Phys. **B 282** (1987) 253.

[35] The L3 detector simulation is based on GEANT Version 3.15.
R.Brun *et al.*, GEANT3, CERN-DD/EE/84-1(Revised), 1987;
The GHEISHA program (H.Fesefeldt, RWTH Aachen Report PITHA 85/02,1985)
is used to simulate hadronic interactions.

[36] H.Fesefeldt, RWTH Aachen Preprint PITHA 85/02, 1985.

[37] KandY runs concurrently KORALW version 1.51 and YFSWW3 version 1.16
S.Jadach *et al.*, *The Monte Carlo Program KoralW version 1.51 and the Concurrent Monte Carlo KoralW & YFSWW3 with all Background Graphs and First Order Corrections to W-pair production*, Comp. Phys. Comm.**140** (2001) 475.

[38] *The Monte Carlo Program KoralW version 1.51 for All Four Fermion Final States in* e^+e^- *Collisions* , S.Jadach *et al.* Comp. Phys. Comm. **119** (1999) 272.

[39] YFSWW3 version 1.16 is used,
Precision Predictions for (Un)Stable W^+W^- *Pair Production At and Beyond LEP2 Energies*, S.Jadach *et al.*, Phys. Rev. **D 65** (2002) 093010.

[40] PYTHIA versions 5.722 and 6.1 are used
High-Energy Physics Event Generation with PYTHIA 5.7 and JETSET 7.4, T.Sjöstrand, Comp. Phys. Comm. **82** (1994) 74
High-Energy Physics Event Generation with PYTHIA 6.1, T.Sjöstrand *et al.* Comp. Phys. Comm. **135** (2001) 238.

[41] HERWIG version 6.202
A Monte Carlo Event Generator for Simulating Hadron Emission Reactions with Interfering Gluons G.Marchesini *et al.*, Comp. Phys. Comm. **67** (1992) 465; G.Corcella *et al.*, JHEP 0101:010,2001.

[42] ARIADNE version 4.12
A Program for the Simulation of QCD Cascades Implementing the Color Dipole Model, L.Lönnblad, Comp. Phys. Comm. **71** (1992) 15.

[43] KK2f version 4.14 and 4.19 are used.
S.Jadach *et al.* Comp. Phys. Comm. **130** (2000) 260;
S.Jadach *et al.* Phys. Rev. **D 63** (2001) 113009.

[44] KORALZ version 4.02 is used.
S.Jadach, B.F.L.Ward and Z.Was, Comp. Phys. Comm., **79** (1994) 503.

[45] BHAGENE version 3.0 is used.
J.H.Field, Phys. Lett. **B 323** (1994) 432;
J.H.Field and T.Riemann, Comp. Phys. Comm. **94** (1996) 53.

[46] BHWIDE version 1.01 is used.
S.Jadach *et al.* Phys. Rev. **D 40** (1989) 3582;
S.Jadach *et al.* Comp. Phys. Comm. **70** (1992) 305;
S.Jadach *et al.* *$\mathcal{O}(\alpha)$ YFS exponentiated Monte Carlo for Bhabha scattering at wide angles for LEP1/SLC and LEP2*, Phys. Lett. **B 390** (1997) 298.

[47] TEEGG version 7.1 is used.
D.Karlen, Nucl. Phys. **B 289** (1987) 23.

[48] DIAG 36 version 1.0 is used.
F.A.Berends *et al.*, Nucl. Phys. **B 253** (1985) 441.

[49] LEP4F version 2.0 is used.
J.A.M. Vermasseren *et al.*, Phys. Rev. **D 19** (1979) 137;
J.A.M. Vermasseren, Nucl. Phys. **B 229** (1983) 347.

[50] PHOJET version 1.05 is used.
R.Engel, Z. Phys. **C 66** (1995) 203;
R.Engel and J.Ranft, Phys. Rev. **D 54** (1996) 4244.

[51] PHOTOS version 2.3 is used, E.Barberio and Z.Was, Comp. Phys. Comm. **79** (1994) 291.

[52] EXCALIBUR version 1.11 is used,
A Monte Carlo Program to evaluate all Four Fermion Processes at LEP 200 and beyond, F.A.Berends, R.Kleiss and R.Pittau, Comp. Phys. Comm. **83** (1994) 141;
Comp. Phys. Comm. **85** (1995) 437.

[53] *Pair Production of W bosons in e^+e^- Interactions at $\sqrt{s} =$ 161 GeV*, Preprint CERN-PPE/97-14, February 1997, Phys. Lett. **B 398** (1997) 223.

[54] D.Bardin and R.Kleiss, *Event Generators for WW physics* in *Physics at LEP2*, Report CERN 96-01 (1996), Vol.2.

[55] RACOONW version 1.3 is used A.Denner *et al.*, *Electroweak Radiative Corrections to $e^+e^- \to W^+W^- \to 4$ fermions in Double Pole Approximation : the RACOONWW Approach*, Nucl. Phys. **B 587** (2000) 67;
A.Denner *et al.*, preprint hep-ph/0006307 (2000).

[56] L3 Collaboration, P.Achard *et al.*, *Measurement of Bose-Einstein Correlations in $e^+e^- \to W^+W^-$ Events at LEP*, Phys. Lett. **B 547** (2002) 139.

[57] L3 Collaboration, P.Achard *et al.*, *Search for Colour Reconnection Effects in $e^+e^- \to W^+W^- \to$ hadrons through Particle-Flow Studies at LEP*,
Phys. Lett. **B 561** (2003) 202;
L3 Collaboration, P.Achard *et al.*, *Search for Colour Singlet and Colour Reconnection Effects in Hadronic Z Decays at LEP*, Phys. Lett. **B 581** (2004) 19.

[58] T.Sjöstrand and V.A.Khoze,
Phys. Rev. Lett. **72** (1994) 28;
Z. Phys. **C 62** (1994) 281;
Eur. Phys. J. **C 6** (1999) 271.

[59] L.Camilleri *et al.*, *Physics with Very High Energy Electron-Positron Colliding Beams*, CERN-PPE 76-18 (1976);
"Committee for Future Accelerators, General Meeting on LEP", Villars-sur-Ollon 1981, ECFA 81054.

[60] A.A.Zholentz *et al.*, Phys. Lett., **B 96** (1980) 214;
A.S.Artamonov *et al.*, Phys. Lett., **B 118** (1982) 225;
A.N.Skrinskii and Yu.M.Shatunov, Sov. Phys. Usp., **32(6)** (1989) 548;
ARGUS Collaboration, D.P.Barber *et al.*, Phys. Lett., **B 135** (1984) 498;
CUSB Collaboration, W.W.McKay *et al.*, Phys. Rev., **D 29** (1984) 2483.

[61] A.A.Sokolov and I.M.Ternov, Sov. Phys. Dokl., **8** (1964) 1203.

[62] L.Arnaudon *et al.*, *The Energy Calibration of LEP in 1991*,
Preprint CERN-SL/92-37(DI) and CERN-PPE/92-125, 1992.

[63] L.Arnaudon *et al.*, *Accurate Measurement of the LEP Beam Energy by Resonant Depolarisation*,
Preprint CERN-SL/94-71(BI), 1994.

[64] A.Blondel *et al.*, Eur. Phys. J. **C 11** (1999) 573;
R.Assmann *et al.*,The LEP Energy Working Group:
Evaluation of the LEP Center-of-mass energy for data taken in 2000 , Internal Notes, LEP ECAL 01/01.

[65] I.C.Brock *et al.*, *Luminosity measurement in the L3 Detector at LEP*,
Nucl. Instr. Method **A 381** (1996) 236.

[66] F.Beissel *et al.*, *Construction and Performance of the L3 Central Tracking Detector*
Nucl. Instr. Meth. **A 332** (1993) 33.

[67] M.Caccia *et al.*, Nucl. Instr. Meth. **A 315** (1992) 197;
G.Ambrosi *et al.*, Nucl. Instr. Meth. **A 344** (1994) 133;
O.Adriani *et al.*, Nucl. Instr. Meth. **A 348** (1994) 431;
The L3 SMD Collaboration, M.Acciarri *et al.*, Nucl. Instr. Meth. **A 351** (1994) 300;
M.Acciarri *et al.*, Nucl. Instr. Meth. **A 360** (1995) 103.

[68] R.Sumner *et al.*, *The L3 BGO Electromagnetic Calorimeter*,
Nucl. Instr. Meth. **A 265** (1988) 252.

[69] H.Akbari *et al.*, Nucl. Instr. Meth. **A 315** (1992) 197.

[70] A.Bay *et al.*, *The Xenon Monitor of the L3 Electromagnetic Calorimeter*,
Nucl. Instr. Meth. **A 321** (1992) 119.

[71] A.Favara *et al.*, *Calibration of the L3 BGO Calorimeter using a RFQ Accelerator*,
Nucl. Phys. Proc. Suppl. **78** (1999) 465; Nucl. Instr. Meth. **A 461** (2001) 376.

[72] J.Wenninger, *Mesure des paramètres electro-faibles du Z avec la réaction* $e^+e^- \to e^+e^-(\gamma)$, Ph.D. thesis, Université de Genève, 1992.

[73] G.Basti *et al.*, *The L3 Lead Scintillating Fiber Calorimeter*,
Nucl. Instr. Meth. **A 374** (1996) 293.

[74] O.Adriani *et al.*, *Hadron Calorimetry in the L3 detector*,
Nucl. Instr. Meth. **A 302** (1991) 53.

[75] G.Chiefari *et al.*, *Muon Detection in the L3 Experiment at LEP*,
Nucl. Instr. Meth. **A 277** (1989) 187.

[76] I.C.Brock *et al.*, Nucl. Instr. Meth. **A 381** (1996) 236.

[77] T.van Rhee, F.Filthaut and F.Linde, *VSAT Status and Performance*, L3 Note 2117, July 1997, submitted to Nucl. Instr. Method (1996).

[78] G.Basti *et al.*, *The L3 Lead Fiber Scintillating Fiber Calorimeter*, Nucl. Instr. Method **A 374** (1996) 293.

[79] R.Bizzarri *et al.*, *The First Level Energy Trigger of the L3 Experiment: Description of the Hardware*, Nucl. Instr. Method **A 317** (1992) 463;
P.Bagnaia *et al.*, *The First Level Energy Trigger of the L3 Experiment: Software and Performances* , Nucl. Instr. Method **A 324** (1993) 101;
S.Gentile *et al.*, *The Operation of the Upgraded L3 Energy Trigger*, Nucl. Instr. Method **A 344** (1994) 212.

[80] P.Bene *et al.*, *First Level Charged Particle Trigger for the L3 Detector*, Nucl. Instr. Method **A 306** (1991) 150.

[81] D.Haas *et al.*, *The New Inner-Tec Trigger of the L3 Experiment using a Hard-wired Neural Network Processor*, Nucl. Instr. Method **A 420** (1999) 101.

[82] M.Bourquin *et al.*, *The New Level-1 Trigger for the Forward Tagger of the L3 Experiment*, Nucl. Instr. Method **A 411** (1998) 275.

[83] Y.Bertsch *et al.*, *The Second Level Trigger of the L3 Experiment: the Implementation*, Nucl. Instr. Method **A 340** (1994) 309;
S.P.Beingessner *et al.*, *The Second Level Trigger of the L3 Experiment: the Event Selection*, Nucl. Instr. Method **A 340** (1994) 322.

[84] C.Dionisi *et al.*, *The third Level Trigger System of the L3 Experiment at LEP*, Nucl. Instr. Method **A 336** (1993) 78.

[85] S.Banjeree and F.Bruyant, The L3 Event Data Structure, Internal Report L3 Note 748, CERN, 1990
J.Swain and L.Taylor, L3 Computing Guide, Preprint NUB-3065, Northeastern University Boston, 1993;
B.Adeva *et al.*,*The L3 Database System*, Nucl. Instr. Meth. **A 309** (1991) 318.

[86] B.Schroers, *Track Reconstruction in the L3 Vertex Detector*, L3 Note 713, 1988;
J.Alcaraz, *Heliciodal Tracks*, L3 Note 1666, 1995;
J.Alcaraz, *SZ Reconstruction in the L3 Detector*, L3 Note 2318, 1998.

[87] S.Catani *et al.*, *A Cluster Algorithm for Jet Studies*, Z. Phys. **C 8** (1981) 167.

[88] H.J.Daum *et al.*, *New Clustering Algorithms for Multijet Cross sections in e^+e^- Annihilation*, Phys. Lett. **B 269** (1991) 432.

[89] L3 Collaboration, P.Achard *et al.*, *Measurement of the Cross Section of W pair-production at LEP*, Phys. Lett. B 600 (2004) 22-40.

[90] H.J. Daum *et al.*, Z. Phys. **C 8** (1981) 167.

[91] *Mesura della sezione d'urto del processo $e^+e^- \to W^+W^- \to q\bar{q}\tau\nu_\tau$ ad enegia del centro di massa di 189 GeV*, tesi di laurea, Paolo Violini.

[92] D.Bardin *et al.*, Nucl. Phys. (Proc. Suppl.) **B 37** (1994) 148;
F.A.Berends *et al.*, Nucl. Phys. (Proc. Suppl.) **B 37** (1994) 163;
W.Beenakker *et al.*, in *Physics at LEP2*, Report CERN 96-01 (1996), eds G.Altarelli, T.Sjöstrand, F.Zwirner, Volume 1, p 79;
D.Bardin *et al.*, in *Physics at LEP2*, Report CERN 96-01 (1996), eds G.Altarelli, T.Sjöstrand, F.Zwirner, Volume 2, p 3.

[93] The L3 Collaboration, M.Acciarri *et al.*, Phys. Lett. **B 398** (1997) 223.

[94] The L3 Collaboration, M.Acciarri *et al.*, Phys. Lett. **B 496** (2000) 19.

[95] M.Grünewald *et al.*, in LEP2 Monte Carlo workshop: Report of the Working Groups on Precision Calculations for LEP2 physics, HEP-PH/0005309.

[96] K.Hagiwara *et al.*, Phys. Rev. **D 66** (2002) 1.

[97] Lönnblad and T.Sjöstrand, Eur. Phys. J. **C 2** (1998) 165.

[98] B.Webber, J. Phys. **G 24** (1998) 287.

[99] L.Lönnblad, Z. Phys. **C 70** (1996) 107.

[100] The LEP WW Working Group, LEPEWWG/2004-02 prepared for the Summer 2004 conferences and the references therein
http://lepewwg.web.cern.ch/LEPEWWG/stanmod/, to be published.

[101] M.Bilenky, J.L. Knuer, F.M. Renard and D. Schildknecht,
Nucl. Phys. **B 419** (1994) 240.

[102] G.Gournaris, J.Layssac, G.Moultaka and F.M.Renard,
Int. J. Mod. Phys. **A 8** (1993) 3285.

[103] M.Grünewald and G.Passarino, *Four-Fermion Production in Electron-Positron Collisions* in *Reports of the Working Groups on Precision Calculations for LEP2 Physics*, Report CERN 2000-009 (2000), editors S.Jadach, G.Passarino, R.Pittau, pg 1.

[104] M.Dierckxsens, *Measurement of Triple Gauge-Boson Couplings in e^+e^- Collisions at LEP*, Ph.D.thesis, NIKHEF Amsterdam (2004).

[105] Particle Data Group, Hagiwara *et al.*, Phys. Rev. **D 66** (2002) 225.
.

[106] *Probability and Statistics in Particle Physics*,
A.G.Frodesen, O.Skjeggestad and H.Tøfte, Universitetsforlaget, Bergen-Oslo-Tromsø, 1979.

[107] P.R.Bevington, D.K.Robinson, *Data Reduction and Error Analysis for the Physical Sciences*, 3^rd edition, McGraw-Hill, 2003.

[108] G.Gournaris, D.Schildknecht and F.M.Renard, Phys. Lett. **B 263** (1991) 291.

[109] M.Bilenky *et al.*, *Trilinear couplings among the electroweak vector bosons and their determination at LEP2*, Nucl. Phys. **B 409** (1993) 22.

[110] H.Grotch, R.W.Robinett, *New Limits from Single-photon Searches at e^+e^- Colliders*, Phys. Rev. **D 36** (1987) 2153.

[111] UA2 Collaboration, J.Alliti *et al.*, *Direct Measurement of the W-γ Coupling at the CERN $\bar{p}p$ Collider*, Phys. Lett. **B 277** (1992) 194.

[112] F.Boudjema *et al.*, *Anomalous Moments of Quarks and Leptons from Nonstandard $WW\gamma$ Couplings*, Phys. Lett. **D 43** (1991) 2223.

[113] CDF Collaboration, F.Abe *et al. Limits on $WW\gamma$ and WWZ Couplings from WW and WZ Production in $\bar{p}p$ Collisions at $\sqrt{s} = 1.8$ TeV*, Phys. Rev. Lett. **75** (1995) 1017.

[114] ZEUS Collaboration, J.Breitweg *et al. W Production and the Search for Events with an Isolated High-Energy Lepton and Missing Transverse Momentum at HERA*, Phys. Lett. **B 471** (2000) 411.

[115] P.Molnar and M.Grünewald, *Measuring WWZ and $WW\gamma$ Coupling Constants with the Z-pole Data*, Phys. Lett. **B 461** (1999) 149.

[116] O.J.P.Eboli, M.C.Gonzalez-Garcia and S.F.Novaes, *Indirect Constraints on the Triple Gauge Boson Couplings from $Z \to b\bar{b}$ Partial Width: Update*,
Phys. Lett. **A 15** (2000) 1.

[117] S.Godfrey, and H.König, *Atomic Parity Violation as a Probe for Anomalous Gauge Boson Couplings*, Phys. Rev. **D 45** (1992) 3196.

[118] CLEO Collaboration, M.S.Alam *et al.*, *First Measurement of the Rate for the Inclusive Penguin Decay* $b \to s\gamma$, Phys. Rev.Lett. **74** (1995) 2885.

[119] G.Baillie, *Observing* $b \to s\mu+\mu-$ *Decays at Hadron Colliders*, Z. Phys. **C 61** (1994) 667.

[120] L3 Collaboration, P.Achard *et al.*, *Measurement of the Triple-Gauge-Boson Couplings of the W boson at LEP*, Phys. Lett. **B 586** (2004) 151-166.

[121] M.Diehl and O.Nachtmann, Z. Phys. **C 62** (1994) 397.

[122] ALEPH Collaboration, A.Heister *et al.*, Eur. Phys. J. **C 21** (2001) 423;
ALEPH Collaboration, Aleph Note 2003-015;
DELPHI Collaboration, P.Abreu *et al.*, Phys. Lett. **B 502** (2001) 9;
DELPHI Collaboration, Delphi Note 2003-051;
OPAL Collaboration, G.Abbiendi *et al.*, Eur. Phys. J. **C 33** (2004) 463.

[123] OPAL Collaboration, *Measurement of W boson Polarisations and* CP*-violating Triple Gauge Couplings from WW Production at LEP* Eur. Phys. J. **C 19** (2001), 229-240.

[124] M.Dobbs, *Probing the Three Gauge-boson Couplings in 14 TeV Proton-Proton Collisions*, Ph.D. thesis, University of Victoria (2002).

[125] Y.Kulik, on behalf of the DO Collaboration, *Recent Top Quark Results at D0*, to appear in the proceedings of the $XXXIX^{th}$ Rencontres de Moriond, Electroweak Interactions and Unified Theories (2004).

[126] F.Boudjema,*Aspects of W Physics at the Linear Collider*, preprint HEP-PH/9701409;
W.Beenakker, Acta. Phys. Polon. **B 28** (1997) 1461, preprint HEP-PH/9704401;
K.Monig,*Physics of Electroweak Gauge Bosons*, to appear in *Linear Collider Physics in the New Millenium*, World Scientific, preprint HEP-PH/0303023.

[127] W.Menges, *A Study of Charged Current Triple Gauge Couplings at TESLA*, LC-PHSM-2001-022.

[128] *Introduction to experimental particle physics*, R.Farrow, Cambridge University Press 1986.

[129] R.K.Bock, H.Grote, D.Notz and M.Regler, *Data Analysis Techniques for High-Energy Physics Experiments*, Cambridge University Press 1990.

[130] KK2F version 4.13 ; S.Jadach, B.F.L.Ward and Z.Was,
Comp. Phys. Comm. **130** (2000) 260.